Investigation of Presynaptic Plasticity Mechanisms at the Hippocampal Mossy Fiber Bouton

Inaugural-Dissertation
to obtain the academic degree
Doctor rerum naturalium (Dr. rer. nat.)

submitted to the Department of Biology, Chemistry, Pharmacy
of Freie Universität Berlin

by

Felicitas Brüntgens

31st January 2024

The experimental work underlying this thesis was performed between July 2018 and December 2023 under the supervision of Prof. Dr. Dietmar Schmitz at the Neuroscience Research Centre (NWFZ) of the Charité – Universitätsmedizin Berlin.

1st reviewer: Prof. Dr. Dietmar Schmitz

2nd reviewer: Prof. Dr. Stephan Sigrist

Date of defense: 08.07.2024

Acknowledgements

First and foremost, I want to thank **Dietmar Schmitz** for the opportunity to do my doctorate in his laboratory. Thanks to him, I had the freedom to explore different methods, to participate in conferences and seminars and thus to learn and develop as a scientist. I also want to thank **Stephan Sigrist** for taking over the position of my second reviewer and the possibility to use the STED microscope in his facility.

I sincerely want to thank my supervisor **Jörg Breustedt**, who always supported me on my way. Thanks to him, I gained a lot of factual knowledge, but also learned that modesty and caution would be desirable qualities for any researcher. I will especially remember the outstanding analysis consulting and data discussion by telephone during the lockdown of the COVID-19 pandemic. Thanks go also to **Benjamin Rost**, who accompanied me in the early days and continued to show interest in my work along the way. He was always open to share his knowledge and technical equipment.

A particular big thank goes to **Marta Orlando**, my mentor, ally and scientific role model. Her relentless interest in my work, her unconditional support and empowering personality helped me to keep my motivation up. She is an incredible and strong woman and I am grateful that we could work together in the "Team Mossy Fiber"! Thank you for your patience and support in all circumstances!

Judith von Sivers was a never-ending source of encouragement and I am thankful for our friendship. It was a pleasure to experience the first GRC conference together and sometimes nothing else helps better than having an after-work beer with you! In this context, I also want to thank **Aileen Hakus**, whose sunny and supportive character is unparalleled.

A huge tribute goes to **Daniel Parthier**, without whom I would have never expanded my statistical knowledge and programming skills as far as I did. Thank you for the encouragement, support and a lot of good conversations and funny moments over the past years! Your advice was always valuable, your perfectionism contagious and you never hesitated when your help was needed.

I also want to thank **Laura Moreno Velasquez** and **Alexander Stumpf**, who introduced me to the world of mossy fiber field recordings. Furthermore, I want to thank **Laura**, **Rosanna Sammons** and **Anne-Kathrin Trappe** for their companionship and many happy moments.

I am sincerely thankful for the excellent technical assistance during the past years. **Susanne Rieckmann** was always ready to help, no matter how much she had on her own plate, and always willing to find hand-crafted solutions for special experimental problems. Thanks go to **Berit Söhl-Kielczynski,** who generously shared her knowledge and equipment for the preparation and staining of cryosections. I also want to thank **Katja Czieselsky**, **Monika Dopatka**, **Anny Kretschmer** and **Anke Schönherr** for their support in cell culture work and beyond. Furthermore, I would also like to thank **Marta Maglione**, who dedicated time to introduce me to the STED microscope and image processing.

I would like to thank **all members of the Schmitz lab** for creating such a nice working environment. Thank you for the vital exchange of scientific ideas, the energizing lunch breaks and entertaining social events!

Finally, I would like to thank my **family and friends** for their support and interest in my work over so many years. Special thanks go to my sister **Kea Brüntgens**, my comrade-in-arms **Lina Kenzler** and in particular to my partner **Matthias Ripplinger**. You made having a work-life balance desirable.

Declaration of Independence

Herewith I certify that I, Felicitas Brüntgens, have prepared and written my thesis independently and that I have not used any sources and aids other than those indicated by me.

Berlin, 31.01.2024

Table of Content

Abstract

Hippocampal mossy fiber boutons are giant plastic synapses, connecting dentate gyrus granule cells to CA3 pyramidal cells. They play a crucial role in mnemonic processes, especially during the encoding and consolidation of declarative memory, and are also implicated in neurodegenerative diseases. Upon increased granule cell activity, mossy fiber boutons are able to drive postsynaptic pyramidal cells through enhanced neurotransmission over short and long timescales, creating sparse but strong inputs into the highly recurrent CA3 network. Despite decades of research, detailed knowledge regarding various forms of mossy fiber plasticity is still lacking. In contrast to many other synapses, the long-term strengthening of the mossy fiber synapse is induced and expressed presynaptically. It depends on a calcium-calmodulin dependent increase in presynaptic cAMP levels and results in sustained enhancement of transmitter release. This presynaptic potentiation can be induced via the chemical adenylyl cyclase activator forskolin. However, the complete cascade underlying presynaptic long-term potentiation is not yet clarified. To dissect the molecular mechanisms underlying presynaptic potentiation, I investigated the possible involvement of three presynaptic molecules in mossy fiber plasticity: voltage-gated calcium channels, Munc13-1 and synapsin.

I aimed to measure the coupling distance between voltage-gated calcium channels and vesicle release sites in potentiated and non-potentiated mossy fiber boutons. The coupling distance is crucially influencing the peak Ca^{2+} concentration at the release site and thereby the release probability. A shortening of this distance could support enhancement of transmission upon presynaptic potentiation. By combining immunohistochemistry in thin acute mouse brain slices with three-color super-resolution STED microscopy, I measured the distance between the release site marker Munc13-1 and voltage-gated calcium channels of family Ca_v2 at the mossy fiber bouton. I found that the average coupling distance between Munc13-1 and Ca_v2 channels was unchanged after chemical potentiation. These results indicate that presynaptic potentiation is not accompanied by a tightening in the coupling distance. While distances measured between Munc13-1 and the $Ca_v2.1$-containing and $Ca_v2.2$-containing calcium channels were in line with predicted loose coupling at the mossy fiber bouton, the $Ca_v2.3$-containing channel was significantly closer to release sites. This peculiar location could indicate special functions of this calcium channel type at the mossy fiber bouton.

To test whether an increase in release sites might underlie presynaptic potentiation I examined a possible increase in Munc13-1 intensity in *stratum lucidum* after chemical potentiation. By analyzing fluorescence intensities in confocal image stacks of mouse brain cryosections, I compared the Munc13-1 content in potentiated versus non-potentiated mossy fibers. I found that the mean fluorescence was unchanged after two different incubation times with forskolin, indicating that there is no net change in the Munc13-1 content in potentiated mossy fibers. Within the hippocampus, I found reduced Munc13-1 intensities in area CA3a

compared to area CA3c. This gradient of Munc13-1 expression along the proximal-distal axis of CA3 might suggest differential connectivity within these subregions.

Finally, we scrutinized the role of synapsins in mossy fiber transmission and plasticity. We were especially interested in the role of synapsin III due to its peculiar expression in adult mossy fiber boutons. Mossy fiber field recordings in a mouse model lacking all synapsin isoforms revealed changes in excitability and presynaptic plasticity compared to wildtype mice. To take into consideration the onset of epileptic seizures in this mouse model, we compared two age groups: one before and one after the onset of epileptic seizures. We found increased excitability and synaptic depression, while frequency facilitation and post-tetanic potentiation were reduced in both age groups of knockout animals. These alterations likely can be attributed to structural changes in mossy fiber vesicle pools following the deletion of synapsins. Long-term potentiation was increased in presymptomatic knockout animals, while it was unchanged in the older age group compared to wildtype mice. Here, one could speculate that specificly the loss of synapsin III might lead to increased long-term potentiation. The onset of epileptic seizures could subsequently lead to network changes that compensate for the increased long-term potentiation observed in presymptomatic animals.

In summary, the results of my thesis indicate that mossy fiber presynaptic long-term potentiation is not accompanied by major changes in the distance between calcium sources and release sites. Additionally, I found unchanged Munc13-1 content in mossy fibers after potentiation, indicating that potential changes in release site numbers are mediated by existing Munc13-1 supplies rather than local translation. Finally, elevated release during long-term potentiation might be regulated by synapsin III, as indicated from experiments in mice lacking all synapsins. These findings contribute to a better understanding of mossy fiber presynaptic plasticity. They open up new research questions regarding the mechanisms underlying the astonishing properties of hippocampal mossy fiber boutons. Resolving these mechanisms will help to understand the function of this synapse within the hippocampal circuitry and thereby also in mnemonic processes in health and disease.

Zusammenfassung

Hippokampale Moosfaser *Boutons* sind große, plastische Synapsen, die Körnerzellen aus dem *Gyrus dentatus* mit CA3 Pyramidenzellen verbinden. Sie spielen eine substanzielle Rolle in Gedächtnisprozessen, insbesondere in der Bildung und Konsolidierung von deklarativen Gedächtnisinhalten. Weiterhin sind sie in neurodegenerativen Erkrankungen involviert. Moosfasersynapsen sind im Stande, auf präsynaptische Aktivitätsanstiege mit erhöhter Neurotransmission zu reagieren und so ihre postsynaptischen Partner über kurze und lange Zeiträume zu aktivieren. Dadurch nehmen sie einen sporadischen, aber starken Einfluss auf das in sich hochgradig verschaltete CA3 Netzwerk. Trotz jahrzehntelanger Forschung mangelt es noch immer an detailliertem Wissen zu den verschiedenen präsynaptischen Plastizitätsformen an der Moosfasersynapse. Im Gegensatz zu vielen anderen Synapsen wird die langanhaltende Stärkung hier präsynaptisch induziert und exprimiert. Die Stärkung beruht auf einem Kalzium-Calmodulin abhängigen Anstieg in der präsynaptischen cAMP Konzentration, welcher in einer langanhaltenden Erhöhung von Transmitterfreisetzung resultiert. Dieser Anstieg kann chemisch durch den Adenylylzyklase-Aktivator Forskolin induziert werden. Jedoch ist die genaue Kaskade für Moosfaser Langzeitpotenzierung noch nicht abschließend geklärt. Um die molekularen Mechanismen präsynaptischer Potenzierung besser zu verstehen, habe ich die mögliche Beteiligung dreier Moleküle in der Moosfasersynapse untersucht: spannungsabhängige Kalziumkanäle, Munc13-1 und Synapsine.

Es war mein Ziel, die Kopplungsdistanz zwischen spannungsabhängigen Kalziumkanälen und vesikulären Freisetzungsstellen in potenzierten Moosfasersynapsen zu messen. Diese Distanz nimmt maßgeblichen Einfluss auf die Spitzenkonzentration von Kalziumionen an der Freisetzungsstelle und damit auf die Freisetzungswahrscheinlichkeit. Eine Verkürzung der Kopplungsdistanz zwischen Kalziumkanälen und Kalziumsensoren könnte somit zu einer erhöhten Transmitterfreisetzung führen. Die Kombination aus Immunhistochemie in akuten Gewebeschnitten und hochauflösender, dreifarbiger STED Mikroskopie hat es mir ermöglicht, die Distanz zwischen Munc13-1 – einem Marker für Freisetzungsstellen – und spannungsabhängen Ca_v2 Kalziumkanälen an der Moosfasersynapse zu messen. Die Messungen ergaben, dass sich die durchschnittliche Kopplungsdistanz nach Potenzierung nicht verändert und suggerieren somit, dass die präsynaptische Potenzierung an dieser Synapse nicht von einer Verkürzung der Kopplungsdistanz begleitet wird. Während die gemessenen Distanzen zwischen Munc13-1 und den $Ca_v2.1$ und $Ca_v2.2$ Kalziumkanälen mit einer losen Kopplungsdistanz an der Moosfasersynapse übereinstimmten, befand sich der $Ca_v2.3$ Kanal signifikant näher an den Freisetzungsstellen. Diese besondere Positionierung könnte spezielle Funktionen dieses Kanaltyps an der Moosfasersynapse andeuten.

Um zu untersuchen, ob präsynaptische Plastizität an der Moosfasersynapse von einem Anstieg in der Zahl der Freisetzungsstellen begleitet sein könnte, habe ich eine mögliche Intensivierung der Munc13-1

immunhistochemischen Färbung nach chemischer Potenzierung geprüft. Durch die Analyse von Fluoreszenzintensitäten in konfokalen Bildstapeln aus kryostatischen Gehirnschnitten konnte ich den Munc13-1 Inhalt in potenzierten und nicht-potenzierten Moosfasern vergleichen. Die durchschnittliche Fluoreszenzintensität war unverändert nach zwei verschiedenen Inkubationszeiten mit Forskolin. Dies lässt vermuten, dass keine Nettoänderung von Munc13-1 in potenzierten Moosfasern auftritt. Innerhalb des Hippokampus' konnte ich reduzierte Munc13-1 Intensitäten in der CA3a Region im Vergleich mit CA3c beobachten. Solch ein Gradient in der Munc13-1 Expression innerhalb der proximal-distalen Achse von CA3 deutet verschiedene Konnektivitäten innerhalb von CA3 Subregionen an.

Schließlich haben wir die Rolle von Synapsinen in Moosfasertransmission und –plastizität studiert. Durch die auffällige Expression in adulten Moosfasersynapsen waren wir besonders an der Rolle von Synapsin III interessiert. Feldmessungen haben offenbart, dass sich in Mäusen ohne Synapsine sowohl die Erregbarkeit als auch die präsynaptische Plastizität der Moosfasersynapse von wildtypischen Mäusen unterscheidet. Um die altersbedingte Entwicklung des epileptischen Phänotyps in der *Knockout*-Maus nicht außer Acht zu lassen, haben wir zwei verschiedene Altersgruppen verglichen: Eine vor und eine nach Beginn der epileptischen Anfälle. In den *Knockout*-Tieren konnten wir einen Anstieg in der Erregbarkeit und der synaptischen Depression beobachten, während Frequenzfazilitation und post-tetanische Potenzierung in beiden Altersgruppen reduziert waren. Diese Änderungen resultieren vermutlich aus strukturellen Abweichungen in Vesikelspeichern nach der Deletion von Synapsinen. Langzeitpotenzierung war in jungen *Knockout*-Tieren erhöht, während sie in älteren Tieren unverändert blieb. Man könnte spekulieren, dass speziell der Verlust von Synapsin III zu der erhöhten Langzeitpotenzierung führt. Anschließend könnte der altersbedingte Ausbruch von Epilepsie zu Netzwerkveränderungen beitragen, die die erhöhte Langzeitpotenzierung in präsymptomatischen Tieren kompensieren.

Zusammenfassend deuten die Ergebnisse meiner Dissertation an, dass Moosfaser Langzeitpotenzierung nicht mit größeren Veränderungen in der Kopplungsdistanz zwischen Kalziumkanälen und Freisetzungsstellen einhergeht. Außerdem weisen unveränderte Munc13-1 Inhalte nach der Moosfaserpotenzierung darauf hin, dass eventuelle Veränderungen in der Anzahl von Freisetzungsstellen vermutlich durch bereits existierende Munc13-1 Vorräte gespeist werden und keine lokale Proteintranslation nötig ist. Schließlich könnte der verstärkte Anstieg in Transmitterfreisetzung während der Langzeitpotenzierung in Synapsin-*Knockout*-Moosfasern auf eine Rolle für Synapsin III als Freisetzungsregulator hindeuten. Diese Befunde tragen zu einem besseren Verständnis von präsynaptischer Moosfaserplastizität bei und eröffnen neue Fragestellungen bezüglich der Mechanismen, die den erstaunlichen Eigenschaften dieser Synapse zugrunde liegen. Ein tiefergehendes Verständnis dieser Mechanismen wird dabei helfen, die spezifische Funktion der Moosfasersynapse im hippokampalen Schaltkreis sowie in Gedächtnisprozessen und neurodegenerativen Erkrankungen besser zu verstehen.

Introduction

„No matter how we twist and turn, we shall eventually come back to the cell. “

- Rudolf Virchow, 1858 -

Learning is essential for the development and everyday life of all animals, from aplysia to humans (Kandel, 2001). It describes the ability to form new or adjust existing memories and it facilitates survival across animal species. An animal, that learns and remembers where to find food and how to avoid predators will have higher chances to survive and reproduce. Although scientific knowledge is advancing, the exact ways of how we form and where we store memories are still not understood. Nowadays, the idea is accepted that different memory systems exist, each serving individual goals, which could evolutionarily not be targeted by just one system (Schacter, 2022). Long-term forms of memory are broadly classified into two main categories: declarative and non-declarative memory, describing roughly the “*knowing that*” (declarative) and “*knowing how*” (non-declarative) (Milner et al., 1998). A highly relevant brain structure for the formation of declarative memories is the hippocampus (Andersen et al., 2007, chapter 2; Kandel et al., 2013, chapter 65).

Structure and Function of the Hippocampus

The hippocampus is a paired structure in the temporal lobes of many vertebrates (Rodríguez et al., 2002), which is anatomically and functionally largely conserved across mammals (Manns and Eichenbaum, 2006). Human lesion studies in the mid-20th century provided first evidence of hippocampal function in memory, with patient H.M. as the most famous example (Scoville and Milner, 1957). This patient suffered from severe epilepsy and had to undertake a resection of both medial temporal lobes, thereby losing most of his hippocampi and nearby structures. From this moment on, H.M. suffered from anterograde amnesia, making him unable to form new declarative memories (Corkin, 2002). Since then, many studies in humans and animals confirmed this role of the hippocampus (Eichenbaum, 1997). Episodic memories, which are autobiographical declarative memories (Kandel et al., 2013, chapter 65), usually also have a spatial component, linking memories of events to places (Rolls, 2017). This hippocampal role in spatial navigation was first demonstrated in 1978 by O’Keefe and Nadel (O’Keefe, J., and Nadel, 1978), and has been established since (Buzsáki and Moser, 2013; Eichenbaum, 2017). Further suggestions for more specific functions of the hippocampus include for example imagining the future (Addis et al., 2007; Hassabis et al.,

2007), decision making (McCormick et al., 2016), working memory (Xie et al., 2023), social processes (Montagrin et al., 2018) and visual perception (Lee et al., 2012; McCormick et al., 2021). Additionally, the hippocampus is implicated in several neurological disorders (Sendrowski and Sobaniec, 2013; Terreros-Roncal et al., 2021; Rao et al., 2022).

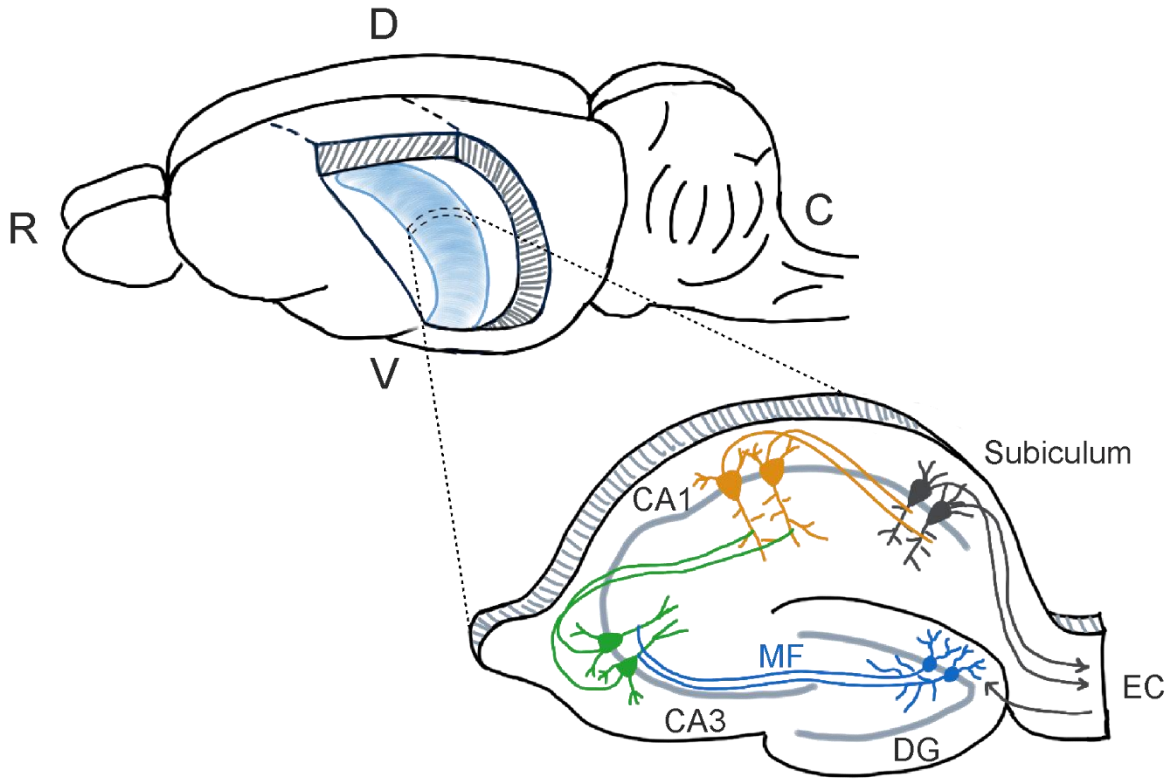

Figure 1: Schematic overview of the hippocampal structure. *Inspired by Amaral and Witter, 1989.* ***Back:*** *Schematic of a rodent brain. R: rostral, C: caudal, D: dorsal, V: ventral. The cerebral cortex is laterally opened, so that the hippocampus (blue) is visible along most of its septotemporal axis. Dashed lines on the hippocampus indicate the transversal axis, enclosing one of the many lamellae.* ***Front:*** *Schematic of a hippocampal cross-section, depicting the principal cell types and 2D connections of the trisynaptic circuit. Granule cells of the dentate gyrus (DG) are shown in blue and receive inputs from the entorhinal cortex (EC). Granule cell axons, the mossy fibers (MF), contact CA3 pyramidal cells (green). From there, further connections link to CA1 pyramidal cells (orange) and then to subicular pyramidal cells (grey) and back to the EC. CA:* cornu ammonis.

The hippocampus with its noticeable structure has sparked interest in scientists for many centuries (Andersen et al., 2007, chapter 2.2 and 3.2). Its 3D structure in rodents is banana-shaped and spans from the septal area to the temporal cortex (Figure 1), with the more medial parts also being more rostral and dorsal, and the lateral parts being ventrocaudal (Amaral and Witter, 1989). Orthogonal to the longitudinal axis is the transversal axis, in which the hippocampal subfields can be detected (Figure 1). Along the longitudinal axis, the hippocampus is thereby built up by many "lamellae", each containing the different subfields and cell types. The hippocampus proper consists of the *cornu ammonis* (CA), subdivided into the areas CA1, CA2 and CA3. Together with the dentate gyrus, the subicular complex and the entorhinal cortex it forms the hippocampal formation (Amaral and Witter, 1989). However, the terms hippocampus and hippocampal are not always used in the same ways (Andersen et al., 2007, chapter 3.2.1). In this work, I will refer to the hippocampus as the entity of dentate gyrus and *cornu ammonis*.

Information transfer within the hippocampus occurs via the so-called trisynaptic circuit (Andersen et al., 1971): Neurons from the entorhinal cortex form connections onto dentate gyrus granule cells via the perforant path (Ramón y Cajal, 1911; Lorente De Nó, 1934; Hjorth-Simonsen and Jeune, 1972; Steward and Scoville, 1976). Granule cells then connect onto the CA3 pyramidal cells via the mossy fibers (Blackstad and Kjaerheim, 1961; Claiborne et al., 1986) and Schaffer collaterals connect the CA3 and CA1 pyramidal cells (Schaffer, 1892; Ishizuka et al., 1990; Li et al., 1994; Kajiwara et al., 2008). From there, CA1 axons project to the subiculum and back to the entorhinal cortex (Figure 1) (Witter et al., 2017). However, the connectivity within the hippocampus is much more complex (Yeckel and Berger, 1990; Rolls and Treves, 1994; Kitamura et al., 2015). Instead of a simple trisynaptic loop, there are several parallel loops arising from separate perforant path inputs to the dentate gyrus and *cornu ammonis* subfields. Thus, each region in the hippocampus proper likely receives both direct input from the entorhinal cortex as well as pre-processed information from the preceding hippocampal region (Yeckel and Berger, 1990; Hainmueller, 2020). Additionally, the hippocampus receives inputs from other cortical areas (Goldman-Rakic, 1984; Rockland and Van Hoesen, 1999; Agster and Burwell, 2013). These inputs do not only target specific subfields within the transversal axis of hippocampus but also show divergence regarding the input location on the septotemporal axis (Dalton et al., 2022). Finally, the excitatory feedforward connections between principal neurons of the hippocampal formation are fine-tuned via a variety of feedback, inhibitory feedforward and recurrent connections (Frotscher et al., 1994; Li et al., 1994; Le Duigou et al., 2014).

Structure and Function of the Dentate Gyrus

The major input from the entorhinal cortex enters the hippocampus through the dentate gyrus (Witter, 2007a). The dentate gyrus has been called ‘filter’ or ‘gate’, because it blocks incoming activity from the entorhinal cortex in specific ranges (Hsu, 2007). Upon pathological states like medial temporal lobe epilepsy, this filter breaks down, leading to seizure propagation within the hippocampus (Heinemann et al., 1992; Nadler, 2003). The dentate gyrus is implicated in memory encoding and consolidation (Hainmueller, 2020) and might also have a role in memory retrieval (Tayler et al., 2013). Furthermore, the dentate gyrus is known for processes called pattern separation (Leutgeb et al., 2007; Neunuebel and Knierim, 2014) and completion (Nakashiba et al., 2012). Those processes underlie the generation of discrete memories and the reactivation of memory traces with incomplete activity patterns, respectively. The dentate gyrus is also thought to be important for connecting information to a spatial context (Lee and Jung, 2017) and might participate in short-term memory forms like working memory (Hainmueller, 2020).

Granule cells are the principal cells of the dentate gyrus, densely packed in the granule cell layer (Ribak and Shapiro, 2007). Around one million of them can be found in the rat brain (Amaral et al., 1990), arranged in two blades; the suprapyramidal blade and the infrapyramidal blade (Amaral et al., 2007). The dentate gyrus is supposedly one of the few neurogenic regions in the adult brain (Altman and Das, 1965; Gross, 2000; Boldrini et al., 2018). A small subset of the granule cell population consists of adult-born, immature cells (Imayoshi et al., 2008), while the majority of granule cells are mature ones, that were born early in development (Schlessinger et al., 1975; Altman and Bayer, 1990). These two age groups exhibit distinct biophysical properties, with differential implications for the network. For instance, immature granule cells are more excitable (Schmidt-Hieber et al., 2004; Marín-Burgin et al., 2012) and show increased synaptic plasticity (Schmidt-Hieber et al., 2004; Ge et al., 2007). This might facilitate memory formation (Shors et al., 2001; Snyder et al., 2005) and they are also thought to specifically contribute to pattern separation (Nakashiba et al., 2012). Mature granule cells generally show a lower activity (Diamantaki et al., 2016; Senzai and Buzsáki, 2017; Hainmueller and Bartos, 2018). They are further divided into subpopulations with functional differences: A mature granule cell subtype in the suprapyramidal blade shows distinct morphology, physiology (Williams et al., 2007) and gene expression (Erwin et al., 2020) and is largely recruited during memory-associated tasks (Erwin et al., 2020).

Dentate gyrus granule cells receive direct glutamatergic input from the medial and lateral entorhinal cortex (Witter, 2007a) onto their apical dendrites (Amaral et al., 2007). Other inputs on the granule cells come from the medial septum (Giocomo and Hasselmo, 2007), the ventral tegmental area and the locus coeruleus (Takeuchi et al., 2016; Wagatsuma et al., 2018). These subcortical inputs probably have a modulatory role and relay information on the global brain state, like locomotion, arousal or sleep (Hainmueller, 2020). Furthermore, granule cells receive intra-hippocampal inputs from hilar mossy cells, CA3 pyramidal cells

and inhibitory neurons (Li et al., 1994; Buckmaster et al., 1996; Scharfman, 2007; Larimer and Strowbridge, 2008; Sun et al., 2017). While mossy cell and CA3 pyramidal cell inputs can directly excite granule cells (Hashimotodani et al., 2017), their main targets are more likely dentate gyrus interneurons, thereby inducing disynaptic inhibition on granule cells (Scharfman, 2007; Larimer and Strowbridge, 2008).

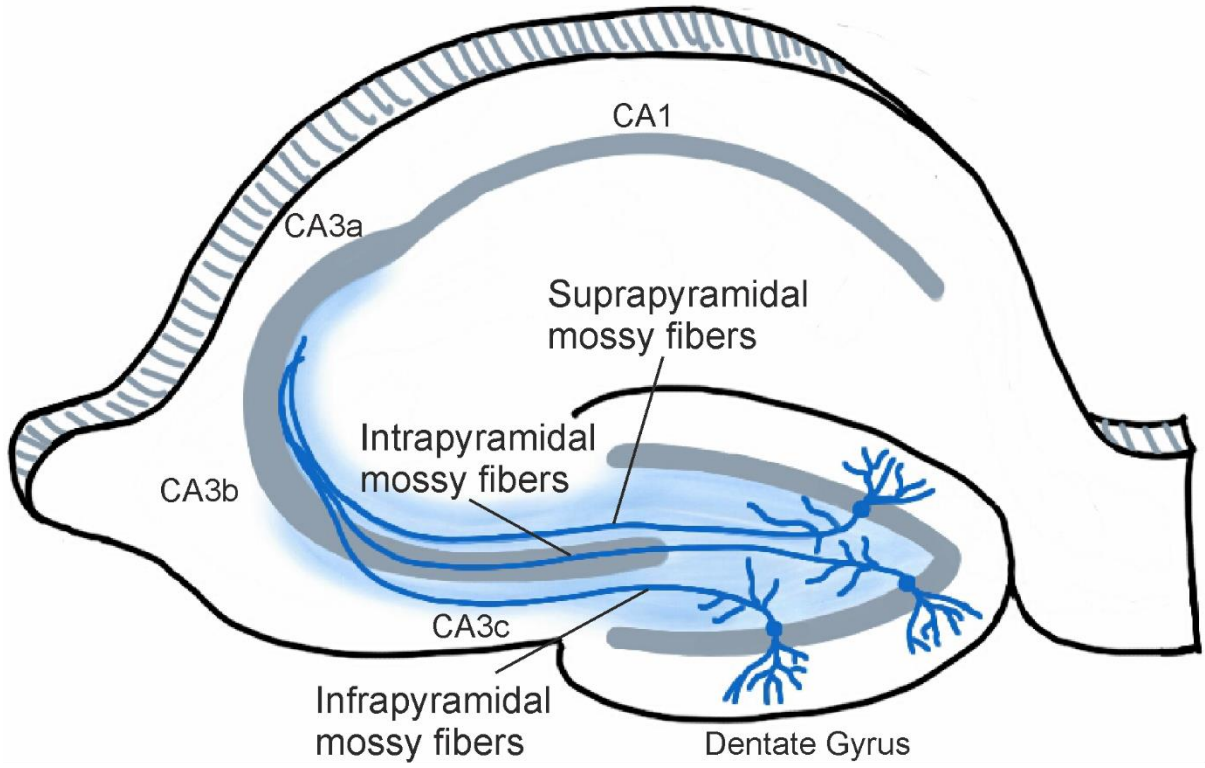

Figure 2: Schematic overview of the mossy fiber tracts. *Adapted from Römer et al., 2011. Mossy fibers, the axons from dentate gyrus granule cells (shown in blue), run through the transversal axis of the hippocampus through the complete area CA3. The fibers are structured into bundles: the suprapyramidal fibers arise from granule cells in the suprapyramidal blade and travel through the* stratum lucidum *just above the pyramidal cell layer (shown in grey). The intrapyramidal fibers arise from granule cells at the crest of the dentate gyrus and travel within the pyramidal cell layer before they turn to the* stratum lucidum *in more proximal parts of CA3. The infrapyramidal mossy fibers arise from granule cells in the infrapyramidal blade and run below the pyramidal cell layer for some extent of the CA3, but then cross the pyramidal cell layer and unite with the other mossy fiber in more distal parts of CA3.*

The axons of dentate gyrus granule cells are the so-called mossy fibers (Ramón y Cajal, 1911). They project to the *stratum lucidum* in the hippocampal area CA3, but also form local connections within the dentate gyrus (Amaral et al., 2007). These unmyelinated fibers (Blackstad and Kjaerheim, 1961) run along the transversal axis of the hippocampus throughout the whole area CA3 (Amaral et al., 2007) and are bundled into different tracts: the supra-, intra- and infrapyramidal tract, dependent on the position relative to the CA3

pyramidal cell layer (Figure 2). At one point, infra- and intrapyramidal fibers cross the pyramidal cell layer and converge with the suprapyramidal fibers just above the pyramidal layer, in the *stratum lucidum*. Thus, the proximal part of the *stratum lucidum* in CA3c might primarily be targeted by a subpopulation of granule cell, likely located in the suprapyramidal blade (Amaral et al., 2007). While mossy fibers follow the transversal axis within 1 mm thick lamella for most of their length (Amaral et al., 2007), it has been noted that they turn by 90 degrees in the distal CA3, close to CA2, and run along the longitudinal axis (Lorente De Nó, 1934; Swanson et al., 1978; Acsády et al., 1998). By this, they might form contacts on a subset of CA3 pyramidal cells, that are special integrator cells along the longitudinal axis (Amaral et al., 2007).

The local circuitry of granule cells consists of recurrent connections – especially numerous in epileptic phenotypes (Nadler, 2003) – and short mossy fiber collateral projections onto hilar cell types (Frotscher et al., 1994). Together with the mossy fiber projections to area CA3, this results in four cell types targeted by dentate gyrus granule cells: excitatory mossy cells and GABAergic interneurons in the hilus, as well as excitatory CA3 pyramidal cells and GABAergic interneurons in *stratum lucidum* of area CA3 (Acsády et al., 1998). Notably, the terminals onto the different cell types differ in their morphology (Ramón y Cajal, 1911; Acsády et al., 1998). The so-called mossy fiber boutons are large synapses contacting the principal hippocampal neurons (Blackstad and Kjaerheim, 1961; Chicurel and Harris, 1992), i.e. hilar mossy cells (Frotscher et al., 1994) and CA3 pyramidal cells (Blackstad and Kjaerheim, 1961; Acsády et al., 1998). Inhibitory neurons, on the other side, are contacted by small *en passant* synapses and filopodial extensions (Amaral and Dent, 1981; Acsády et al., 1998; Szabadics and Soltesz, 2009). Filopodial extensions arise from the synapse body of the large mossy fiber boutons, but are themselves presynaptic terminals (Amaral, 1979; Claiborne et al., 1986).

The Mossy Fiber to CA3 Pyramidal Cell Synapse

Mossy fiber boutons in the *stratum lucidum* target the proximal dendrites of CA3 pyramidal cells (Acsády et al., 1998). They are huge, structurally complex synapses with diameters ranging between 2 – 10 µm in rodents (Blackstad and Kjaerheim, 1961; Acsády et al., 1998; Rollenhagen et al., 2007) (Figure 3). They form close contacts with the postsynaptic spine, which is called thorny excrescence due to its complex morphology (Blackstad and Kjaerheim, 1961; Chicurel and Harris, 1992; Rollenhagen et al., 2007). There are two types of contact points with the postsynaptic partner. (1) So-called puncta adherentia, that are probably sites for adhesion complexes and (2) active zones, the main sites for transmitter release (Rollenhagen et al., 2007). Mossy fiber boutons contain on average 20 to 30 active zones (Chicurel and Harris, 1992; Acsády et al., 1998; Rollenhagen et al., 2007; Pelkey et al., 2023), with variable numbers dependent on animal species and age (Rollenhagen et al., 2007). In humans, mossy fiber boutons are larger than in rodents and have larger individual active zone areas. However, they only contain six active zones on average, leading to comparable total active zone areas for humans and rodents (Pelkey et al., 2023).

The rat mossy fiber bouton contains on average 20,000 synaptic vesicles (Rollenhagen et al., 2007), to supply the active zones for transmitter release. However, the vesicle clusters are substantially larger than what would be actually needed for release under intense conditions (Hallermann et al., 2003). There are different types of vesicles present: Small clear vesicles, large clear vesicles and dense-core vesicles (Rollenhagen et al., 2007). Small clear vesicles contain neurotransmitter, that is primarily glutamate in the case of mossy fiber boutons (Storm-Mathisen et al., 1983; Terrian et al., 1990; Amaral et al., 2007), but co-release of glutamate and *gamma*-aminobutyric acid (GABA) has been suggested to occur during development (Walker et al., 2002; Beltrán and Gutiérrez, 2012). Also zinc is stored and released from small clear vesicles of mossy fiber boutons (Palmiter et al., 1996; Cole et al., 1999; Pan et al., 2011), with possible modulatory roles (McAllister and Dyck, 2017). The second vesicle type – large clear vesicles – makes up approximately 1 % of the total vesicle pool (Henze et al., 2002a; Rollenhagen et al., 2007) and might also contain glutamate. The spontaneous fusion of those large clear vesicles could lead to so-called ‘giant minis’ (Henze et al., 2002a). Finally, dense-core vesicles contain various neuropeptides and neurotrophins (Salio et al., 2006; van den Pol, 2012). Amongst others they contain the brain-derived neurotropic factor (BDNF) (Dieni et al., 2012), that has been implicated in plasticity at mossy fiber boutons (Schildt et al., 2013; Lituma et al., 2021) and other synapses (Li et al., 1998; Park et al., 2014). Dense-core vesicles might also be involved in active zone build-up by transporting active zone material to presynaptic membranes (Ziv and Garner, 2004).

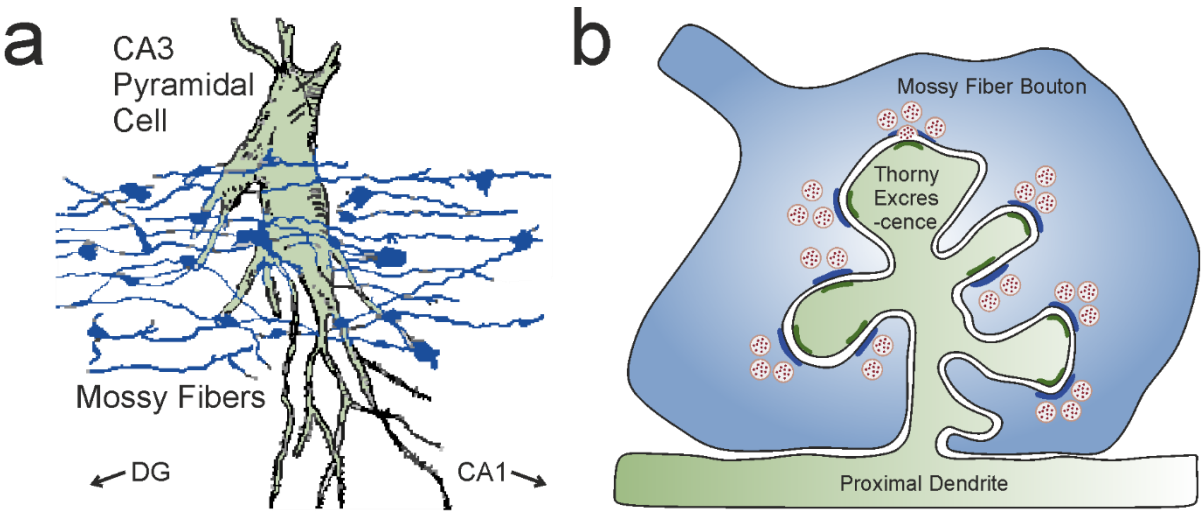

Figure 3: The mossy fiber to CA3 pyramdial cell synapse. a) *Schematic overview of mossy fibers (blue) and the giant synapses (blue swellings), that travel just above the somata of CA3 pyramidal cells (green). DG: dentate gyrus. Adapted from Takei et al., 1995.* ***b)*** *Schematic cross-section through a mossy fiber bouton (blue) contacting the thorny escrescence of a proximal dendrite of a CA3 pyramidal cell (green). Several neurotransmitter-filled synapstic vesicles are outlined exemplarily close to active zones (dark blue). Adapted from Nicoll and Schmitz 2005.*

Synaptic vesicles can be classified into three different functional pools: the readily releasable pool (RRP), the recycling pool and the reserve pool (Rizzoli and Betz, 2005; Denker and Rizzoli, 2010). The RRP comprises vesicles ready for immediate release (Rosenmund and Stevens, 1996; Schikorski and Stevens, 2001). Its morphological correlate are docked vesicles within 10 nm from the active zone membrane (Imig et al., 2014), but other definitions include vesicles within 30 to 60 nm (Hess et al., 1993; Richmond et al., 1999; Rollenhagen et al., 2007). It is thought that 4 % of all vesicles belong to the RRP of mossy fiber boutons (Rollenhagen et al., 2007). The refilling of the RRP probably depends on the mobilization of vesicles from the other two vesicle pools (Rizzoli and Betz, 2005). The reserve pool, is a distal cluster where vesicles are stored and only mobilized upon intense activity (Rizzoli and Betz, 2005). The recycling pool arises from recycled vesicles after endocytosis (Rizzoli and Betz, 2005) and can feed both the reserve pool and the RRP (Denker and Rizzoli, 2010).

Mossy fiber boutons are structurally equipped for powerful transmission. Indeed, they are able to induce large postsynaptic currents and potentials in CA3 pyramidal cells (Geiger and Jonas, 2000a; Henze et al., 2002b; Lawrence et al., 2004). However, activation of the dentate gyrus network at low firing rates has a net inhibitory effect on the target area CA3 (Jung and McNaughton, 1993; Zucca et al., 2017; Hainmueller, 2020). Each mossy fiber has on average 15 large boutons connecting onto CA3 pyramidal cells and each pyramidal cell receives inputs from approximately 50 granule cells (Amaral et al., 1990). At the same time, small mossy fiber synapses onto *stratum lucidum* GABAergic interneurons are at least four times more frequent (Acsády et al., 1998). Indeed, granule cell firing at frequencies below 1 Hz mostly recruits

GABAergic interneurons (Henze et al., 2002b; Mori et al., 2004; Zucca et al., 2017), leading to feedforward inhibition in CA3 (Torborg et al., 2010). Basal granule cell activity is usually very sparse (Diamantaki et al., 2016; Hainmueller and Bartos, 2018), with frequencies below 1 Hz (Jung and McNaughton, 1993; Vandael et al., 2020). Additionally, the release probability at mossy fiber boutons is low (Jonas et al., 1993), due to the tonic activation of presynaptic A1 adenosine receptors (Moore et al., 2003; Nicoll and Schmitz, 2005) and loose coupling between calcium channels and sensors at release sites (Vyleta and Jonas, 2014). This stands in stark contrast to other excitatory inputs on the CA3 pyramidal cells. Thousands of inputs from the entorhinal cortex via the perforant path and from other CA3 pyramidal cells via the associational commissural fibers (Amaral et al., 1990) create an excitable and associative network within area CA3.

The necessity of the mossy fiber equipment comes into play when granule cell firing increases to frequencies larger than 10 Hz, which fits the *in vivo* frequency of granule cell bursts (Henze et al., 2002b; Mori et al., 2004; Vyleta et al., 2016). Upon these frequencies, mossy fiber boutons show pronounced ways of enhanced synaptic transmission (Salin et al., 1996b) and CA3 pyramidal cells are recruited reliably (Henze et al., 2002b), leading to their bynames “conditional detonator” or “high pass filter” (Henze et al., 2002b; Pelkey and McBain, 2005; Vyleta et al., 2016). Mossy fiber synapses formed onto inhibitory neurons show a different physiology (Maccaferri et al., 1998; Toth et al., 2000) of frequency-induced depression (Zucca et al., 2017). Together, this leads to a net excitatory effect in area CA3 and activation of the associative CA3 network.

Synaptic Transmission

Information between neurons is conveyed via synapses, which can be electrical or chemical, while the latter are more abundant (Kandel et al., 2013, chapter 8). In chemical synapses, depolarization of the presynaptic terminal by an incoming action potential opens voltage-gated calcium channels (VGCC). The resulting influx of calcium ions triggers the release of chemical neurotransmitters via fusion of synaptic vesicles with the presynaptic membrane (Katz and Miledi, 1969), at specialized compartments called active zones. This electrochemical coupling leads to a change in the postsynaptic potential within a few hundred microseconds (Sabatini and Regehr, 1999), thanks to the highly specialized release machinery at the presynaptic active zone (Südhof, 2013). Neurotransmitters (and other vesicular contents) are released into the synaptic cleft and diffuse to the postsynaptic membrane, where they bind to receptors, which usually results in ion influx into the postsynaptic compartment (Kandel et al., 2013, chapter 12). Neurotransmitters can be excitatory or inhibitory, dependent on the potential change they induce at the postsynaptic site (Kandel et al., 2013, chapter 13).

Neurotransmitter release mainly occurs at specialized membrane compartments, called active zones. They are fully equipped to support smooth neurotransmitter release and involved in four major tasks: (1) docking and priming of synaptic vesicles, (2) recruitment of VGCC to enable fast synchronous release, (3) positioning of pre- and postsynaptic compartments into functional transsynaptic columns and (4) mediation of synaptic plasticity (Südhof, 2012). Release of neurotransmitters from synaptic vesicles can only occur when several prerequisites are met. First of all, neurotransmitter-filled vesicles must be available close to the active zones. Second, a specific molecular release machinery is necessary to render the vesicles fusion-competent and mediate the fusion process. And third, calcium ions – the trigger for release – must be present in sufficient amounts at the vesicle release site (Südhof, 2013). The release machinery comprises a calcium sensor on the vesicular membrane, the active zone protein complex as well as the core fusion machinery (Figure 4).

The Calcium Sensor

The long postulated vesicular calcium sensor for the initiation of release has been identified to be synaptotagmin (Südhof, 2013). It is an evolutionary conserved protein (Perin et al., 1990, 1991), that binds Ca^{2+} (Brose et al., 1992). Sixteen brain isoforms encompass distinct properties that result in a functional variety of release types (Südhof, 2013). For instance, synaptotagmins 1, 2 and 9 are implicated in fast, synchronous release (Maximov and Südhof, 2005; Xu et al., 2007), while synaptotagmin-7 plays a role in asynchronous release (Bacaj et al., 2013; Huson and Regehr, 2020). Fusion is triggered upon cooperative binding of calcium ions to the calcium binding sites of synaptotagmin (Kochubey and Schneggenburger, 2011).

The Active Zone Complex

The Ca^{2+}-triggered fusion can only occur if the synaptic vesicle and voltage-gated calcium channels (VGCC) are in place. Here, the active zone protein complex is involved; in the docking and priming of synaptic vesicles as well as in the positioning of calcium channels close to the release sites (Neher and Brose, 2018). Docking describes the physical and close attachment of synaptic vesicles to the membrane, while priming actually renders the vesicles "fusion-ready" (Imig et al., 2014). The active zone complex consists of Munc13, RIM, RIM-BP and VGCC (Figure 4). RIM has a central scaffolding role as it interlinks many proteins of the complex. First, it interacts with the vesicular proteins Rab3a and Rab27 (Südhof, 2013), thereby facilitating the docking of synaptic vesicles to the active zone (Rizo, 2022). Second, together with RIM-BP, it recruits VGCC to release sites, enabling local calcium entry to trigger the release process (Kaeser et al., 2011; Südhof, 2013). VGCC implicated in synaptic transmission all possess binding sites for RIM and/or RIM-BP (Kaeser et al., 2011). Third and final, RIM recruits, binds and activates Munc13 (Deng et al., 2011). Munc13 has proposed roles in vesicle docking, priming (Aravamudan et al., 1999; Augustin et al., 1999b; Richmond et al., 1999; Deng et al., 2011; Imig et al., 2014) and the assembly of the core fusion

complex (Rizo, 2022). Recently, it has been shown that the minimal components required for vesicle priming only comprise parts of Munc13, the zinc finger domain of RIM and a binding site to the calcium channel (Tan et al., 2022). However, the presence of the complete active zone complex is likely needed for the high speed and efficiency of the process.

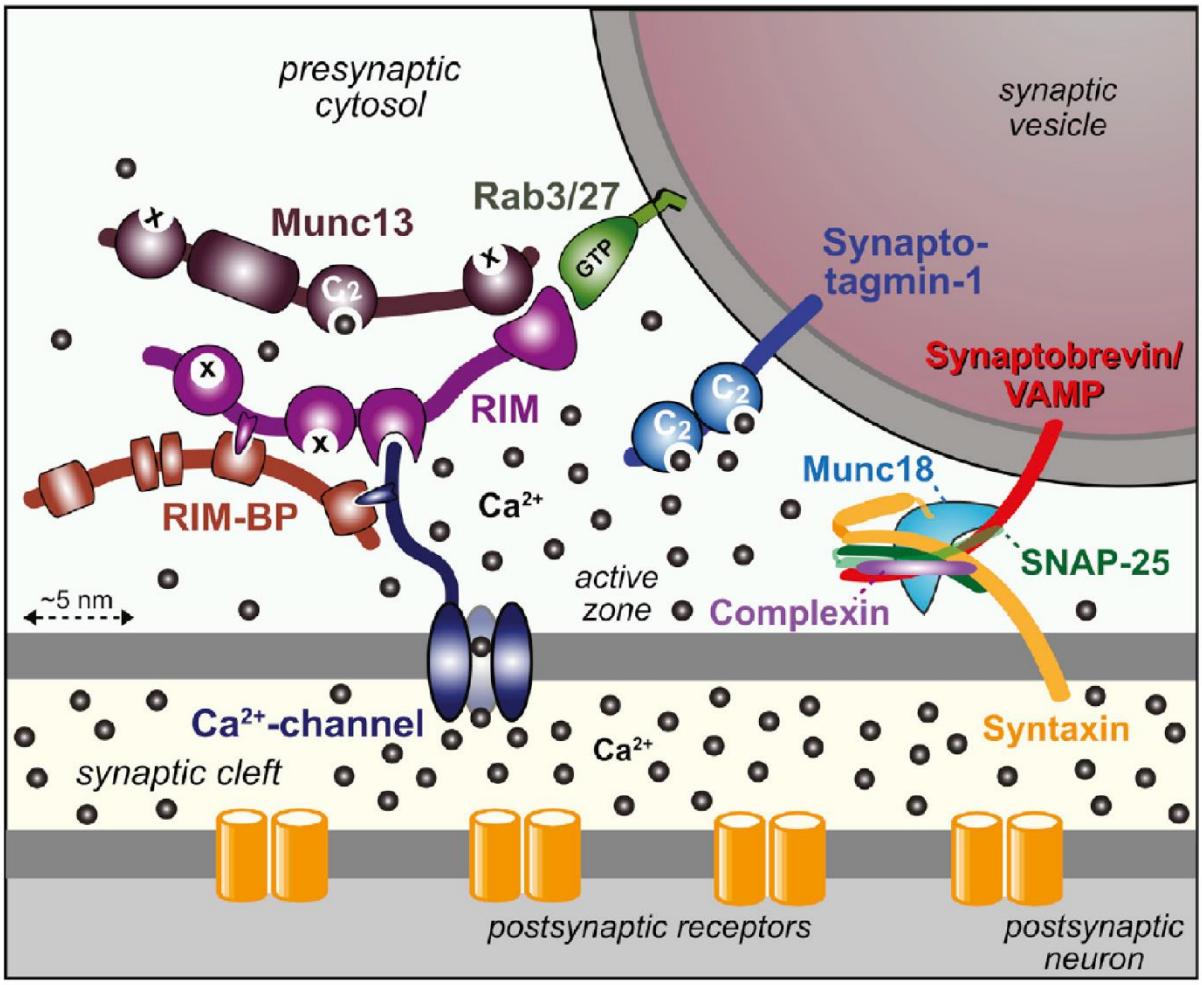

Figure 4: Schematic overview of the release machinery. *From left to right: On the presynaptic side, active zone core proteins Munc13, RIM-BP and RIM interact with calcium channels as well as vesicular proteins. The vesicular calcium sensor synaptotagmin initiates release upon the binding of Ca^{2+}, which leads to zippering of the fusion machinery, consisting of SNARE proteins (synaptobrevin, syntaxin and SNAP-25), supported by SM proteins (Munc18). Adapted from Südhof 2013.*

The Core Fusion Machinery

The actual fusion step requires the core fusion machinery, that brings the vesicular and plasma membranes close together and opens the fusion pore. The core fusion machinery consists of SNARE and SM (Sec1/Munc18-like) proteins (Südhof, 2013), which mediate the fusion between vesicles and the plasma membrane (Figure 4). In short, SNARE proteins on both membranes (synaptobrevin, syntaxin and SNAP-25 (Dulubova et al., 1999; Misura et al., 2000)) form a complex (Söllner et al., 1993), that anchors the vesicle to the plasma membrane. Then, in a progressive procedure called zippering (Gao et al., 2012; Rizo, 2012), membranes are brought in close proximity to each other (Hanson et al., 1997). Subsequently, the membrane destabilization results in the formation of a fusion pore (Südhof, 2013). For successful complex assembly and fusion, syntaxin needs to undergo a conformational change that is mediated by the SM protein Munc18-1 in concert with Munc13 (Südhof, 2013; Ma et al., 2015; Shu et al., 2020; Rizo, 2022).

Despite all the work on the precise mechanisms of neurotransmitter release, many details are still missing. A simplified three step model for fusion has been proposed recently: At first, synaptic vesicles are loosely docked and primed at active zones while the core of the fusion machinery assembles. Then, docking and priming reach a tight, but reversible state, that involves conformational changes in the fusion machinery. This sets the floor for the final step, the Ca^{2+}-triggered fusion (Neher and Brose, 2018).

Types of Neurotransmitter Release

There are different types of neurotransmitter release: spontaneous release, that occurs independent of an action potential (Kavalali, 2015), and evoked release in response to a presynaptic depolarization. Evoked release can be synchronous or asynchronous, dependent on the timepoint after an action potential: Synchronous release is defined as the release within 1-5 ms after an action potential. Asynchronous release occurs tens to hundreds of milliseconds later (Kaeser and Regehr, 2014). Synchronous release ensures fidelity of information transfer at synapses (Kaeser and Regehr, 2014) and can occur in an univesicular or multivesicular fashion (Rudolph et al., 2015). Asynchronous release is thought to regulate other aspects of synaptic functions, like spike timing precision, coincidence detection and postsynaptic responses (Diamond and Jahr, 1995; Atluri and Regehr, 1998; Lu and Trussell, 2000; Evstratova et al., 2014). Asynchronous release seems to be increased at synapses with low release efficacy (Mendonça et al., 2022). Recently, it has been proposed that synchronous and asynchronous release take place at different positions within the active zone. Asynchronous release might occur more towards the active zone center (Kusick et al., 2020) and is aligned with postsynaptic NMDA receptors (Li et al., 2021), while synchronous release sites can be found at the active zone edges (Kusick et al., 2020) where they are aligned with postsynaptic AMPA receptors (Li et al., 2021).

Release Probability

The strength of a synapse is defined as the product of three parameters: the number of presynaptic release sites (N), the vesicular release probability (P_v) and the postsynaptic response to the presynaptic release of one vesicle also known as quantal size (q) (Katz and Miledi, 1969; Branco Tiago and Staras Kevin, 2009; Dittman and Ryan, 2019). At the presynaptic side, a plethora of structural and molecular parameters influences release probability and the number of release sites. Among them is the number of active zones per synapse, the number, type and spatial arrangement of presynaptic calcium channels at the active zone, changes in calcium channel or action potential properties, the number of vesicles in the RRP, as well as changes in vesicle docking and priming (Atwood and Karunanithi, 2002).

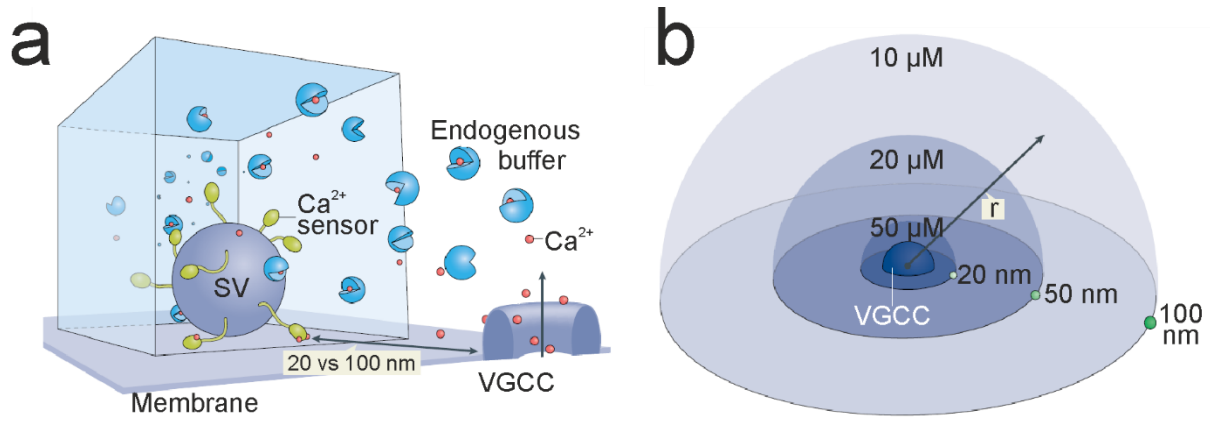

Figure 5: Schematic indicating the influence of coupling distance between the voltage-gated calcium channel and the Ca^{2+} sensor at the vesicular release site. a) *To the left, a synaptic vesicle (SV) situated close to the membrane is shown with its calcium sensors (green). To the right, a voltage-gated calcium channel (VGCC) is indicated within the membrane, allowing calcium ions (red) to flux in. The distance between channel and vesicle release site is variable and influences the possible interactions by endogeneous calcium buffers (shown in light blue).* ***b)*** *Schematic estimation of calcium concentration dependent on the distance from the voltage-gated calcium channel (VGCC). The VGCC is shown at the center, concentric balls indicate calcium concentrations in the µM range within 100 nm from the channel. If the channel would be situated within 20 nm, the peak concentration would be as high as 50 µM, while a calcium channel at 100 nm distance would lead to a calcium concentration around 10 µM. Adapted from Dittman and Ryan 2019.*

The amount of calcium present close to synaptotagmin critically affects the release probability. This can be influenced by the number and properties of calcium channels and their distance to the sensor, thereby changing local calcium concentrations. The distance between calcium channel and calcium sensor is called coupling distance and can be tight (< 20 nm) or loose (> 20 nm) (Bornschein and Schmidt, 2019). However, these definitions are arbitrary and heterogenous (Eggermann et al., 2012) and it is likely that distances between calcium channels and release sites occur on a continuous scale (Ricoy and Frerking, 2014). Most importantly, a tight coupling would lead to a calcium nanodomain, defined as a high local Ca^{2+} concentration close to the release site (Eggermann et al., 2012; Dittman and Ryan, 2019) (Figure 5). Thereby, efficacy and speed of synaptic transmission can be increased, due to the non-linear relationship between calcium ion concentration and release (Katz and Miledi, 1968; Dittman and Ryan, 2019). A 20 nm tighter coupling would result in a tenfold increase in release probability (Bucurenciu et al., 2008). Short coupling distances are associated with high vesicular release probability (Rozov et al., 2001; Bucurenciu et al., 2008), short synaptic delays and fast release (Bucurenciu et al., 2010; Nakamura et al., 2015). The topography of calcium channels at the active zones is interlinked with the coupling distance and several topographies for tight and loose arrangements have been described (Dolphin and Lee, 2020). For example, at a weak synapse in the cerebellum, calcium channels are arranged outside an exclusion zone of 50 nm around the release sites, in contrast to a strong cerebellar synapse where channels are tightly coupled in a perimeter release model (Rebola et al., 2019). This distance also influences how endogenous or exogenous calcium buffers can interfere with release (Eggermann et al., 2012; Vyleta and Jonas, 2014). Loose coupling at weak synapses allows more interference by buffers than tight coupling at strong synapses (Rebola et al., 2019). This fact can also be used experimentally to investigate the coupling distance between voltage-gated calcium channels and the Ca^{2+} sensor at the vesicle. By applying two exogenous Ca^{2+} chelators with different binding kinetics – usually BAPTA and EGTA – the distance can be estimated based on the their effects on release (Adler et al., 1991; Borst and Sakmann, 1996; Meinrenken et al., 2002; Fedchyshyn and Wang, 2005; Eggermann et al., 2012).

Synaptic Plasticity at the Hippocampal Mossy Fiber Bouton

Synaptic plasticity describes the ability of neurons to react to activity changes by strengthening or weakening their synaptic connections. This concept of "information storage" in synaptic connections was already suggested by Ramon y Cajal, although terms like synapse were not defined yet (Sotelo, 2003). There are three broad categories of synaptic plasticity, encompassing short-term plasticity, long-term plasticity and homeostatic plasticity (Regehr and Abbott, 2004). Short-term plasticity includes increases and decreases in synaptic transmission on time scales of milliseconds to minutes (Zucker and Regehr, 2002) and might underlie forms of short-term memory (Vandael et al., 2020; Xie et al., 2023). Long-term plasticity can be differentiated into long-term potentiation and long-term depression, resulting in strengthening or weakening of synaptic connections for hours to days (Bear and Malenka, 1994; Malenka and Bear, 2004). Such changes are thought to underlie memory formation (Morris, 2003; Lynch, 2004), as it has been recently demonstrated for fear memories (Ryan et al., 2015). The same synapse can undergo different forms of presynaptic plasticity (Markram and Tsodyks, 1996; Trommershäuser et al., 2003), and their timely interplay is potentially important for successful computation (Regehr and Abbott, 2004). Moreover, the prevalent form of plasticity and the induction mechanisms can vary dependent on the target cell (Maccaferri et al., 1998; Reyes et al., 1998; Toth et al., 2000).

Short-term Plasticity

Short-term plasticity can be roughly categorized into plastic changes that lead to increase (enhancement) or decrease (depression) in synaptic transmission, dependent on the synapse type (Salin et al., 1996b; Reyes et al., 1998) and initial release probability (Tsodyks and Markram, 1997). Synaptic enhancement is thought to be partially mediated via increased presynaptic calcium concentrations and comprises facilitation and post-tetanic potentiation, that occur on different time-scales (Zucker and Regehr, 2002). Synaptic depression might have pre- and postsynaptic influences, but one important presynaptic factor for synaptic depression is the exhaustion of presynaptic vesicle pools (Zucker and Regehr, 2002). The precise mixture of presynaptic short-term mechanisms depends on the target cell (Reyes et al., 1998; Rozov et al., 2001; Éltes et al., 2017). For instance, mossy fiber synapses onto excitatory partners facilitate strongly, while mossy fiber synapses onto interneurons show depression following the same stimulation (Toth et al., 2000).

Facilitation

Facilitation is an enhancement of synaptic transmission in response to several stimuli in close succession (Zucker and Regehr, 2002). For two stimuli it is called paired-pulse facilitation. Hippocampal mossy fiber boutons show pronounced paired-pulse facilitation with paired-pulse ratios (second by first response amplitude) of two or larger (Salin et al., 1996b). High paired-pulse ratios are usually correlated with a low

release probability and vice versa (Thomson, 2000; Zucker and Regehr, 2002). Thus, a change in paired-pulse facilitation can indicate a change in release probability. Indeed, mossy fiber boutons have a low release probability at basal conditions (Jonas et al., 1993; Lawrence et al., 2004). The increase in transmission on the second pulse is thought to depend on a rise in intraterminal free Ca^{2+} (Regehr et al., 1994). This effect is likely mediated via a saturation of presynaptic calcium buffers (Regehr et al., 1994; Salin et al., 1996b; Rozov et al., 2001), more specifically the fast endogenous buffer calbindin-D28k (Blatow et al., 2003).

Synaptic enhancement during longer stimulation trains is called frequency facilitation and is thought to be due to an increase in release probability (Katz and Miledi, 1968; Zucker, 1989; Atluri and Regehr, 1996). Facilitation might play a role in information transfer (Henze et al., 2002b; Mori et al., 2004), circuit dynamics and short-term memory (Jackman and Regehr, 2017). Facilitating synapses, as the hippocampal mossy fiber bouton, are often high-pass filters (Atluri and Regehr, 1996), encoding burst activity. Thus, frequency facilitation is likely enabling the mossy fiber synapse to "detonate" and recruit its postsynaptic partner (Vyleta et al., 2016; Chamberland et al., 2017). At this synapse, frequency facilitation is especially prominent and has been detected *in vitro* (Salin et al., 1996b; Toth et al., 2000; Moore et al., 2003) and *in vivo* (Klausnitzer and Manahan-Vaughan, 2008). For example, facilitation can reach 600 % in mossy fiber boutons while a neighboring synapse between CA3 pyramidal cell reaches values below 150 % at the same conditions (Salin et al., 1996b).

For short time scales up to a few hundreds of milliseconds, frequency facilitation is dependent on increased Ca^{2+} concentrations (Fisher et al., 1997; Jackman and Regehr, 2017). Also at the mossy fiber bouton, frequency facilitation has a presynaptic origin (Chamberland et al., 2014) and depends on increase in presynaptic Ca^{2+} concentration (Chamberland et al., 2017). Proposed mechanisms for this increase include action potential broadening (Geiger and Jonas, 2000a), endogenous buffer saturation (Scott and Rusakov, 2006; Vyleta and Jonas, 2014), synchronization of multivesicular release, recruitment of additional release sites (Chamberland et al., 2014, 2017) as well as Ca^{2+} release from internal stores (Lauri et al., 2003). Also presynaptic glutamate receptors – kainate and NMDA receptors – have been proposed to play a role in facilitation (Schmitz et al., 2001; Lituma et al., 2021). Kainate receptor activation by low glutamate concentrations (Schmitz et al., 2000) mediates facilitation (Contractor et al., 2001; Schmitz et al., 2001; Lauri et al., 2003) by increasing the release probability (Schmitz et al., 2001; Ji and Stäubli, 2002). Their activation might induce the Ca^{2+} release from internal stores (Lauri et al., 2003). Recently, it has been suggested that presynaptic NMDA receptors contribute to the presynaptic Ca^{2+} rise during facilitation (Paoletti et al., 2013; Lituma et al., 2021). Pharmacological or genetic manipulation of presynaptic NMDA receptors at the mossy fiber bouton impaired frequency facilitation specifically at the synapse onto CA3 pyramidal cells, while it reduced presynaptic BDNF release that might have modulatory roles in mossy fiber plasticity mechanisms (Lituma et al., 2021).

Post-tetanic Potentiation

Prolonged high-frequency stimulation is accompanied by synaptic depression during the stimulation train. But, in a second instance, it leads to post-tetanic potentiation, which becomes visible after recovery from depression (Zucker and Regehr, 2002). Post-tetanic potentiation (PTP) is a form of synaptic enhancement that lasts from tens of seconds to several minutes (Zucker and Regehr, 2002) and is thought to result from presynaptic increase in calcium and release probability (Regehr et al., 1994; Zucker and Regehr, 2002; Habets and Borst, 2007). Recently, PTP was suggested to underlie short-term memory in the hippocampus (Vandael et al., 2020), because it is likely held in synapses (Mongillo et al., 2008; Jackman and Regehr, 2017) and it matches the duration of this memory form in the hippocampus (Squire and Zola-Morgan, 1991). Indeed, PTP at the mossy fiber leads to the formation of a so-called "pool engram" of synaptic vesicles close to the active zone, that can be stable for several minutes and might therefore provide the structural basis for an enhancement in synaptic strength, as suggested by the authors (Vandael et al., 2020). Similar observations were made at invertebrate synapses and in cell culture before (Habets and Borst, 2007; Humeau et al., 2011; Valente et al., 2012). The increase in the RRP is most likely mediated via the vesicle-associated protein synapsin, as suggested by several studies in which synapsin KO models showed impaired PTP (Rosahl et al., 1995; Valente et al., 2012; Farisello et al., 2013; Nikolaev and Heggelund, 2015; Cheng et al., 2018). At hippocampal mossy fiber boutons, PTP could help to switch the synapse into a "burst-to-burst" transmission mode, which might be critical for the mnemonic functions of this synapse (Vyleta et al., 2016).

Long-term Potentiation

Long-term potentiation (LTP) strengthens synaptic transmission in the timescale of hours to days (Bliss and Gardner-Medwin, 1973; Bliss and Lømo, 1973). This strengthening is likely to underlie learning and memory processes (Nicoll, 2017), as already postulated by Donald Hebb in 1949 (Hebb, 1949). First experimental evidence for LTP was presented by Lomo in recordings at the synapse between perforant path axons and dentate gyrus granule cells (Bliss and Lømo, 1973). For the induction of this form of LTP, simultaneous postsynaptic depolarization and synaptic stimulation are necessary (Malenka et al., 1989), as for example during repetitive stimulation at high frequencies. This activates postsynaptic NMDA receptors, that act as coincidence detectors and allow calcium influx into the postsynaptic terminal (Nicoll, 2017). Subsequently, the expression of LTP is mediated via the insertion of postsynaptic AMPA receptors (Hayashi et al., 2000), thereby elevating the postsynaptic sensitivity to glutamate. Most excitatory synapses express this form of postsynaptic LTP (Nicoll, 2017).

However, in the 1980s, a presynaptic form of LTP was discovered at the mossy fiber to CA3 synapse (Harris and Cotman, 1986). Here, the long-lasting strengthening occurs via an increase in presynaptic glutamate release instead of changes at the postsynaptic site (Nicoll and Schmitz, 2005). Other synapses where the induction and/or expression of LTP is presynaptic have since been described, at both excitatory and

inhibitory synapses. Examples span from synapses in the hippocampal formation (Kokaia, 2000; Zakharenko et al., 2001; Lysetskiy et al., 2005; Wozny et al., 2008; Oren et al., 2009), the amygdala and the thalamus to synapses in the cerebellum and cortical regions (Castillo, 2012). While these synapses all show increased transmitter release during LTP expression, the locus for induction can be pre- or postsynaptic and can involve also neighboring synapses (Castillo, 2012). However, at the mossy fiber to CA3 synapse, both induction and expression of LTP are thought to be solely presynaptic (Nicoll and Schmitz, 2005).

Induction of Mossy Fiber Long-term Potentiation

The induction of mossy fiber LTP was shown to be independent of NMDA receptors (Harris and Cotman, 1986; Zalutsky and Nicoll, 1990). Proposed alternative mechanisms for LTP induction included postsynaptic calcium influx via alternative pathways as well as presynaptic calcium influx. Indeed, extracellular calcium is needed for mossy fiber LTP (Castillo et al., 1994). Although controversial publications led to an unclear picture of the site of calcium influx (Nicoll and Schmitz, 2005), presynaptic calcium influx is the more likely mechanism for LTP induction (Nicoll and Malenka, 1995; Mellor and Nicoll, 2001). In particular, the presynaptic R-type voltage-gated calcium channel is an interesting candidate and has been proposed to play a role in the induction of mossy fiber LTP (Breustedt et al., 2003; Dietrich et al., 2003). Additionally, presynaptic non-NMDA receptors could be involved (Nicoll and Schmitz, 2005), for example by inducing Ca^{2+} release from internal stores (Lauri et al., 2003). Other proposed LTP induction mechanisms involve EphB receptor tyrosin kinases (Contractor et al., 2002; Armstrong et al., 2006), TrkB receptors (Huang et al., 2008; Schildt et al., 2013), β-adrenergic receptors (Huang and Kandel, 1996) and presynaptic $GABA_A$ receptors (Ruiz et al., 2010). Also modulators like zinc (Xie and Smart, 1994) or BDNF (Gómez-Palacio-Schjetnan and Escobar, 2008; Schjetnan and Escobar, 2012; Martínez-Moreno et al., 2020) might be involved, although the precise mechanisms are still controversial (Lu et al., 2000; Vogt et al., 2000; Li et al., 2001; Ando et al., 2010; Lavoie et al., 2011; Pan et al., 2011; Edelmann et al., 2014).

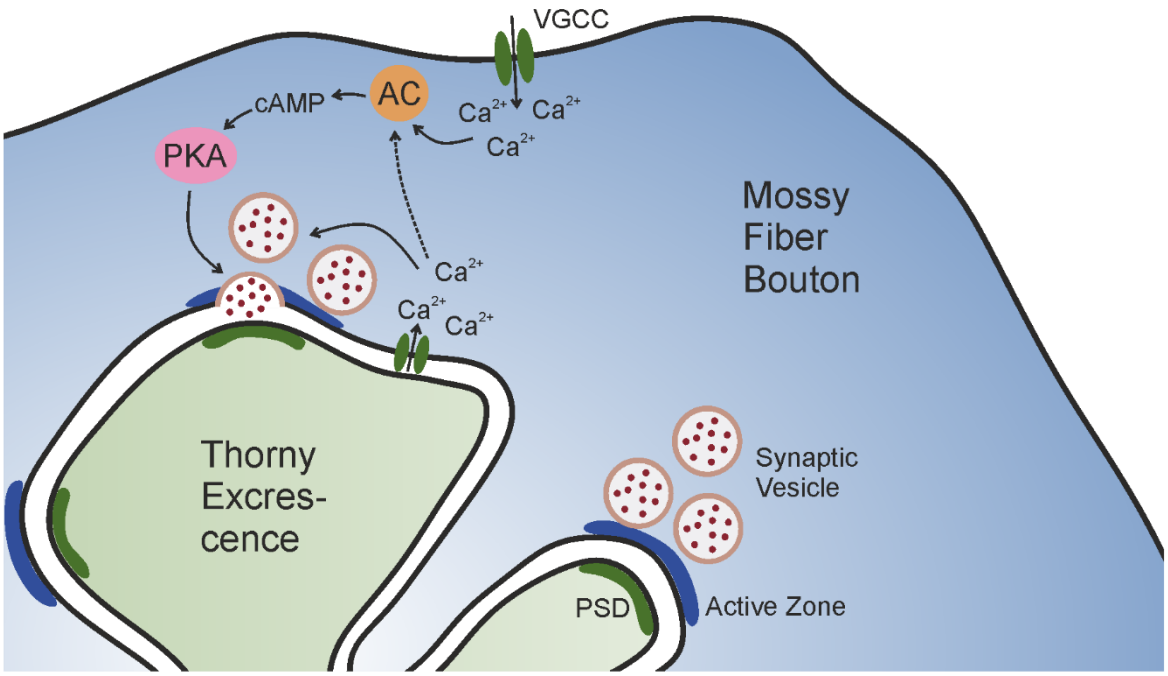

Figure 6: Schematic overview of the presynaptic mossy fiber LTP cascade. *Release at an active zone (dark blue) of a mossy fiber bouton (blue) is initiated by calcium influx through voltage-gated calcium channels (VGCC; green) close to the active zone. Presynaptic release is enhanced after induction of presynaptic LTP by Ca^{2+}-induced activation of adenylyl cyclases (orange), that leads to an increase in presynaptic cAMP concentration and activation of PKA (pink). Downstream of cAMP/PKA, an unidentified link in the cascade leads to a sustained increase in transmitter release. Adapted from Nicoll and Schmitz 2005.*

Expression of Mossy Fiber Long-term Potentiation

The expression of mossy fiber LTP culminates in an increased transmitter release at the presynaptic bouton (Zalutsky and Nicoll, 1990; Xiang et al., 1994; Maeda et al., 1997; Kawamura et al., 2004) that can last from minutes to hours. This is due to an increase in release probability (Xiang et al., 1994; Weisskopf and Nicoll, 1995; Tong et al., 1996), that can be confirmed by a reduction in paired-pulse ratio during mossy fiber LTP (Zalutsky and Nicoll, 1990). An extensive body of literature points to a presynaptic expression cascade (Figure 6), in which the increased presynaptic calcium levels activate calcium/ calmodulin dependent adenylyl cyclases, increasing the presynaptic cAMP concentration. Cyclic AMP is then thought to mainly activate protein-kinase A-dependent pathways (Nicoll and Schmitz, 2005), resulting in the sustained increase in transmitter release. However, other cAMP-mediated pathways could be involved as well (Shahoha et al., 2022). Although an extensive body of literature points to a solely presynaptic form of mossy fiber LTP, some literature suggests postsynaptic forms of LTP at this synapse (Contractor et al., 2002; Kwon and Castillo, 2008; Rebola et al., 2011; Carta et al., 2018). Such mechanisms could potentially explain the mixed findings regarding the locus of calcium influx during induction (Nicoll and Schmitz,

2005). However, if different forms of mossy fiber LTP exist and how these alternative mechanisms could be useful, is still a question to be solved.

Adenylyl Cyclases

Presynaptic calcium influx during mossy fiber LTP activates adenylyl cyclases (ACs), which catalyze the formation of cyclic adenosine monophosphate (cAMP) (Tang and Hurley, 1998) and are highly expressed in the dentate gyrus (Worley et al., 1986). AC1 and AC8 are calcium calmodulin-dependent (Hanoune and Defer, 2001) and their individual deletion impairs mossy fiber LTP (Villacres et al., 1998; Wang et al., 2003). Surprisingly, combined knockouts of AC1 and AC8 do not abolish mossy fiber LTP completely (Wang et al., 2003), suggesting that other ACs might be involved as well. Apart from AC1, AC2 and AC9 also show high expression levels, while AC8 levels were actually rather low (Shahoha et al., 2022). These results indicate that also AC2 and AC9 could have potential roles in mossy fiber physiology, while the role of AC8 needs to be reassessed (Shahoha et al., 2022). For instance, AC2 and AC9 could be activated through G-proteins (Hanoune and Defer, 2001) of serotonergic, adrenergic or dopaminergic metabotropic receptors (Hamblin et al., 1998; Girault and Greengard, 2004; Johnson, 2006). Nevertheless, AC1 is likely the predominant isoform in mossy fiber boutons and probably primarily involved in long-term plasticity. Interestingly, especially synapses with presynaptic forms of LTP express high levels of AC1 (Saunders et al., 2018). Furthermore, AC1 is also suggested to play a predominant role in mossy fiber LTD cascade, further underpinning its role in mossy fiber plasticity (Shahoha et al., 2022).

Protein-kinase A

The activation of adenylyl cyclases leads to an increase in presynaptic cyclic adenosine monophosphate (cAMP) concentration that activates protein-kinase A (PKA) (Villacres et al., 1998; Wang et al., 2003). Genetic and pharmacological inhibition of PKA function (Huang et al., 1994, 1995; Weisskopf et al., 1994; Tong et al., 1996) have demonstrated a role of this kinase in mossy fiber LTP. Also, manipulation of the PKA interactors PKAa and AKAP7 lead to impaired mossy fiber plasticity (Huang et al., 1995; De Lecea et al., 1998; Jones et al., 2016). Hence, PKA is thought to be a substantial regulator of mossy fiber presynaptic plasticity (Nicoll and Schmitz, 2005; Shahoha et al., 2022). Experimentally, mossy fiber presynaptic potentiation can be induced by the application of the adenylyl cyclase activator forskolin (Weisskopf et al., 1994) as well as by cAMP analogues (Weisskopf et al., 1994; Wang et al., 2003; Kaeser-Woo et al., 2013) or via a genetically-encoded, light-activated form of AC (Oldani et al., 2021).

Downstream Targets

Many potential direct and indirect PKA targets have been tested for their role in mossy fiber LTP (Nicoll and Schmitz, 2005; Shahoha et al., 2022). For example, impaired or abolished LTP has been reported for knockouts or knockdowns of Rab3A (Castillo et al., 1997), RIM1a (Castillo et al., 2002), Synaptotagmin-12 (Kaeser-Woo et al., 2013) and Tomosyn (Ben-Simon et al., 2015). However, several of those targets show

only impairment in electrically induced LTP, but not upon induction with forskolin (Shahoha et al., 2022). These induction mechanisms might activate distinct or only partially overlapping pathways (Shahoha et al., 2022; Fukaya et al., 2023b), therefore leading to differential effects in the knockout studies. Furthermore, forskolin activates nine out of ten AC isoforms (Hanoune and Defer, 2001) and is thus not specific to mossy fiber ACs, but probably also activates ACs in neighboring neurons and glia cells (Zhou et al., 2019). However, the deletion of synaptotagmin-12, Tomosyn or Epac2 leads to impaired LTP for both induction methods (Kaeser-Woo et al., 2013; Ben-Simon et al., 2015; Fernandes et al., 2015).

Apart from PKA, there are other cAMP-dependent downstream pathways present at mossy fiber boutons, namely the Epac2 and the Rapgef2 pathway. The knockout of Epac2 does impair mossy fiber potentiation by reducing the RRP of vesicles, while basal transmission and short-term plasticity are not affected (Fernandes et al., 2015). Interestingly, Epac2 is highly expressed in the *stratum lucidum* (Kawasaki et al., 1998). At the cerebellar parallel fiber to Purkinje cell synapse, a cascade involving cAMP activation of Epac2, but not PKA, was necessary for presynaptic LTP, that is expressed at this synapse (Salin et al., 1996a), and led to an increase in the RRP (Martín et al., 2020). Taken together, there might be parallel cAMP-dependent pathways present and involved in mossy fiber bouton presynaptic plasticity (Shahoha et al., 2022). Future work is needed to untangle the precise activation and possible interaction of those pathways and how they are involved in presynaptic plasticity.

Structural Plasticity

It has long been suggested, that memories are physically encoded and stored (Ramón y Cajal, 1911; Hebb, 1949; Tonegawa et al., 2015). Two main theories – the structural plasticity theory and the engram theory – have long existed in parallel and evidence for both theories has been provided independently (Takeuchi et al., 2014; Tonegawa et al., 2015). Recently, these theories were unified in a study showing that hippocampal cells participating in an engram of a fear memory also undergo synaptic strengthening and structural plasticity (Ryan et al., 2015). It is known that dentate gyrus granule cells can participate in engram formation and that hippocampal mossy fiber to CA3 synapses undergo physical strengthening during presynaptic potentiation (Hainmueller and Bartos, 2018; Hainmueller, 2020).

Possible structural changes are manifold and involve both physical remodeling of the synapse as well as changes in the number or position of single molecules (Ortega-de San Luis and Ryan, 2022). For instance, it has been shown that large mossy fiber terminals can dynamically change their shape within a few hours, while small mossy fiber terminals and filopodial extensions onto interneurons can even appear and disappear completely within a few days (De Paola et al., 2003). Changes in the number of filopodial extensions could also be triggered by contextual fear conditioning (Ruediger et al., 2011) and changes in the length of

filopodial extensions were observed in mice which were held in an enriched environment (Monday et al., 2022). Such changes might be mediated via local protein translation of structural proteins, as it has been shown for β-actin in the mossy fiber bouton (Monday et al., 2022). Hippocampal mossy fiber boutons can also increase or decrease in their complexity or size, dependent on the stimulus. Decreased complexity was observed when boutons were deprived of stimulation (Chierzi et al., 2012). Increases in complexity were observed in response to chemical (Zhao et al., 2012; Orlando et al., 2021) or electrical stimulation (Maruo et al., 2016), when mice were kept in an enriched environment (Galimberti et al., 2006; Gogolla et al., 2009) or after spatial learning (Holahan et al., 2006; Routtenberg, 2010). Consequently, also the density of postsynaptic thorny excrescences is plastic (Zhao et al., 2012; Gómez-Padilla et al., 2020).

Changes in synaptic strength might comprise changes in release probability, the quantal size or the number of release sites (see before). Recently, it has been shown that mossy fiber boutons have an increased density in active zones after chemical potentiation, while the individual active zone area stays the same (Orlando et al., 2021). The same study showed an increase in the presynaptic release area of glutamate upon chemical potentiation (Orlando et al., 2021), underpinning the ultrastructural observation. Furthermore, after potentiation, individual active zones were equipped with an increased number of docked and tethered vesicles, indicating an increased recruitment of vesicles into the RRP and potentially an increase in the number of available release sites within the active zone (Orlando et al., 2021). This observation was confirmed in a recent preprint (Kim et al., 2023) and also detected after PTP at mossy fiber synapses (Vandael et al., 2020). There, it has been called “pool engram” and was shown to be stable for minutes of inactivity (Vandael et al., 2020).

At the nanoscale, changes in synaptic transmission might be underpinned by a remodeling of molecules in the active zone (Sigrist and Schmitz, 2011; Kim et al., 2023). Increases in the number of specific active zone proteins might for example be important for the recruitment of vesicles to release sites (Sigrist and Schmitz, 2011). The dispersion of vesicles could promote a similar process, as it has been observed after chemical potentiation (Orlando et al., 2021). Other molecules that might increase in number could be those that promote the release itself, as for example Munc13-1 or presynaptic calcium channels. Also, the relative position of these molecules to each other could change, thereby influencing the release probability (Jackman and Regehr, 2017). Indeed, experiments in dissociated hippocampal synapses have indicated, that calcium channels might move closer towards release sites upon cAMP-induced plasticity (Midorikawa and Sakaba, 2017). Due to the non-linear relationship between the Ca^{2+} concentration and release, such a movement could increase the release massively (Dittman and Ryan, 2019). Taken together, a plethora of structural changes might occur at the hippocampal mossy fiber to CA3 pyramidal cell synapse to promote the strengthening of this connection and to potentially take part in an engram.

Voltage-gated Calcium Channels

Calcium ions are important intracellular second messengers in various processes and cell types (Berridge et al., 2003). However, high intracellular calcium concentrations for prolonged times are toxic and result in cell death (Hajnóczky et al., 2003), which is why the calcium concentration within the cell is closely controlled and maintained at low levels in the range of 100 nm, thanks to an interplay of calcium buffers, intracellular stores and machinery for calcium efflux (Berridge et al., 2003; Clapham, 2007). These circumstances lead to a massive chemical gradient between extra- and intracellular calcium ions, with approximately 20.000 fold higher concentrations outside the cell (Hajnóczky et al., 2003; Clapham, 2007). Opening of calcium-permeable ion channels in the cell membrane will thus usually lead to a calcium influx, creating domains in which the Ca^{2+} concentration reaches the micromolar range (Wadel et al., 2007). There is a variety of calcium-permeable channels, that operate via ligands or voltage sensors (Berridge et al., 2003). At presynaptic terminals, calcium influx is the trigger for release (Katz and Miledi, 1967; Augustine et al., 2003) and mainly occurs through voltage-gated calcium channels (VGCC) in the plasma membrane. Subsequently, calcium-induced calcium release from intracellular stores might also contribute to the presynaptic calcium rise (Narita et al., 1998; Emptage et al., 2001), also at hippocampal mossy fiber boutons (Liang et al., 2002). The opening of VGCC depends on the membrane potential. An incoming action potential depolarizes the membrane, leading to conformational changes, opening the VGCC at voltages specific for a certain channel type (Catterall, 2011).

Voltage-gated Calcium Channels

There are ten members of voltage-gated calcium channels, which are molecularly defined via their α1 subunit (Catterall, 2011) (Table 1). Originally, calcium channels were characterized via their Ca^{2+} currents and current blockers, leading to an additional physiological/pharmacological division (Catterall, 2011). I will hereafter refer to the channel type following the more common classification into three subfamilies of VGCC (Ca_v1, Ca_v2 and Ca_v3) and specify the subtype dependent on their pore-forming α1 subunit (Snutch Reiner 1992, Ertel 2000). The Ca_v1 subfamily has four members, that are all characterized by L-type currents (Catterall, 2011). These currents are long-lasting and mediate processes like muscle contraction, gene transcription, and secretion in endocrine cells or at ribbon synapses (Catterall, 2011). Subfamily Ca_v2 has three members, which all conduct different types of calcium currents, namely P/Q-type currents for the α1-subunit $Ca_v2.1$ (Mori et al., 1991; Starr et al., 1991), N-type currents for $Ca_v2.2$ (Dubel et al., 1992; Williams et al., 1992) and R-type currents for $Ca_v2.3$ (Soong et al., 1993). Ca_v2 channels are mainly involved in synaptic transmission of fast and synchronous release in neurons (Catterall, 2011). Finally, subfamily Ca_v3 has three members that all show T-type Ca^{2+} currents (Perez-Reyes et al., 1998). Due to the transient nature of these currents and electrophysiological properties similar to those of Na^+ channels (Catterall, 2011), they are involved in repetitive firing and pacemaking, for example in the cardiac

muscle (Mangoni et al., 2006). Apart from subunit α1, the pore-forming subunit, calcium channels comprise up to four additional subunits – α2, β, γ and δ – which can influence the exact calcium channel function and expression level (Catterall, 2011).

Granule cells express members of all three VGCC subfamilies at different locations within the cell. At the mossy fiber terminal, L-type channels are probably present (Castillo et al., 1994; Tokunaga et al., 2004; Tippens et al., 2008) but their contribution to fast synaptic transmission is likely negligible (Castillo et al., 1994; Breustedt et al., 2003; Tokunaga et al., 2004). They might have a role in Ca^{2+} release from internal stores during the induction of mossy fiber LTP (Lauri et al., 2003) or in mossy fiber sprouting (Ikegaya et al., 2000). T-type channels are not present in the large mossy fiber bouton (Tokunaga et al., 2004), but at the axon initial segment of mossy fibers where they are likely involved in burst firing of granule cells (Dumenieu et al., 2018). However, they were also suggested to play a role in newborn granule cell plasticity (Schmidt-Hieber et al., 2004). Lastly, Ca_v2 family members are all expressed in mossy fiber boutons (Table 1) and involved in synaptic transmission and plasticity (Castillo et al., 1994; Breustedt et al., 2003; Pelkey et al., 2006; Li et al., 2007). A total number of approximately 2000 Ca_v2 channels per bouton has been calculated from direct bouton recordings, in which the majority is made up by P/Q-type channels (66 %), followed by N-type (26 %) and R-type (8 %) channels (Li et al., 2007). The presence of different VGCC at the mossy fiber bouton, as well as at other synapses, might help to generate differential responses dependent on presynaptic activity patterns (Dolphin and Lee, 2020).

Ca_v2 Calcium Channels

Channels $Ca_v2.1$ and $Ca_v2.2$ play a predominant role in fast synaptic transmission at most synapses releasing glutamate, GABA and acetylcholine (Catterall, 2011; Dolphin and Lee, 2020). They are recruited to release sites by RIM and RIM-BP (Kaeser et al., 2011; Grauel et al., 2016; Brockmann et al., 2019) and they also directly interact with other parts of the release machinery (Catterall, 2011). Furthermore, these calcium channels might be involved in the alignment of nanocolumns, thereby positioning release sites opposite to postsynaptic receptors (Biederer et al., 2017). However, the number of interaction partners for Ca_v2 might be as high as 200 (Müller et al., 2010), opening up endless possibilities for calcium channel actions and modulation.

Table 1: Overview of voltage-gated calcium channels.

Family	α1 subunit	Ca^{2+} current type	Expressed at MFB?	References
Ca_v1	$Ca_v1.1$ / α-1S	L-type	Yes	Castillo et al., 1994; Tokunaga et al., 2004; Tippens et al., 2007
	$Ca_v1.2$ / α-1C			
	$Ca_v1.3$ / α-1D			
	$Ca_v1.4$ / α-1F			
Ca_v2	$Ca_v2.1$ / α-1A	P/Q-type	Yes	Li et al., 2007; Castillo et al., 1994; Breustedt et al., 2003
	$Ca_v2.2$ / α-1B	N-type	Yes	Li et al., 2007, Castillo et al., 1994, Breustedt et al., 2003
	$Ca_v2.3$ / α-1E	R-type	Yes	Day et al., 1996; Li et al., 2007; Parajuli et al., 2012; Soong et al., 1993
Ca_v3	$Ca_v3.1$ / α-1G	T-type	No	Tokunaga et al., 2004; Meir et al., 1999
	$Ca_v3.2$ / α-1H			
	$Ca_v3.3$ / α-1I			

$Ca_v2.1$ is the main contributor to basal synaptic transmission in hippocampal mossy fiber boutons (Castillo et al., 1994; Breustedt et al., 2003; Pelkey et al., 2006); as it has been shown with pharmacological experiments involving the P/Q-type blocker ω-Agatoxin (Mintz et al., 1992). When overexpressed in cultured hippocampal neurons, $Ca_v2.1$ is mobile within presynaptic membranes (Schneider et al., 2015), which could dynamically influence release probability. At most central synapses, $Ca_v2.1$ channels have been shown to participate in nanodomain coupling to release sites (Eggermann et al., 2012), while the precise position might depend on the splicing of the channels' C-terminus (Heck et al., 2019). However, in mossy fiber boutons, the coupling distance between Ca^{2+} channels and release sites is loose (Vyleta and Jonas, 2014; Brockmann et al., 2019), allowing for a dynamic range in presynaptic plasticity (Böhme et al., 2018). Indeed, in mossy fiber short-term facilitation, $Ca_v2.1$ seem to produce a homogenous Ca^{2+} influx via microdomains, recruiting additional release sites to facilitate transmission (Chamberland et al., 2017). In mossy fiber long-term potentiation, however, these channels are not needed for induction (Castillo et al., 1994; Breustedt et al., 2003; Dietrich et al., 2003).

Blocking basal synaptic transmission at mossy fiber boutons with the N-type blocker ω-Conotoxin (Cox and Dunlap, 1992), results in inhibition of approximately 45 % of the total transmission (Castillo et al., 1994; Breustedt et al., 2003; Pelkey et al., 2006). Thus, $Ca_v2.2$ is also involved in basal synaptic transmission but to a lesser extent than $Ca_v2.1$. During short-term facilitation $Ca_v2.2$ channels create spatially heterogenous Ca^{2+} elevations and induce multivesicular release (Chamberland et al., 2017). However, they are not needed for the induction of mossy fiber LTP (Castillo et al., 1994; Breustedt et al., 2003; Dietrich et al., 2003). When activity is increased to over 20 Hz, the proportion of N-type gating in synaptic transmission decreases in relation to the P/Q type gating (Ricoy and Frerking, 2014).

A completely opposite picture emerges for the $Ca_v2.3$ Ca^{2+} channel at mossy fiber boutons. This channel is likely not involved in basal synaptic transmission (Castillo et al., 1994; Breustedt et al., 2003; Dietrich et al., 2003). However, its mRNA is enriched in granule cells (Soong et al., 1993; Day et al., 1996) and the protein has been detected within the bouton (Day et al., 1996) and at the active zone (Parajuli et al., 2012). A likely interaction site for RIM strengthens the putative localization to active zones (Kaeser et al., 2011). Like basal transmission, facilitation of the mossy fiber bouton is also not changed upon pharmacological or genetic disturbance of this channel type (Breustedt et al., 2003; Dietrich et al., 2003). However, induction of LTP with weak tetanic stimulation was impaired (Breustedt et al., 2003; Dietrich et al., 2003). Calcium imaging furthermore revealed that 34 % of the total Ca^{2+} influx was still present when P/Q- and N-type channels are blocked under basal conditions (Breustedt et al., 2003). This residual component is due to R-type currents as it could be partially blocked with R-type blockers SNX-482 (Newcomb et al., 1998) and nickel (Soong et al., 1993). An in-depth analysis of VGCC in mossy fiber boutons reveiled that $Ca_v2.3$ calcium channels are activated at lower membrane potentials than $Ca_v2.1$ and 2.2 (Li et al., 2007). Furthermore, R-type channels, together with N-type channels, are preferentially recruited during action potential broadening (Li et al., 2007), which occurs during frequent stimulation of granule cells (Geiger and Jonas, 2000a).

Interestingly, the gating properties of $Ca_v2.3$ can be changed through binding of Zn^{2+} in a concentration-dependent manner (Neumaier et al., 2020b). $Ca_v2.3$ is among the most sensitive targets for Zn^{2+} and Cu^{2+} currently known (Neumaier et al., 2020b) and regions in the brain with high $Ca_v2.3$ expression colocalize with regions containing Zn^{2+} (Sochivko et al., 2002; Weiergräber et al., 2006). Mossy fiber boutons release Zn^{2+} (Vogt et al., 2000), thus this channel could be implicated in a complex modulatory cascade, further involving excitatory transmitters (Shcheglovitov et al., 2012; Neumaier et al., 2018). Finally, $Ca_v2.3$ channels have been implicated in asynchronous transmitter release (Ermolyuk et al., 2013).

Munc13

Members of the Munc13 family are core proteins of the active zone (Südhof, 2012) and necessary for synaptic release (Augustin et al., 1999b; Varoqueaux et al., 2002). They are involved in docking and priming of synaptic vesicles, thus rendering the vesicle fusion competent (Rizo, 2022). There are three orthologues present in the brain, Munc13-1, Munc13-2 and Munc13-3 (Augustin et al., 1999a, 1999b; Varoqueaux et al., 2002). Munc13-1 is essential for release at 90 % of glutamatergic synapses, while Munc13-2 is likely mediating vesicle priming at the remaining synapses. GABAergic synapses probably use a mix of Munc13-1 and Munc13-2-dependent release (Varoqueaux et al., 2002). Also in dentate granule cells, both Munc13-1 and Munc13-2 are expressed (Breustedt et al., 2010). Munc13-3 is only expressed in the cerebellum (Augustin et al., 1999a).

Munc13-1

Munc13-1 is a cytosolic protein highly expressed at presynaptic terminals, including hippocampal mossy fiber boutons (Betz et al., 1998). Due to its co-localization to core fusion machinery, Munc13-1 is considered a marker for release sites (Sakamoto et al., 2018). Upon the deletion of Munc13-1, the RRP and residual spontaneous as well as evoked release are vanished (Augustin et al., 1999b; Varoqueaux et al., 2002; Imig et al., 2014), confirming its crucial role in release. It covers multiple roles in docking and priming and is therefore implicated in both synaptic transmission as well as in plasticity mechanisms (Südhof, 2012; Rizo, 2022). Munc13-1 can form heterodimers with RIM via its C_2A domain (Betz et al., 2001), thereby influencing RIM-dependent plasticity (Camacho et al., 2017). Also other Munc13-1 domains are implicated in plasticity mechanisms (Junge et al., 2004; Basu et al., 2007; Shin et al., 2010; Lipstein et al., 2021). Furthermore, Munc13-1 is involved in tethering of vesicles to the active zone, the SNARE complex assembly (Basu et al., 2005; Ma et al., 2011; Yang et al., 2015) and the bridging between vesicles and the plasma membrane (Liu et al., 2016; Quade et al., 2019; Papantoniou et al., 2023). Apart from small clear vesicles, Munc13-1 is also implicated in the priming and release of dense-core vesicles (van de Bospoort et al., 2012). At the mossy fiber bouton, Munc13-1 knockout hindered the structural remodeling of the bouton after chemical LTP in form of increased active zone density and bouton complexity (Zhao et al., 2012).

Although Munc13-1 is the primary isoform implicated in release, Munc13-2 is also expressed in mossy fiber boutons (Breustedt et al., 2010). *In vitro* recordings at the mossy fiber to CA3 synapse in a Munc13-2 knockout model revealed impaired transmission and increased paired-pulse and frequency facilitation. Together with pharmacological experiments, these results elucidated a reduction in release probability at mossy fibers lacking Munc13-2. However, LTP was unchanged for both electrical and chemical induction protocols (Breustedt et al., 2010). This study indicates a role for Munc13-2 in shaping mossy fiber synaptic transmission and plasticity, together with the primary isoform Munc13-1.

Synapsins

Synapsins are phosphoproteins associated with synaptic vesicles, which are important regulators of neurotransmission and plasticity. Their relevance is indicated by the facts that (1) synapsins belong to the most abundant synaptic proteins (Huttner et al., 1983), (2) synapsin genes are conserved throughout the phylogenetic tree of life (Humeau et al., 2011) with a synapsin-like sequence present even in protozoa (Candiani et al., 2010), (3) they are associated with several neuropathological phenotypes (Garcia et al., 2004; Fassio et al., 2011; Porton et al., 2011; Mirza and Zahid, 2018) and (4) virtually every neuron expresses at least one synapsin isoform (Südhof et al., 1989; Fassio et al., 2011), leading to its frequent use as a neuron-specific promotor. Synapsins discovery and characterization is inevitably linked to Paul Greengard (Ferry, 2019). The first members of the synapsin family were discovered in his lab in the early 1970s in fractions of synaptic membrane as substrates of protein kinase-A (Ueda et al., 1973), then named protein I and II. By that, they were among the first vesicle-associated proteins to be described (Fdez and Hilfiker, 2006).

There are three synapsin genes in mammals – *SYN1, SYN2, SYN3* – leading to at least ten differentially spliced isoforms in humans (Südhof et al., 1989; Hosaka and Südhof, 1998; Kao et al., 1998). However, synapsin III is usually downregulated early in development (Kao et al., 1998; Ferreira et al., 2000) (Figure 8), leaving synapsin I and II as the predominant isoforms. Synapsins are expressed throughout the nervous system (Fassio et al., 2011). But more recently, synapsins have also been identified in non-neuronal tissue: They have been detected in osteoblasts (Bhangu et al., 2001), human sperm (Coleman et al., 2015), rat insulin-secreting cells (Matsumoto et al., 1999), liver cells (Bustos et al., 2001) and in cells of the *Octopus vulgaris* gonads (Maiole et al., 2019).

Synapsins are associated with the surface of small synaptic vesicles (De Camilli et al., 1983; Huttner et al., 1983; Benfenati et al., 1989; Kao et al., 1998), but more recent literature also suggests an association with dense-core vesicles in *C. elegans* synapses (Yang et al., 2021; Yu et al., 2021). Synapsin I alone makes up 6 % of all synaptic vesicle proteins (Huttner et al., 1983) and, on average, 8.3 synapsin proteins are associated with one synaptic vesicle (Takamori et al., 2006). Within the nerve terminal, synapsins are mainly concentrated in the distal vesicle pool – the reserve pool – and get less abundant towards the active zone (Evergren et al., 2007; Orlando et al., 2014).

Synapsin Function

The postulated main function of synapsins is the regulation of the reserve pool of synaptic vesicles, as it has been shown that synapsin knockout models lack this vesicle pool (Li et al., 1995; Rosahl et al., 1995; Ryan et al., 1996a). The reserve pool comes into play when sustained high-frequent activity depletes the RRP of synapses. Then, vesicles from the reserve pool replenish the vesicles at the active zone (Pieribone et al.,

1995; Shupliakov et al., 2011), thereby enabling incessant release and response options to changes in synaptic activity (Rosenbaum et al., 2012). Recently it has been suggested that the mobilization of vesicles underlies short-term memory in the hippocampus, potentially mediated by synapsins (Vandael et al., 2020). The precise role of synapsins in regulating synaptic vesicle availability is not yet clear, but it is thought that they maintain the reserve pool in some physical or biochemical way (Zhang and Augustine, 2021). Upon activity-dependent phosphorylation of synapsins, they detach from the synaptic vesicles, allowing the vesicles to disperse (Sihra et al., 1989; Hosaka et al., 1999; Chi et al., 2001, 2003). This has also been shown in synapsin-regulated liquid phases upon the addition of CaMKII (Milovanovic et al., 2018). Notably, among multiple phosphorylation sites for several kinases, all synapsin isoforms possess conserved phosphorylation sites for PKA (Kao et al., 1999; Piccini et al., 2015) and could thus be involved in PKA-dependent plasticity mechanisms at the mossy fiber bouton.

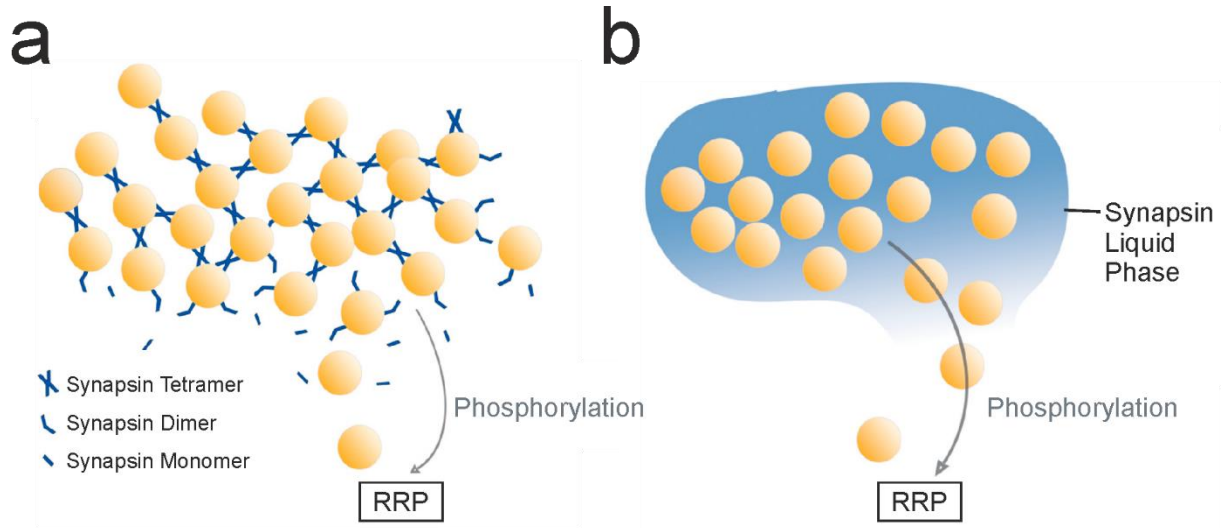

*Figure 7: **Proposed mechanisms for synapsin-mediated maintenance of the synaptic vesicle reserve pool. a)** The first mechanism proposes that synapsins act like tethers and crosslink synaptic vesicles with each other within the reserve pool. **b)** The second mechanism suggests that synapsins form a liquid phase in which synaptic vesicles from the reserve pool are captured. Both panels are adapted from Zhang and Augustine, 2021.*

There are several hypotheses as to how synapsins maintain the reserve pool. One model suggested that synapsins are connected with both synaptic vesicles and actin (Greengard et al., 1993), implying that the actin cytoskeleton might maintain the vesicles in a cluster. However, more evidence is pointing in other directions (Zhang and Augustine, 2021). Two models have been described, that could possibly work in concert (Zhang and Augustine, 2021). (1) Synapsins could crosslink synaptic vesicles to each other, either by being or supporting a molecular tether (Hirokawa et al., 1989), forming dimers and tetramers (Orlando

et al., 2014). (2) Synapsins could form liquid phases and capture synaptic vesicles in it (Milovanovic et al., 2018) (Figure 7). A recent publication further proposed that the prevalent mechanisms might depend on the cell type: They describe that glutamatergic neurons rather express the crosslinking mechanism while in GABAergic neurons liquid-liquid phase separation occurs (Song and Augustine, 2023).

Indeed, it has been suggested before that excitatory and inhibitory neurons might have different mechanisms for vesicle trafficking and recruitment (Fassio et al., 2011). Synapsins are differentially expressed in excitatory versus inhibitory neurons and synapsin knockout models lead to differential effects in these cell types (Gitler et al., 2004, 2008; Fassio et al., 2011). In neurons lacking synapsin I, synapsin III or all three synapsins, basal synaptic transmission is reduced for inhibitory but not excitatory neurons (Terada et al., 1999; Feng et al., 2002; Gitler et al., 2004; Baldelli et al., 2007; Chiappalone et al., 2009). At the same time, synaptic depression in response to high-frequency stimulation is enhanced in excitatory neurons lacking various forms of synapsins (Feng et al., 2002; Gitler et al., 2004; Hvalby et al., 2006; Kielland et al., 2006; Bogen et al., 2009) while it is largely unchanged in inhibitory knockout cells (Feng et al.,2002; Gitler et al., 2004; Chiappalone et al., 2009). These facts are probably responsible for the disturbed excitation-inhibition balance in synapsin knockout animals observed *in vitro*, serving as a potential explanation for the advent of epileptic seizures in these animals (Chiappalone et al., 2009; Fassio et al., 2011; Farisello et al., 2013).

Synapsin III

Synapsin III is usually downregulated early in development (Kao et al., 1998; Ferreira et al., 2000) (Figure 8) and thus may have different primary functions than synapsin I and II. Indeed, in contrast to synapsin I and II, synapsin III can be found in somata and growth cones (Ferreira et al., 2000) and its knockdown or knockout leads to disturbed neurogenesis and axogenesis (Ferreira et al., 2000; Feng et al., 2002; Porton et al., 2011). In neurogenic regions, such as the detate gyrus (Kempermann and Gage, 2000), synapsin III expression is maintained throughout adulthood (Kao et al., 1998; Pieribone et al., 2002). Indeed, synapsin III can be found in young precursors of dentate gyrus granule cells (Pieribone et al., 2002) as well as in mossy fiber boutons of mature tissue (Owe et al., 2009). In neuronal cultures of synapsin III knockout animals, synaptic transmission is reduced in inhibitory cells, while less depression was observed in excitatory neurons (Feng et al., 2002), suggesting a role for synapsin III in transmission and plasticity. Interestingly, in the striatum, synapsin III specifically regulates dopamine release: its knockout results in increased dopamine release (Kile et al., 2010), providing a potential explanation for the involvement of synapsin III in neuropsychiatric disorders (Porton et al., 2011).

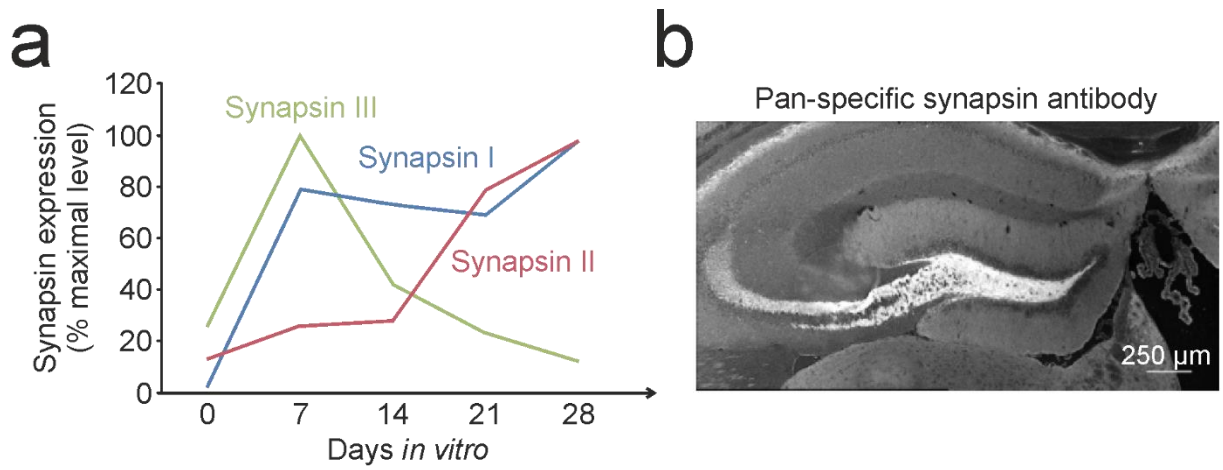

Figure 8: Overview of synapsin III expression. a) *Relative expression of the synapsin isoforms in whole-cell extracts of cultured hippocampal neurons. Adapted from Ferreira et al., 2000. Note the decrease in synapsin III expression after seven days in culture.* ***b)*** *Immunolabeling of synapsin III in the hippocampus of an adult SynDKO mouse with a pan-specific antibody. Adapted from Pieribone et al., 2002.*

Despite the presence of synapsin III in mossy fiber boutons (Pieribone et al., 2002; Owe et al., 2009), the effects of synapsins on mossy fiber synaptic transmission and plasticity have only been investigated in animals lacking synapsin I and II (Spillane et al., 1995; Owe et al., 2009). These studies describe a reduced frequency facilitation (Owe et al., 2009), a slightly reduced PTP (Spillane et al., 1995) but no change in long-term potentiation (Spillane et al., 1995). Of note, the animals used in these studies were less than two months (Spillane et al., 1995) and three to six months old (Owe et al., 2009). All synapsin knockouts, with the exeption of synapsin III knockouts (Feng et al., 2002), develop epileptic seizures at two months of age (Rosahl et al., 1995; Gitler et al., 2004; Ketzef et al., 2011), with likely consequences for the network. This should be kept in mind when assessing the mossy fiber recordings obtained so far in synapsin knockout models.

Aim of the Study

Presynaptic plasticity at the hippocampal mossy fiber to CA3 pyramidal cell synapse is implicated in many mnemonic functions (Hainmueller, 2020). However, the precise underlying mechanisms are still not fully understood. In this thesis, I wanted to test three main hypotheses, that have been proposed for the mediation of long-lasting increase in neurotransmission at potentiated mossy fiber boutons.

Hypothesis I: Change in coupling distance during presynaptic potentiation

It is known that presynaptic long-term plasticity at mossy fiber boutons is accompanied by a sustained increase in release probability (Zalutsky and Nicoll, 1990; Xiang et al., 1994; Maeda et al., 1997; Kawamura et al., 2004), resulting in an increase in transmitter release. Voltage-gated calcium channels are needed at active zones to trigger release upon depolarization of the terminal (Catterall, 2011). Distinct to many other central synapses (Eggermann et al., 2012), mossy fiber boutons exhibit a loose coupling between voltage-gated calcium channels and release sites (Vyleta and Jonas, 2014). Interestingly, a slow acting calcium buffer was unable to reduce transmission in mossy fiber boutons after chemical activation of presynaptic potentiation (Midorikawa and Sakaba, 2017). Together with the fact that voltage-gated calcium channels are mobile within presynaptic membranes (Schneider et al., 2015), these findings resulted in the following hypothesis:

During presynaptic potentiation at hippocampal mossy fiber boutons, the loose coupling between voltage-gated calcium channels and release sites tightens, thereby increasing the probability for release.

To test this hypothesis, I combined immunohistochemistry with superresolution gSTED microscopy. I measured the distance between Ca_V2 calcium channels and Munc13-1, a marker for release sites (Sakamoto et al., 2018) in acute mouse brain slices. Measurements were restricted to *stratum lucidum* in hippocampal area CA3, where mossy fiber boutons terminate (Amaral et al., 2007). Distances were compared between control and chemically potentiated slices.

Hypothesis II: Increase in the number of release sites during presynaptic potentiation

The strength of a synapse depends on many possible factors, among them also the number of release sites (Dittman and Ryan, 2019). It has been shown that hippocampal mossy fiber boutons have an increased density of active zones after chemical potentiation, while the individual area of active zones is unchanged (Orlando et al., 2021). Furthermore, potentiation leads to the increase in presynaptic glutamate release area and an increase in the number of tethered vesicles (Orlando et al., 2021). Since Munc13 proteins are

indispensable for neurotransmitter release at synapses (Augustin et al., 1999b; Varoqueaux et al., 2002) and they were shown to be a marker for release sites (Sakamoto et al., 2018), the second hypothesis was:

During presynaptic potentiation at hippocampal mossy fiber boutons, there is an increase in the active zone protein Munc13-1.

I tested this hypothesis in acute mouse brain slices stained for Munc13-1 and ZnT-3, a marker for mossy fibers (Wenzel et al., 1997). In ZnT-3 positive regions of hippocampal area CA3 I measured the fluorescence intensity of immunolabeled Munc13-1 in confocal stacks. I compared intensities between stacks from control and chemically potentiated slices. Furthermore, I compared different incubation times for the chemical activator, to discriminate possible translational effects (Monday et al., 2022) from short-term effects.

Hypothesis III: The absence of synapsins leads to impaired presynaptic plasticity in hippocampal mossy fiber boutons

Synapsins are synaptic phosphoproteins, involved in the maintenance of presynaptic vesicle pools (Zhang and Augustine, 2021). They have been implicated in the replenishment of the readily releasable pool of vesicles during periods of high activity. The knockout of synapsin I and II, the isoforms present in mature synapses, did not change long-term potentiation of hippocampal mossy fiber boutons (Spillane et al., 1995). However, the third isoform, synapsin III, which is usually downregulated early in development (Kao et al., 1998; Ferreira et al., 2000), is still expressed at adult mossy fiber terminals (Pieribone et al., 2002). The following hypothesis was therefore tested:

In mice lacking all synapsin isoforms, presynaptic plasticity is disturbed.

The hypothesis was tested by performing electrophysiological mossy fiber field recordings in acute mouse brain slices of wildtype and knockout mice. Because synapsin knockout animals develop epileptic seizures approximately two months after birth (Gitler et al., 2004; Ketzef et al., 2011), two age groups were compared: one before and one after the onset of seizures. The experimental protocol included short-term as well as long-term plasticity types.

Material and Methods

Material

Table 2: Key resources used in this thesis ordered by type. A*ntibodies used in immunohistochemical stainings are listed in separate tables, except for the Fab fragment used for blocking (see below).*

Reagent type or resource	Designation	Source or reference	Identifier/ Order number	Additional information
Antibody	Goat-anti-mouse-IgG (Fab-specific)	Sigma Aldrich	M6898-1ML	
Chemical compound, drug	Agarose Low Melt	Carl Roth	#6351.5	
Chemical compound, drug	DCG-IV	Tocris Bioscience	#0975	
Chemical compound, drug	DMSO	Thermo Fisher	#D12345	
Chemical compound, drug	Forskolin	Cayman Chemical via AdipoGen Lifesciences	AG-CN2-0089-M050	
Chemical compound, drug	n-Hexan	Carl Roth	3907.1	
Chemical compound, drug	Normal Goat Serum	Biozol	0060-01	
Chemical compound, drug	ProLong Gold Antifade Mountant	Thermo Fisher	#P36930	
Chemical compound, drug	Tissue-Tek O.C.T. Compound	Science Services	SA62550-01	
Chemical compound, drug	Triton X-100	Carl Roth	3051.3	
Consumable	Borosilicate capillaries	Science Products	GB150EFT-10	

Consumable	High precision coverslip	Carl Roth	#LH25.1	
Consumable	PAP-pen	Sigma Aldrich	Z672548	
Consumable	Silver wire	Science Products	AG-8W and E-205	
Consumable	SuperFrost Plus coverslides	VWR	#J1800AMNZ	
Software plugin	"GaussFit OnSpot" for Fiji	https://imagej.net/ij/plugins/gauss-fit-spot/index.html		Written by Peter Haub and Tobias Meckel
Software plugin	"Modified multichannel plot profile plugin" for Fiji	DOI: 10.5281/zenodo.597784		Written by Tiago Ferreira
Software package	emmeans for R	https://github.com/rvlenth/emmeans	RRID:SCR_018734	Version 1.8.5
Software	Excel	Microsoft	RRID:SCR_016137	Microsoft Office 2016
Software	Fiji (ImageJ)	Schindelin et al., 2012	RRID:SCR_002285	Version 1.52n and higher
Software	Igor Pro	WaveMetrics	RRID:SCR_000325	Version 6 (for recording) Version 8 (for analysis)
Software	Imspector	Abberior Instruments, Germany		Version 16.1.6477 and higher
Software	LAS X	Leica Microsystems	RRID:SCR_013673	
Software package	lme4 for R	Bates et al., 2015	RRID:SCR_015654	

Software plugin	NeuroMatic for Igor Pro	Rothman and Silver, 2018	RRID:SCR_004186	
Software	Prism	GraphPad by Dotmetrics	RRID:SCR_002798	Version 8.4.0 for Windows
Programming Language	Python		RRID:SCR_008394	Version 3.8
Software	Spyder		RRID:SCR_017585	Version 4.1.5
Programming Language	R for Computing	R Core Team (2022). https://www.R-project.org	RRID:SCR_001905	Version 4.2.2
Software	R Studio		RRID:SCR_000432	RStudio version 2022.12.0
Strain, strain background (*Mus musculus,* male)	C57BL/6J; control; wildtype	The Jackson Laboratory	RRID:IMSR_JAX:000664	
Strain, strain background (*Mus musculus,* male)	C57BL/6N; control; wildtype	Charles River	RRID:MGI:2159965	
Strain, strain background (*Mus musculus,* male)	SynI/SynII/SynIII triple knockout; SynTKO	The Jackson Laboratory	RRID:MMRRC_041434-JAX	Gitler et al., 2004
Technical equipment	Laser scanning confocal microscope	Leica	TCS SP5	
Technical equipment	HC PL APO CS2 Objective	Leica	#11506343	20x oil-immersion, NA: 0.75
Technical equipment	HCX PL APO Objective	Leica	#11506328	100x oil-immersion, NA: 1.4
Technical equipment	Time-gated three color STED microscope	Abberior Instruments, Germany	Expert Line	

Technical equipment	Cryostat	Leica	CM3050S	
Technical equipment	Cryostat	Microm	HM 500 OM	
Technical equipment	Vibratome	Leica Biosystems	VT1200 S; RRID:SCR_018453	
Technical equipment	Pipette-puller	Narishige	PC-10	
Technical equipment	Pipette-puller	Zeitz-Instrumente	DMZ-Universal	
Technical equipment	Micro forge	Narishige	MF-830	
Technical equipment	Micromanipulator	Luigs & Neumann GmbH	Mini 23 / Mini 25	
Technical equipment	Control system for micromanipulators	Luigs & Neumann GmbH	SM-5 / SM-7 / SM-10	
Technical equipment	Amplifier	Axon Instruments	MultiClamp 700A / 700B; RRID:SCR_018455	
Technical equipment	Stimulation box	A.M.P.I.	ISO-Flex; RRID:SCR_018945	
Technical equipment	Pattern generator	A.M.P.I.	Master 8; RRID:SCR_018889	
Technical equipment	Digitizer	Axon Instruments	Digidata 1550B	

Solutions

Table 3: Solutions for the preparation of acute slices. *Artificial cerebrospinal fluid (ACSF), high-sucrose cerebrospinal fluid (hsACSF) and HEPES-buffered solution (HEPES). pH values for ACSF and hsACSF refer to the time point of saturation with 95 % O_2 (vol/vol) / 5 % CO_2 (vol/vol). All chemicals were purchased from Sigma Aldrich.*

Chemical compound	**Concentration for ACSF (mM)**	**Concentration for hsACSF (mM)**	**Concentration for HEPES (mM)**
NaCl	119	50	145
KCl	2.5	2.5	2.5
$NaHCO_3$	26	25	-
NaH_2PO_4	1	1	-
$MgCl_2$	1.3	7	1
$CaCl_2$	2.5	0.5	1
Glucose	10	10	10
Sucrose	-	150	-
HEPES	-	-	10
Osmolarity (mOsm)	290 - 300	340	300
pH	7.4	7.4	7.4

Table 4: Solutions for immunohistochemical stainings. *Phosphate-buffered saline (PBS) and phosphate buffer (PB). All chemicals were purchased from Sigma Aldrich.*

Chemical compound	**Concentration for 0.1 M PBS (in mM)**	**Concentration for 0.1 M PB (in mM)**
NaCl	154	-
NaH_2PO_4 x H_2O	23.7	22.5
Na_2HPO_4 x $2H_2O$	75.4	76.8
pH	7.4	7.4

Animal Welfare Statement

All animal experiments were carried out according to the guidelines stated in Directive 2010/63/EU of the European Parliament on the protection of animals used for scientific purposes and were approved by the animal welfare committee of Charité – Universitätsmedizin Berlin and the Landesamt für Gesundheit und Soziales (LaGeSo) Berlin (permit T 0100/03 and permit G 0146/20).

All animals were housed in cages offering shelter in form of a house and tubes. They were kept in a 12L:12D hour light-dark cycle and water and food were provided *ad libitum*. When transferred to another cage, tubes were used for handling whenever possible to reduce stress for the animal (Hurst and West, 2010). For SynTKO animals, risk of seizures was reduced by keeping the cages in remote shelves to minimize exposure to light and possible noises.

Study Design

Only male mice were used for experiments in this thesis, to exclude possible indirect estrogen effects on mossy fiber plasticity (Harte-Hargrove et al., 2013). However, future experiments must contain female animals.

Distance Measurements

Samples were prepared from male C57BL/6N mice in the age of 4-5 weeks from at least three different litters per individual dataset. For the $Ca_v2.1$ dataset, 12 mice were used, of which one was excluded because treatment conditions were unclear, resulting in data from 11 mice (Appendix, Table 16). For the $Ca_v2.2$ and $Ca_v2.3$ datasets a cohort of nine mice was shared (Appendix, Table 17, Table 18). However, the staining for $Ca_v2.3$ had to be repeated. For the repeated $Ca_v2.3$ staining, 13 mice were used, from which six had to be excluded, because the Homer1 staining did not work (Appendix Table 18). This resulted in data from seven individual animals for $Ca_v2.3$.

Each brain resulted in ~20 acute 100 µm thick slices. Slices were randomly distributed into two different beakers for the two different treatments. All intact slices were incubated and fixed. Sometimes, individual slices were lost or damaged during the procedure. A subset of several slices per condition (chosen via visual quality inspection) was stained, to account for possible losses during staining or mounting as well as quality differences only visible at the confocal microscope.

Finally, at the gSTED microscope, one slice per condition and animal was imaged. Per slice, six images were taken per region (CA3, CA1). More images were only taken when adjusting the microscope at the start of imaging or if imaging artefacts, bleaching or miss-targeting of the images occurred and were noticed

during imaging. Samples of three animals for both conditions were imaged per day, leading to multiple imaging days per dataset. Images were taken in *stratum lucidum* of area CA3 for slices of both conditions (control and forskolin). Control slices were additionally imaged in the area CA1, *stratum radiatum*, on the same imaging day. For the first five animals in the $Ca_v2.1$ dataset, imaging in CA1 was performed ~45 days later than imaging in CA3.

Pre-imaging, slices were excluded when the ZnT-3 signal was too weak, the slice had cracks or holes in the regions of interest or when the slice was not mounted flat. Post-imaging, images were excluded when not located in the right imaging area, i.e. when located outside the ZnT-3-positive region for CA3 (for example when shifted into CA2 or *stratum oriens*) or when located in *stratum oriens* for CA1. Other exclusion criteria were imaging artefacts, unclear treatment or missing deconvolution (see Appendix, Tables 16-18).

After incubation with either 50 µM forskolin or DMSO-containing ACSF as control solution, slices were transferred to 24-well plates (one plate per animal) for fixing and staining. One half of the plate was allocated to control, the other half to forskolin-treated slices. The position of control/ forskolin allocated halves of the well plate changed randomly throughout experiments. Wells containing slices were labeled with ascending numbers in a way that treatment could not be assigned to the numbers. Like this, I was blinded to the condition of the slices during imaging and analysis. After distance analysis, data files were allocated back to their treatment condition and analyzed statistically.

During the analysis of the Cav2.1 dataset, the number of measurements varied between two and 17 – dependent on the image quality. For the other two images, I improved the constancy of measured distance by always measuring eight constellations per image (see Appendix, Tables 16-18).

Munc Intensity Measurements

Samples were prepared from eight male C57BL/6N mice at the age of 4-5 weeks from at least three litters. After slicing, samples were incubated in forskolin or control solution, either for 15 minutes or 1 hour. Cryosections were prepared in batches, but not all cryosections were stained right away. Some were stored for ~4 months at -20 °C before staining and imaging. The imaging usually took place within one month after staining, but earliest after a curation period of one week. Intact brain slices were chosen for imaging. In each slice, subareas CA3a, CA3b and CA3c were imaged, with the exception of one slice, in which area CA3a could not be imaged. We only analyzed experiments for which we had slices from the same animal and both conditions. During imaging and analysis, I was blinded to the condition of the slice. Due to a necessary repair on the Leica cryostat, a Microm cryostat was used for a subset of samples (Table 2).

SynTKO Field Recordings

We used male SynI/SynII/SynIII triple knockout (SynTKO) mice for our experiments, which are based on work by Gitler et al. (Gitler et al., 2004). They were compared to male C57BL/6J WT mice with matching age. Because SynTKO animals develop epileptic seizures in the age of two months (Farisello et al., 2013), experiments were conducted in two different age groups: one before and one after the onset of epileptic seizures. Presymptomatic mice and their age-matched controls were 4-6 weeks old, while symptomatic animals and the corresponding WTs had an age of 17-19 weeks.

Presymptomatic SynTKO animals used in our experiments came from two different cohorts. The first was sent to us from Prof. Dr. Fabio Benfenati (Instituto Italiano di Tecnologia, Genova, Italy). The second cohort was housed and bred in the Charité animal facility (FEM; Forschungseinrichtungen für Experimentelle Medizin) and provided by Dr. Dragomir Milovanovic (DZNE, Berlin, Germany). Data from both cohorts were pooled, because they were not significantly different (Appendix, Table 98). All WT animals as well as symptomatic SynTKO animals were also bred and housed in the Charité animal facility.

Every experimental dataset from every subgroup (genotypes and age groups) contains data from at least three individual animals (Appendix, Table 96) from more than one litter. Per animal, several slices were used for recordings, which are shown as individual data points in some of the figures. If possible, two mice with different genotypes were recorded on the same day. However, the phenotype of SynTKO animals was so strong, that blinding was not possible.

Exclusion criteria were based on the following: mossy fiber specificity, size of the baseline and technical failures (Appendix, Table 97). Mossy fiber specificity was tested by the application of 1 µM DCG-IV at the end of the experiment, which suppresses release specifically in mossy fibers (Kamiya et al., 1996). Only recordings in which suppression was 75 % or more were included in the analysis. If the fEPSP amplitude size was smaller than two times the noise, it was excluded. Noise was around 25 µV, so we only included measurements with a baseline fEPSP bigger than 50 µV.

Sometimes, the stimulation at 1 Hz or 25 Hz failed or no 25 Hz stimulation was conducted. The corresponding measurements were excluded in the analysis, but the other parameters from that recording were included (i.e. input-output, paired-pulse etc.). We were not able to record the input-output relation in all slices: In these cases, we took averaged PFV and fEPSP values from the baseline instead. If the PFV was not clearly identifiable, we excluded the respective recording from the input-output analysis.

Sample Preparation

For all experiments, sagittal mouse brain slices were prepared, because they are ideal for mossy fiber measurements.

The dissection of the brain and the cutting of acute slices followed the procedures described in Bischofberger et al. 2006 (Bischofberger et al., 2006). Briefly, mice were anesthetized with isoflurane and decapitated with sharp scissors. The head was placed in ice-cold high sucrose artificial cerebrospinal fluid (hsACSF, Table 3) and the brain was removed quickly: the skin on top of the head was cut from rostral to caudal with a scalpel. Then, the skull was opened carefully with fine scissors cutting on top of the *fissura longitudinalis cerebri*, as well as orthogonal to that between cerebrum and olfactory bulbs and between cerebrum and cerebellum. The skull was bent open with the help of forceps, detaching the meninges from the skull, and the brain was taken out with a small spatula.

For recovery, the brain was placed in oxygenated frozen hsACSF for three minutes. Then, it was placed on a closed, ice-filled petri dish, on top of a filter paper. First, the cerebellum and the frontal lobe were cut off. Then, the two hemispheres were separated along the *fissura longitudinalis cerebri* and placed on the medial cut surface. Some superglue was added to the magnetic platform of the vibratome. Excess ACSF was removed from both hemispheres with a filter paper and hemispheres were mounted on the superglue area with their medial side.

The specimen disc was placed in the ice-cooled buffer tray of the vibratome and carefully filled with ice-cold hsACSF. During cutting, the hsACSF in the buffer tray was oxygenated continuously. Some thicker sagittal brain sections were cut until the hippocampal formation was visible and appeared as two separate parts (from lateral to medial). Dependent on the experiment, sagittal sections of different thickness were cut (see specific subsections).

All slices were transferred with a wide-lumen pipette from the buffer tray to an oxygenized beaker containing hsACSF at 34 °C, on a fine mesh made from nylon stockings. Slices stayed in the hsACSF at 34 °C for 30 minutes, before both beakers were taken out of the water bath and the slices were transferred to the second beaker containing ACSF (Table 3) for 30 minutes at room temperature.

Thin Slices for STED Microscopy

In order to be able to cut even and intact 100 µm thin acute slices, mouse brain tissue was embedded into low-melt agarose before cutting. Low-melt agarose has a melting temperature of ~65 °C but once melted it stays liquid down to ~30° C. At this temperature, it can be used to embed acute tissue. Below ~28 °C it solidifies quickly and stabilizes the embedded tissue for cutting. Low-melt agarose solution was prepared at 4 % (mass percentage), heating up 4 g low-melt agarose in 100 ml HEPES-buffered solution (Table 3) in a water bath to 70 °C until it formed a uniform jelly substance. It was stored at 4 °C until use. On the day of experiments, the low-melt agarose was melted in a water-bath on a magnetic stirrer and cooled down to ~40 °C before tissue embedding.

Preparation was done as described above until the part where hemispheres were glued on the specimen holder. Then, a small plastic ring (top part of a 15 ml falcon tube) was put around the hemispheres and filled with the liquid low-melt agarose. The sample was put into the - 20 °C freezer for 3 minutes until the agarose was solidified. The plastic ring was gently lifted and surplus agarose was carefully removed with a scalpel. More superglue was added around the agarose block, using a 100 µl pipette. Then, sagittal sections of 100 µm thickness were cut manually. Most slices were cropped with a bent injection needle, removing unneeded parts around the hippocampus. Cutting, slice transfer and storage were done as described above.

Subsequently, slices were incubated either in ACSF containing 50 µM forskolin or in ACSF containing DMSO (1:1000) as a control for 15 minutes. All solutions were continuously oxygenated. Afterwards they were fixed in 4 % paraformaldehyde for one hour at room temperature. PFA was exchanged with phosphate-buffered saline (PBS) (Table 4) or PBS + 0.1 % NaN_3 for storage. Slices were stored at 4 °C until immunohistochemical stainings (Figure 9).

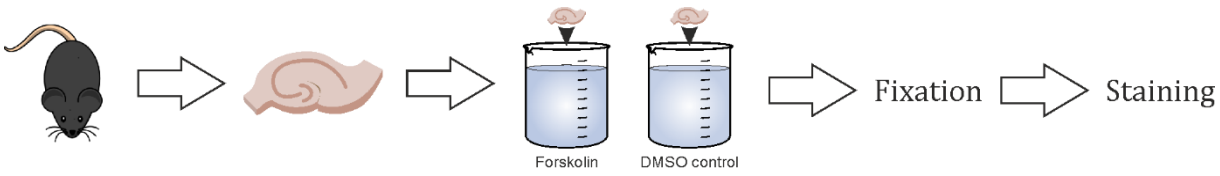

Figure 9: Schematic overview of the preparation of brain slices for STED and confocal experiments. *A mouse brain was prepared and sagittal slices were cut (thickness depended on the experiment). Slices were randomly divided into beakers and incubated either in ACSF containing DMSO (control) or in ACSF containing DMSO and forskolin.*

Cryosections for Munc Intensity Measurements

Preparation of Brain Slices

Sagittal sections of 300 – 500 µm thickness were prepared as described above. Subsequently, slices were incubated either in ACSF containing 50 µM forskolin or DMSO (1:1000) as a control. Some of the slices were incubated for 15 minutes, other slices were incubated for one hour. Afterwards they were fixed in 4 % paraformaldehyde (PFA) for one hour at room temperature. PFA was exchanged with PBS (Table 4) or PBS containing 0.1 % NaN_3 for storage.

Freezing of Slices

To prepare for the freezing, slices were cryoprotected with sucrose solution. On the day of the last preparation and fixation, all slices were incubated in a 10 % sucrose solution (sucrose in PBS) at 4 °C, after 24 hours the solution was exchanged to 20 % sucrose solution and after another 24 hours to 30 % sucrose solution, always at 4 °C.

For the freezing, n-hexan was cooled down in liquid nitrogen to -60 – (-70) °C. The slices were individually placed in cryomolds and excess of liquid was removed with a pipette. A drop of embedding medium for cryotomy (Tissue-Tek O.C.T.) was placed on top of the flat slice and the bottom of the cryomold was held into the cold n-hexan until the medium was frozen and became white. Then, a sample tag was added and the rest of the cryomold was filled with Tissue-Tek and quickly put into the n-hexan for complete freezing (Figure 10). The frozen samples were stored in 50 ml falcon tubes, which contained a drop of frozen *Aqua dest.* to avoid drying out of the sample, at -20 °C until re-sectioning at the cryostat (2 hours – 21 hours later).

Cryosectioning

A Leica cryostat (CM3050S) or Microm cryostat (HM 500 OM) was used for re-sectioning. Cryostat temperature and object holder temperature were set to -18 °C and -19 °C. Frozen samples were glued on a holder with Tissue-Tek and trimmed with a razor blade. Slices of 25 µm thickness were manually cut using a sharp blade and a glass insert to straighten the slice. Slices were collected on superfrost glass slides with the help of a brush. Per glass slide, approximately five slices were placed next to each other. Glass slides were stored at -20 °C until further use.

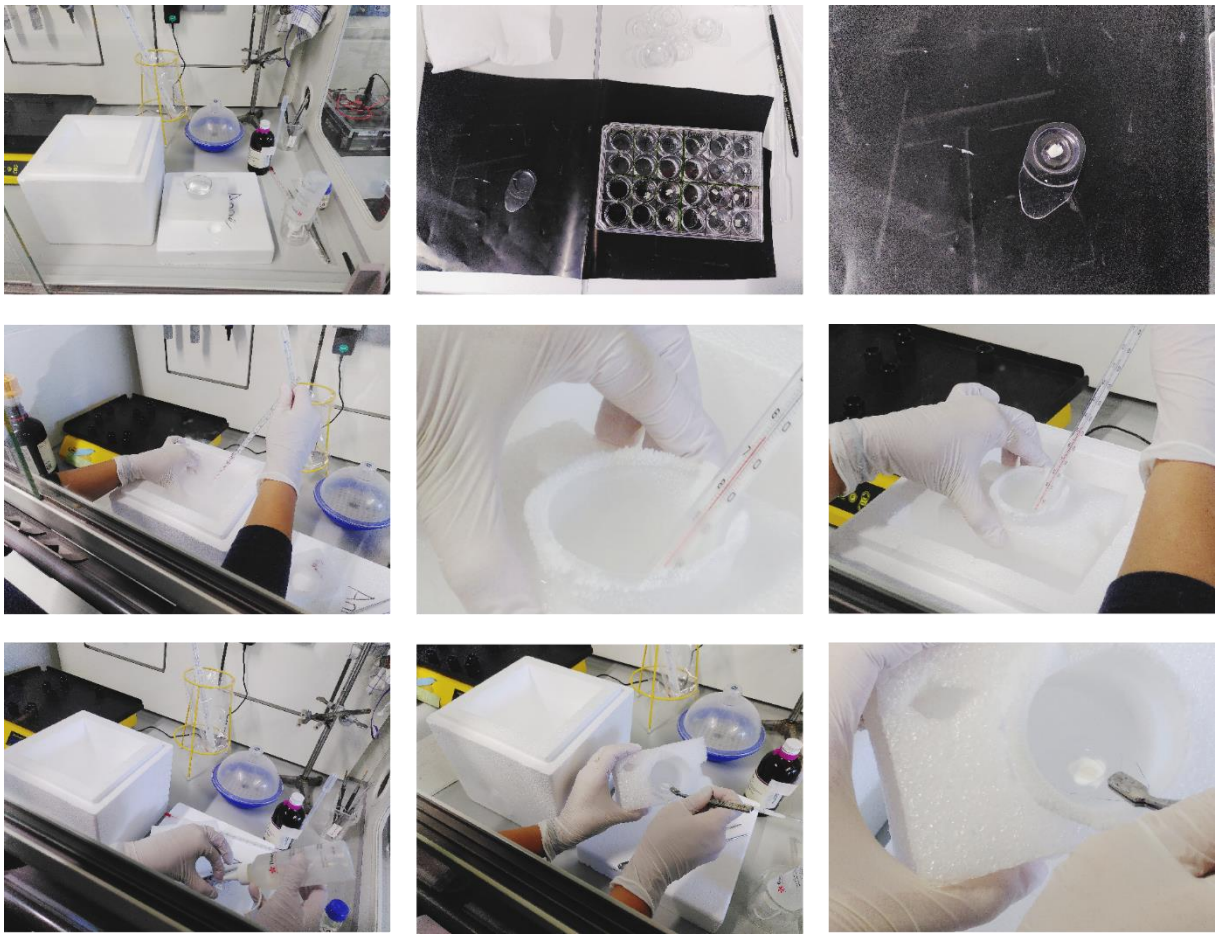

Figure 10: Overview of the freezing procedure. *From left to right and top to bottom: Equipment was placed in a safety cabinet. Fixed and dehydradet slices were transferred into cryomolds. N-hexan was cooled down to -60 – (-70) °C in liquid nitrogen. Then, the slice in the cryomold was covered with Tissue-Tek and frozen in a two-step procedure.*

Slices for SynTKO Field Recordings

Sagittal brain slices of 300 µm thickness were prepared as described above. Slices were kept submerged in ACSF in a beaker at room temperature until the start of experiments.

Immunohistochemical Stainings

Histological stainings allow the detection of specific cell types or structures within tissues. There is a variety of methods available, including chemical, molecular biology and immunological techniques (Schmitz and Desel, 2018). Immunohistological stainings make use of the fact that immune systems produce antibodies against epitopes of exogenous and potentially harmful molecules. Thus, antibodies can be specifically raised against a molecule of choice in host animals like rabbits, guinea pigs or chicken. The antibodies are then used to target this molecule in the tissue sample. To detect these primary antibodies, usually a second antibody tagged with a probe comes to play, that was raised against the host species of the primary antibody (Luttmann et al., 2014). Probes can for example be immunogold particles of different sizes for electron microscopy (Robinson et al., 2000) or fluorescent dyes for fluorescence microscopy (Murphy and Davidson, 2013, chapter 11).

Staining for STED Microscopy

Fixed, 100 µm thick slices were stored in PBS containing 0.1 % NaN_3 at 4 °C in 24-well plates. Those well plates were also used for the staining procedure. First, PBS (Table 4) was removed and slices were washed three times for 15 minutes in phosphate buffer (PB) (Table 4) containing 20 mM glycine, to remove the aldehyde caps from the fixation. Liquids were carefully exchanged with 1000 µl pipettes and well plates were continuously shaken horizontally at 80 rpm at room temperature. Then, slices were permeabilized and blocked for 3 hours in PB containing 0.3 % Triton X-100 and 10 % normal goat serum. Afterwards, slices were rinsed three times with PB containing 0.3 % Triton X-100 before blocking another hour in PB containing Fab fragments anti mouse IgG (1:25, Table 2). After rinsing another three times with PB containing 0.3 % Triton X-100, primary antibodies were applied dissolved in PB containing 5 % normal goat serum and 0.3 % Triton X-100.

Primary antibodies (Table 5, 7, 9, 11) were incubated two times overnight (~40 hours). Then, slices were washed every 20 minutes for 3 hours with 0.3 % Triton X-100 PB. In the meanwhile, the secondary antibody solution was prepared in 0.3 % Triton X-100 PB containing 5 % normal goat serum and was centrifuged for 30 minutes at 4 °C and a speed of 1300 rpm. Secondary antibodies (Tables 6, 8, 10, 12) were incubated for 2 hours in the dark at room temperature. Subsequently, slices were washed three times for 15 minutes in PB and mounted on superfrost glass slides. For the mounting, slices were quickly transferred with brushes into a petri dish with *Aqua dest.* and then on the glass slide, where their position was corrected carefully with the brush. After some time for drying (in the dark for a few minutes), several drops of ProLong Gold antifade mountant were applied on the slide and a high precision coverslip was laid on top. Possible air bubbles were gently removed. Samples were cured for at least 18 hours at room temperature and in the dark before they were stored at 4 °C until imaging.

Table 5: Overview of primary antibodies used for the $Ca_v2.1$ dataset.

Primary Antibody	Company	RRID	Concentration
guinea-pig anti $Ca_v2.1$	synaptic systems #152 205	RRID:AB_2619842	1:500
rabbit anti Munc13-1	synaptic systems #126 102	RRID:AB_887734	1:150
mouse anti ZnT-3	synaptic systems #197 011	RRID:AB_2189665	1:500
chicken anti Homer1	synaptic systems #160 006	RRID:AB_2631222	1:200

Table 6: Overview of secondary antibodies used for the $Ca_v2.1$ dataset.

Secondary Antibody	Company	RRID	Concentration
goat anti guinea-pig – Alexa Fluor 594	Molecular Probes (Invitrogen) #A-11076	RRID:AB_141930	1:100
goat anti rabbit – ATTO 647N	Activ Motif #15048		1:200
goat anti mouse – Alexa Fluor 405	Thermo Fisher Scientific #31553	RRID:AB_221604	1:200
goat anti chicken – Alexa Fluor 488	Molecular Probes (Invitrogen) #11039	RRID:AB_142924	1:200

Table 7: Overview of primary antibodies used for the $Ca_v2.2$ dataset.

Primary antibody	Company	RRID	Concentration
guinea-pig anti $Ca_v2.2$	synaptic systems #152 305	RRID:AB_2619845	1:500
rabbit anti Munc13-1	synaptic systems #126 102	RRID:AB_887734	1:150
mouse anti ZnT-3	synaptic systems #197 011	RRID:AB_2189665	1:500 / 1:200
chicken anti Homer1	synaptic systems #160 006	RRID:AB_2631222	1:200

Table 8: Overview of secondary antibodies used for the $Ca_v2.2$ dataset.

Secondary antibody	Company	RRID	Concentration
goat anti guinea-pig – Alexa Fluor 594	Invitrogen #A-11076	RRID:AB_141930	1:100
goat anti rabbit – Alexa Fluor ATTO 647N	Activ Motif #15048	-	1:200
goat anti mouse – ATTO 490LS	Hypermol #2109-1MG	RRID:AB_2848169	1:100 / 1:150
goat anti chicken – Alexa Fluor 488	Invitrogen #11039	RRID:AB_142924	1:200

Table 9: Overview of primary antibodies used for the $Ca_v2.3$ dataset - first staining.

Primary antibody	Company	RRID	Concentration
guinea-pig anti $Ca_v2.3$	synaptic systems #152 404	RRID:AB_2619849	1:500
rabbit anti Munc13-1	synaptic systems #126 102	RRID:AB_887734	1:150
mouse anti ZnT-3	synaptic systems #197 011	RRID:AB_2189665	1:500 / 1:200
chicken anti Homer1	synaptic systems #160 006	RRID:AB_2631222	1:200

*Table 10: **Overview of secondary antibodies used for the $Ca_v2.3$ dataset - first staining.***

Secondary antibody	Company	RRID	Concentration
goat anti guinea-pig – Alexa Fluor 594	Invitrogen #A-11076	RRID:AB_141930	1:100
goat anti rabbit – Alexa Fluor ATTO 647N	Activ Motif #15048	-	1:200
goat anti mouse – ATTO 490LS	Hypermol #2109-1MG	RRID:AB_2848169	1:100 / 1:150
goat anti chicken – Alexa Fluor 488	Invitrogen #11039	RRID:AB_142924	1:200

Table 11: Overview of primary antibodies used for the $Ca_v2.3$ dataset - second staining.

Primary Antibody	Company	RRID	Concentration
rabbit anti $Ca_v2.3$	Alomone #ACC-006	RRID:AB_2039777	1:100
guinea pig anti Munc13-1	Synaptic systems #126 104	RRID:AB_2619806	1:250
mouse anti ZnT-3	Synaptic systems #197 011	RRID:AB_2189665	1:200 / 1:100
chicken anti Homer1	Synaptic systems #160 006	RRID:AB_2631222	1:200

Table 12: Overview of secondary antibodies used for the $Ca_v2.3$ dataset - second staining.

Secondary Antibody	Company	RRID	Concentration
goat anti rabbit – ATTO 647N	Activ Motif #15048	-	1:200
goat anti guinea-pig – Alexa Fluor 594	Invitrogen #A-11076	RRID:AB_141930	1:100
goat anti mouse – ATTO 490LS	Hypermol #2109-1MG	RRID:AB_2848169	1:150
goat anti chicken – Alexa Fluor 488	Invitrogen #11039	RRID:AB_142924	1:200

Staining for Munc13-1 Intensity Measurements

Per animal and condition, at least one glass slide, containing several cryosections, was chosen for staining with the help of a binocular. A PAP-pen (Table 2) was used to draw a circle around all slices on the slide to create a hydrophobic barrier. The slides were then placed into a humid chamber for the staining process. Slices were washed for 10 minutes in PB (Table 4) and then three times for 15 minutes in PB containing 20 mM glycine. Subsequently, all slices were blocked and permeabilized in PB containing 0.3 % Triton X-100 and 5 % normal goat serum for 3 hours at room temperature. Slices were rinsed three times with PB containing 0.3 % Triton X-100 before they were blocked another hour in 0.1 M PB containing anti mouse IgGs (1:10). Next, slices were rinsed again three times with PB containing 0.3 % Triton X-100 before the primary antibody solution was incubated at 4 °C. Primary antibodies (Table 13) were solved in a PB solution containing 0.3 % Triton X-100 PB and 2.5 % normal goat serum. At least once a negative control without primary antibodies was processed at the same time, only with PB containing 0.3 % Triton X-100 and 2.5 % normal goat serum.

Table 13: Overview of primary antibodies used for the Munc13-1 intensity dataset.

Primary Antibody	Company	RRID	Concentration
rabbit anti Munc13-1	synaptic systems #126 102	RRID:AB_887734	1:1000
mouse anti ZnT-3	synaptic systems #197 011	RRID:AB_2189665	1:500

Table 14: Overview of secondary antibodies used for the Munc13-1 intensity dataset.

Secondary Antibody	Company	RRID	Concentration
goat anti rabbit – Alexa Fluor 647	Molecular Probes (Invitrogen) A-21245	RRID:AB_141775	1:100
goat anti mouse – Alexa Fluor 488	Thermo Fisher Scientific (Invitrogen) A-10680	RRID:AB_2534062	1:100

After two nights (~40 hours) slices were washed thoroughly for three hours: every 20 minutes, the solution was exchanged with fresh PB containing 0.3 % Triton X-100. The secondary antibody solution was prepared in the meanwhile, containing 5 % normal goat serum and the antibodies (Table 14), and was centrifuged for 30 minutes at 4 °C and 1300 rpm. Secondary antibodies were incubated for 2 hours at room temperature in the dark. Finally, slices were washed three times for 15 minutes with PB. Then the solution was sucked off completely and slides were put to dry a bit, before they were mounted with the mountant ProLong Gold Antifade (Table 2) and sealed with high precision coverslips (Table 2). They were cured at room temperature for two to three days before they were stored at 4 °C until imaging.

Microscopy

The detection of a specific target within a biological sample at a microscope usually requires some form of staining. For example, fluorescent probes can be combined with specific primary-secondary antibody constructs. These target molecules of interest in the sample, making them detectable under a fluorescent light microscope. In response to their specific excitation wavelength, fluorophores emit photons, that are collected by a detector system in the microscope. Many light microscopes nowadays are equipped for fluorescence imaging. However, different systems offer different characteristics, as for example the detectable spectrum or the resolution (Murphy and Davidson, 2013, chapter 11).

Confocal laser scanning microscopes are equipped with lasers at different wavelengths for the excitation of the different fluorophores. Furthermore, they also contain a scanner, that is moving the focused laser beam

across the specimen point-by-point. A special feature of a confocal laser scanning microscope is the pinhole aperture in the light path. This technical component restricts the collection of emitted photons to only one focal plane, thereby excluding background fluorescence signal from above and below. Thanks to the pinhole, optical sections can be created with an improved vertical resolution, and be acquired in form of image stacks (Murphy and Davidson, 2013, chapter 13), allowing a three-dimensional view of the specimen. However, confocal microscopes are limited in their resolution (Sahl et al., 2017), due to the diffraction of light.

When light interacts with an object, it becomes diffracted. A self-luminous point, like a fluorescent molecule, does not appear as a single point on the image plane of the microscope, but as a diffraction pattern, also called Airy pattern after Sir George Airy. A central maximum of light (Airy disc) is surrounded by diffraction rings of descending maxima (Figure 11). The central Airy disc diameter can be influenced both by the numerical aperture (NA) of the objective and by the wavelength used for illumination. The higher the NA and the shorter the wavelength, the smaller the diameter of the Airy disc, which increases the optical resolution. Two points are defined as resolved when the *Rayleigh criterion* is fulfilled, which is that the maximum of the Airy disc of one point coincides with the first minimum of the Airy pattern of the second point (Figure 11). The resolution of two points is limited to around 200 nm for standard light microscopy systems, as described in Abbe's law (Murphy and Davidson, 2013, chapter 5 and 6).

However, some methods were developed which overcame this diffraction limit and are therefore found under the term super-resolution microscopy or nanoscopy (Hell and Wichmann, 1994). One of those methods is the so-called stimulated emission depletion (STED) microscopy, developed by Stefan Hell who, together with Eric Betzig and William Moerner won the Nobel prize in chemistry in 2014 for overcoming the resolution limits in fluorescence microscopy. In this technique, the Airy pattern around the central Airy disc is artificially cut to a minimum with the use of a doughnut-shaped depletion laser. During the imaging, the fluorophore is first excited with the respective wavelength. While the photons are emitted, the depletion laser turns on and quenches all photons within its reach (i.e. in the doughnut ring) (Figure 11). The sample is scanned with both lasers in a confocal-like fashion, leading to an image with much higher resolution (Sahl et al., 2017). The so-called time-gated STED microscopy (gSTED) increases the time between depletion and collection of photons, to avoid the detection of indepleted photons from outside the doughnut-center (Vicidomini et al., 2013). Post-hoc, image deconvolution can even increase the resolution, depending on the research question. These techniques have also been successfully applied in neuroscience (Maglione and Sigrist, 2013).

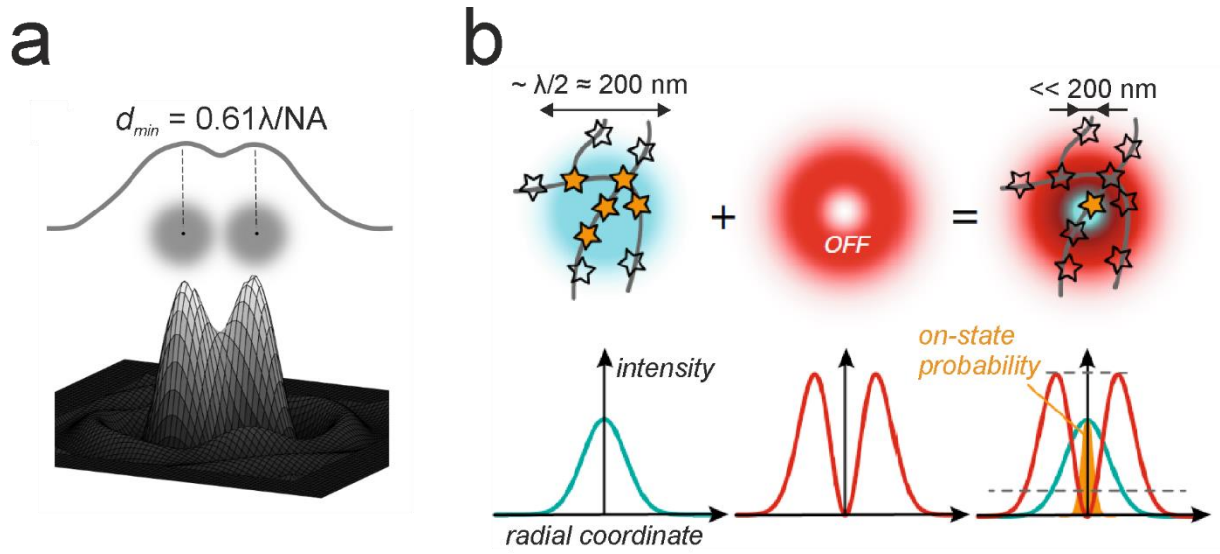

Figure 11: The principle of STED microscopy. a) *Schematic representation of two partially resolved point sources in one dimension (top), two dimensions (middle) and three dimension (bottom). In the 3D representation, the fusion of the Airy patterns of those two points can be seen. The minimal resolution (d_{min}) is defined by the wavelength of the excitation light (λ) and the numerical aperture of the objective (NA). Adapted from Blom and Widengren, 2017.* ***b)*** *Schematic representation of the stimulated-emission depletion.* ***Left:*** *An excitation laser beam (blue) excites several fluorophores (symbolized as stars) attached to the molecule of interest. The laser intensity signal is shown in side view at the bottom. Like this, the minimal resolution that can be achieved is ~200 nm.* ***Middle:*** *The depletion laser (red) of a STED microscope is doughnut-shaped and has a higher intensity than the excitation laser (bottom part).* ***Right:*** *The combination of excitation and depletion laser results in an on-state probability for a reduced number of fluorophores (in the example one) in the center of the depletion laser, thereby increasing the possible resolution manifold. Adapted from Jahr et al., 2019.*

.

STED Microscopy

Imaging

The same slices were imaged three consecutive times: first at a confocal microscope (Table 2), equipped with a 40x oil immersion objective, to check the staining and slice quality and to select the slices to image. I chose slices that showed an intact hippocampal formation and had a detectable ZnT-3 staining in the *stratum lucidum*. Then, the chosen samples (one per animal and condition) were imaged at the gSTED microscope (Table 2) and finally again at the confocal microscope to check, if the imaging areas were situated in the correct regions.

A three-color gSTED microscope was used for super-resolution imaging, equipped with an inverted IX83 microscope (Olympus), a 100x, 1.40 NA oil immersion objective and a 20x oil immersion objective. First, the 20x objective was used for orientation in the slice and choice of the rough imaging area. After switching to the 100x objective, confocal overview images were scanned that measured 75 x 75 µm, in the *stratum lucidum* of area CA3 or in the *stratum radiatum* of area CA1. Within the overview, several 10 x 10 µm ROIs

were defined for STED imaging. 2D images were acquired with a 16-bit depth and a pixel size of 20 x 20 nm, with a laser dwell time of 2 µs and line accumulation of 10 or 30, for confocal or STED mode, respectively. In CA3, *stratum lucidum*, ROIs were chosen proximal to the CA3 pyramidal cell bodies (Figure 15), while in CA1, *stratum radiatum*, they were acquired more distal from the CA1 pyramidal cell bodies (Figure 15).

Images were scanned in the line-by-line mode and, for three channels (Ca_V2, Munc13-1, Homer1), both confocal and STED images were imaged in parallel. Pulsed excitation lasers had wavelengths of 640 nm, 561 nm, and 488 nm and depletion lasers were at 775 nm and 595 nm wavelengths. First, the fluorescent probes ATTO 647N and Alexa Fluor 594 were excited with the 640 and 561 nm lasers, respectively, and depleted with the 775 nm STED laser (0.98-ns pulse duration, up to 80-MHz repetition rate). Next, Alexa Fluor 488 and ATTO 490LS were excited with the 488 nm laser and Alexa Fluor 488 was depleted with the 595 nm STED laser (0.52 ns pulse duration, 40 MHz repetition rate). The ATTO 490LS signal was imaged in confocal mode only. Time gating was set to 750 ps. Photons were collected with Avalanche photodiode detectors. Imaging was performed in the Imspector software. In each individual experiment laser powers were kept constant.

Deconvolution

Imaging at the microscope includes various sources for aberration, leading to slightly distorted images. One way of trying to correct for such aberrations is image deconvolution, the application of which depends on the research question. There are different types of deconvolution, for example some that de-blur the image and some that restore it (Swedlow, 2013). One method which is applicable for composite images, where each individual image has another underlying point-spread function, is the Richardson-Lucy deconvolution (Richardson, 1972; Lucy, 1974).

In the Imspector software (Table 2), raw STED images were deconvolved with the Richardson-Lucy algorithm. First, images were pre-processed, then they were deconvolved. Pre-processing involved the interpolation of images with the resample algorithm of the software, creating a float image. This was then used for deconvolution with the Richardson-Lucy algorithm. Image depth changed from 16 bit to 32 bit after deconvolution. The point-spread function was created using a Lorentzian 2D distribution, assuming a minimal bead size of 40 nm.

Confocal Microscopy for Munc13-1 Intensity Measurements

Slices were imaged at a Leica confocal microscope (Table 2) approximately one week after the staining. A few slices were re-imaged approximately four months after the staining due to a change in the methodical approach: In pilot experiments I only imaged and analyzed one focal plane, but then switched to the acquisition and analysis of image stacks.

A 20x oil-immersion HC PL APO CS2 objective with a numerical aperture of 0.75 was used for orientation within the slice. Within hippocampal area CA3, three sites were chosen for imaging at sub-areas CA3a, CA3b and CA3c respectively. Here, stacks were acquired using a 100x oil-immersion HCX PL APO objective with a numerical aperture of 1.4. Beginning and end of the stacks were based on fluorophore signals, the step size between focal planes was 1.01 µm and most stacks were between 10 and 20 µm thick. Images were acquired with a resolution of 1024 x 1024 pixels at 100 Hz in a frame by frame mode, starting with the longer wavelength, to minimize bleaching. The pinhole width was 151.63 µm and I used a line average of 2. Laser intensity and gain were consistent throughout an imaging day, but varied slightly between imaging days. The white-light-laser at 645 nm was used to excite Alexa Fluor 647 and the Argon laser at 488 nm was used to excite Alexa Fluor 488. Photo multiplier tubes were used for collection of emitted photons.

Electrophysiological Field Recordings

All equipment, software and consumables are listed in Table 2.

Before the recordings, slices were left to recover for at least 30 minutes and up to 8 hours at room temperature in the beaker, submerged with oxygenated ACSF. During the recording, they were placed in a recording chamber, superfused with oxygenated ACSF at a rate of approximately 2.5 ml/min.

For slice stimulation and recording of field potentials, silver wire electrodes were prepared and placed into glass pipettes filled with ACSF. Glass pipettes were pulled from borosilicate capillaries with a pipette-puller. Their tips were broken at a micro forge to receive low-resistance pipettes.

Both electrodes were placed on micromanipulators and carefully positioned via a control system. The stimulation electrode was placed in the hilus of the dentate gyrus close to the granule cells. The recording electrode was connected to a headstage of an amplification system and positioned in the *stratum lucidum*, above the somata of CA3 pyramidal cells (Figure 12). Positions were adjusted, if necessary, to obtain mossy fiber signal.

Stimuli were generated with a stimulation box and their patterns were controlled with a Master 8 generator. Signals were amplified using the Axon MultiClamp amplifier in current clamp mode I=0, with filtering of 2 kHz, and were digitized at 20 kHz Measurements were recorded and controlled with the Igor Pro software.

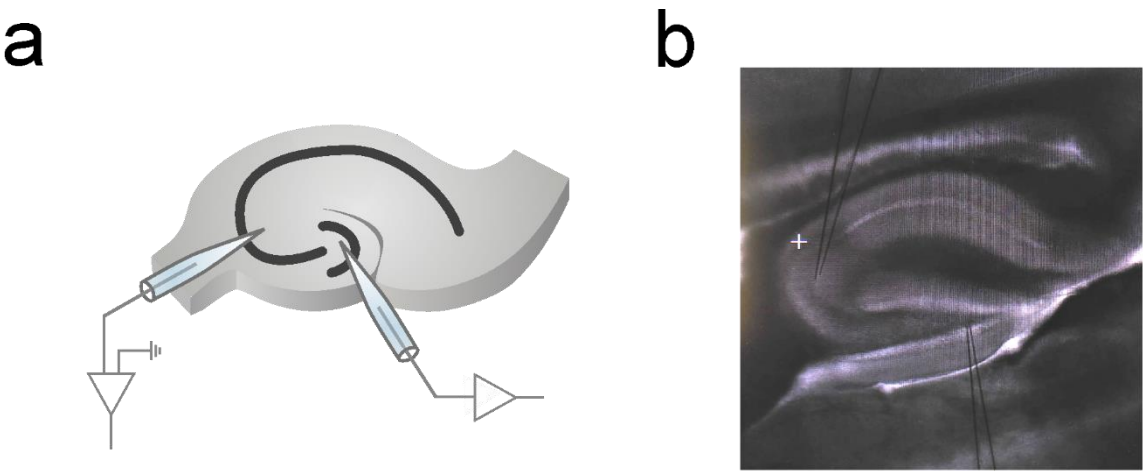

Figure 12: Setup for recording mossy fiber field potentials in acute brain slices. a) *Schematic showing the stimulation electrode in the hilus of the dentate gyrus and the recording electrode in the* stratum lucidum *of area CA3.* ***b)*** *Example image from an experiment with the stimulation electrode towards the tip of the hilus and the recording electrode in the* stratum lucidum *of area CA3b. The image was adjusted for brightness and contrast; the position of the electrodes is labelled for better visibility.*

The recording started when the positioning of both electrodes resulted in a mossy fiber signal. The baseline stimulation frequency was 0.05 Hz and the recorded sweep length was 0.5 s, except for the high-frequency stimulation, where we recorded 5.5 s sweeps. At first, we recorded the input-output curve by changing the stimulation strength. We aimed for PFV sizes of 0.05 mV, 0.1 mV, 0.2 mV, 0.3 mV and ended with the maximal stimulation strength (10 mA). Each of these steps was recorded for three sweeps. Subsequently, a medium stimulation strength was chosen for the rest of the recording. Ten sweeps of baseline were recorded before the stimulation was increased to 1 Hz for 20 seconds to record frequency facilitation. After a few sweeps baseline, a paired-pulse stimulus was given in three consecutive sweeps, with an inter-stimulus interval of 50 ms. Next, a baseline was recorded for at least 10 minutes (30 sweeps), or longer if it was unstable at first. Only once, this baseline was only 20 sweeps long; this recording was nevertheless included because the baseline was stable. To induce PTP and LTP, four consecutive high-frequency trains were given, each consisting of 125 pulses at 25 Hz. Those trains were always 20 s apart (0.05 Hz). After induction, signals were recorded at 0.05 Hz for at least 30 minutes (90 sweeps). At the end of the recording, 1 µM DCG-IV was washed-in to check for mossy fiber specificity of the signal.

Analysis

Distance Analysis

$Ca_V2.1$

For the analysis, I used deconvolved gSTED images and merged them into a composite using the Fiji software. For this set of stainings, the ZnT-3 signal could not be aquired with acceptable brightness at the STED level, probably due to the quality of the secondary antibody. The position of imaging areas within ZnT-3 positive *stratum lucidum* was subsequently verified at the confocal microscope and I used the whole image for analysis. I was looking for constellations where the fluorophores labeling Munc13-1 and $Ca_V2.1$ were next to each other and opposing the fluorophore labeling Homer1. In the beginning, I restricted the choice of constellations to the ones which had a planar organization, but I later broadened the criteria for the choice of constellation (Figure 18).

After finding a constellation, I defined the maximum intensity peak of the two fluorophores with the "Find maxima" tool in Fiji and set the prevalence to > 20, except for a subset of measurements in CA1 where the prevalence was set to > 10. The intensity maxima were shown as point selections in the composite. Next, I used the line tool with a thickness of 1 pixel to measure the distance between the selected pixels. The "modified multichannel plot profile" plugin (written by Tiago Ferreira) was used to plot the intensities of all three channels: Munc13-1, $Ca_V2.1$ and Homer1 fluorophore intensities. The distance between the maxima of Munc13-1 and $Ca_V2.1$ labelling fluorophores was calculated using Microsoft Excel.

$Ca_V2.2$

There were two major limitations in the measurements for $Ca_V2.1$, which I addressed when I repeated the analysis for the $Ca_V2.2$ and $Ca_V2.3$ stainings. First, the ZnT-3 staining could not be imaged with a 100x objective. The first limitation was tackled by choosing another secondary antibody for the ZnT-3: ATTO 490LS. This was still fitting in the fluorophore spectrum of the experiment, since this fluorophore has a long stoke shift. Therefore, it was now possible to image the ZnT-3 signal at the STED microscope and to restrict the choice of constellations the ZnT-3 positive signal during analysis in the image composite. For that purpose, the ZnT-3 confocal image was pre-processed before merging it, using the Gaussian Blur filter with sigma = 5. In single cases, the ZnT-3 staining did not work and I analyzed distances from the whole corresponding STED images.

Second, the measurements from the $Ca_V2.1$ dataset appeared as discrete data although the underlying data was indeed continuous. The reason for this is that in Fiji the distances were output as number of pixels, so the measurable distances had increments of 20 nm. In very extreme cases, the positioning of the line tool between two pixels could lead to different distance values, dependent on how the line was drawn. Also, the analysis demanded a lot of manual steps which were time-consuming and prone to human errors. The second

limitation – the artificial introduction of discrete values – was solved by introducing a Fiji plugin into the process, which is called “GaussFit OnSpot” and was written by Peter Haub and Tobias Meckel. Here, the “true” intensity maximum is searched in and around the pixel, which was marked by the Fiji “find maxima” tool. The plugin fits a gauss function on the existing intensity values in an iterative way (one can choose when it should stop) and gives you a nm precise location of the “true” maximum within a pixel. The values are output as coordinates for all the channels of interest within the composite.

Eight constellations of $Ca_v2.2$, Munc13-1 and Homer1 were chosen manually in the ZnT-3 positive region and for both Munc13-1 and $Ca_v2.2$ corresponding signals the maxima were marked with a point selection by using the “Find maxima” tool. Then, a custom-written Fiji script was applied to the list of maxima for Munc13-1 and $Ca_v2.2$ individually, applying the GaussFit On Spot plugin onto the respective gray scale image. For the plugin, the shape was set to “ellipse with varying angle” and the fitmode was set to NelderMead. Usually, a maximum of 2000 iterations was set for a rectangle half size of 2 pixels with a pixel size of 20 nm. The pixel correction was 1.0 and the base level 100 photons (both default values). Per image, 16 individual tsv-files were saved with individual coordinates for each Ca_v and Munc13-1 cluster.

To extract the distance from the coordinates, a custom-written Python script was used, calculating the distance between pairs of voltage-gated calcium channels and Munc13-1 clusters via the Pythagorean theorem.

$Ca_v2.3$

Staining and analysis for the $Ca_v2.3$ dataset was done in parallel with the $Ca_v2.2$ dataset, on slices of the same animals. However, the primary antibody was an antiserum and not knock-out verified. I therefore later decided to repeat the staining with another antibody, which was knock-out validated (Table 11 + 12). For this round of stainings, the primary antibody for Munc13-1 also was changed, to avoid an overlap of antibody host species. When comparing the distance results from the first and second staining, no difference could be detected (Figure 25). We excluded some samples from the second set of experiments with the knock-out verified antibody, because the Homer1 staining was not always successful (Appendix, Table 18).

Munc13-1 Intensity Analysis

The intensity analysis was performed with Fiji. Acquired stacks were loaded and the z-axis intensity profile was plotted for both channels: Channel 1 corresponded to the ZnT-3 signal and channel 2 to the Munc13-1 signal. The intensity of the five brightest images (same Z-planes for both channels, chosen by Munc13-1 signal intensity) was summed with the "ZProjection" function and the "sum slices" option.

Based on the summed ZnT-3 signal, regions of interest (ROIs) were defined: a background correction with a rolling ball size of 50 pixels was applied, then the image was filtered using a Gaussian blur with a sigma of 5. A binary mask was created, using the default threshold, and smoothed, using the "fill holes" function. This was followed by a median filtering (sigma of 5 pixels) step and by calling the "close-" function from the binary menu. To create the ROIs, the "analyze particles" function was applied to this mask, outlining the white (= ZnT-3 signal) parts of the binary image and adding them to the ROI manager (Figure 32).

Next, summed intensity images of both channels were background-corrected using the "rolling ball" algorithm with a size of 300 pixels. The pre-defined ROIs were applied to the images and the "multi measure" function was run to measure the area and intensity within ROIs for both channels. ROIs were filtered by size (area > 50 μm^2) to make sure that only relevant areas were included into the analysis.

Field Recording Analysis

For analysis of the field recordings we used the software Igor Pro with the installed plugin NeuroMatic as well as Microsoft Excel. The input-output relations were analyzed by averaging the three sweeps at the same stimulation strength and measuring the size of the averaged presynaptic fiber volley (PFV) and field excitatory postsynaptic potential (fEPSP). If no input-output curve was recorded, all sweeps from the initial baseline were averaged and analyzed. PFV were measured peak to peak. For measurement of fEPSPs amplitudes, each sweep was baseline-corrected (50 ms before stimulus) and the maximum was measured ± 2 ms around the peak. For analysis of frequency facilitation, all fEPSP amplitudes were normalized to the initial baseline. For the paired-pulse ratio the size of the second fEPSP was divided by that of the first. Here, only the value from the first paired-pulse sweep was taken.

In the high-frequency trains we measured all the fEPSP amplitudes and normalized them to the baseline before the induction. Field EPSP amplitudes for PTP and LTP were also normalized to the baseline before induction. The magnitude of LTP was assessed by averaging fEPSP amplitudes at minutes 20 to 30 after LTP induction. At the end of the recording, 1 µM DCG-IV was applied for approximately 30 sweeps. To assess the level of suppression, the last 15 sweeps during DCG-IV wash-in were averaged and normalized to the baseline before the high-frequency trains.

Statistics

Statistics for the distance measurements as well as for the Munc13-1 intensity measurements were performed using R for Computing. The data from the field recording experiments were statistically analyzed in the GraphPad Prism software. The alpha significance level was always at 5 %.

R for Computing

Many statistical tests require independent observations to yield robust results. However, in neuroscience, most data are not independent, leading to inflation of false positive conclusions if ignored in the choice of statistical tests (Aarts et al., 2014). Data is not considered independent when obtained by a nested experimental design, i.e. a design in which several data points arise from the same unit, such as an animal, a slice, a cell or a region of interest (Galbraith et al., 2010). Such designs can have several nested levels, as in my case: Several distance measurements come from the same image, which is one of several images from the same slice, which is one of two slices from the same animal (Figure 12). The main problem is that measurements coming from the same unit are likely to be more similar to measurements coming from independent units, leading to higher unexplained intra-class correlations, smaller p-values and thus more false positive conclusions (Aarts et al., 2014). The use of multilevel models to account for nested data structures can address this issue.

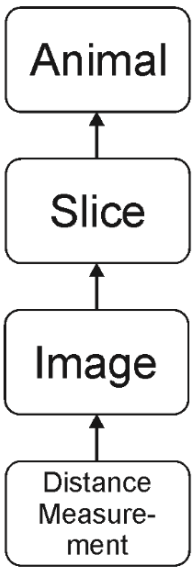

Figure 13: Classification diagram showing the nested structure of the distance measurement data as an example: *Several distances (level 1) were measured per image. Several images (level 2) were acquired per slice. Several slices (level 3) were imaged per animal (level 4).*

I wrote generalized linear mixed models in the open source software R for computing R Project for Statistical Computing in RStudio to account for the nested structure of my data (Figure 12). I used the glmer function from the R package: lme4 (Bates et al., 2015) to write models predicting the distance, including fixed and random effects. I used a Gamma distribution with a log link (due to the non-normal distribution of my data) and the 'bobyqa' optimizer to fit the models. When convergence of a model failed because of singularity, I simplified the model by reducing the number of random effects (Barr et al., 2013). In some cases, this led to the use of the glm function (Gamma distribution with a log link) instead, because even a two-level model did not converge.

I built the full models based on my experimental design. First, I included all possible fixed and random effects, allowing for random intercepts. If several fixed effects were included in the model, I allowed for an interaction between them. I also compared random slopes to random intercepts models. In the end, I decided for the simplest full model possible with regard to my experimental design and compared this to the corresponding null model in an ANOVA. If the

null-hypothesis was rejected, paired comparisons were post-hoc performed using the R package: emmeans. Marginal means were estimated and compared in a marginal effects test with false discovery rate correction (Benjamini and Hochberg, 1995). The results from the marginal contrasts analysis are given as ratios for the given pair of measurements. All respective tables can be found in the Appendix.

GraphPad Prism

For statistical analysis of the field recording data we used the GraphPad Prism software (Table 2). In time plots, data from all recordings are shown as mean ± SEM. In scatter plots, data points come from individual recordings and are shown with the median and interquartile ranges (25 % - 75 % quartiles). For the analysis of the input-output relation, data points were fitted with a simple linear regression. The slopes of the regressions are shown with the 95 % confidence bands and were compared with a two-tailed ANCOVA. Time plots were statistically evaluated using mixed-effects models, testing for the factors time, genotype and the interaction of both. Single time points within these time plots were tested in a post-hoc Sidak's test for multiple comparisons. Data from single time points were either tested with Mann-Whitney *U* or Kruskal-Wallis test with a post-hoc Dunn's test for multiple comparisons.

Results

Parts of this chapter are published in Orlando, Bruentgens, Dvorzhak et al., 2021. Other parts are made publicly available on bioRxiv as Bruentgens et al., 2023 and were already submitted to a journal.

Coupling Distances at the Mossy Fiber Bouton

Previous findings led to the suggestion that the coupling distance between voltage-gated calcium channels and the vesicular calcium sensor in hippocampal mossy fiber boutons might change upon long-term potentiation (LTP). First, the coupling distance at mossy fiber boutons is loose compared to other synapses (Vyleta and Jonas, 2014). Second, calcium channels are mobile within presynaptic synapses (Schneider et al., 2015). Third and foremost, experiments from the laboratory of Takeshi Sakaba described increased fusion upon chemical potentiation of mossy fiber boutons. In unpotentiated boutons release could be inhibited with *ethylene glycol-bis(β-aminoethyl ether)-N,N,N',N'-tetraacetic acid* (EGTA), a slow-acting calcium buffer, as well as with the faster acting calcium buffer *1,2-bis(o-amino phenoxy)ethane-N,N,N',N'-tetraacetic acid* (BAPTA). This indicates a loose coupling between calcium source and -sensor (Eggermann et al., 2012). While BAPTA reduced release also in potentiated boutons, EGTA could not achieve this effect any more, indicating a shortened coupling distance due to chemical potentiation (Midorikawa and Sakaba, 2017).

To test the hypothesis that the coupling distance between calcium channels and release sites shortens in hippocampal mossy fiber boutons upon potentiation, I performed time-gated stimulated emission depletion (gSTED) microscopy experiments. 100 µm thick acute mouse brain slices were incubated in either control or forskolin solution before they were fixed and stained. Forskolin is a chemical activator of adenylyl cyclases (Hanoune and Defer, 2001) and activates the presynaptic mossy fiber LTP cascade (Weisskopf et al., 1994). In subsequent stainings – leading to three different datasets – I used antibodies against the three subtypes of voltage-gated calcium channels of the group Ca_v2 as a marker for the calcium entry site. Munc13-1 was stained as a marker for release sites (Sakamoto et al., 2018) and was used as the reference point for the distance measurement.

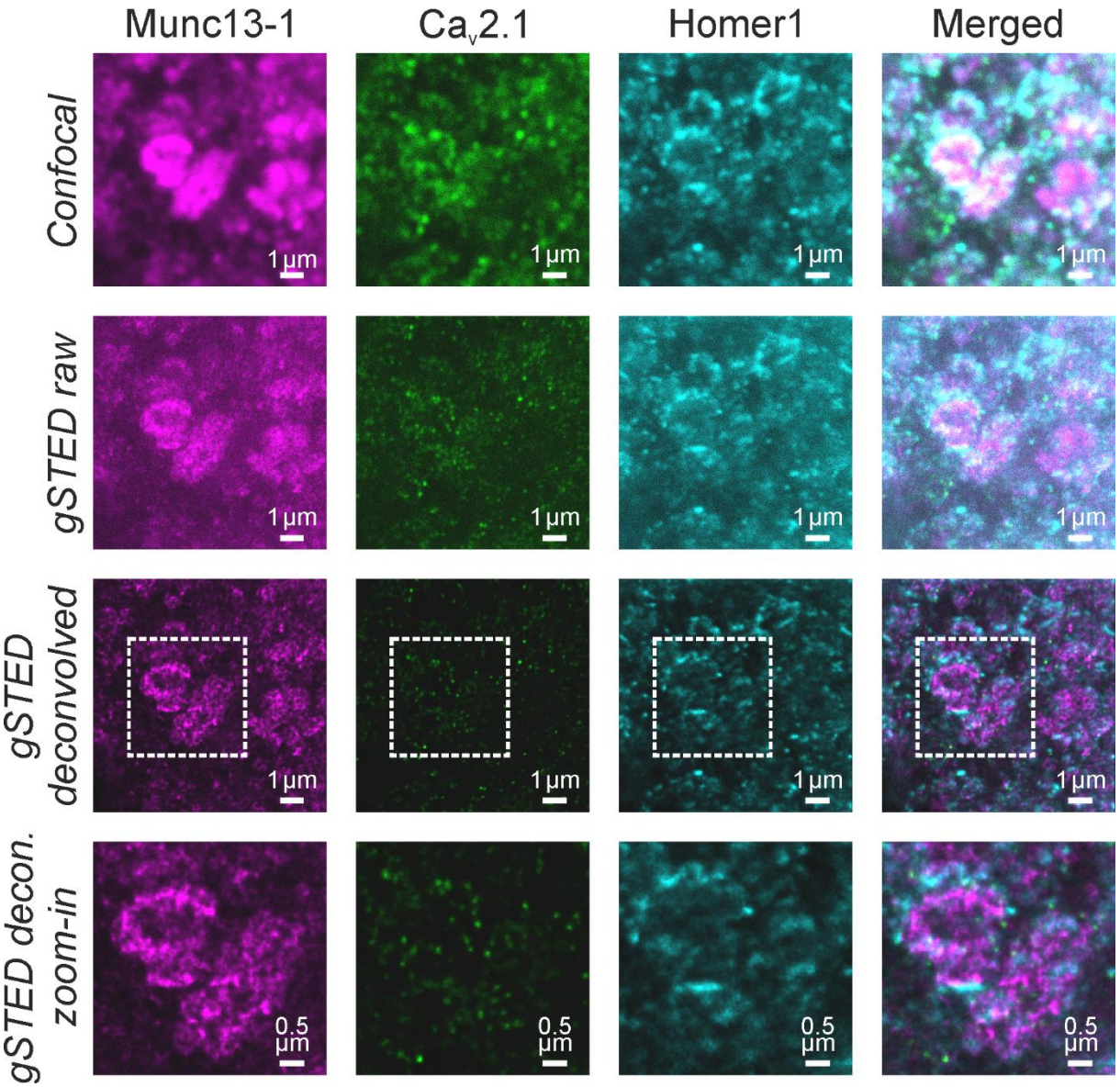

Figure 14: Imaging with a three color gSTED microscope. *Example images from the area CA3,* stratum lucidum*. From left to right: An acute mouse brain slice was stained for Munc13-1 (magenta, first column), $Ca_v2.1$ (green, second column) and Homer1 (cyan, third column). The composite of all three channels is shown in column four. At the STED microscope, both confocal and STED images were taken. From top to bottom: Confocal images are shown in the first row, raw STED images are shown in the second row. Note the better resolution of single fluorophor clusters, especially in denser regions. Images in the third row show STED images after deconvolution with the Richardson-Lucy algorithm. Note the punctate distribution of fluorophore clusters and the improved signal to noise ratio. The framed area indicates the zoom-in area for the images in the last row. They show an area with a potential mossy fiber bouton, indicated by size and shape of the structure. Note the condensed fluorophore clusters referring to a marker for release sites, Munc13-1, as well as the more ring- or band-like appearance of the fluorophore clusters referring to the postsynaptic molecule Homer1.*

The stained slices were imaged at a gSTED microscope to resolve structures below the Abbe resolution limit of approximately 200 nm (Abbe, 1882; Heintzmann and Ficz, 2006), with a lateral resolution of approximately 40 nm and a pixel size of 20 nm. Imaging areas were confined to *stratum lucidum* of area CA3 and in control slices additionally to *stratum radiatum* of area CA1 in the hippocampus. Subsequently, I manually measured distances between pairs of calcium channel and Munc13-1 clusters in deconvolved gSTED images. To restrict measurements to calcium channels and Munc13-1 molecules at intact, excitatory synapses, I used an antibody against Homer1, a postsynaptic marker for excitatory synapses (Sugiyama et al., 2005; Sheng and Hoogenraad, 2007; Gutierrez-Mecinas et al., 2016). Measurements were only carried out when calcium channel and Munc13-1 clusters were opposing a Homer1 cluster. The measured coupling distances were then compared between the two different conditions, control and forskolin, and in control conditions between the two different regions, CA3 and CA1.

Figure 14 shows example images from the gSTED microscope, at which both confocal and gSTED scans were performed. The raw gSTED images were deconvolved post-imaging with the Imspector software, using the Richardson-Lucy algorithm (Richardson, 1972; Lucy, 1974; Ingaramo et al., 2014). The zoom-in area of the deconvolved gSTED images highlights structures which could be mossy fiber boutons, indicated by their size and shape (Figure 14).

Mossy fiber boutons from the suprapyramidal mossy fibers are located in the *stratum lucidum* of the hippocampus (Amaral et al., 2007). They contact their target cells, the CA3 pyramidal neurons, on their proximal apical dendrites (Blackstad and Kjaerheim, 1961). Thus, to target mossy fiber boutons I restricted my imaging areas close to the pyramidal cell body. I also used a fourth antibody against the Zinc transporter 3 (ZnT-3), which is specifically expressed in mossy fibers (Wenzel et al., 1997), in order to ensure anatomical specificity of imaging areas. Figure 15a shows the expression pattern throughout the hippocampus with strong signal in the hilus of the dentate gyrus and along the mossy fiber bands. For the $Ca_V2.1$ dataset, ZnT-3 signal was imaged post-hoc at another confocal microscope and at a lower magnification, with Alexa-Fluor 405 bound to the secondary antibody (Figure 15a). For the $Ca_V2.2$ and $Ca_V2.3$ datasets, ZnT-3 signal was imaged in confocal mode at the gSTED microscope, in parallel to the STED imaging (Figure 15b). Here, ATTO 490LS was used as the probe to label ZnT-3. Figure 15b shows an example of a raw confocal image obtained at the STED microscope as well as the processed image after filtering with a Gaussian blur. The composite of the processed ZnT-3 image together with the three deconvolved gSTED images is shown at the bottom. It can be seen that the majority of stained calcium channel, Munc13-1 and Homer1 clusters are situated within the ZnT-3-positive area (Figure 15b zoom-in).

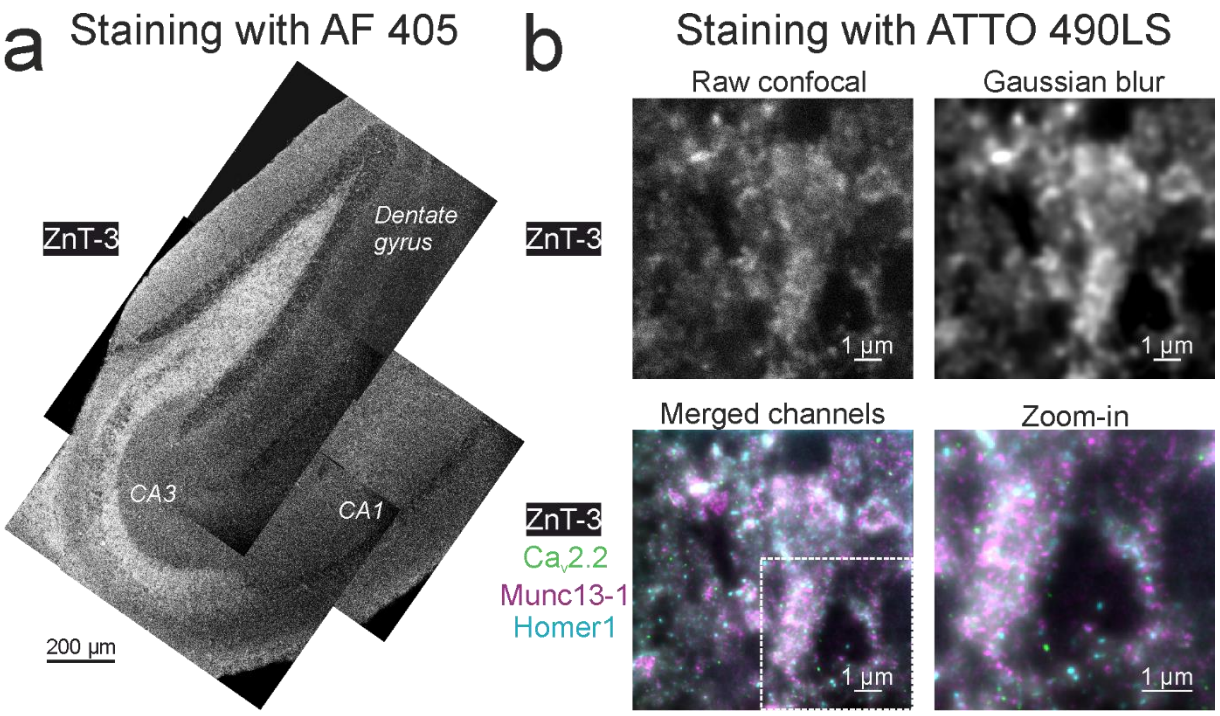

Figure 15: Staining mossy fibers with an antibody against ZnT-3. *Mossy fibers specifically express high amounts of the ZnT-3 (Wenzel et al., 1997), which can therefore be used as a mossy fiber marker.* ***a)*** *In the first dataset including all stainings for $Ca_v2.1$, I used a primary/secondary antibody combination against the ZnT-3 with Alexa Fluor 405 as the fluorophore. It was only detectable with a 40x objective at a confocal microscope. Note the distribution of the ZnT-3 throughout the hippocampus: hilus and the mossy fiber bands in area CA3 are strongly stained.* ***b)*** *In the datasets including all stainings for $Ca_v2.2$ and $Ca_v2.3$ I used a secondary antibody combined with ATTO490LS for detection of the ZnT-3, which was also detectable at the gSTED microscope in confocal mode with a 100x objective.* ***Top left:*** *ZnT-3 signal in a raw confocal image from the gSTED microscope.* ***Top right:*** *same image after filtering it with a Gaussian blur.* ***Bottom:*** *The processed ZnT-3 image merged with the deconvolved gSTED images with fluorophore clusters indicating $Ca_v2.2$ (green), Munc13-1 (magenta) and Homer1 (cyan) together with the blurred ZnT-3 signal (white) in full-view (left) and as a zoom-in (right). Note that almost no fluophore clusters for $Ca_v2.2$, Munc13-1 or Homer1 are located within ZnT-3-negative areas.*

After imaging at the gSTED microscope, I validated imaging areas at the confocal microscope. The second gSTED laser at 595 nm was bleaching the fluorophores in the red channel within the field-of-view, aiding to post-hoc identify if the imaging areas were located correctly (Figure 16). When imaging areas were not located in CA3 *stratum lucidum*, close to or within the *stratum pyramidale* or in CA1 *stratum radiatum*, they were excluded from the analysis (Tables 16 – 18, Appendix).

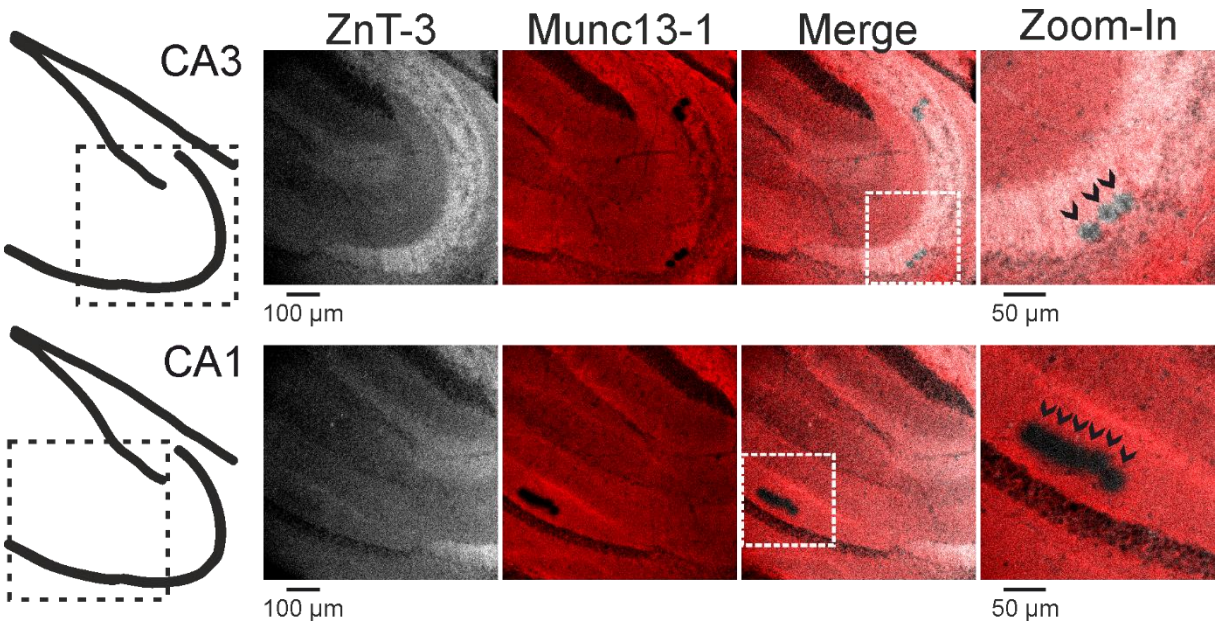

Figure 16: Post-gSTED-imaging check for location of imaging areas. *Slices were imaged at a confocal microscope after gSTED-imaging to check if the imaging areas were located correctly. The second gSTED laser at 595 nm bleached the fluorophore attached to Munc13-1 (ATTO 647N). The* ***top row*** *shows imaging areas in CA3. The shape and orientation of the hippocampus is schematically shown at the left; the dashed line indicates the field-of-view of the images at the right. The ZnT-3 signal was imaged as a marker for mossy fibers. In the scan for the Munc13-1 signal, small black dots are detectable, which correspond to the bleached areas. In the merged image it is apparent that these bleached areas are located within the ZnT-3-positive band in CA3. The dashed line indicates the area of the zoom-in. In the zoom-in, three out of six imaging areas are shown, indicated by the arrowheads. Note that the imaging areas are located right below the* stratum pyramidale*, detectable as a band of darker somata. The* ***bottom row*** *shows imaging areas in CA1. The field-of-view within the hippocampus is marked by the dashed lines in the schematic at the left. There is almost no signal detectable for ZnT-3 at the low magnification level. The black dots indicating the imaging areas are located in* stratum radiatum *– a bit further away from the packed band of CA1 pyramidal cell somata – where Schaffer collaterals project to (Ishizuka et al., 1990; Li et al., 1994; Kajiwara et al., 2008). Arrowheads in the zoom-in of the merged image indicate the six imaging areas.*

Coupling Distance Between $Ca_V2.1$ and Munc13-1

First, I measured the coupling distance between the voltage-gated calcium channel $Ca_V2.1$ and Munc13-1 in forskolin-treated and control slices. $Ca_V2.1$ is the most abundant voltage-gated calcium channel in the mossy fiber bouton (Li et al., 2007) and is the main contributor to calcium influx leading to transmitter release (Castillo et al., 1994; Pelkey et al., 2006; Li et al., 2007). The coupling distance was measured indirectly as the distance between the intensity peaks of the fluorophores labeling the target molecules $Ca_V2.1$ and Munc13-1.

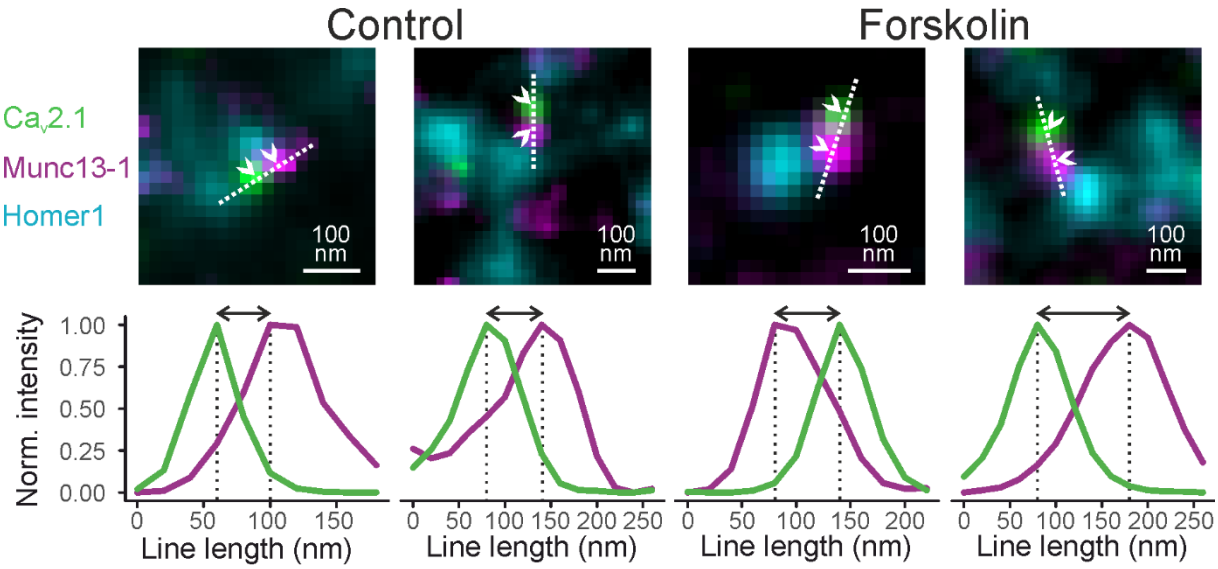

Figure 17: Distance measurement between fluorophore clusters representing $Ca_V2.1$ and Munc13-1 with the Fiji line tool. *Individual configurations for distance measurement were chosen by eye. The **upper row** shows examples for "strict" (1st and 3rd image) and "open" (2nd and 4th image) configurations in control and forskolin-treated slices, respectively. The fluorophore signal referring to $Ca_V2.1$ is shown in green, Munc13-1 signal is shown in magenta and Homer1 is shown in cyan. The arrow heads point to the pixels with the highest intensity within the clusters. The dotted lines indicate how the line tool was placed through the intensity maxima. The **lower row** shows intensity plots along the dotted line, corresponding to the images in the upper row. Color code: Green refers to the intensity of the $Ca_V2.1$ cluster and magenta to the Munc13-1 cluster. The profiles along the line were retrieved with the "multichannel plot profile" plugin for Fiji. Intensities were normalized to the highest and lowest value within each channel. The dotted vertical lines indicate the position on the line of the intensity maxima and the arrows depict the actual distance (nm) between those maxima.*

The distance analysis was performed on composite images in the open-source software Fiji. In brief, synaptic configurations (Figure 17, top row) were chosen by eye and the intensity maxima of the fluorophores labeling $Ca_V2.1$ and Munc13-1 (marked by arrow heads in Figure 17) were derived with the "find maxima" tool in Fiji. A line was placed through both maxima (Figure 17, indicated by the dashed lines) and the intensity profiles along this line were plotted with the "multichannel plot profile" plugin

(Figure 17, bottom row). The coupling distance was then calculated as the distance between the two intensity peaks. In the software version that I used (ImageJ version 1.52n), the distance along the line was given as the summed length of pixels. This method resulted in discrete distance data, although the underlying data are continuous. The steps in the distance measurements refer to the pixel size of 20 nm (Figure 19 and 21).

When choosing synaptic configurations for distance measurements, several criteria needed to be fulfilled. The fluorophore clusters indicating $Ca_v2.1$ and Munc13-1 needed to be adjacent to each other and opposing a Homer1 cluster. The clusters for $Ca_v2.1$ and Munc13-1 also should be clearly distinguishable, i.e. clusters within bulks of clusters could not be measured, because beginning and end of a single cluster was not clear. Furthermore, the spatial relation between $Ca_v2.1$ and Munc13-1 to Homer1 was a criterion. However, it was unclear if this criterion was needed and in which way it should be defined, leading to the following comparison of configurations.

A conservative definition would be that $Ca_v2.1$ and Munc13-1 need to be parallel to Homer1, either in the side or in the top view (Figure 18a and b) (Brockmann et al., 2019). However, the 3D arrangement of the molecules cannot be derived by looking at a 2D image. It is unclear in which angle one looks at the synapses and how this affects the perception of the spatial arrangement. To determine whether taking heterogeneous 2D synapse configurations into account is changing the outcome, I measured distances from varying configurational arrangements and classified them as “strict” if following the parallel criterion (Figure 18a and b, “strict”) and as “open” if the criterion was not fulfilled (Figure 18a and b, “open”).

Categorizing the configurations in the $Ca_v2.1$ dataset led to 443 “strict” configurations in control conditions while only 141 configurations were defined as “open”. In forskolin-treated slices, 389 configurations were defined as “strict” and 136 as “open”. In control conditions, strict configurations had a mean distance ± SD of 64.61 ± 35.45 nm while it was 64.68 ± 32.13 nm for “open” configurations. In forskolin-treated slices, “strict” configurations had a mean distance of 65.3 ± 33.82 nm and “open” configurations 58.82 ± 29.19 nm (Figure 18c). The distributions of distances with and without “open” configurations were very similar with a median and range of 60 [40; 80] nm for both “strict” and all configurations (Figure 18d).

I fitted a generalized linear mixed model (GLMM) (Gamma family with a log link) to estimate the distance given the synaptic configuration and the condition, including the animal as a random effect (Appendix, Table 19). From here on, all GLMMs were using Gamma-distributed errors fitted with a log link function. I compared the full model to a null model without the synaptic configuration as explanatory variable (Appendix, Table 20) to test the hypothesis if the configuration influenced the distance significantly. When compared with a likelihood ratio test (Appendix, Table 21), the models were not significantly different ($p = 0.5547$). In conclusion, there is no statistical evidence that the measured distances differ between the two synapse configurations. Thus, I decided to include them all into my dataset.

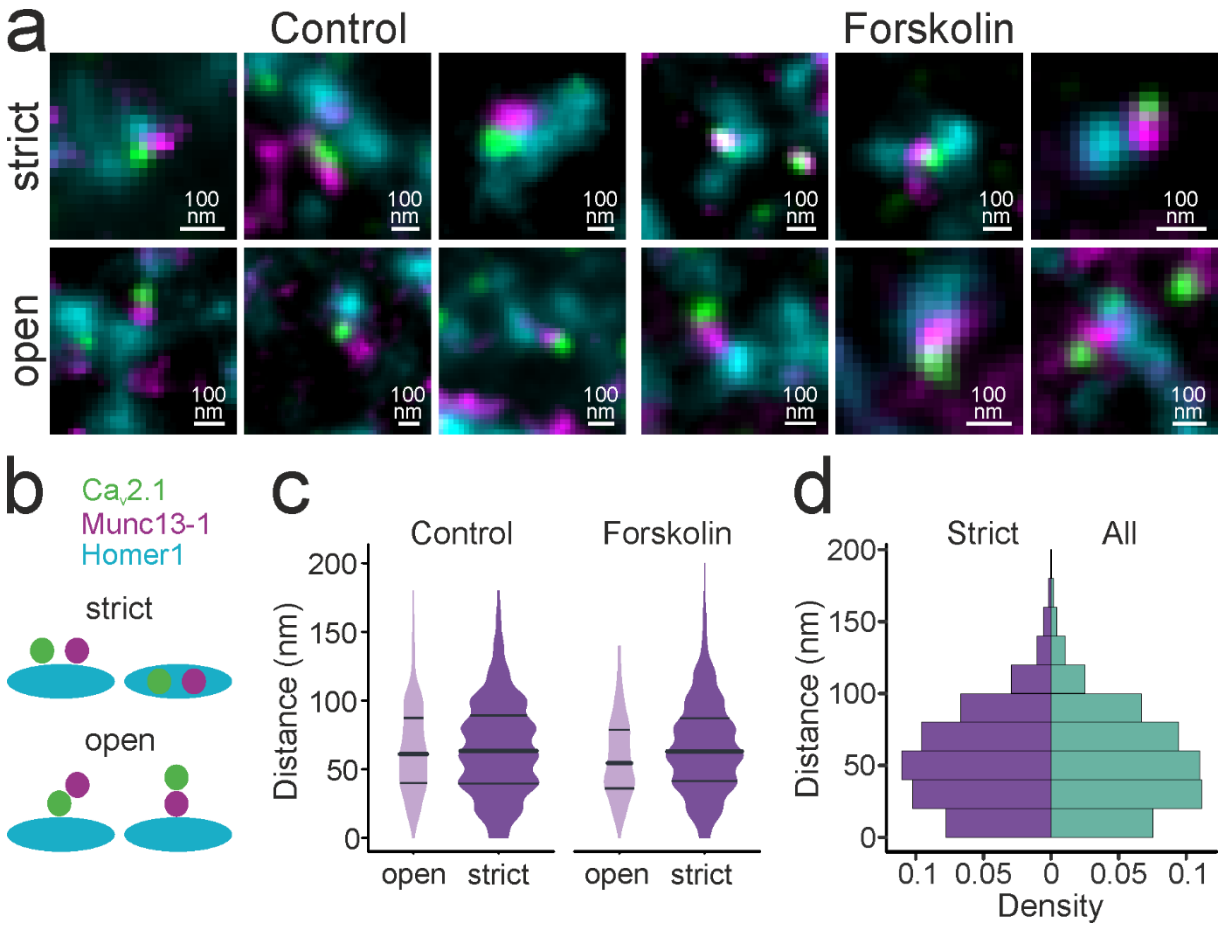

Figure 18: Distance measurements in two categories of synaptic configurations. *When choosing synaptic configurations for distance measurements, two main criteria needed to be fulfilled: The calcium channel cluster should be situated next to a Munc13-1 cluster and both clusters should be opposing Homer1, to make sure to measure from an intact synapse. However, 3D orientation of those three molecules can hardly be determined from a 2D image which is why a third criterion is debatable: Should the calcium channel and Munc13-1 clusters be parallel to Homer1?* ***a)*** *In the upper row there are several examples for the parallel configuration, here called "strict", from both control and forskolin-treated slices. In the lower row are examples not fitting into this definition, thus defined as "open" configuration. Ca$_v$2.1 clusters are shown in green, Munc13-1 in magenta and Homer1 in cyan.* ***b)*** *Schematic for possible examples for "strict" and "open" configurations. The color code is given in the legend and is the same as in a).* ***c)*** *Violin plot showing the distribution of distance measurements (nm) for the two configurations, "open" and "strict" for both conditions, control and forskolin. Black lines correspond to 25 %, 50 % and 75 % quartiles, respectively. A hypothesis test between nested GLMMs gave no evidence for a significant difference in the distance distributions between configurations ($p = 0.5547$).* ***d)*** *Mirrored histogram showing the densities of measured distances (nm) for only "strict" configurations (purple, left side) or all configurations, including the "open" ones (green, right side). The binwidth is 20 nm, leading to summed densities of 1 per histogram.*

For the analysis of coupling distances between $Ca_v2.1$ and Munc13-1, I imaged slices from 11 animals (Figure 19), with one slice per animal and condition and usually six images per slice. Per image I measured between two and 17 synaptic configurations, leading to a total of 584 measurements for control and 525 measurements for forskolin condition (Appendix, Table 15 and 16). The mean coupling distance ± SD was 64.62 ± 34.65 nm for control and 63.62 ± 32.77 nm for forskolin condition (Figure 19a, Appendix Table 15), indicating no change in the average distance after chemical potentiation.

Distances ranged from 0 to 180 nm for control and from 0 to 200 nm for forskolin-treated slices with a median and interquartile range of 60 [40; 80] nm for both conditions. However, the majority of distances were situated between 0 and 100 nm: 91.6 % in control and 91.43 % in forskolin condition (Figure 19c). Variability of distances was very similar between conditions and animals (Figure 19d).

To account for possible variability due to the nested structure of the data, I fitted a GLMM to estimate the coupling distance with the condition (control or forskolin), including the animal as a random effect (Appendix, Table 22). To test the hypothesis that the distance was changed in forskolin-treated slices, I compared this model to a null model without condition as explanatory variable (Appendix, Table 23). When compared with a likelihood ratio test (Appendix, Table 24), these models were not significantly different ($p = 0.8514$). Thus, there is no statistical evidence for a shorter coupling distance after forskolin treatment between $Ca_v2.1$ and Munc13-1 (Figure 19a) in the framework of the experiment.

These results could either mean that there was no change in coupling distance between the two conditions or that the selected method was not suitable to resolve such a difference. To test if shorter distances could be resolved, I aimed at imaging Schaffer collateral synapses in the *stratum radiatum* of the area CA1 (Ishizuka et al., 1990; Li et al., 1994; Kajiwara et al., 2008). At these synapses, shorter coupling distances have been suggested compared to mossy fiber boutons (Scimemi and Diamond, 2012). Thus, I also imaged in the *stratum radiatum* of area CA1 of control slices, a bit further away from the pyramidal cell bodies where Schaffer collateral synapses terminate (Kajiwara et al., 2008) (Figure 16, lower panel). The staining looked more uniform in the area CA1 than in the area CA3 (Figure 20).

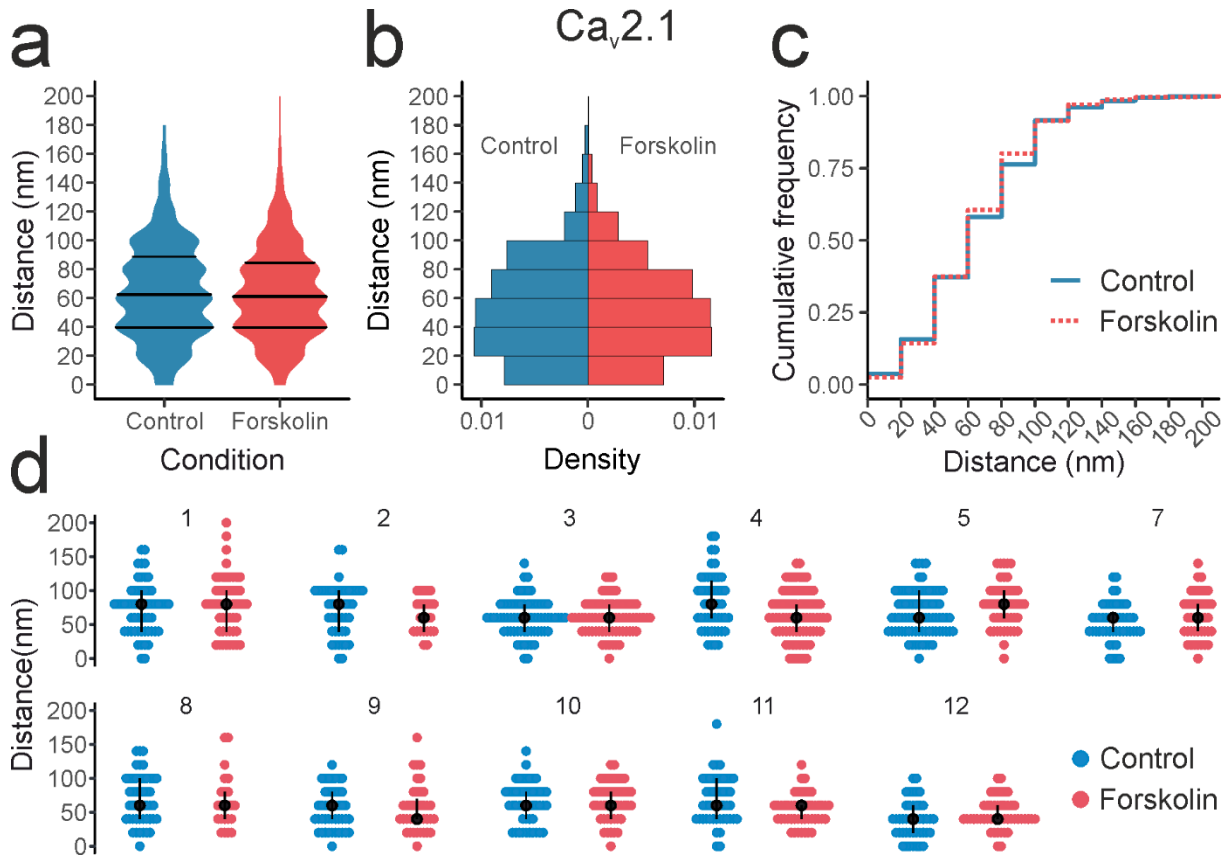

Figure 19: The coupling distance between $Ca_V2.1$ and Munc13-1 is unchanged in control versus forskolin-treated slices. *Distances between $Ca_V2.1$ and Munc13-1 were measured in control and forskolin-treated slices.* ***a)*** *Violin plot showing the distribution of the measured distances (nm) in control (blue) and forskolin (red) condition. Black lines show 25 %, 50 % and 75 % quartiles, respectively. A hypothesis test between GLMMs gave no evidence for a significant difference in the distance between conditions ($p = 0.8514$).* ***b)*** *Mirrored histogram showing the densities of measured distances (nm) for control (blue, left) and forskolin (red, right). Note the symmetry in the shape of distributions. The binwidth is 20 nm, leading to summed densities of 1 per histogram.* ***c)*** *Cumulative frequency of distances (nm) measured in control (blue, straight line) and forskolin (red, dotted line) conditions. The step-like appearance is due to the discrete distance steps of 20 nm, the size of a pixel.* ***d)*** *Scatter plots showing individual distance measurements (nm) per animal. The discrete outcome in the measurements due to the pixel size led to a lot of overlap between individual points. Numbers above the plots indicate the number of the animal. Blue dots correspond to distances measured under control conditions, red dots to forskolin. The black dot indicates the median distance value and the black vertical line the interquartile range.*

In CA1, I analyzed 491 measurements from 11 slices, the same slices I used for imaging CA3 in control condition. Measurements between $Ca_V2.1$ and Munc13-1 clusters resulted in a mean coupling distance ± SD of 54.87 ± 32.49 nm, shorter than the distance measured in CA3 under control conditions (64.62 ± 34.65 nm; Figure 19a). Distance values ranged between 0 and 160 for CA1 (0 – 180 for CA3) and the distribution of distances in CA1 was shifted towards smaller values compared to CA3 (Figure 21b, c). 85.5 % of distances lay between 0 and 80 nm, while it was 76.4 % of distances for CA3 (Figure 21c). Variability was similar between animals and regions (Figure 21d).

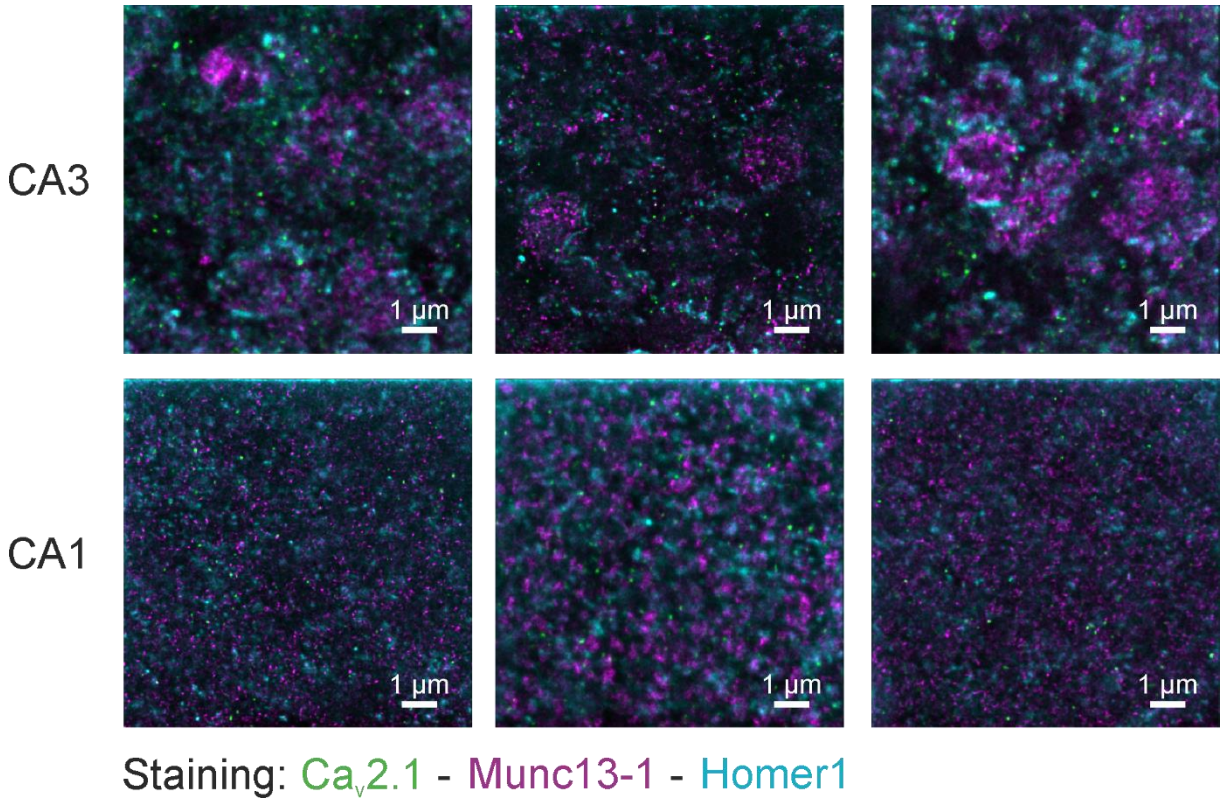

Figure 20: Staining of $Ca_V2.1$, Munc13-1 and Homer1 in the areas CA3 and CA1 of the hippocampus. *Example images from the area CA3 (upper row) and the area CA1 (lower row). Fluorophores labeling $Ca_V2.1$ are shown in green, magenta indicates Munc13-1 and cyan stands for Homer1. Note the denser staining in CA3 and the more uniform distribution in CA1. Images were adjusted for brightness, contrast and intensity.*

I fitted a generalized linear model (GLM) (Gamma family with a log link) to estimate the distance conditional on the hippocampal region (Appendix, Table 25). From here on, all GLMs were using Gamma distributed errors fitted with a log link function. I compared the full model to a null model without region as explanatory variable (Appendix, Table 26) to test the hypothesis that the coupling distance was different between CA1 and CA3. When compared with a likelihood ratio test, these models were significantly different ($p < 0.0001$) (Appendix, Table 27). When comparing the estimated marginal means for both regions, it was shorter in CA1 than in CA3 (Appendix, Table 28) and significantly different in a post-hoc marginal contrast analysis with p-value adjustment ($p < 0.001$) (Appendix, Table 29).

These control measurements indicate that (1) the coupling distance is shorter in CA1 than in CA3 and (2) that gSTED imaging allows us to detect coupling distances shorter than those found in mossy fiber boutons under control conditions. This result also corroborates the finding that there is probably no change in coupling distance in the mossy fiber boutons between $Ca_V2.1$ and Munc13-1 during potentiation (Figure 19). However, the average distance change has likely to be 10 nm or more to be detectable in this experimental approach (Figure 21).

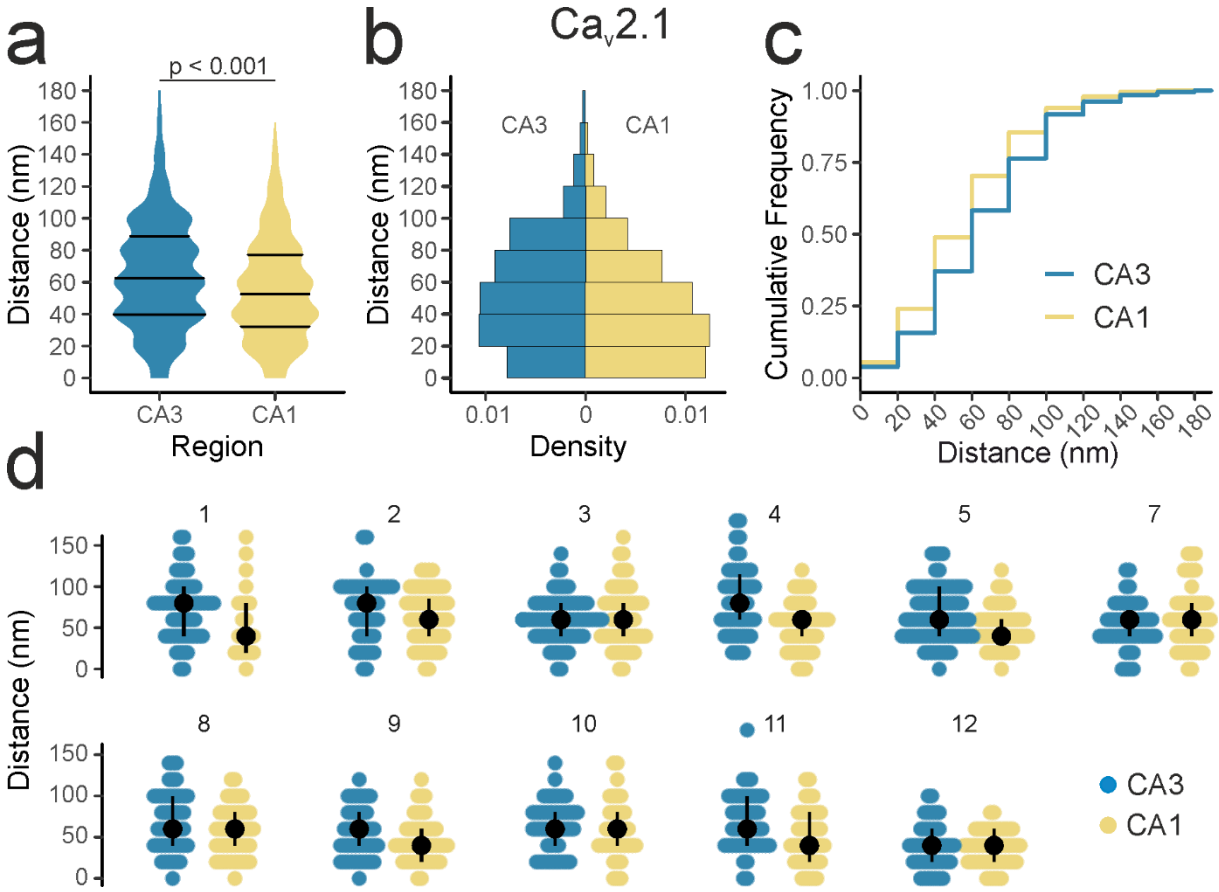

Figure 21: The coupling distance between $Ca_V2.1$ and Munc13-1 is shorter in CA1 than in CA3. *Distances were measured between $Ca_V2.1$ and Munc13-1 in areas CA3 and CA1 in control slices.* ***a)*** *Violin plot showing the distribution of the measured distances (nm) in areas CA3 (blue) and CA1 (yellow). Black lines show 25 %, 50 % and 75 % quartiles, respectively. A hypothesis test between GLMs gave evidence for a significant difference in the distance between CA3 and CA1 with $p < 0.001$.* ***b)*** *Mirrored histogram showing the densities of measured distances (nm) for CA3 (blue, left) and CA1 (yellow, right). Note the moderate asymmetry in the shape of distributions with a shift towards smaller values in CA1. The binwidth is 20 nm, leading to summed densities of 1 per histogram.* ***c)*** *Cumulative frequency of distances (nm) measured in CA3 (blue) and CA1 (yellow). The step-like appearance is due to the discrete distance steps of 20 nm, the size of a pixel. Note the shift of the yellow line towards smaller values.* ***d)*** *Scatter plots showing individual distance measurements (nm) per animal. The discrete outcome in the measurements due to the pixel size led to a lot of overlap between individual points. Numbers above the plots indicate the number of the animal. Blue dots correspond to distances measured in CA3, yellow dots to CA1. The black dot indicates the median distance value and the black vertical line the interquartile range.*

Coupling Distance Between $Ca_V2.2$ and Munc13-1

$Ca_V2.2$, another crucial voltage-gated calcium channel, is also expressed at the hippocampal mossy fiber bouton (Li et al., 2007) and contributes to release (Castillo et al., 1994; Pelkey et al., 2006; Li et al., 2007). Thus, I next measured the coupling distance between the voltage-gated calcium channel $Ca_V2.2$ and Munc13-1 for forskolin-treated and control slices.

Since the analysis with the line tool led to discrete data in the $Ca_V2.1$ dataset, I aimed to improve the analysis pipeline by using the "GaussFit OnSpot" plugin for Fiji instead of the line tool measurement. This plugin uses a given intensity maximum – retrieved with the "find maxima" function in Fiji – and places a Gaussian fit in a defined area around this pixel, to estimate the maximum of the Gaussian distribution (Figure 22b). At first, I wanted to compare the new to the old analysis pipeline to estimate the rigor of the new approach.

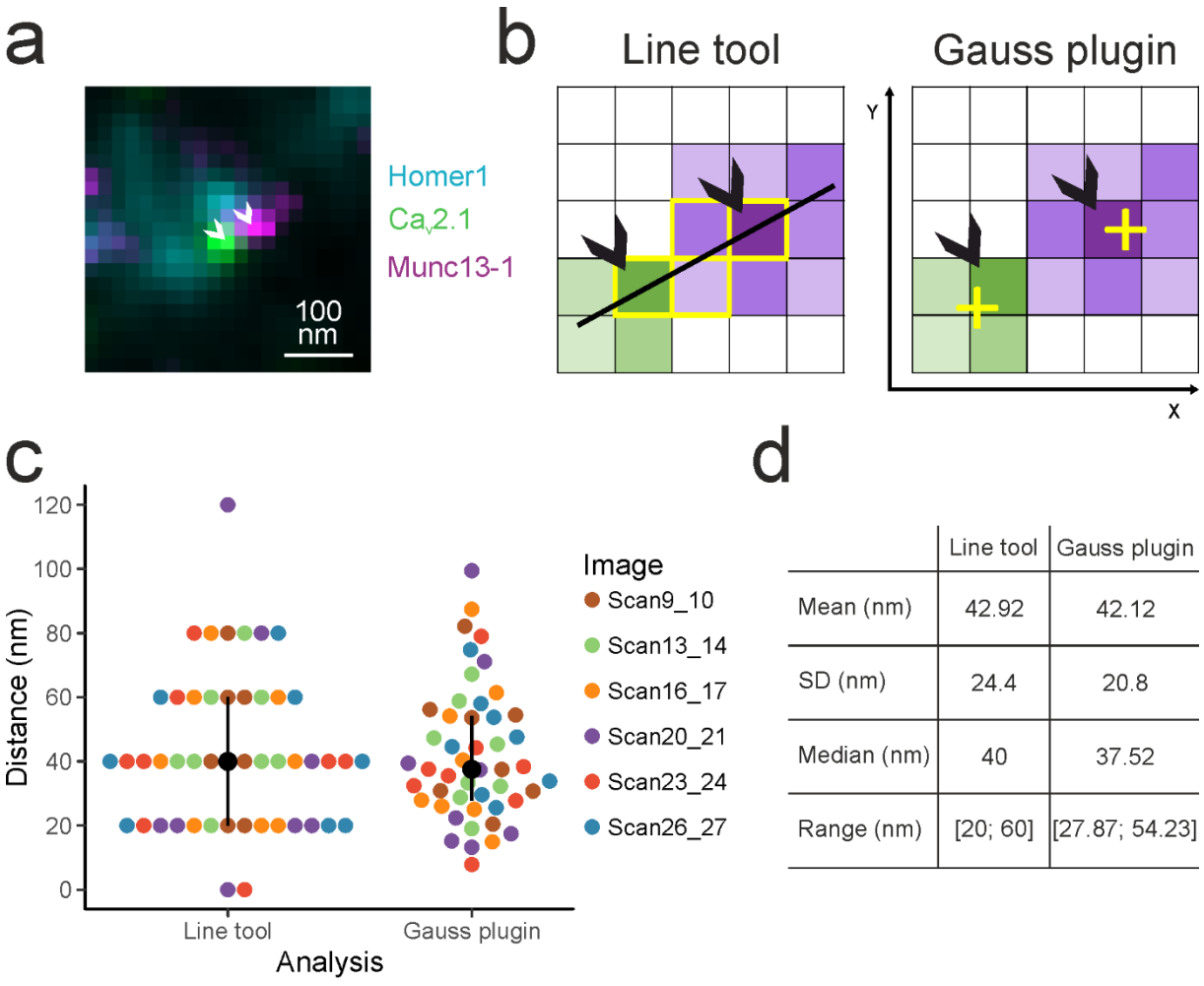

	Line tool	Gauss plugin
Mean (nm)	42.92	42.12
SD (nm)	24.4	20.8
Median (nm)	40	37.52
Range (nm)	[20; 60]	[27.87; 54.23]

Figure 22: Comparison of distance measurements with the Fiji line tool and the Gauss fit plugin. *Distance measurements were carried out both with the line tool and the Gauss fit plugin for 48 synaptic configurations from six images of one example slice.* ***a)*** *Example synaptic configuration showing $Ca_V2.1$ signal in green, Munc13-1 in magenta and Homer1 in cyan. Arrow heads indicate the pixel with the highest fluorescence intensity. This example configuration does not come from the slice analyzed in c)*

and d). Image was adjusted for brightness, contrast and intensity. ***b)*** *Schematics showing how the distance is measured with the line and the Gauss plugin. The schematics are inspired by the example from a) but are not an exact reproduction. Green indicates the signal of the calcium channel and magenta indicates the signal of Munc13-1. Homer1 signal is omitted for simplicity.* ***Left:*** *The line tool is placed through the pixels with the highest intensities (indicated by the black arrow heads). The distance between intensity maxima is given as the summed length of all pixels through which the line passes (indicated by the yellow frame). In this example it would be 4 pixels, summing up to a distance of 80 nm.* ***Right:*** *The Gauss plugin needs the pixels with the highest intensity (indicated by the black arrow heads) as input value. Based on this input the plugin fits a Gaussian function through the intensity values in a given area around this pixel to retrieve the maximum of the Gaussian distribution. The maximum is given as coordinates in a sub-pixel resolution, here indicated by the yellow crosses. In a later analysis step, the distance between the coordinates for both yellow crosses is retrieved using the Pythagorean theorem.* ***c)*** *Scatter plot including all 48 distance measurements (nm) from one example slice, once analyzed with the line tool and once with the Gauss fit plugin. The black dots indicate the median and the black vertical lines the interquartile range. Dots with the same color come from the same image, as indicated in the legend to the right. A hypothesis test between GLMs gave no evidence for a significant difference in the outcome of distances between analysis methods (p = 0.861).* ***d)*** *Table reporting basic statistics for the example slice for both analyses. Note: The example slice was a staining against $Ca_v2.3$, Munc13-1 and Homer1 with an antiserum for $Ca_v2.3$ (see later), leading to shorter mean and median coupling distances than in the $Ca_v2.1$ dataset.*

For one test slice, I analyzed all images both with the aforementioned line tool and the "GaussFit OnSpot" plugin (Figure 22b). The mean distance ± SD using the line tool was 42.92 ± 24.4 nm and 42.11 ± 20.81 nm using the Gauss plugin (Figure 22c, d). The median and range were 40 [20; 60] nm for the line tool and 37.52 [27.87; 54.23] nm for the Gauss plugin (Figure 22c, d). Distances of different lengths were distributed randomly across images and the same configurations had comparable distances between methods (Figure 22c).

I fitted a GLM to estimate the distance with the analysis tool (line tool or Gauss plugin) (Appendix, Table 30). I compared this model to a null model without the analysis tool as explanatory variable (Appendix, Table 31) and found no significant difference between the models (p = 0.861) when compared in a likelihood ratio test (Appendix, Table 32). Hence, there is no evidence that the type of analysis would lead to different distance results. I conclude that I can use the Gauss plugin as an equally suitable tool to estimate the distance. The analysis with the Gauss plugin also allows a continuous data distribution without arbitrary values at zero and therefore a less biased variance.

For the $Ca_v2.2$ dataset images from both CA3 and CA1 were analyzed (Figure 23). The staining patterns looked similar to the ones in the $Ca_v2.1$ staining (Figure 20). Area CA1 is more uniformly patterned than the mossy fiber bouton-containing CA3.

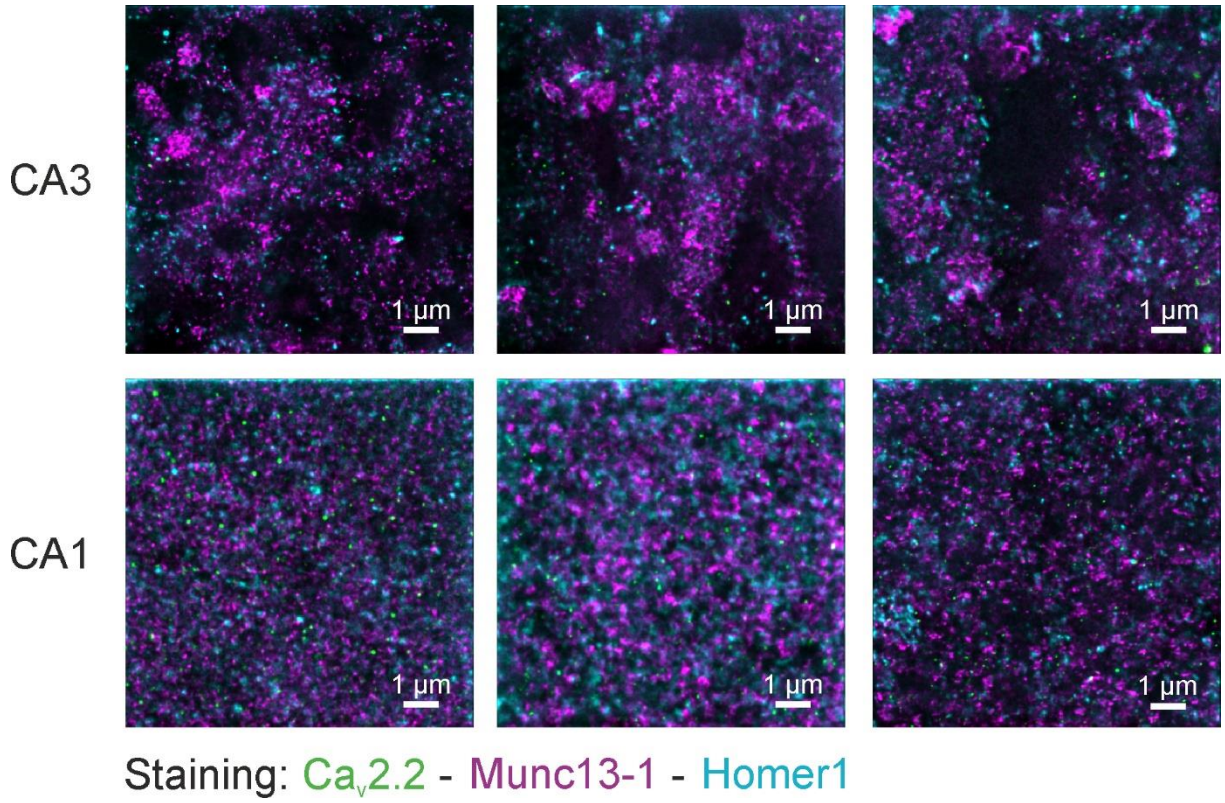

Figure 23: Staining of $Ca_v2.2$, Munc13-1 and Homer1 in the areas CA3 and CA1 of the hippocampus. *Example images from the area CA3 (upper row) and the area CA1 (lower row). Fluorophores labeling $Ca_v2.2$ are shown in green, magenta indicates Munc13-1 and cyan stands for Homer1. Note the denser regions in CA3 and the more uniform distribution in CA1. Images were adjusted for brightness, contrast and intensity.*

For $Ca_v2.2$, distance measurements from nine animals were included in the analysis, with one slice per animal and condition. Per slice, usually six images were taken and per image I measured eight configurations, if possible. An overview of included images and reasons for exclusions are given in Table 17 (Appendix). I measured the distance between $Ca_v2.2$ and Munc13-1 in the *stratum lucidum* of area CA3 for forskolin-treated and control slices. This resulted in 376 measurements for control and 363 measurements for forskolin condition. The mean distance ± SD was comparable between conditions with 61.26 ± 29.83 nm for control and 64.23 ± 33.55 nm for forskolin-treated slices (Figure 24a, Appendix Table 15).

The distributions of distances were similar in the two conditions with a median and interquartile range of 58.99 [37.28; 78.48] nm for control and 60.13 [40.52; 79.98] nm for forskolin-treated slices (Appendix, Table 15, Figure 24b). In general, distances ranged between 6.96 and 213.12 nm for control and 1.38 and 240.91 nm for forskolin (Figure 24b). Values above 200 nm are not shown in the plots for visibility reasons. In control conditions, 90.7 % of distances were situated between 0 and 100 nm, while it was 87.6 % for forskolin (Figure 24c).

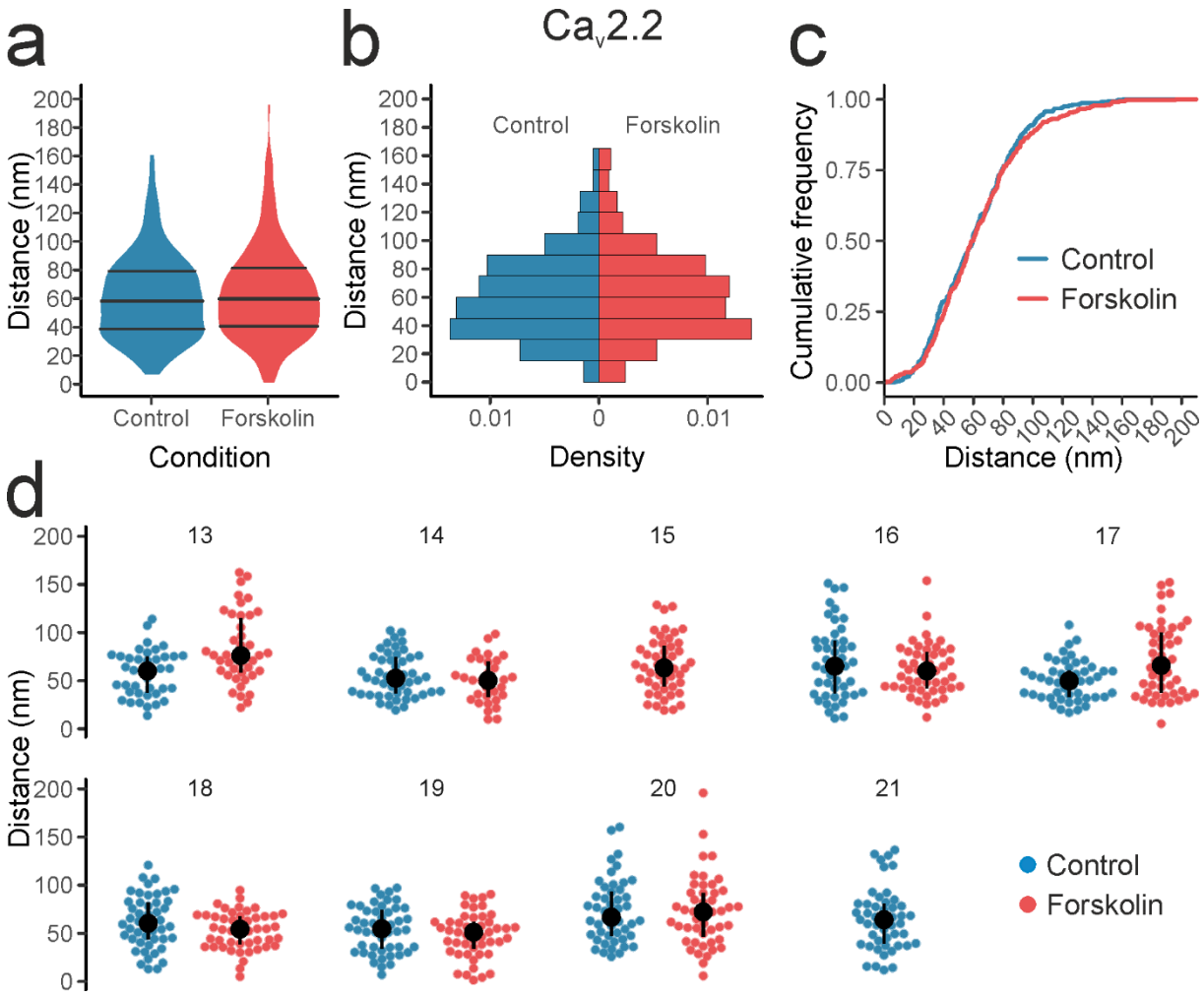

Figure 24: The coupling distance between $Ca_V2.2$ and Munc13-1 is unchanged in control versus forskolin-treated slices. *Distances between $Ca_V2.2$ and Munc13-1 were measured in control and forskolin-treated slices. Distances beyond 200 nm are not shown in the plots for visibility reasons.* ***a)*** *Violin plot showing the distribution of the measured distances (nm) in control (blue) and forskolin (red) condition. Black lines show 25 %, 50 % and 75 % quartiles, respectively. A hypothesis test between GLMMs gave no statistical evidence for a significant change in the distance between conditions ($p = 0.7292$).* ***b)*** *Mirrored histogram showing the densities of measured distances (nm) for control (blue, left) and forskolin (red, right). The bin width was 15 nm, leading to summed densities of 1 per histogram.* ***c)*** *Cumulative frequency of distances (nm) measured in control (blue) and forskolin (red) conditions.* ***d)*** *Scatter plots showing individual distance measurements (nm) per animal. Numbers above the plots indicate the number of the animal used. Individual dots correspond to distances measured under control (blue) or forskolin (red) conditions. The black dot indicates the median distance value and the black vertical line the interquartile range. For animal 15 and 21 only one condition could be analyzed, respectively. Reasons are given in Table 17 (Appendix).*

I fitted a GLMM to estimate the distance given the condition (control or forskolin), including the slice and the animal as random effects (Appendix, Table 33). I compared this model to a null model without condition as explanatory variable (Appendix, Table 34) and found no significant difference ($p = 0.7292$) between the models in a likelihood ratio test (Appendix, Table 35). Thus, there is no statistical evidence for a shorter coupling distance between $Ca_v2.2$ and Munc13-1 after presynaptic potentiation with forskolin in the framework of the experimental approach.

Control measurements were performed in *stratum radiatum* of the area CA1 in the same slices, in which CA3 control measurements were taken. In total, 424 CA1 distance measurements from nine animals were included in the analysis. An overview of included images and reasons for exclusions are given in Table 17 (Appendix). The mean distance ± SD was 56.84 ± 31.25 nm in CA1 (Appendix Table 15, Figure 25a), a bit shorter than the mean distance measured in area CA3 *stratum lucidum* in control conditions (61.26 ± 29.83 nm). In comparison, the distribution was slightly shifted towards a bit smaller values for area CA1 with a median and range of 52.84 [33.85; 76.1] nm compared to 58.99 [37.28; 78.48] in CA3 (Figure 25b, c). Distances ranged between 2.82 and 308.36 nm in CA1 and between 6.96 and 213.12 nm in CA3. Values above 200 nm are not shown in the plots for better visualization. In CA1, 91.5 % of measured distances lay between 0 and 100 nm (Figure 25c). In CA3 control slices, 90.7 % of distances were situated between 0 and 100 nm. The variability of measured distances was comparable between animals and regions (Figure 25d).

I fitted a GLMM to estimate the distance given the hippocampal region (CA3 or CA1), including slice and animal as random effects (Appendix, Table 36). I compared this model to a null model lacking the hippocampal region as explanatory variable (Appendix, Table 37). The models were not significantly different ($p = 0.1184$) when compared with a likelihood ratio test (Appendix, Table 38), concluding that there is no evidence for a shorter coupling distance in CA1 between $Ca_v2.2$ and Munc13-1 in the framework of the experiment.

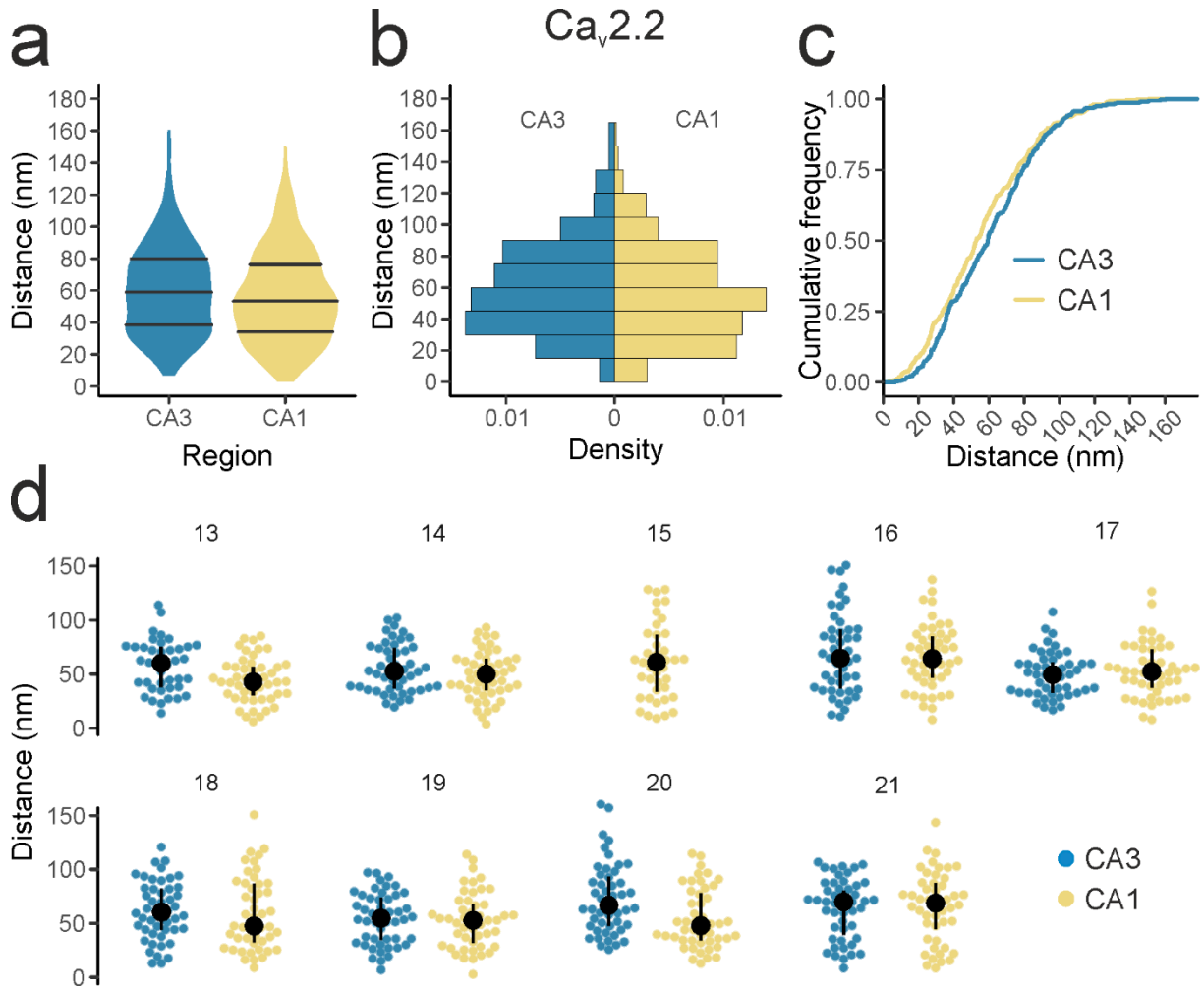

Figure 25: The coupling distance between $Ca_V2.2$ and Munc13-1 is similar for areas CA1 and CA3. *Distances were measured between $Ca_V2.2$ and Munc13-1 in areas CA3 and CA1 in control slices. Distances beyond 200 nm are not shown in the plots for visibility reasons.* ***a)*** *Violin plot showing the distribution of the measured distances (nm) in areas CA3 (blue) and CA1 (yellow). Black lines show 25 %, 50 % and 75 % quartiles, respectively. A hypothesis test between GLMMs gave no evidence for a significant difference in the distance between areas with p = 0.1184.* ***b)*** *Mirrored histogram showing the densities of measured distances (nm) for CA3 (blue, left) and CA1 (yellow, right). Note the asymmetry in the shape of distributions with a shift towards smaller values in CA1. The binwidth is 15 nm, summing up to densities of 1 per histogram.* ***c)*** *Cumulative frequency of distances (nm) measured in CA3 (blue) and CA1 (yellow) conditions. Note the shift of the yellow line towards smaller values.* ***d)*** *Scatter plots showing individual distance measurements (nm) per animal. Numbers above the plots indicate the number of the animal used. Blue dots correspond to distances measured in CA3, yellow dots to CA1. The black dot indicates the median distance value and the black vertical line the interquartile range. For animal 15 only one condition could be analyzed. Reasons are given in Table 17 (Appendix).*

Coupling Distance Between $Ca_v2.3$ and Munc13-1

The third member of the voltage-gated calcium channel group 2 is $Ca_v2.3$ (Catterall, 2011). It is expressed to a lesser extent in mossy fiber boutons than $Ca_v2.1$ and $Ca_v2.2$ (Li et al., 2007) and most likely not involved in the basal release (Breustedt et al., 2003; Dietrich et al., 2003). However, it plays a role in the induction of presynaptic LTP at mossy fiber boutons (Breustedt et al., 2003; Dietrich et al., 2003). Although its distance to adenylyl cyclases is likely more relevant for the role in induction (Dietrich et al., 2003), it has also been found to be expressed at mossy fiber active zones (Parajuli et al., 2012). Therefore, also $Ca_v2.3$ might be an interesting candidate for changing its coupling distance during potentiation. Hence, I proceeded in measuring the distance between Munc13-1 and $Ca_v2.3$ in control and forskolin-treated slices.

To keep the staining parameters as comparable as possible, I only changed the primary antibody for the calcium channel, as in the stainings before. I used an antiserum against $Ca_v2.3$ (Synaptic Systems Cat# 152 404, RRID:AB_2619849), raised in guinea pigs. The 432 measured distances from five animals were unexpectedly shorter than coupling distances measured for $Ca_v2.1$ and $Ca_v2.2$. This finding resulted in the follow-up question if the antiserum led to unspecific binding or if this finding was reproducible. I repeated the stainings with a knock-out validated antibody (Alomone Labs Cat# ACC-006, RRID:AB_2039777), raised in rabbits. Due to this unavoidable change in the host species, I also had to swap the antibody against Munc13-1 and the combination with the secondary antibodies (Tables 9-12, Methods). I analyzed 968 measurements in 14 stained slices from seven animals (one slice per animal and condition) with the antibody from Alomone and compared the values to the antiserum staining. Details regarding both stainings and reasons for exclusion are given in Table 18 (Appendix).

Mean distances were comparable between the two sets of stainings (referred to as “antiserum” for the first set of staining and as “antibody” for the second set), for both regions and conditions (Figure 26a). In CA3, under control conditions, the mean distance ± SD was 48.84 ± 22 nm for the antiserum and 50.01 ± 28.55 nm for the antibody. In forskolin-treated slices it was 49.4 ± 23.8 nm (antiserum) and 48.72 ± 28.96 nm (antibody). In CA1, the distances were also comparable with 48.87 ± 20.73 for the antiserum and 51.95 ± 31.1 nm for the antibody. Plotting the histograms for all distances measured in CA3 for each staining (including both conditions) resulted in similar distributions (Figure 26b) with median and range of 46.79 [32.59; 63.89] nm for the antiserum and 43.57 [27.2; 66.96] nm for the antibody and a similar range (Figure 26c). 99.07 % of distances were located between 0 and 100 nm for the antiserum and 93.07 % for the antibody (Figure 26c). Overall, the stainings had a similar appearance (Figure 26d), although the antiserum stainings looked more similar to the stainings against $Ca_v2.1$ and $Ca_v2.2$ (Figure 26d, Figure 20, Figure 23).

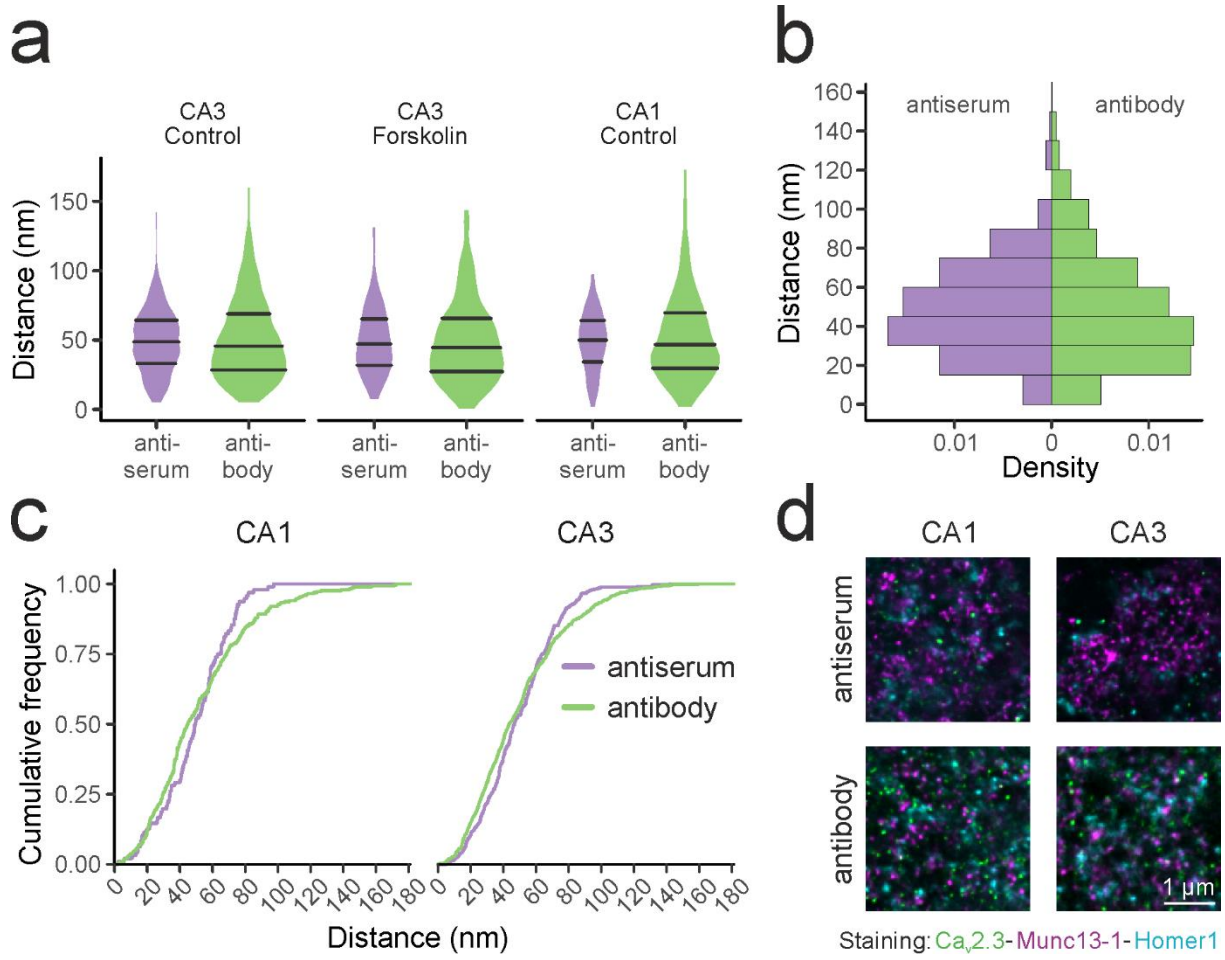

Figure 26: Comparison of distances between $Ca_V2.3$ and Munc13-1 obtained from two sets of stainings. *Distances were measured using the Gauss plugin for both sets of stainings. "Antiserum" stands for a staining with an antiserum against $Ca_V2.3$ raised in guinea pigs (Synaptic Systems Cat# 152 404, RRID:AB_2619849) and "antibody" stands for a staining with an antibody against $Ca_V2.3$ (Alomone Labs Cat# ACC-006, RRID:AB_2039777). See methods for details. For the antiserum staining, data from five animals were analyzed, while it was data from seven animals for the "antibody" staining (Table 18, Appendix). Distances beyond 200 nm are not shown in the plots for visibility reasons.* ***a)*** *Violin plot showing the distribution of distance measurements between $Ca_V2.3$ and Munc13-1 for the two sets of stainings, split up by condition and region. Width of the violin indicates the relative number of data points. Black lines indicate 25 %, 50 % and 75 % quartiles, respectively. A hypothesis test between GLMMs gave no evidence for a significant difference of distances between staining types ($p = 0.8743$).* ***b)*** *Mirrored histogram with a binwidth of 15 nm showing the densities of different distances (nm) for the two stainings with the antiserum in purple (left side) and the antibody in green (right side). Densities are relative to the respective dataset and sum up to 1 per histogram. Here, all distances from CA3 are included for both control and forskolin, as there was no indication for a change in distances in a).* ***c)*** *Cumulative frequency of distances (nm) measured in the "antiserum" and "antibody" dataset, respectively, split up by region. Note that substantially less datapoints are included in the "antiserum" dataset, most likely leading to the discrepancies between lines.* ***d)*** *Example images for regions CA1 and CA3 for the "antiserum" and "antibody" staining. Images were adjusted for brightness, contrast and intensity.*

To statistically compare the outcome from these two sets of stainings, I fitted a GLMM to estimate the distance with the staining (antiserum or antibody), the condition (control or forskolin) and the region (CA1 or CA3), including the images, slices and animals as random effects (Appendix, Table 39). I tested the hypothesis whether the distance was different between the stainings by comparing the full model to a null model without staining as explanatory variable (Appendix, Table 40). I found no statistical difference ($p = 0.8743$) between the models when compared with a likelihood ratio test (Appendix, Table 41). In conclusion, there is no evidence for a difference in measured distances due to the set of staining (Figure 26), indicating that the distance to Munc13-1 is shorter for $Ca_v2.3$ compared to $Ca_v2.1$ and $Ca_v2.2$.

For the following figures and analyses, I only used the data obtained from the antibody stainings (Figure 26). For the distance measurements between $Ca_v2.3$ and Munc13-1, I imaged in regions CA3 and CA1 of the hippocampus. Differences in staining patterns were not as obviously different as in $Ca_v2.1$ and $Ca_v2.2$ stainings. However, some areas in CA3 accumulated more Munc13-1 signal than CA1 (Figure 27).

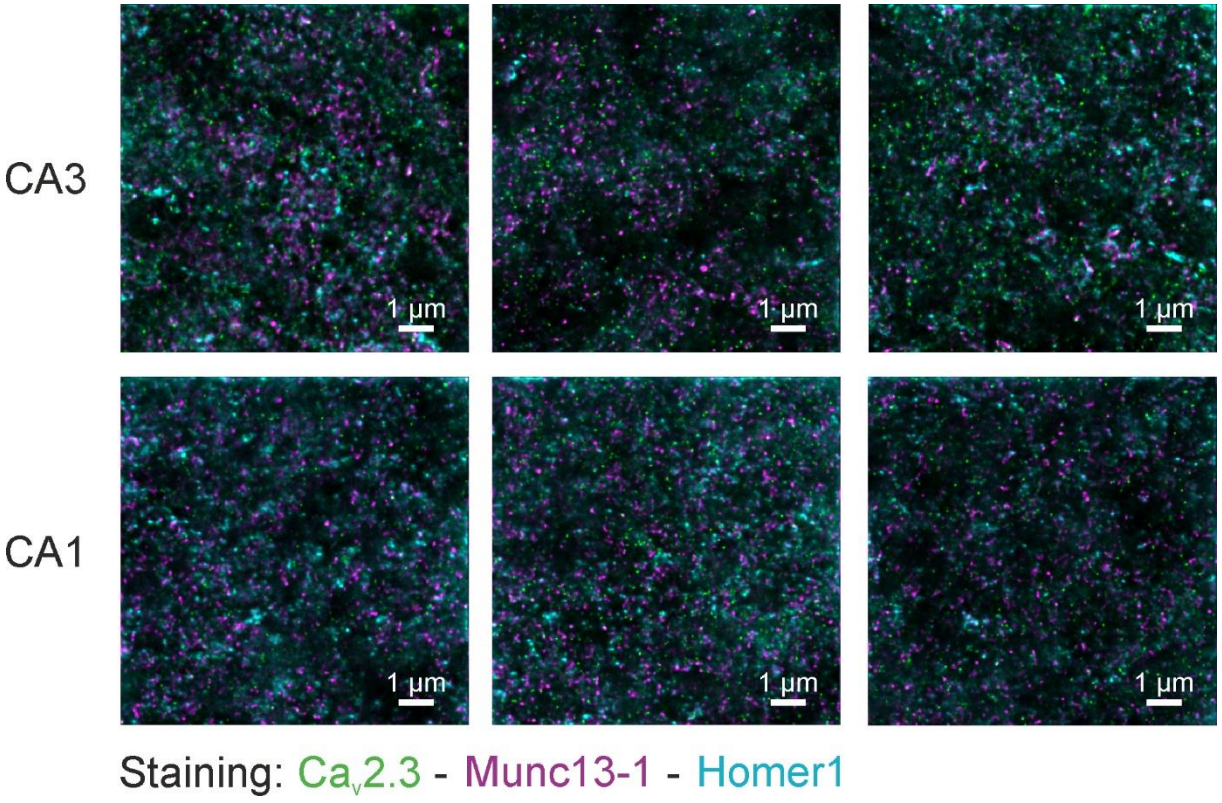

Figure 27: Staining of $Ca_v2.3$, Munc13-1 and Homer1 in the areas CA3 and CA1 of the hippocampus. *Example images from the area CA3 (upper row) and the area CA1 (lower row). Fluorophores labeling $Ca_v2.3$ are shown in green, magenta indicates Munc13-1 and cyan stands for Homer1. Images are from the dataset using the Alomone antibody against $Ca_v2.3$ (Figure 26). Images were adjusted for brightness, contrast and intensity for better visibility.*

In area CA3, I measured distances in 14 slices from seven animals (one slice per animal and condition), resulting in 344 distances for control and 336 distances for forskolin-treated slices (Appendix, Table 15). Distances were similar between the two conditions with a mean distance ± SD of 50.01 ± 28.55 nm for control and 48.73 ± 28.96 nm for forskolin-treated slices (Figure 15a). The distribution of distances between conditions was also similar with a median and range of 44.01 [27.66; 68.66] nm for control and 43.32 [26.5; 65.65] nm for forskolin-treated slices (Figure 28b, c).

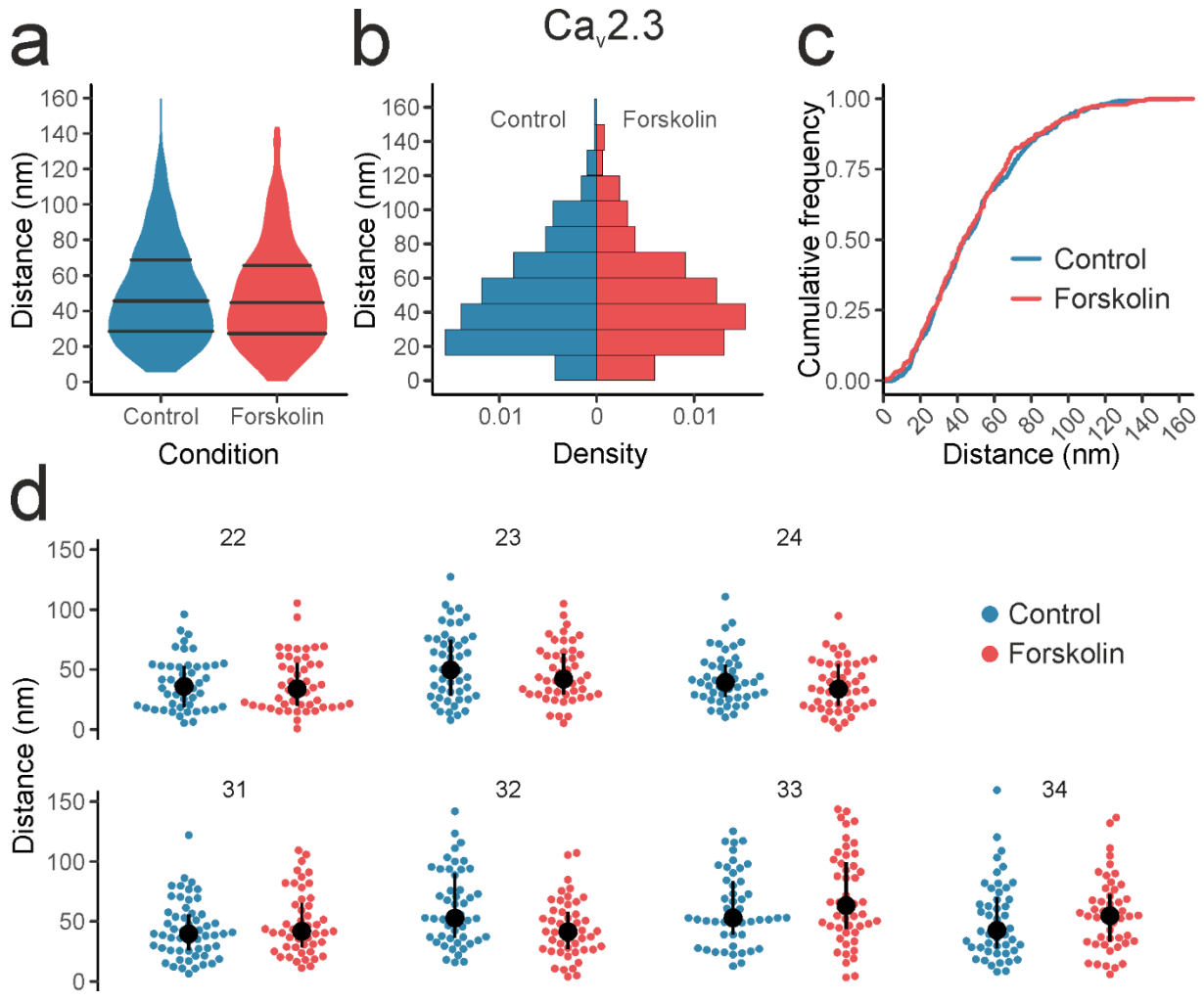

Figure 28: The coupling distance between $Ca_V2.3$ and Munc13-1 is unchanged in control versus forskolin-treated slices. *Distances between $Ca_V2.3$ and Munc13-1 were measured in control and forskolin-treated slices. Distances beyond 200 nm are not shown in the plots for visibility reasons.* ***a)*** *Violin plot showing the distribution of the measured distances (nm) in control (blue) and forskolin (red) condition. Black lines show 25 %, 50 % and 75 % quartiles, respectively. A hypothesis test between GLMMs gave no evidence for a significant difference in the distance between conditions (p = 0.6504).* ***b)*** *Mirrored histogram with a binwidth of 15 nm, showing the densities of measured distances (nm) for control (blue, left) and forskolin (red, right). Densities sum up to 1 per histogram. Note the symmetry in the shape of distributions.* ***c)*** *Cumulative frequency of distances (nm) measured in control (blue) and forskolin (red) conditions.* ***d)*** *Scatter plots showing individual distance measurements (nm) per animal. Numbers above the*

plots indicate the number of the animal used. Blue dots correspond to distances measured under control conditions, red dots to forskolin. The black dot indicates the median distance value and the black vertical line the interquartile range. Animals 25 to 30 had to be excluded. Reasons are given in Table 18 (Appendix).

I fitted a GLMM to estimate the distance with condition (control or forskolin), including images, slices and animals as random effects (Appendix, Table 42). I compared this model to a null model without condition as an explanatory variable (Appendix, Table 43) to test the hypothesis that the distance changes after treatment with forskolin. When comparing the models with a likelihood ratio test (Appendix, Table 44) I found no significant difference between them ($p = 0.6504$). This result indicates that there is no evidence for a shorter coupling distance between $Ca_v2.3$ and Munc13-1 after forskolin treatment in area CA3 (Figure 28) in the framework of the experiment.

Also for $Ca_v2.3$, I carried out control measurements in the area CA1 of the hippocampus. In control slices, I analyzed 288 distance values from six animals in *stratum radiatum*. Here, the mean distances were similar for CA1 and CA3 with a mean ± SD of 51.95 ± 31.1 nm for CA1 compared to 50.01 ± 28.55 nm for CA3 (Appendix Table 15, Figure 29a). Also, the distributions were similar with a median and range of 44.88 [29.61; 68.51] nm for CA1 compared to 44.01 [27.66; 68.66] nm for CA3 (Figure 29b, c). In CA3 93.6 % of distances lay between 0 and 100 nm while it was 92.36 % for CA1 (Figure 29c).

I fitted a GLMM to estimate the distance given the hippocampal region (CA3 or CA1), including the images and animals as random effects (Appendix, Table 45). I compared this model to a null model without hippocampal region as explanatory variable (Appendix, Table 46) to test the hypothesis that the distance was different between CA1 and CA3. When compared with a likelihood ratio test (Appendix, Table 47), I found no significant difference between those models ($p = 0.3977$). In conclusion, there is no statistical evidence for different coupling distances between Munc13-1 and $Ca_v2.3$ in hippocampal areas CA3 and CA1 in the framework of the experiment.

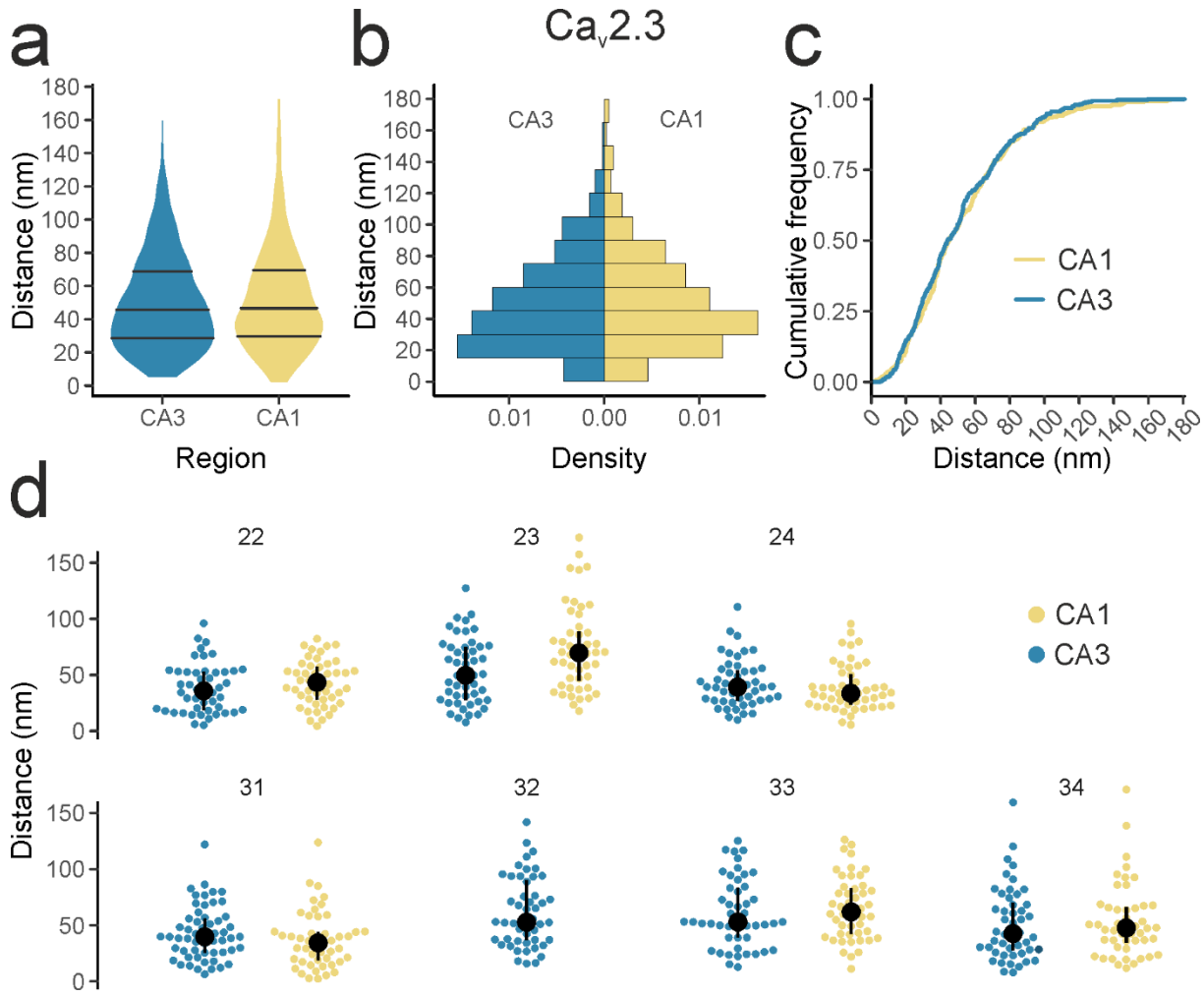

Figure 29: The coupling distance between $Ca_V2.3$ and Munc13-1 is similar between area CA3 and CA1. *Distances were measured between $Ca_V2.3$ and Munc13-1 in areas CA3 and CA1 in control slices. Distances beyond 200 nm are not shown in the plots for visibility reasons.* ***a)*** *Violin plot showing the distribution of the measured distances (nm) in areas CA3 (blue) and CA1 (yellow). Black lines show 25 %, 50 % and 75 % quartiles, respectively. A hypothesis test between GLMMs gave no evidence for a significant difference in the distance between areas (p = 0.3977).* ***b)*** *Mirrored histogram showing the densities of measured distances (nm) for CA3 (blue, left) and CA1 (yellow, right) with a binwidth of 15 nm. Note the symmetry in the shape of distributions. Densities sum up to 1 per histogram.* ***c)*** *Cumulative frequency of distances (nm) measured in CA3 (blue) and CA1 (yellow) conditions.* ***d)*** *Scatter plots showing individual distance measurements (nm) per animal. Numbers above the plots indicate the number of the animal used. Blue dots correspond to distances measured in CA3, yellow dots to CA1. The black dot indicates the median distance value and the black vertical line the interquartile range. For animal 32 only one condition could be analyzed. Animals 25 to 30 had to be excluded. Reasons are given in Table 18 (Appendix).*

Comparison of the Coupling Distances Between Munc13-1 and Ca_v2 Subtypes

The coupling distances in CA3 were unchanged after forskolin treatment for all subtypes of calcium channels from the family Ca_v2 in the framework of my experiments. However, the distance between $Ca_v2.3$ and Munc13-1 was shorter than for the other two calcium channel subtypes: With a median distance of approximately 44 nm it was on average 25 % closer to Munc13-1 than $Ca_v2.1$ and $Ca_v2.2$ with their respective median distance of approximately 60 nm (Table 15, Appendix). The distribution of coupling distances was also shifted more towards shorter distances for $Ca_v2.3$ (Figure 30b, c). All mean and median values are given in Table 15 (Appendix).

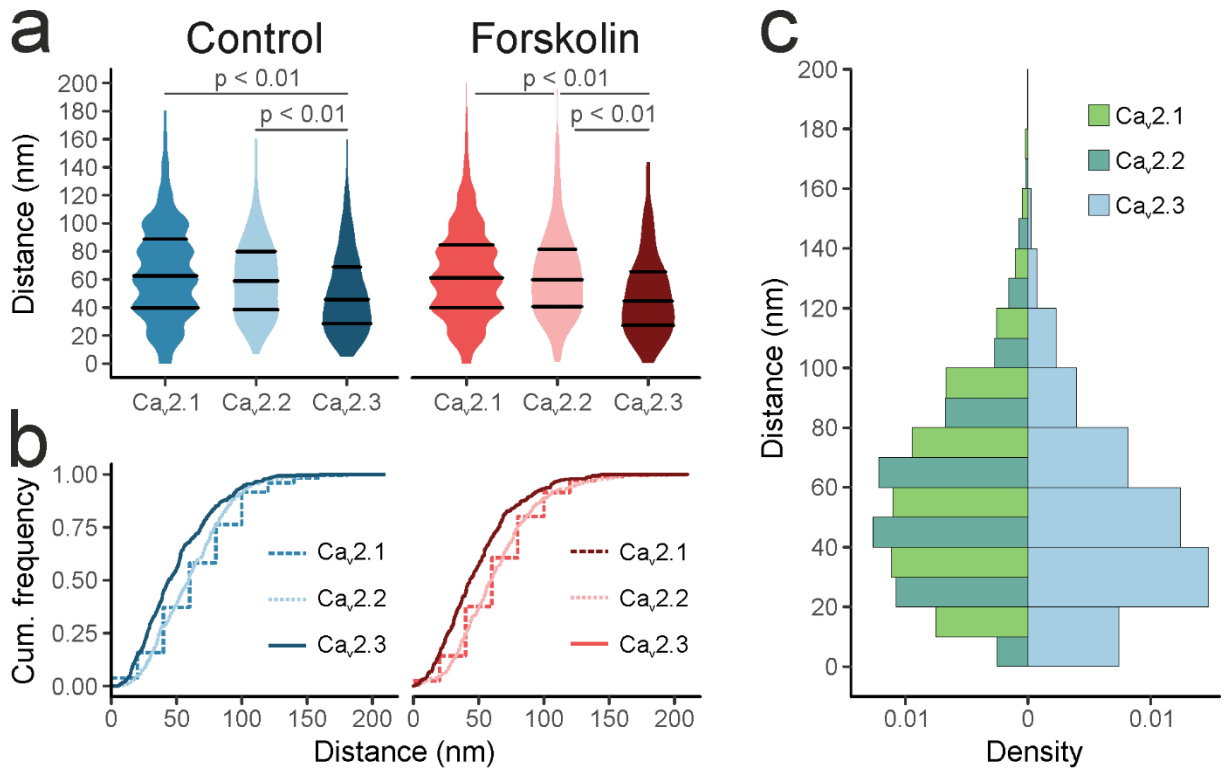

Figure 30: In CA3, the coupling distance to Munc13-1 is shorter for $Ca_v2.3$ than for $Ca_v2.1$ and $Ca_v2.2$. *Comparison of distance measurements between three subtypes of calcium channels of the family Ca_v2 and Munc13-1 in* stratum lucidum *of area CA3 in control and forskolin condition. Distances beyond 200 nm are not shown in the plots for visibility reasons.* ***a)*** *Violin plots showing the distribution of distances (nm) for the three calcium channel subtypes and the two conditions, control (blue colors) and forskolin (red colors). A hypothesis test comparing GLMMs and a post-hoc marginal contrasts analysis gave statistical evidence for a significantly shorter coupling distance between $Ca_v2.3$ and Munc13-1 compared to $Ca_v2.1$ and $Ca_v2.2$ in both conditions. Coupling distances between $Ca_v2.1$ and $Ca_v2.2$ were not significantly different.* ***b)*** *Cumulative frequency of distances (nm) for the three calcium channel subtypes and two conditions control (blue colors) and forskolin (red colors). The dashed lines indicate the $Ca_v2.1$ distances in a middle blue for control and a middle red for forskolin. $Ca_v2.2$ distances are shown as dotted lines in light blue (control) and light pink (forskolin). $Ca_v2.3$ distances are shown as solid lines in dark blue (control) and dark red (forskolin). Note the shift of the $Ca_v2.3$ frequency distribution towards smaller values.* ***c)*** *Mirrored histogram showing the densities of distances (nm)*

for $Ca_V2.1$ (green) and $Ca_V2.2$ (light blue) to the left and of $Ca_V2.3$ (turquoise) to the right. Data from both control and forskolin condition are merged here, since there were no differences between control and forskolin for either of the calcium channel datasets. Binwidth is 20 nm, with densities summing up to 1 for each individual histogram. Note the asymmetry in the distribution of $Ca_V2.3$ compared to the other two with a shift towards smaller values. Bars for $Ca_V2.1$ and $Ca_V2.2$ are narrower than for $Ca_V2.3$ for visibility reasons, but the binwidth is the same for all.

To compare the coupling distances statistically, I fitted a GLMM to estimate the distance with condition (control or forskolin) and type of calcium channel ($Ca_V2.1$, $Ca_V2.2$, $Ca_V2.3$), including the slice and the animal as random effects (Appendix, Table 48). I compared this model to a null model without the calcium channel as explanatory variable (Appendix, Table 49), to test the hypothesis that the distance to Munc13-1 was different for different channel subtypes. The models were significantly different ($p < 0.001$) in a likelihood ratio test (Appendix, Table 50). The estimated marginal means (Appendix, Table 51) were shorter for $Ca_V2.3$ in both conditions. When compared in a contrast analysis, I found that the distance to Munc13-1 was significantly shorter for $Ca_V2.3$ compared to $Ca_V2.1$ both in control ($p = 0.0043$) and forskolin ($p = 0.0043$) condition (Appendix, Table 52). It was also significantly shorter for $Ca_V2.3$ compared to $Ca_V2.2$ in control ($p = 0.0073$) and forskolin condition ($p = 0.0073$). In conclusion, I found evidence for a shorter coupling distance between Munc13-1 and $Ca_V2.3$ than between Munc13-1 and $Ca_V2.1$ as well as $Ca_V2.2$ (Figure 30a).

Control measurements in area CA1 revealed a shorter coupling for $Ca_V2.1$ when compared to its coupling distance in area CA3. This was not the case for the other two calcium channels $Ca_V2.2$ and $Ca_V2.3$. However, their coupling distances to Munc13-1 in area CA1 could be different dependent on the calcium channel subtype, as it was the case in area CA3 (Figure 30). To this end, I ought to compare their coupling distances in area CA1. However, I found similar average coupling distances between all Ca_V2 subtypes and Munc13-1 in the range of 52 to 57 nm (Figure 31a) as well as similar distributions of all measured distances (Figure 31b, c). All mean and median values are given in Table 15 (Appendix).

I fitted a GLMM to estimate the distance with the calcium channel subtype ($Ca_V2.1$, $Ca_V2.2$, $Ca_V2.3$), including the animal as a random effect (Appendix, Table 53). To test the hypothesis that the distance between Munc13-1 and the different calcium channel subtypes was different in area CA1, I compared this model to a null model without calcium channel type as explanatory variable (Appendix, Table 54). In a likelihood ratio test (Appendix, Table 55), they were not significantly different ($p = 0.3855$). Thus, statistical evidence indicates that coupling distances in CA1 are similar between Munc13-1 and the three subtypes of calcium channels from family Ca_V2 in the framework of my experiments.

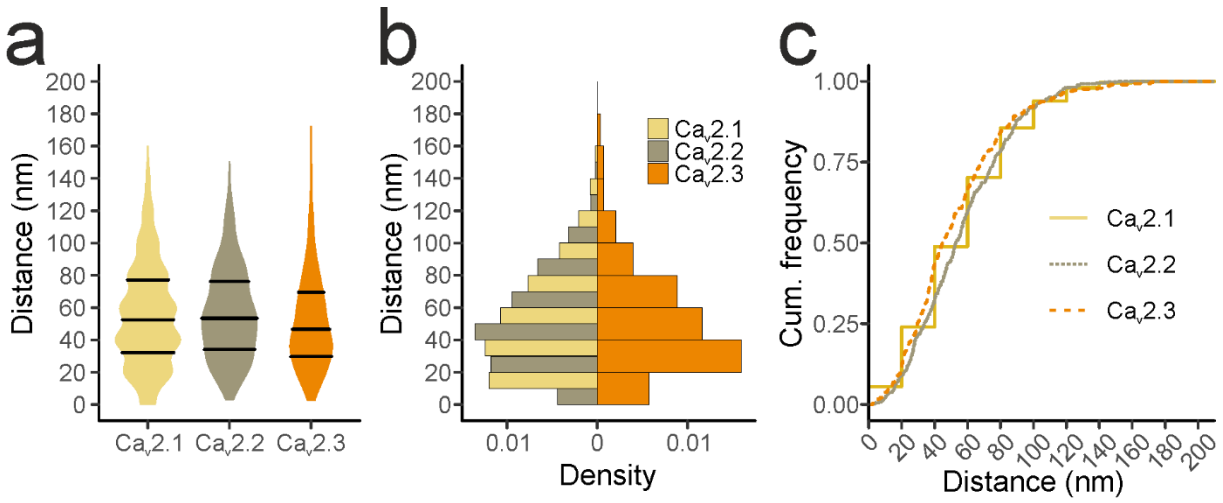

Figure 31: In CA1, the coupling distance to Munc13-1 is similar for all three calcium channel subtypes of family Ca$_v$2. *Comparison of distance measurements between three subtypes of calcium channels of the family Ca$_v$2 and Munc13-1 in the area CA1. Distances beyond 200 nm are not shown in the plots for visibility reasons.* ***a)*** *Violin plots showing the distribution of distances (nm) for the three calcium channel subtypes. A hypothesis test between GLMMs gave no evidence for significant differences in coupling distance between the three calcium channel subtypes and Munc13-1 ($p = 0.3855$).* ***b)*** *Mirrored histogram showing the densities of distances (nm) for Ca$_v$2.1 (yellow) and Ca$_v$2.2 (gray) to the left and of Ca$_v$2.3 (orange) to the right. Binwidth is 20 nm for all three datasets, leading to summed densities of 1 per histogram. Note the symmetry in the distribution of Ca$_v$2.3 compared to the other two. Bars for Ca$_v$2.1 and Ca$_v$2.2 are narrower than the bars for Ca$_v$2.3 for visibility reasons, but the binwidth is the same.* ***c)*** *Cumulative frequency of distances (nm) for the three calcium channel subtypes. The straight line indicates the Ca$_v$2.1 distances (yellow), the dotted line indicates Ca$_v$2.2 distances (gray). The dashed line indicates Ca$_v$2.3 distances (orange).*

Conclusion

The initial hypothesis stated that the coupling distance between calcium entry site and the calcium sensor at the release ready vesicle would become shorter during long-term potentiation of hippocampal mossy fiber boutons. I tested this hypothesis in chemically potentiated versus untreated mouse brain slices. I measured distances between Munc13-1 – a marker for release sites – and all three members of the Ca$_v$2 group of voltage-gated calcium channels. In CA3 *stratum lucidum*, where mossy fiber boutons are located, the coupling distance was unchanged after forskolin treatment for either of the three calcium channel subtypes. However, control measurements revealed shorter coupling distances for Ca$_v$2.1 in area CA1, confirming that the chosen approach would be suitable to measure a shortening in coupling distance. Interestingly, for the Ca$_v$2.3 calcium channel subtype I found significantly shorter coupling distances than for Ca$_v$2.1 and Ca$_v$2.2 in area CA3. Together, these data indicate that (1) the coupling distance might not be changed at hippocampal mossy fiber boutons during presynaptic potentiation and (2) that calcium channel subtypes potentially show a cell-type dependent distinct distribution within active zones.

Number of Release Sites in the Mossy Fiber Bouton

Previous results from our lab showed that, after chemical potentiation, the density of active zones in mossy fiber boutons increases (Orlando et al., 2021). At the same time, chemical potentiation leads to more synchronous and elevated glutamate release at individual boutons (Orlando et al., 2021). Both results suggest that potentiation of mossy fibers leads to a re-structuring of the giant boutons, likely building the architectural foundation for an increased transmitter release during presynaptic LTP.

It is known that proteins from the Munc13 family render synaptic vesicles fusion-competent and are therefore necessary for neurotransmission (Augustin et al., 1999b; Varoqueaux et al., 2002; Imig et al., 2014). Without Munc13s, neurons are silent. More recent literature points out, that Munc13-1 can even prime vesicles for release without most of the active zone scaffolding proteins around (Tan et al., 2022). Thus it is not surprising that the location of Munc13-1 has been shown to be a marker for release sites (Sakamoto et al., 2018). With an increase in active zone density and transmitter release during mossy fiber LTP, I hypothesized that also the number of Munc13-1 clusters increases upon potentiation.

To test this hypothesis, I measured the intensity of antibody-labeled Munc13-1 in control and chemically potentiated cryosections of mouse brain tissue. I compared two incubation times: 15 minutes and 1 hour, because recent findings from the laboratory of Pablo Castillo have suggested that translation takes place in hippocampal mossy fiber boutons during presynaptic LTP within a longer time frame (Monday et al., 2022). Furthermore, I decided to image at three different locations within area CA3 of the hippocampus, because the region itself is heterogenous (Hunt et al., 2018) and proximal parts receive differential inputs from mossy fiber bundles than distal parts (Witter, 2007b).

The cryosections were stained for Munc13-1 and ZnT-3. The latter is a label for zinc transporter 3, that is highly expressed in mossy fibers (Wenzel et al., 1997) and was used to delineate them. Signal is detectable in the hilus of the dentate gyrus as well as in infra- and suprapyramidal bands in the region CA3 (Figure 32a). At the confocal microscope, I imaged stacks in three subregions of CA3: CA3a, CA3b and CA3c (Figure 32a). The intensity of the five brightest images within the stack were summed, for Munc13-1 and ZnT-3 labelling respectively. Based on the ZnT-3 signal, regions of interest (ROIs) were defined and the intensity was analyzed within those ROIs for both channels (Munc13-1 and ZnT-3) (Figure 32b).

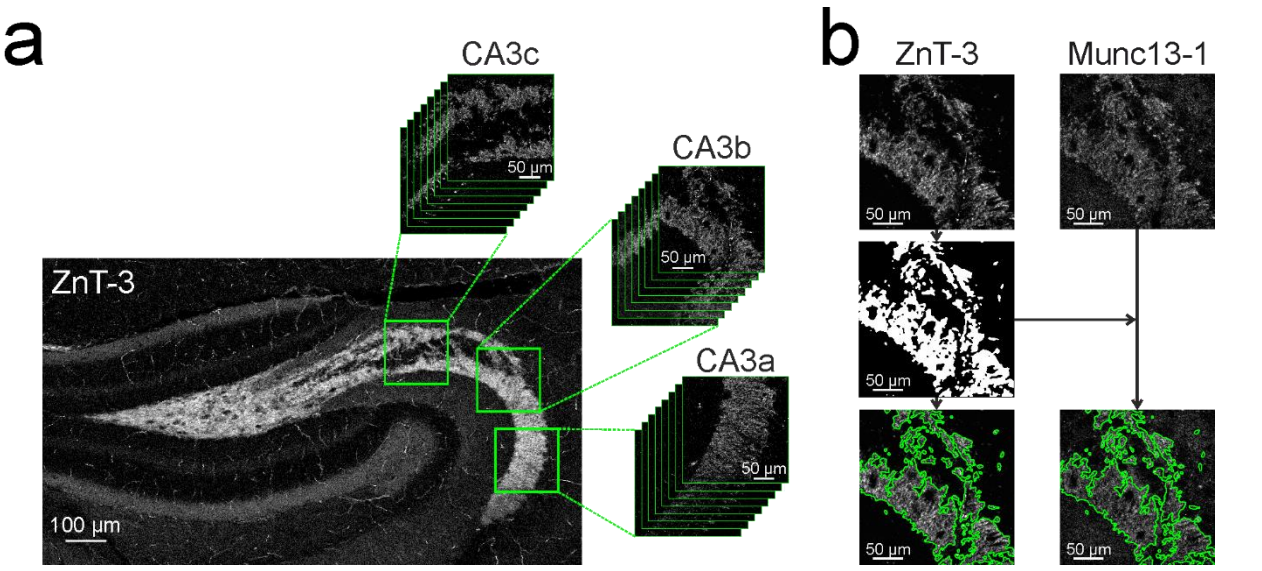

Figure 32: Overview of Munc13-1 intensity analysis. a) *Imaging of acute mouse brain slices stained with Munc13-1 and ZnT-3. Example images show the ZnT-3 signal, which indicates the presence and location of hippocampal mossy fibers (Wenzel et al., 1997). Stacks of images were taken in the three subregions CA3a, CA3b and CA3c for both Munc13-1 and ZnT-3 signals. Images were adjusted for brightness, contrast and intensity for better visibility.* ***b)*** *Overview of intensity analysis. Example images for ZnT-3 and Munc13-1 summed intensity from the five brightest images (top row). Based on the ZnT-3 signal, a mask was created (middle). Outlines of this mask were used as regions of interest (ROIs) for the intensity measurements in both channels (bottom).*

ZnT-3 Area

At first, I was interested, if the area of the ZnT-3 signal would change within subregions (CA3a, CA3b, CA3c) when treated with forskolin, and if that would depend on the length of the incubation time (15 minutes, 60 minutes). This is interesting, because it could indicate translational changes after treatment with forskolin. Local protein synthesis has been suggested as a general presynaptic mechanism during plasticity (Castillo et al., 2023) and potentiation-induced translation of β-actin and an increase in bouton size has been described at the mossy fiber bouton (Monday et al., 2022). Furthermore, possible changes in the area would influence the choice of the parameter used for the intensity analysis. The raw integrated density, for example, is the sum of all grey values within one ROI. Naturally, this will be a larger value for a large region compared to a small one, even if all individual pixels in the large region are rather dim (have lower grey values) and all individual pixels in the small region are very bright. Thus, if the analyzed areas differ between conditions, CA3 subregions or incubation times, I should analyze the mean intensity of ROIs instead, because this parameter is independent of the area.

Average ZnT-3 Area

The image processing resulted in several ROIs per image, including small speckles (Figure 32b and 33) and sometimes also blood vessels that were non-specifically stained (for example the longer fragment in the right lower corner of the example image for CA3a in control condition). To exclude those ROIs from the analysis, I defined a threshold for minimal ROI size at 50 µm^2.

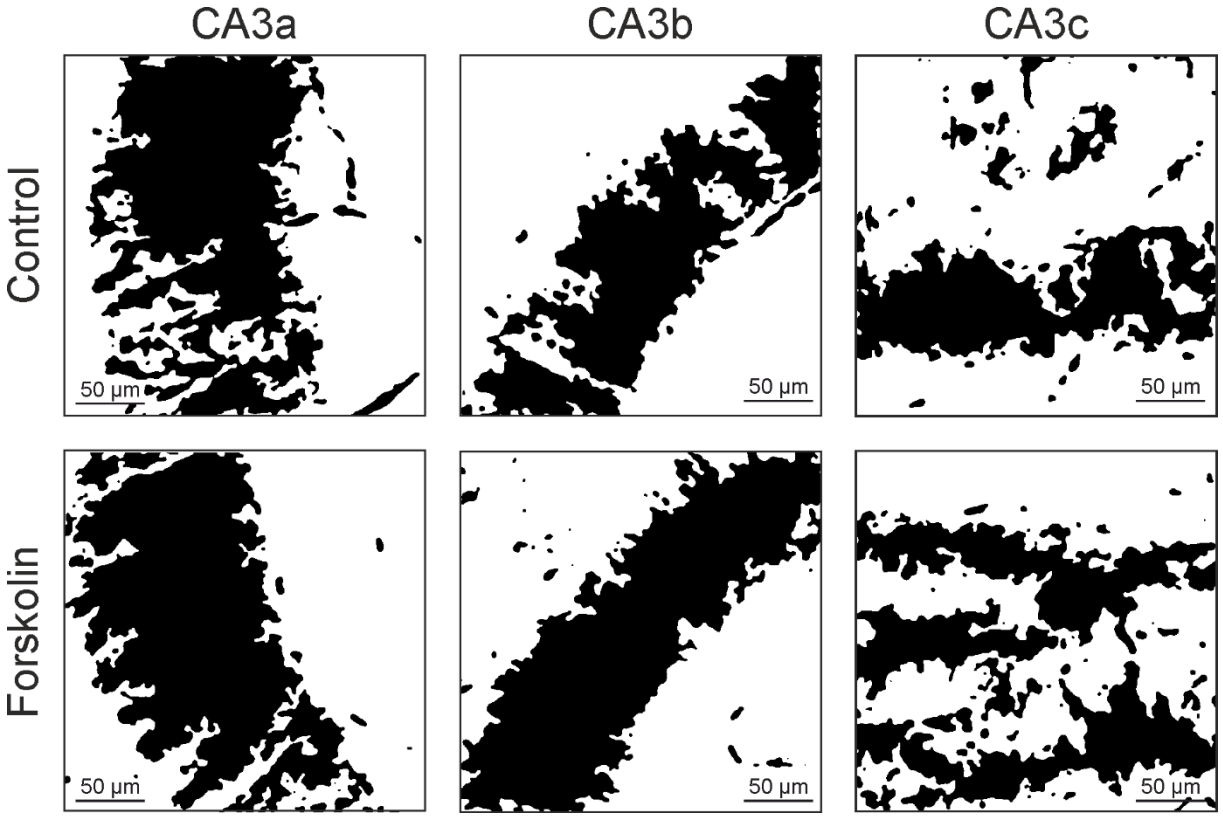

Figure 33: Example images for ZnT-3 area as binary masks after 60 minutes incubation. *The top row shows images from a slice in control condition, the bottom row images from a forskolin-treated slice of the same animal. Black indicates the area within the image, that was positive for ZnT-3, white denotes the background without signal (negative version of the actual image used, for visibility reasons. See Figure 32 for the original). Note that the areas seem to be more joined after forskolin treatment in all three subregions.*

When analyzing the ZnT-3 area from all ROIs above the size threshold of 50 µm^2, I found that the mean ROI area in CA3c was smaller than in areas CA3a and CA3b. In control condition, the mean area ± SD for CA3c was 845.583 ± 1663.121 µm^2, while it was 1433.119 ± 2661.236 µm^2 in CA3a and 1560.314 ± 2591.885 µm^2 in CA3b. This effect could be explained with anatomy: In CA3c, the mossy fibers are split into different bands (Figure 32 and 33), resulting in smaller and more ROIs through the ZnT-3 mask-procedure (Figure 33).

In forskolin-treated slices this trend was similar with smaller average areas in CA3c. For CA3c, the mean area was 982.3416 ± 1506.223 µm^2, for CA3b it was 2737.515 ± 3608.802 µm^2 and for CA3a it was

2861.257 ± 4047.47 μm^2. Additionally, these values showed a trend for larger average ROI sizes after forskolin treatment for all subregions.

To evaluate these observations, I wrote a GLM to estimate the ZnT-3 area given the condition (control or forskolin), region (CA3a, CA3b or CA3c) and incubation time (15 minutes or 60 minutes) as explanatory variables (Appendix, Table 56). I tested several hypotheses by comparing this full model against null models lacking one of the explanatory variables. First, I tested if the treatment condition (Appendix, Table 57) had an influence on the estimated ZnT-3 area and found a significant difference ($p = 0.0458$) between the models in a likelihood ratio test (Appendix, Table 58). The estimated marginal mean was larger for forskolin condition (Appendix, Table 59) and significantly different ($p = 0.05$) to control condition in a post-hoc marginal contrast analysis (Appendix, Table 60). These findings indicate that the average ROI size is larger after forskolin treatment.

Next, I tested if the estimated area was different between the three CA3 subregions. When comparing the nested models (Appendix, Table 56 and 61) in a likelihood ratio test (Appendix, Table 62), there was a significant difference between the models ($p = 0.0004$). The estimated marginal means (Appendix, Table 63) revealed a smaller value for the area CA3c than for the other two. In fact, in a marginal contrast analysis (Appendix, Table 64), the average ROI size in area CA3c was significantly smaller than in area CA3a ($p = 0.0042$) and CA3b ($p = 0.003$).

Last, I tested if the factor incubation time had a significant influence on the estimated ZnT-3 area by comparing the full model (Appendix, Table 56) with the null model lacking incubation time as a variable (Appendix, Table 65) in a likelihood ratio test (Appendix, Table 66). The models were not significantly different ($p = 0.1113$), indicating that the average ROI size did not depend on how long slices were incubated in forskolin before fixation.

I finally compared all marginal mean pairs (Appendix, Table 67) between condition, region and incubation time in a post-hoc marginal effects test (Appendix, Table 68). When factoring in all explanatory variables, the ZnT-3 area was significantly different in area CA3c compared to CA3b in both conditions and for both incubation times (Figure 34a and b). These results suggest that both the treatment and the subregion within CA3 influence the estimate for the ZnT-3 area of the average ROI.

However, while the mean area increased after forskolin treatment, the number of ROIs was reduced (Figure 34a and b, number of dots). This observation shows that there were less, but bigger ROIs present in images from forskolin-treated slices and could indicate that the ZnT-3 stained regions were less separated. Hence, measuring the mean ROI area might not be a suitable measure of a potential change in the overall area stained by ZnT-3 after treatment with forskolin.

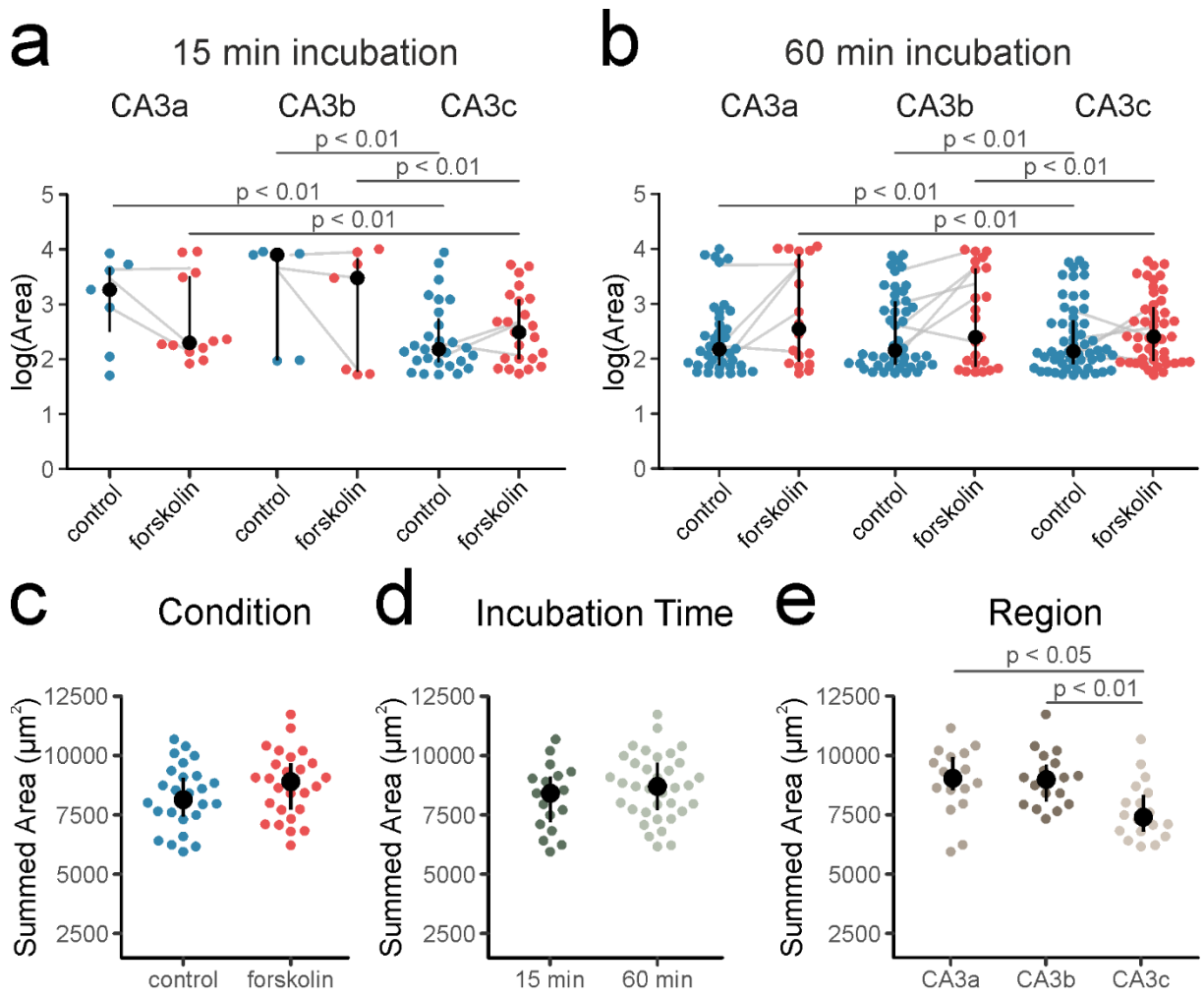

Figure 34: ZnT-3 positive area is smaller in CA3c. a) *ZnT-3 area of individual ROIs in subregions CA3a, CA3b and CA3c for control and forskolin condition after 15 minutes incubation. Values for area are plotted as the logarithm of area (µm²) for better visibility. Hypothesis tests between GLMs revealed significant differences between conditions (p = 0.0458) and regions (p = 0.0004). A post-hoc marginal contrast analysis confirmed significant differences between area CA3a and CA3c as well as between CA3b and CA3c for both conditions (p < 0.01, respectively). Grey lines connect median values of both conditions from the same animal. Black circles show the median, the black line denotes the interquartile range.* ***b)*** *ZnT-3 area of individual ROIs in subregions CA3a, CA3b and CA3c for control and forskolin condition after 60 minutes incubation. Values for area are plotted as the logarithm of area (µm²) for better visibility. Hypothesis tests between GLMs revealed significant differences between conditions (p = 0.0458) and regions (p = 0.0004). A post-hoc marginal contrast analysis confirmed significant differences between area CA3a and CA3c as well as between CA3b and CA3c for both conditions (p < 0.01, respectively). Grey lines connect median values of both conditions from the same animal. Black circles show the median, the black line denotes the interquartile range.* ***c)*** *Summed ZnT-3 area (µm²) for control and forskolin condition. Each dot represents one image. Data points are pooled across region and incubation time. A hypothesis test between GLMs revealed no significant difference between conditions (p = 0.1836). Black circles show the median, the black line denotes the interquartile range.* ***d)*** *Summed ZnT-3 area (µm²) for the two incubation times. Each dot represents one image. Data points are pooled across region and condition. A hypothesis test between GLMs revealed no significant difference between incubation times (p = 0.2533). Black circles show the median, the black line denotes the interquartile range.* ***e)*** *Summed ZnT-3 area (µm²) for the CA3 subregions. Each dot represents one image. Data points are pooled across condition and incubation time. A hypothesis test between GLMs revealed significant differences between CA3 subregions*

(p = 0.0024). In a post-hoc marginal contrast analysis, the total area in CA3c was significantly different to the total area in CA3a (p = 0.0154) und CA3b (p = 0.0078). Black circles show the median, the black line denotes the interquartile range.

Total ZnT-3 Area

To solve this issue, I analyzed the total area of all ROIs in each image, leading to one data point per image. I wrote a GLM to estimate the summed ZnT-3 area per image given the condition, region and incubation time (Appendix, Table 69). Again, I tested three hypotheses by comparing the full model against the respective null models. I found that both condition (p = 0.1836) and incubation time (p = 0.2533) did not have significant influence on the total ZnT-3 area (Appendix, Table 70, 71, 76, 77, Figure 34c and d). However, a model lacking region as explanatory variable (Appendix, Table 72) was significantly different (p = 0.0024) to the full model in a likelihood ratio test (Appendix, Table 73), indicating that the total ZnT-3 area was different between the three CA3 subregions. Indeed, a post-hoc marginal contrast analysis (Appendix, Table 75) comparing the marginal means of the CA3 subregions (Appendix, Table 74) reported significant differences between areas CA3a and CA3c (p = 0.0154) as well as between CA3b and CA3c (p = 0.0078) (Figure 21e).

In summary, these analyses show that the total ZnT-3 area is smaller in CA3c compared to CA3a and Ca3b, but does not change after forskolin treatment (Figure 34c and e). However, when looking at individual ROIs, fewer but bigger ROIs were detected after forskolin treatment (Figure 34a and b), indicating changes in the distribution of the ZnT-3 signal after forskolin treatment.

Munc13-1 Intensity

The Munc13-1 intensity gives an indirect estimate for the amount of release sites present (Sakamoto et al., 2018) and was therefore the main parameter of interest. I aimed to compare the fluorescence intensity of immunolabeled Munc13-1 in control and forskolin-treated slices, to see if there was a change in intensity after chemical potentiation of hippocampal mossy fibers. Additionally, I compared incubation times of 15 and 60 minutes to elucidate if a longer incubation of one hour might be needed to detect changes indicative of the translation of new proteins.

Images were acquired and processed as described above. In a final step, images containing the summed intensity from the five brightest images of the stack were background-corrected to increase the signal-to-noise ratio. Examples for both conditions and all CA3 subregions are given in Figure 35. The mean intensity was measured in regions of interest, predefined by the ZnT-3 signal. The mean intensity was the measure of choice, because single ROIs had significantly different areas between conditions as well as between subregions of CA3 (Figure 34a and b).

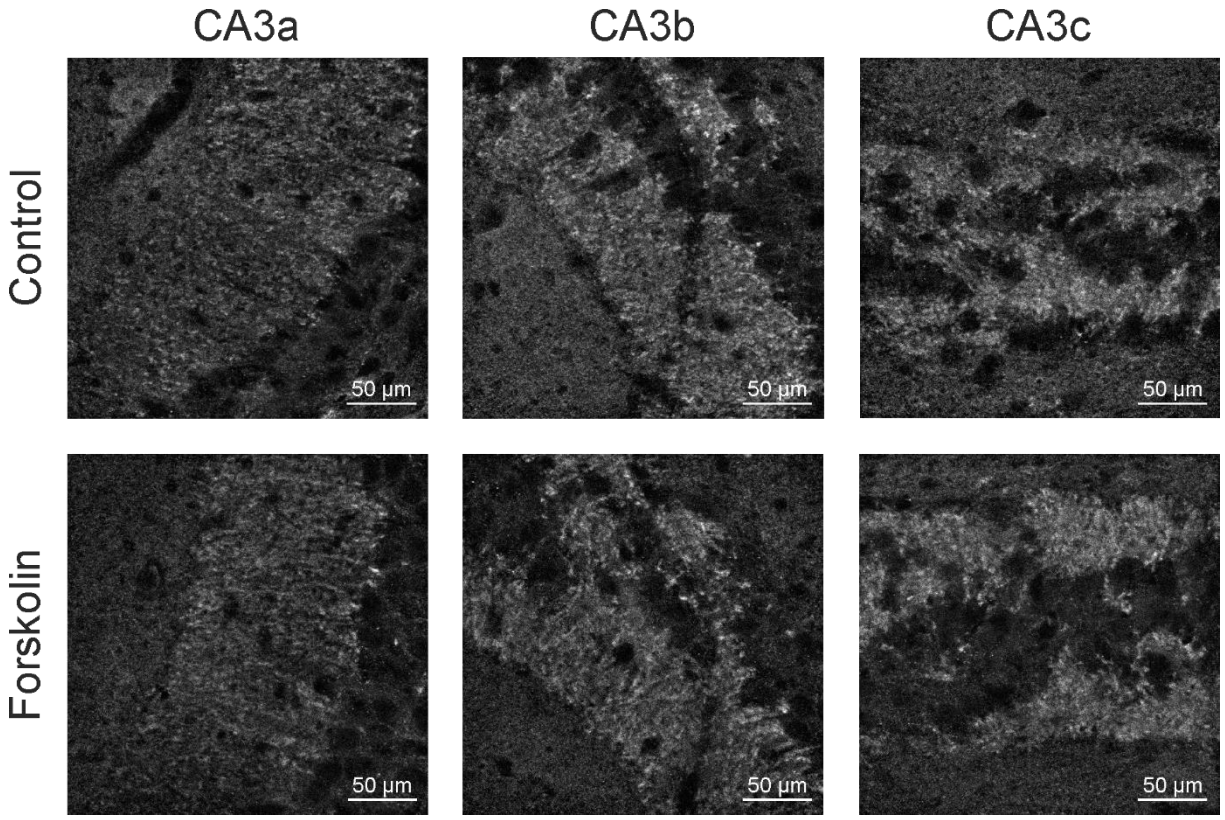

Figure 35: Munc13-1 staining in the area CA3 of the hippocampus. *Munc13-1 is present everywhere, but the signal is accumulated in the* stratum lucidum *and* stratum oriens *in area CA3, where mossy fibers are present. The upper row shows example images of summed Munc13-1 intensities from a control slice for subregions CA3a, CA3b and CA3c, respectively. The lower row shows example images from a forskolin-treated slice, from the same animal. Images were adjusted for brightness, contrast and intensity for better visibility.*

The means of those mean intensities were comparable for all three subregions in CA3. In control conditions the mean intensity ± SD was 206.683 ± 79.984 for CA3a, 234.677 ± 93.526 for CA3b and 249.703 ± 94.746 for CA3c. Intensities in forskolin-treated slices were in general a bit lower with a mean intensity of 144.942 ± 56.283 for CA3a, 175.745 ± 56.108 for CA3b and 197.87 ± 86.813 for CA3c. To compare the intensities of all ROIs with regard to their nested structure and all explanatory variables, I wrote a GLMM. This model estimated the mean Munc13-1 intensity given the condition (control or forskolin), incubation time (15 minutes or 60 minutes) and subregion within CA3 (CA3a, CA3b, CA3c), including the sample and the animal as random effects (Appendix, Table 78).

I compared this full model to three null models, to test several hypotheses. First, I asked if the treatment condition of the slice influenced the Munc13-1 intensity. I found that a model without condition as explanatory variable (Appendix, Table 79) was not significantly different to the full model ($p = 0.0689$) in a likelihood ratio test (Appendix, Table 80). This result indicates that there is no statistical evidence for an effect of condition on the Munc13-1 intensity in the framework of the experiment.

Next, I tested whether the Munc13-1 intensity was different between shorter and longer incubation times. A null model without incubation time as explanatory variable (Appendix, Table 85) was not significantly different ($p = 0.4715$) to the full model in a likelihood ratio test (Appendix, Table 86), suggesting that incubation time has no significant effect on Munc13-1 intensity.

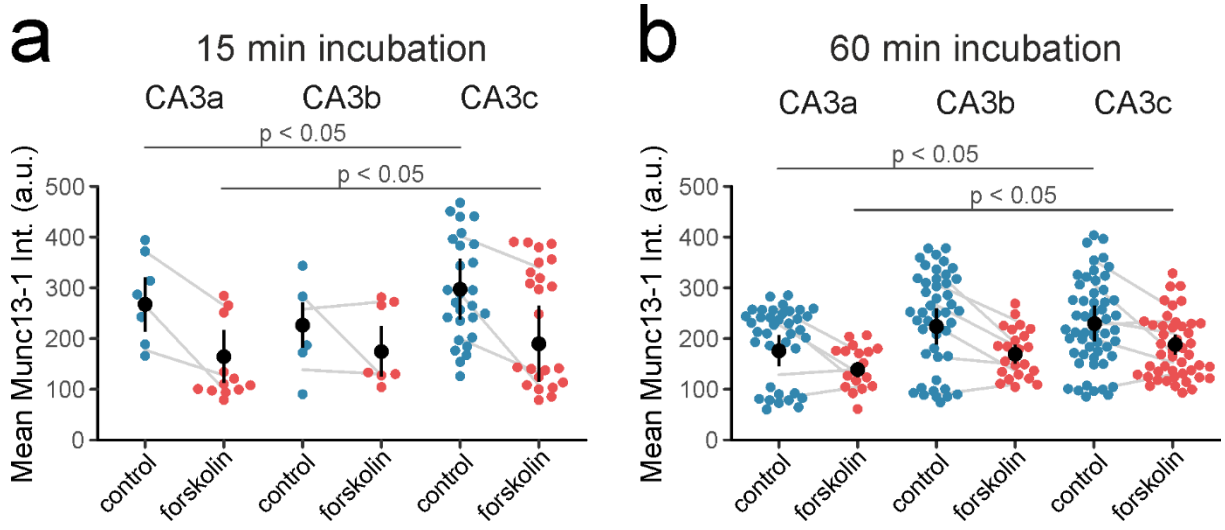

Figure 36: Munc13-1 mean intensity does not change after incubation with forskolin. a) *Munc13-1 mean intensity (a.u.) after 15 minutes incubation for the CA3 subregions and both control (blue dots) and forskolin (red dots) condition. Each dot represents one ROI (see Figure 32). Grey lines connect the mean values of individual animals between conditions. Black dots represent the weighted average and the SEM is shown as a black line. A hypothesis test between GLMMs revealed significant differences between subregions of CA3 ($p < 0.0001$). A post-hoc marginal contrast analysis revealed significant differences between CA3a and CA3c for both conditions ($p < 0.05$).* ***b)*** *Munc13-1 mean intensity (a.u.) after 60 minutes incubation for the CA3 subregions and both control (blue dots) and forskolin (red dots) condition. Each dot represents one ROI (see Figure 32). Grey lines connect the mean values of individual animals between conditions. Black dots represent the weighted average and the black line represents the SEM. A hypothesis test between GLMMs revealed significant differences between subregions of CA3 ($p < 0.0001$). A post-hoc marginal contrast analysis revealed significant differences between CA3a and CA3c for both conditions ($p < 0.05$).*

Finally, I asked if the mean Munc13-1 intensity was different between the subregions of area CA3. I compared a null model lacking the region as explanatory variable (Appendix, Table 81) to the full model in a likelihood ratio test (Appendix, Table 82) and found a significant difference between the models ($p < 0.0001$). When comparing the estimated marginal means, the mean intensity was lowest in area CA3a and highest in area CA3c (Appendix, Table 83). A marginal contrast analysis (Appendix, Table 84) revealed significant differences between CA3a and CA3c ($p = 0.0133$).

When comparing the marginal means (Appendix, Table 87) of all possible combinations between condition, region and incubation time in a marginal contrast analysis (Appendix, Table 88), the outcome was the same. After an incubation time of 15 minutes, the mean Munc13-1 intensity was significantly different ($p = 0.0216$) between area CA3a and CA3c for both conditions (Figure 36a). Also after an incubation time of 60 minutes the mean Munc13-1 intensity was significantly different ($p = 0.0216$) between CA3a and CA3c for both conditions (Figure 36b). None of the comparisons revealed a difference between conditions, which in summary indicates that the mean Munc13-1 intensity does not change significantly after treatment with forskolin (Figure 36).

In summary, my results indicate that there is no detectable change in Munc13-1 immunohistochemical signal intensity in confocal images after induction of chemical potentiation in hippocampal mossy fibers. There were differences in Munc13-1 intensity within the area CA3, with a higher intensity towards the hilus and a lower intensity towards CA2. This could indicate less mossy fiber boutons in CA3a than in CA3c, although this would be contradictory to the larger total ZnT-3 area in CA3a compared to CA3c (Figure 34e). To clarify the findings so far, I next ought to compare the ZnT-3 intensity.

ZnT-3 Intensity

The mean ZnT-3 intensity was measured in the same way as the Munc13-1 intensity. Intensities between conditions and subregions were comparable (Figure 37). The average mean intensities ± SD in control conditions were similar between subregions with 209.858 ± 79.486 for CA3a, 184.286 ± 88.187 for CA3b and 212.288 ± 79.988 for CA3c. They were also comparable to intensities in forskolin-treated slices. Here, the mean intensities were 191.747 ± 70.477 for CA3a, 201.496 ± 69.239 for CA3b and 185.944 ± 68.857 for CA3c.

To estimate the ZnT-3 mean intensity given the condition (control or forskolin), region (CA3a, CA3b, CA3c) and incubation time (15 minutes or 60 minutes), I fitted a GLMM including the sample as random effect (Appendix, Table 89). I tested several hypotheses by comparing this full model to models lacking one of the explanatory variables. None of the comparisons were significantly different. First, I tested against a null model lacking condition as explanatory variable (Appendix, Table 90) and found no significant

difference (p = 0.183) between the models when compared in a likelihood ratio test (Appendix, Table 91). Next, I compared the full model to a null model lacking region as explanatory variable (Appendix, Table 92). Again, there was no significant difference (p = 0.1072) between the models in a likelihood ratio test (Appendix, Table 93). A last comparison of the full model to a null model lacking incubation time as explanatory variable (Appendix, Table 94) revealed no significant difference (p = 0.06968) between the models in a likelihood ratio test (Appendix, Table 95).

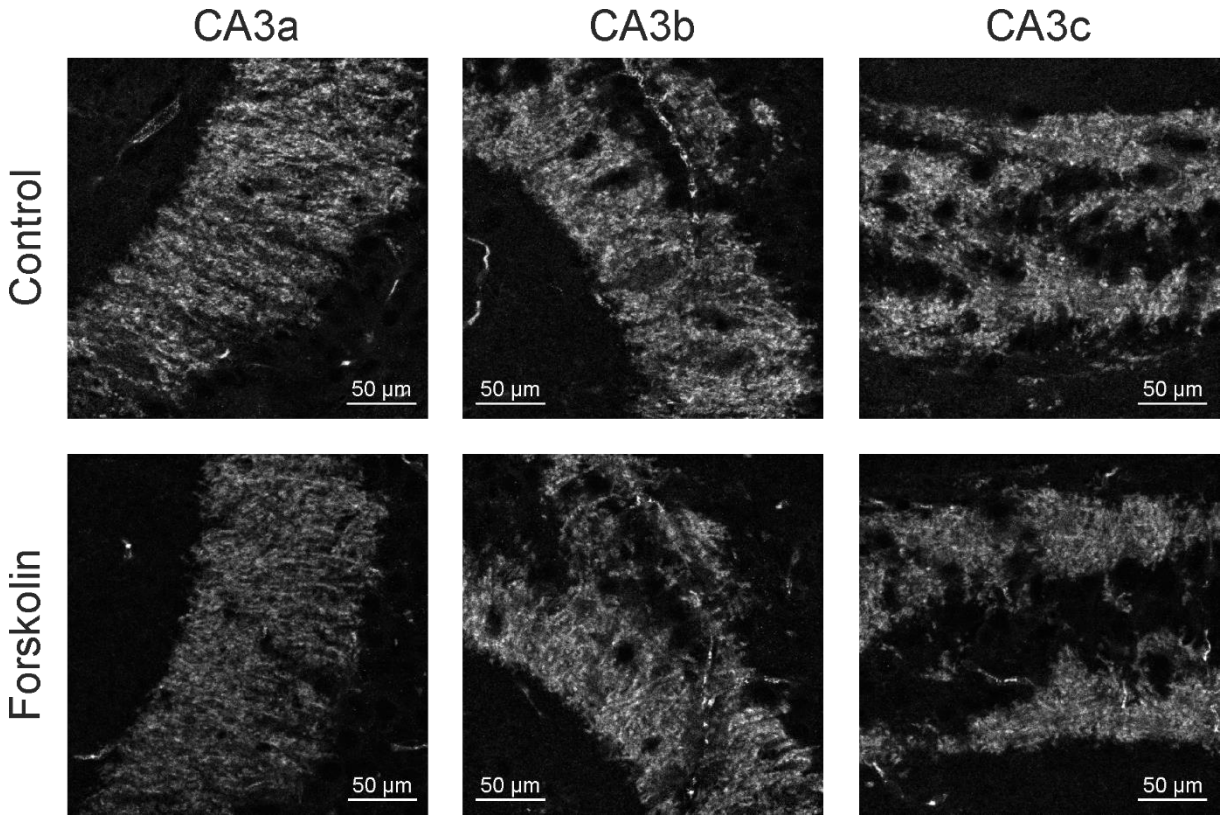

Figure 37: ZnT-3 staining in the area CA3 of the hippocampus. *ZnT-3 is only present in the* stratum lucidum *and* stratum oriens *of area CA3, where mossy fibers are present (Wenzel et al., 1997). The upper row shows example images of summed ZnT-3 intensities from a control slice for subregions CA3a, CA3b and CA3c. The lower row shows example images from a forskolin-treated slice from the same animal. Within subregions of CA3 the intensities were of comparable brightness between the two conditions. Images were adjusted for brightness, contrast and intensity for better visibility.*

Thus, in the experimental framework neither the incubation time, nor the forskolin treatment or the subregion was influencing the mean ZnT-3 intensity (Figure 38), indicating that the density of mossy fibers containing vesicles with zinc is likely comparable between all subregions and conditions and does not depend on incubation time.

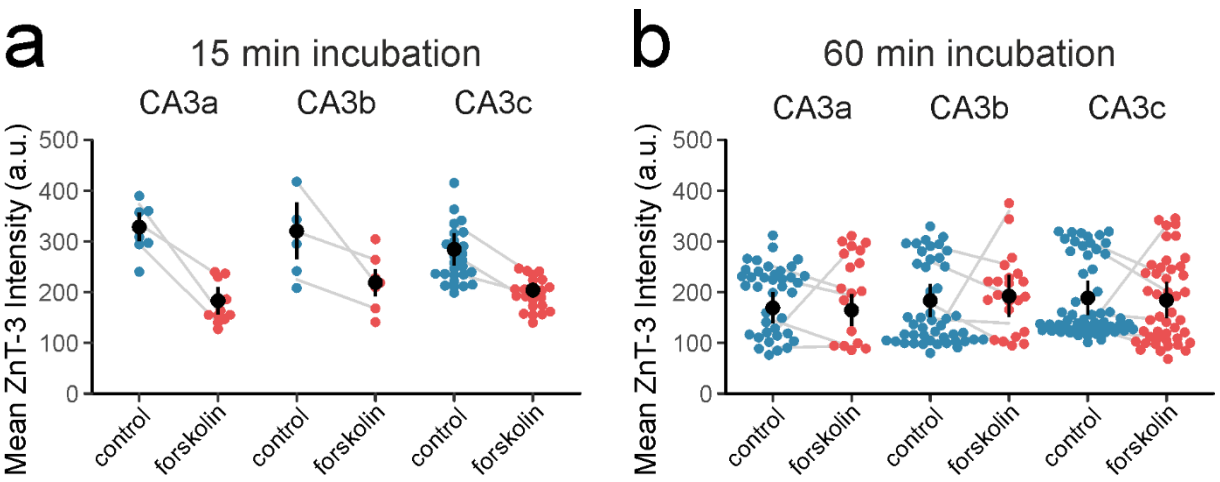

Figure 38: ZnT-3 mean intensity does not change after incubation with forskolin. a) *ZnT-3 mean intensity (a.u.) after 15 minutes incubation for the CA3 subregions and both control (blue dots) and forskolin (red dots) condition. Each dot represents one ROI (see Figure 32). Grey lines connect the mean values of individual animals between conditions. Black dots represent the weighted average and the black line represents the SEM. A hypothesis test between GLMMs revealed no significant differences between subregions (p = 0.1072) or conditions (p = 0.183).* ***b)*** *ZnT-3 mean intensity (a.u.) after 60 minutes incubation for the CA3 subregions and both control (blue dots) and forskolin (red dots) condition. Each dot represents one ROI (see Figure 32). Grey lines connect the mean values of individual animals between conditions. Black dots represent the weighted average and the black line represents the SEM. A hypothesis test between GLMMs revealed no significant differences between subregions (p = 0.1072) or conditions (p = 0.183).*

Conclusion

Intensity measurements of Munc13-1 in area CA3 of the hippocampus revealed weaker Munc13-1 intensities in area CA3a than in area CA3c. A thorough comparison between subregions in CA3 and two different incubation times (15 and 60 minutes) gave no evidence for an intensity difference for Munc13-1 after chemical potentiation of mossy fiber boutons. However, I noticed that the ROIs retrieved during the analysis from the ZnT-3 signal were on average larger after forskolin treatment, although the total area of the immunohistological signal did not change. This observation could indicate a redistribution of ZnT-3 within the mossy fiber bouton after chemical potentiation, as it has been shown before: Vesicles in the mossy fiber boutons decluster after forskolin treatment for 15 minutes (Orlando et al., 2021) and 60 minutes (unpublished observations by Andrea Sannio).

Presynaptic Plasticity in Mossy Fibers Lacking Synapsins

Mossy fiber boutons do not only differ functionally from other central synapses but partly also in their molecular composition. One example for this is synapsin III, which is downregulated early in development in most synapses (Kao et al., 1998; Ferreira et al., 2000), but present in mossy fiber boutons of adult animals (Pieribone et al., 2002).

Synapsins are a family of phosphoproteins present in presynaptic terminals of neurons and are associated with synaptic vesicles (De Camilli et al., 1990; Cesca et al., 2010). They are thought to organize and maintain vesicle pools and thus control availability of synaptic vesicles during transmission and plasticity (Sansevrino et al., 2023). Despite the expression of synapsin III in mossy fiber boutons, presynaptic plasticity at this synapse has only been investigated in mice lacking synapsin I (Takei et al., 1995) or in synapsin I and synapsin II double knockout (SynDKO) animals (Spillane et al., 1995; Owe et al., 2009). Frequency facilitation was described to be lower in SynDKO animals (Owe et al., 2009) while long-term potentiation was unchanged (Spillane et al., 1995; Takei et al., 1995).

Here, we hypothesized that synapsin III plays a crucial role in various forms of presynaptic plasticity at the hippocampal mossy fiber bouton. We investigated our hypothesis in animals lacking all synapsin isoforms, including synapsin III: SynapsinI/synapsinII/synapsinIII triple knockout (SynTKO) animals. Because synapsin knockout animals involving synapsin I and/or II become epileptic in the age of approximately 8 weeks (Fassio et al., 2011; Ketzef et al., 2011), we chose to investigate the SynTKO animals at two different time points: one before and one after the onset of epileptic seizures.

We performed electrophysiological field recordings in acute mouse brain slices from male SynTKO and age-matched wildtype (WT) animals in two age groups. 4-6 weeks old mice are referred to as presymptomatic, and 17-19 weeks old mice are referred to as symptomatic. To record mossy fiber field potentials, we stimulated in the hilus of the dentate gyrus and recorded in the *stratum lucidum* of area CA3 of the hippocampus (Figure 12).

Excitability

SynTKO animals have been shown to have high network excitability and to develop an epileptic phenotype over time (Gitler et al., 2004; Fassio et al., 2011). We wanted to assess the excitability of mossy fibers lacking synapsins and performed input-output measurements in the beginning of the field recordings. We varied the stimulation strength to obtain different presynaptic fiber volley (PFV) sizes which indicate how many fibers are stimulated. We plotted the size of the PFV against the corresponding amplitude of the field excitatory postsynaptic potential (fEPSP) to see if the relation between the input (amount of stimulated mossy fibers) to the output (fEPSP in the area CA3) was different between genotypes and age groups (Figure 39).

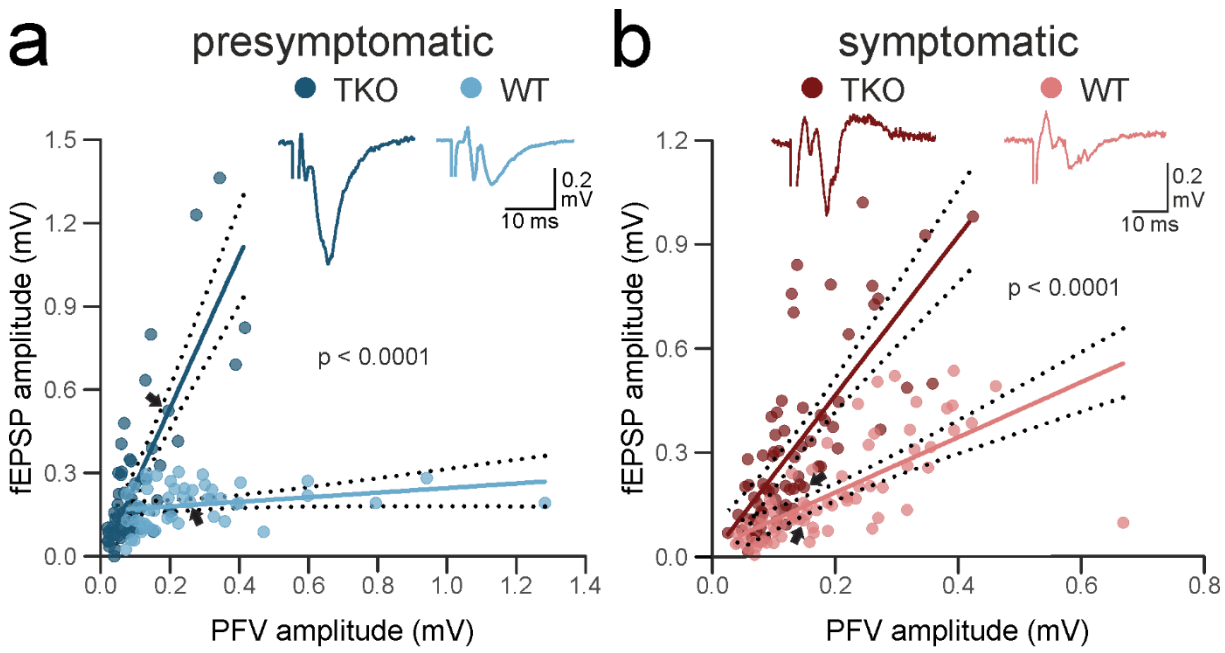

Figure 39: Excitability was increased in SynTKO animals in both age groups. a) *Averaged fEPSP amplitudes (mV) were plotted against averaged presynaptic fiber volley (PFV) amplitudes (mV) for presymptomatic SynTKO animals (dark blue) and age-matched controls (light blue). Straight lines show the linear regression fits, dotted lines show the 95 % confidence bands for the fits. Slopes of the linear regressions were compared in a two-tailed ANCOVA and were significantly different with p < 0.0001.* ***Inset at the top:*** *Averaged example traces from SynTKO (dark blue) and WT (light blue) animals. Note the larger fEPSP amplitude for SynTKO animals when the PFV size is similar to WT. Black arrows indicate the data points referring to the example traces.* ***b)*** *Averaged fEPSP amplitudes (mV) were plotted against averaged PFV amplitudes (mV) for symptomatic SynTKO animals (dark red) and age-matched controls (dusky pink). Straight lines show the linear regression fits, dotted lines show the 95 % confidence bands for the fits. Slopes of the linear regressions were compared in a two-tailed ANCOVA and were significantly different with p < 0.0001.* ***Inset at the top:*** *Example traces from SynTKO (dark red) and WT (dusky pink) animals. Note the larger fEPSP amplitude for SynTKO animals when the PFV size is similar to WT. Black arrows indicate the data points referring to the example traces.*

We found that the excitability was higher in slices from SynTKO animals compared to WT animals (Figure 39). Data points representing corresponding PFV and fEPSP sizes were fitted with a simple linear regression and the slopes of the regression were compared between genotypes. For presymptomatic recordings the slopes and 95 % confidence intervals were 0.083 [0.005 – 0.171] for WT recordings. The slope of the SynTKO regression was substantially steeper with 2.743 [2.159 – 3.326] (Figure 39a). In symptomatic recordings the relation was similar: the slope from WT recordings was 0.795 [0.59 – 0.99] while it was 2.292 [1.806 – 2.777] in the SynTKO recordings (Figure 39b). Slopes were tested with an ANCOVA and were significantly different between genotypes for both age groups ($p < 0.0001$, respectively). With a similar PFV amplitude the fEPSP was bigger for the SynTKO animals than for controls, indicating a higher excitability in CA3 in the knockout animals.

Paired-pulse Facilitation

There are many possible reasons for an increase in excitability like changes in recurrent connectivity (Nadler, 2003), the age of the granule cells giving rise to the mossy fibers (Lopez-Rojas and Kreutz, 2016), the molecular composition of pre- and postsynaptic partners or changes in the quantal parameters of neurotransmission (Redman, 1990), including the release probability.

A measure, which gives an indication for a possible change in release probability is paired-pulse facilitation (Dobrunz and Stevens, 1997). We recorded paired-pulse facilitation with an inter-stimulus interval (ISI) of 50 ms in both genotypes and age groups. Furthermore, we also measured the first two fEPSP amplitudes of a high-frequency train at 25 Hz, which corresponds to an ISI of 40 ms. With shortening of the ISI the paired-pulse facilitation in mossy fibers should become stronger (Salin et al., 1996b).

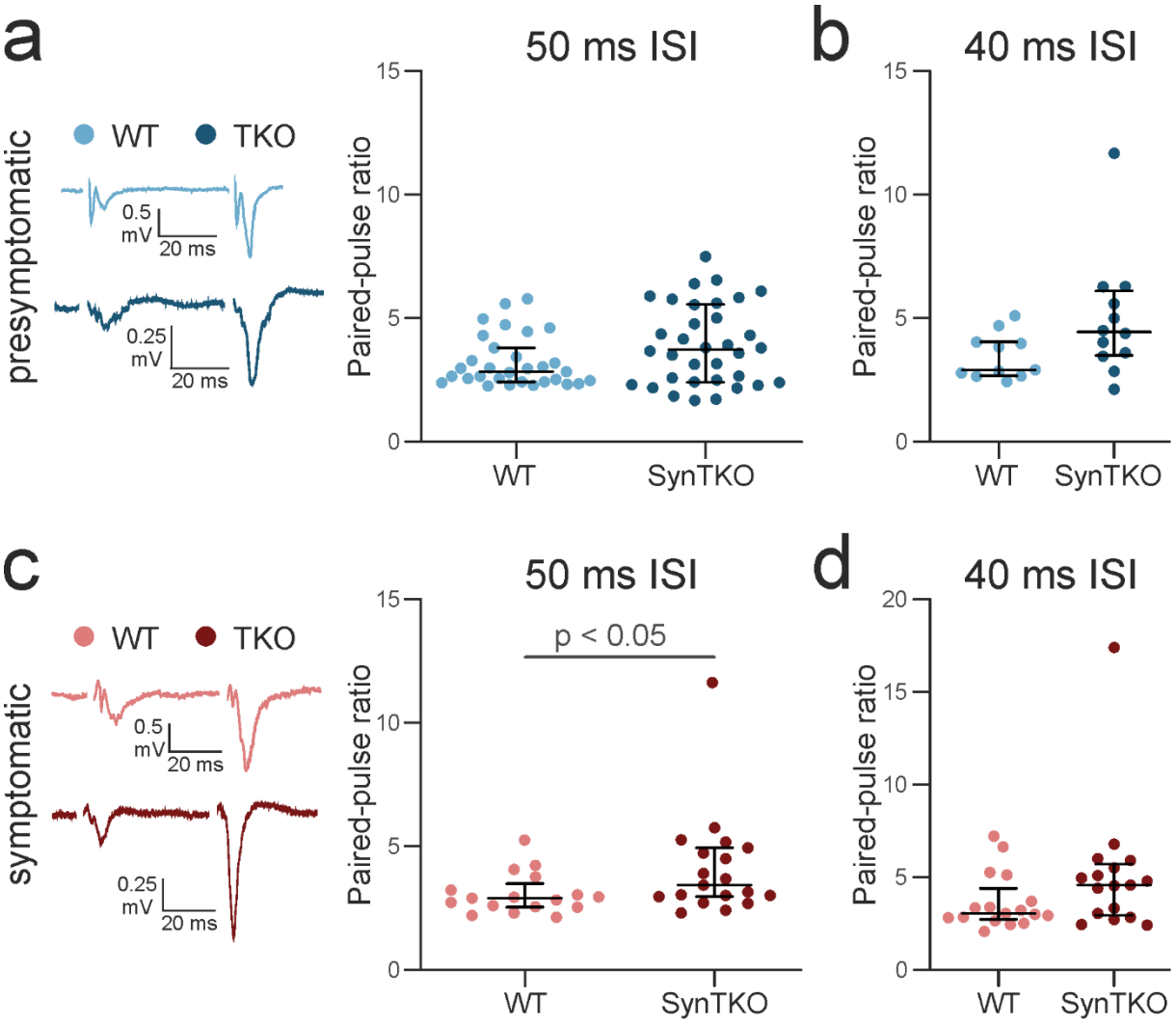

Figure 40: The paired-pulse ratio was slightly increased in symptomatic SynTKO animals. a) *Paired-pulse ratios were unchanged in presymptomatic SynTKO compared to age-matched WT controls.* ***Left:*** *Example traces from WT (top, light blue) and SynTKO (bottom, dark blue) animals showing fEPSPs in response to a paired-pulse with an inter-stimulus interval (ISI) of 50 ms. Stimulation artefacts were removed from traces for clarity.* ***Right:*** *Paired-pulse ratios for all individual WT and SynTKO recordings with an ISI of 50 ms. Ranks were not significantly different between genotypes ($p > 0.05$, Mann-Whitney U test). Black lines and error bars correspond to median values and interquartile ranges.* ***b)*** *Paired-pulse ratios from individual WT and SynTKO recordings of the presymptomatic age group with an ISI of 40 ms. Ranks were not significantly different ($p > 0.05$) between genotypes (Mann-Whitney U test). Note that there is a trend for an increased paired-pulse ratio in SynTKO animals. Black lines and error bars correspond to median values and interquartile ranges.* ***c)*** *Paired-pulse ratios were slightly increased in symptomatic SynTKO compared to age-matched WT controls.* ***Left:*** *Example traces from WT (top, dusky pink) and SynTKO (bottom, dark red) animals showing fEPSPs in response to a paired-pulse with an ISI of 50 ms. Stimulation artefacts were removed from traces for clarity.* ***Right:*** *Paired-pulse ratios for all individual WT and SynTKO recordings with an ISI of 50 ms. Ranks were significantly different between genotypes ($p < 0.05$, Mann-Whitney U test). Black lines and error bars correspond to median values and interquartile ranges.* ***d)*** *Paired-pulse ratios from individual WT and SynTKO recordings of the symptomatic age group with an ISI of 40 ms. Ranks were not significantly different ($p > 0.05$) between genotypes (Mann-Whitney U test). Note that there is a trend for an increased paired-pulse ratio in SynTKO animals. Black lines and error bars correspond to median values and interquartile ranges.*

For presymptomatic animals we found no significant changes in the paired-pulse ratio (PPR). With an ISI of 50 ms we found the median ratio and interquartile range for WT animals to be 2.827 [2.423; 3.795] while it was 3.745 [2.422; 5.570] for SynTKO animals ($p > 0.1$, Mann-Whitney *U* test) (Figure 40a). With shortening of the ISI to 40 ms, the median PPR values were higher in both genotypes (Figure 40b), but not significantly different ($p = 0.068$, Mann-Whitney *U* test). WT animals had a median PPR of 2.91 [2.654; 4.026] while the PPR in SynTKO animals was 4.436 [3.485; 6.094].

In symptomatic animals, the PPR values were slightly increased in SynTKO compared to WT animals with an ISI of 50 ms (Figure 40c). In WT animals the median value was 2.906 [2.549; 3.499] and in SynTKO animals it was 3.435 [2.964; 4.944] ($p = 0.03$, Mann-Whitney *U* test). With shortening of the ISI to 40 ms we again detected an increase in the PPR for both genotypes compared to 50 ms ISI, with a median of 3.045 [2.731; 4.413] for WT and 4.571 [2.945; 5.706] for SynTKO animals (Figure 40d). However, ranks were not significantly different in a Mann-Whitney *U* test ($p = 0.16$).

These mixed results already suggest that the interpretation of the PPR as an indicator for presynaptic release is difficult. Indeed, when recorded via field potentials, many confounders can influence this particular measurement and should be treated with caution (Hanse and Gustafsson, 2001; Sun et al., 2005; Glasgow et al., 2019). In general, the PPR seems to be increased in SynTKO, although this trend is not statistically significant in most cases. An increased PPR would rather indicate a decreased release probability and would therefore not explain the increased excitability.

Frequency Facilitation

Mossy fibers are very plastic when it comes to changes in presynaptic activity patterns (Salin et al., 1996b). Usually, granule cells are characterized by a low firing rate leading to low activity in mossy fibers at rest (Jung and McNaughton, 1993). However, increased firing frequencies – for example switching from 0.05 Hz to 1 Hz stimulation – can lead to massive changes in the release at the mossy fiber bouton (Salin et al., 1996b), for example during frequency facilitation.

Previous work showed that frequency facilitation in mossy fibers was impaired in SynDKO animals (Owe et al., 2009). The authors speculated that the remaining synapsin III isoform could lead to this reduced facilitation, based on two reasons: First, SynIII was shown to be located in the readily-releasable pool, close to the membrane (Owe et al., 2009). Second, neurons from animals lacking SynIII showed less synaptic depression than WT neurons (Feng et al., 2002). Here, we wanted to investigate if the complete absence of synapsins would change the time course of facilitation. We stimulated mossy fibers at 0.05 Hz for baseline recordings and increased the stimulation rate to 1 Hz for 20 s.

We found that SynTKO animals showed reduced frequency facilitation compared to their age-matched controls (Figure 41). This effect was stronger in symptomatic animals (Figure 41c and d). In both presymptomatic and symptomatic SynTKO recordings the time course of facilitation was altered: the fEPSP amplitudes were increasing with number of stimulations but reached a plateau more quickly than in the respective control recordings (Figure 41a and c).

When tested in a mixed-effects model, both presymptomatic and symptomatic frequency facilitation data were significantly different for the factor stimulus number ($p < 0.0001$) and the interaction between stimulus number and genotype ($p < 0.001$ for presymptomatic and $p < 0.0001$ for symptomatic), but not for the factor genotype ($p > 0.05$). A post-hoc Sidak's test for multiple comparisons revealed no significant differences for single time points for the presymptomatic data ($p > 0.05$), but significant differences for two single time points in the symptomatic data ($p < 0.05$).

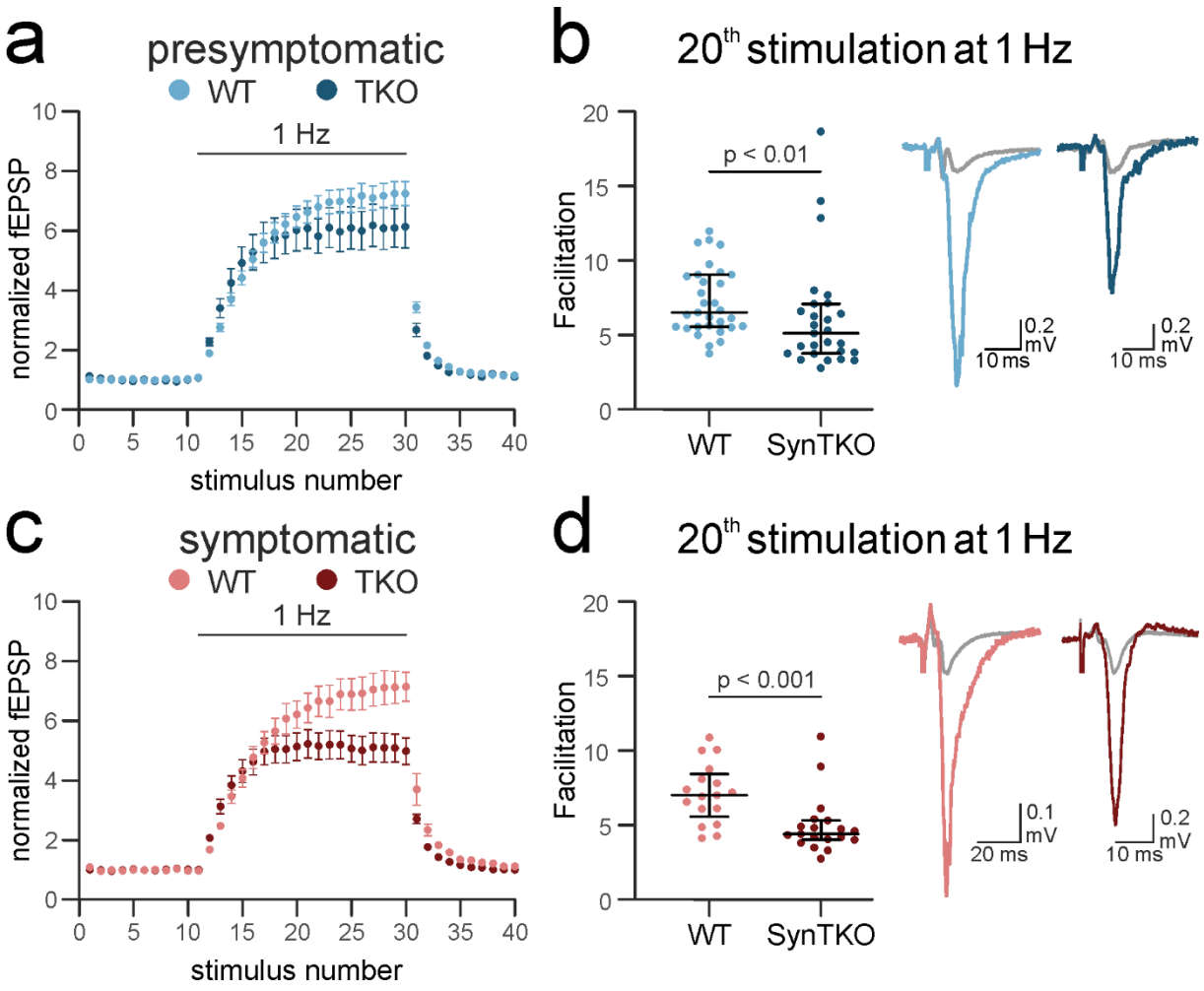

Figure 41: Frequency facilitation is reduced in SynTKO animals in both age groups. a) *The time-course of facilitation was altered in presymptomatic SynTKO animals. Averaged normalized fEPSP amplitudes from presymptomatic SynTKO animals (dark blue) and age-matched controls (light blue) before, during and after stimulation at a frequency of 1 Hz. Stimuli 1-10 were given at 0.05 Hz, stimuli 11-30 at 1 Hz and stimuli 31-40 at 0.05 Hz again. Data points refer to the mean of normalized amplitudes ± SEM of all SynTKO and WT recordings. When tested in a mixed-effects model, both time (stimulus number) and the interaction of time and genotype were significantly different ($p < 0.0001$ and $p < 0.001$). Post-hoc Sidak's test for multiple comparisons revealed no significant differences for single time points.* ***b)*** *Facilitation was reduced in presymptomatic SynTKO animals after 1 Hz stimulation.* ***Left:*** *The plot shows normalized fEPSP amplitudes from all individual WT and SynTKO recordings at the 20th stimulus at 1 Hz. Black lines indicate the median and interquartile ranges. Ranks were significantly different with $p < 0.01$ (Mann-Whitney U test).* ***Right:*** *Example fEPSP amplitudes at the 20th stimulus at 1 Hz for WT (left, light blue) and SynTKO (right, dark blue) recordings. Grey traces show the corresponding baseline before 1 Hz stimulation.* ***c)*** *The time-course of facilitation was altered in symptomatic SynTKO animals. Averaged normalized fEPSP amplitudes from symptomatic SynTKO animals (dark red) and age-matched controls (dusky pink) before, during and after stimulation at a frequency of 1 Hz. Stimuli 1-10 were given at 0.05 Hz, stimuli 11-30 at 1 Hz and stimuli 31-40 at 0.05 Hz again. Data points show the mean of normalized amplitudes ± SEM of all SynTKO and WT recordings. When tested in a mixed-effects model, both time (stimulus number) and the interaction of time and genotype were significantly different ($p < 0.0001$). Post-hoc Sidak's test for multiple comparisons revealed significant differences ($p < 0.05$) for two time points.* ***d)*** *Facilitation was reduced in symptomatic SynTKO animals after 1 Hz stimulation.* ***Left:*** *The plot shows normalized fEPSP amplitudes from all individual WT and SynTKO recordings at the 20th stimulation at 1 Hz. Black lines indicate the median and*

interquartile ranges. Ranks were significantly different with $p < 0.001$ (Mann-Whitney U test). ***Right:*** *Example fEPSP amplitudes at the 20th stimulus at 1 Hz for WT (left, dusky pink) and SynTKO (right, dark red) recordings. Grey traces show the corresponding baseline before 1 Hz stimulation.*

To quantify facilitation, we plotted the normalized fEPSP at the last (20th) stimulus at 20 Hz for both genotypes and age groups (Figure 41b and d). The same effect was visible in both age groups: Facilitation was reduced in SynTKO animals. Presymptomatic WT animals had a median [interquartile range] facilitation of 6.52 [5.553; 9.047] while it was only 5.110 [3.760; 7.080] for SynTKO animals. In symptomatic animals, these differences were stronger. In WT animals, facilitation reached 7.019 [5.574; 8.440] while it was only 4.414 [4.036; 5.330] in SynTKO recordings. Ranks were significantly different between SynTKO and WT animals in a Mann-Whitney U test for both presymptomatic ($p < 0.01$) and symptomatic ($p < 0.001$) animals.

Together, these data demonstrate that facilitation is also impaired in the complete absence of synapsins. This could indicate that the reduced facilitation seen by Owe et al. in SynDKO animals (Owe et al., 2009) is caused rather by the absence of synapsin I and II than by the presence of synapsin III.

High-frequency Stimulation

The reduction in frequency facilitation (Figure 41) could be explained by earlier depletion of synaptic vesicle pools in SynTKO animals. To explore this hypothesis further, we stimulated mossy fibers at higher frequencies with four consecutive trains of 125 pulses at 25 Hz. Over the course of the 125 pulses, mossy fiber fEPSP amplitudes from WT animals showed first an increase and then a decrease, until they reached a steady-state (Figure 42a, light blue traces and data points and Figure 43a dusky pink traces and data points). This course is typical for synapses with a low release probability (Dobrunz and Stevens, 1997) and can be explained by successive facilitation and vesicle store depletion, up to a steady state in which the release equals the vesicle recycling rate.

In our recordings, we observed an earlier and stronger decrease in the normalized fEPSPs in SynTKO animals. In presymptomatic animals, the time-course of normalized fEPSP amplitudes in the first stimulation train was still similar to that of WT animals (Figure 42a). However, in the fourth stimulation train the fEPSP amplitudes were smaller for SynTKO animals in the second half of the train (Figure 42b). When tested in a mixed-effects model the factor time (stimulus number) was significantly different for both the first and fourth stimulation train ($p < 0.0001$). A post-hoc Sidak's test for multiple comparisons revealed no significant differences for single time points.

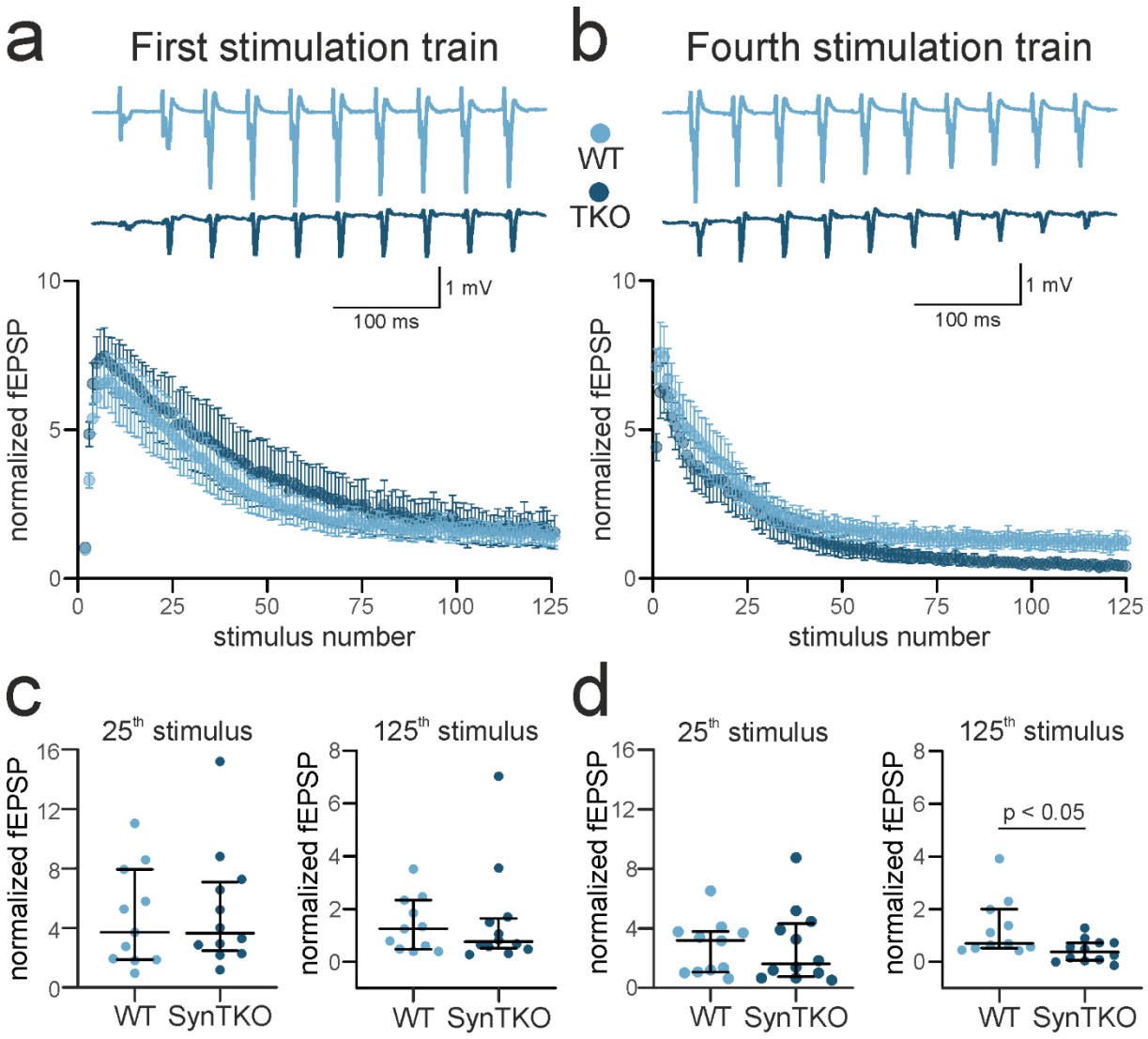

Figure 42: High-frequency stimulation leads to stronger depression in presymptomatic SynTKO animals. a) *Similar time-course of depression in the first high-frequency stimulation train between genotypes.* ***Top:*** *Example traces showing normalized fEPSP amplitudes in response to the first 10 stimuli of the first high-frequency stimulation train for WT (top, light blue) and SynTKO (bottom, dark blue) animals.* ***Bottom:*** *Averaged normalized fEPSP amplitudes plotted against the number of stimuli at 25 Hz for the first of four consecutive stimulation trains for WT (light blue) and SynTKO (dark blue) recordings. Data points and error bars represent mean ± SEM. When tested in a mixed-effects model, there was a significant difference ($p < 0.0001$) for the factor time (stimulus number). A post-hoc Sidak's test for multiple comparisons revealed no significant differences for single time points.* ***b)*** *Stronger depression for presymptomatic SynTKO animals in the last high-frequency stimulation train.* ***Top:*** *Example traces showing normalized fEPSP amplitudes in response to the first 10 stimuli of the last high-frequency stimulation train for WT (top, light blue) and SynTKO (bottom, dark blue) animals.* ***Bottom:*** *Averaged normalized fEPSP amplitudes plotted against the number of stimuli at 25 Hz for the last of four consecutive stimulation trains for WT (light blue) and SynTKO (dark blue) recordings. Data points and error bars show mean ± SEM. When tested in a mixed-effects model, there was a significant difference ($p < 0.0001$) for the factor time (stimulus number). A post-hoc Sidak's test for multiple comparisons revealed no significant differences for single time points.* ***c)*** *Normalized fEPSP amplitudes at the 25th and 125th stimulus of the first stimulation train for individual WT and SynTKO recordings. Median values ± interquartile ranges are shown in black. Ranks were not significantly different for either 25th*

or 125th stimulus (p > 0.05, Mann-Whitney U *test).* ***d)*** *Normalized fEPSP amplitudes at the 25th and 125th stimulus of the fourth stimulation train for individual WT and SynTKO recordings. Median values ± interquartile ranges are shown in black. Ranks were significantly different at the 125th stimulus (p < 0.05, Mann-Whitney* U *test), but not at the 25th stimulus (p > 0.05, Mann-Whitney* U *test).*

We also compared fEPSP amplitudes at different time points within the trains. In the first stimulation train, median normalized fEPSP amplitudes were similar between genotypes. At the 25th stimulus it was 3.704 [1.873; 7.935] for WT and 3.653 [2.426; 7.092] for SynTKO animals (p = 0.695, Mann-Whitney *U* test). At the last (125th) stimulus of the first train, the median normalized fEPSP amplitude from WT recordings was 1.243 [0.473; 2.332] while it was 0.7514 [0.4997; 1.650] for SynTKO animals (p = 0.74, Mann-Whitney *U* test). In comparison, in the last stimulation train at the 25th stimulus the median fEPSPs were reduced for both genotypes to 3.176 [1.039; 3.77] for WT and 1.61 [0.75; 4.314] for SynTKO (p = 0.88, Mann-Whitney *U* test). At the last (125th) stimulus of the fourth stimulation ranks were significantly different between genotypes with median fEPSPs at 0.687 [0.5; 1.987] for WT and 0.3714 [0.0489; 0.7202] for SynTKO animals (p < 0.05, Mann-Whitney *U* test).

In symptomatic animals we also compared normalized fEPSP amplitudes at single time points in the stimulation trains. Here, ranks were significantly different between genotypes for all time points analyzed. In the first train at the 25th stimulus the median fEPSP amplitude was 4.724 [2.423; 7.687] for WT and 1.784 [1.213; 3.349] for SynTKO (p < 0.01, Mann-Whitney *U* test). At the first train's last stimulus (125th) it was 1.424 [0.6992; 2.167] for WT and 0.3162 [0.2169; 0.6108] for SynTKO recordings (p < 0.0001, Mann-Whitney *U* test). In the last stimulation train, fEPSP amplitudes from SynTKO animals were almost not existent any more. Already at the 25th stimulus the median fEPSP amplitude was only 0.4776 [0.2902; 0.9721] for SynTKO while it was 3.051 [1.941; 4.963] for WT (p < 0.0001, Mann-Whitney *U* test). At the last stimulus of that train the remaining normalized fEPSP amplitude was 0.1155 [0.0396; 0.1511] for SynTKO recordings while it was still 1.208 [0.6936; 1.91] for WT (p < 0.0001, Mann-Whitney *U* test).

We checked for stability in PFV sizes during the high frequency stimulation to exclude that a stronger decrease in the PFV of knockout animals – suggestive of a loss of stimulated fibers – caused the stronger reduction in fEPSP amplitudes. The size of PFV reduced slightly during the high-frequency stimulation, but to the same extent in both genotypes (data not shown). Thus, we can likely exclude a larger relative change in the number of stimulated fibers as the reason for stronger fEPSP depression in SynTKO animals. In summary, high-frequency stimulation led to an earlier and stronger reduction of fEPSP amplitudes in SynTKO animals, indicating a faster exhaustion of available vesicles for release in the knockout.

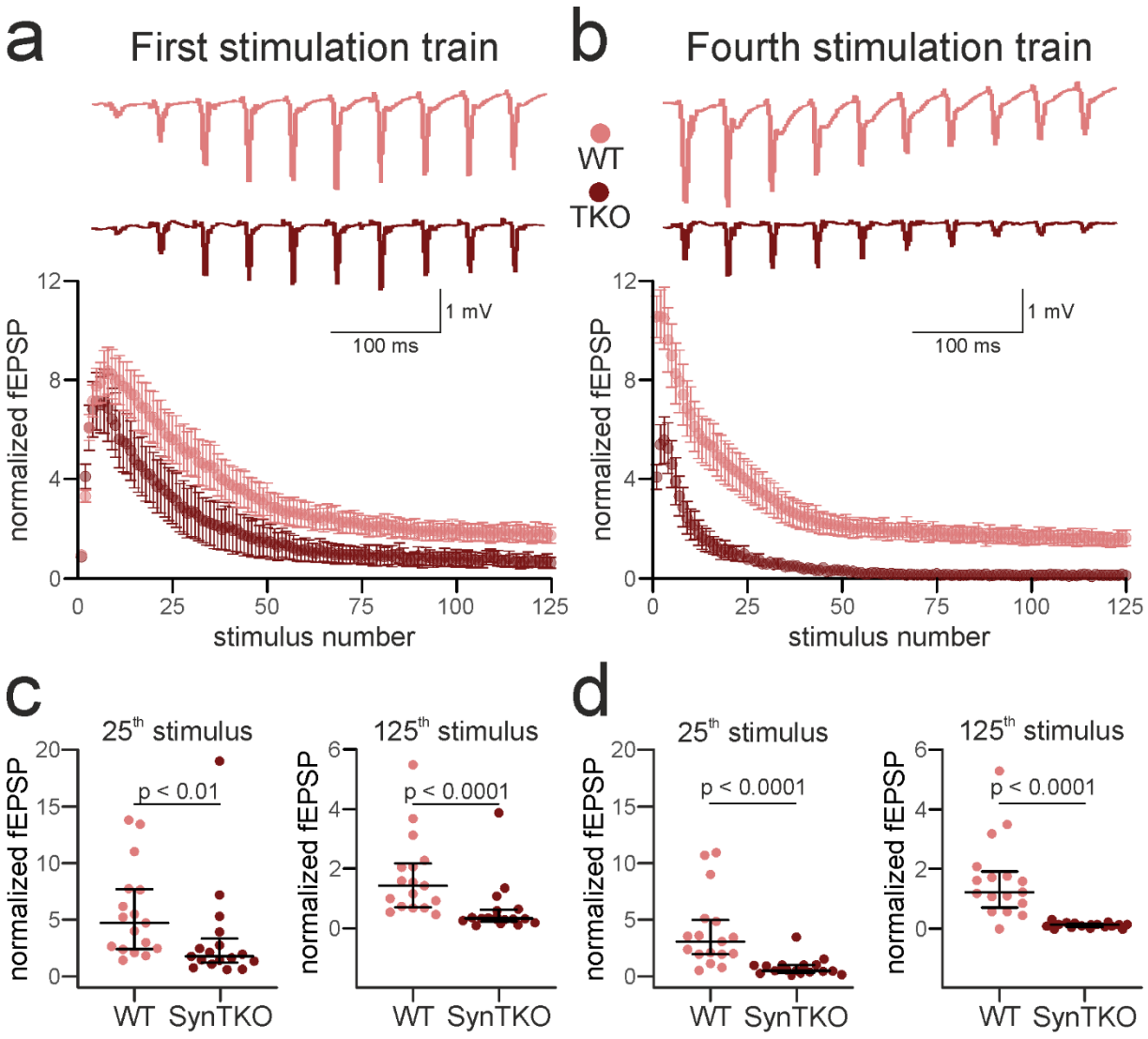

Figure 43: High-frequency stimulation leads to stronger depression in symptomatic SynTKO animals. a) *Stronger depression of symptomatic SynTKO animals is already visible in the first high-frequency stimulation train.* ***Top:*** *Example traces showing normalized fEPSP amplitudes in response to the first 10 stimuli of the first high-frequency stimulation train for WT (top, dusky pink) and SynTKO (bottom, dark red) animals.* ***Bottom:*** *Averaged normalized fEPSP amplitudes plotted against the number of stimuli at 25 Hz for the first of four consecutive stimulation trains for WT (dusky pink) and SynTKO (dark red) recordings. Data points and error bars represent mean ± SEM. When tested in a mixed-effects model, there was no significant difference between genotypes ($p > 0.05$) but significant differences ($p < 0.0001$) for the factor time (stimulus number) and the interaction of time and genotype ($p < 0.001$). A post-hoc Sidak's test for multiple comparisons revealed no significant differences for single time points.* ***b)*** *Stronger depression for symptomatic SynTKO animals in the last high-frequency stimulation train.* ***Top:*** *Example traces showing normalized fEPSP amplitudes in response to the first 10 stimuli of the fourth high-frequency stimulation train for WT (top, dusky pink) and SynTKO (bottom, dark red) animals.* ***Bottom:*** *Averaged normalized fEPSP amplitudes plotted against the number of stimuli at 25 Hz for the last of four consecutive stimulation trains for WT (dusky pink) and SynTKO (dark red) recordings. Data points and error bars show mean ± SEM. When tested in a mixed-effects model, there were significant differences for the factors time (stimulus number), genotype and the interaction of both ($p < 0.0001$, $p = 0.0001$, $p < 0.0001$, respectively). A post-hoc Sidak's test for multiple comparisons revealed significant differences for single time points.* ***c)*** *Normalized fEPSP amplitudes at the 25th and 125th stimulus*

of the first stimulation train for individual WT and SynTKO recordings. Median values ± interquartile ranges are shown in black. Ranks were significantly different for both 25th and 125th stimulus ($p < 0.01$ and $p < 0.0001$, Mann-Whitney U test). ***d)*** *Normalized fEPSP amplitudes at the 25th and 125th stimulus of the fourth stimulation train for individual WT and SynTKO recordings. Median values ± interquartile ranges are shown in black. Ranks were significantly different at both the 25th and 125th stimulus ($p < 0.0001$, Mann-Whitney U test).*

Post-tetanic Potentiation

Recently, it was suggested that post-tetanic potentiation (PTP) is underlying short-term memory by creating a pool-engram of synaptic vesicles close to the active zone of mossy fiber boutons (Vandael et al., 2020). The authors discussed a likely role for synapsins in the creation of this pool engram by mediating synaptic vesicles from the distal pools into the readily-release pool. To test this possibility, we recorded PTP after four consecutive stimulation trains consisting of 125 pulses given at 25 Hz in both presymptomatic and symptomatic SynTKO as well as their age-matched controls.

In fact, as suggested by Vandael et al., we saw a decreased normalized fEPSP amplitude in both age groups at the first stimulus after induction, indicating reduced vesicles available for release. In presymptomatic animals, the size of fEPSPs increased in the following stimuli and were at the same level as WT amplitudes at the third stimulus again (Figure 44a). Afterwards, the fEPSP amplitudes of SynTKO exceeded the ones from WT animals and stayed on a plateau, while the amplitudes in WT recordings decreased further. In symptomatic animals, the fEPSP amplitudes from SynTKO animals were also increasing after the initial drop in PTP. However, here the amplitudes reached the same level as WT amplitudes only after 10 stimuli and stayed at the same level as WT amplitudes from that time point onwards. Since these time courses are the initial part of longer LTP recordings, the respective statistics are going to be reported in the next subchapter.

Comparing the normalized fEPSP amplitudes at three time points of the PTP revealed differences between genotypes and age groups (Figure 44c and d). A Kruskal-Wallis test revealed significant differences in presymptomatic recordings between genotypes ($p < 0.0001$). The median fEPSP amplitude at the first pulse after induction was significantly smaller in SynTKO animals: It was 3.702 [2.683; 5.28] for SynTKO animals while it was 7.229 [5.701; 8.464] in WT ($p < 0.001$, post-hoc Dunn's test). At the third pulse, amplitudes were comparable between genotypes with a median of 4.887 [3.796; 6.419] for SynTKO and 5.323 [4.07; 6.03] for WT ($p > 0.99$, Dunn's test). However, at the tenth pulse, the median fEPSP amplitude was bigger in SynTKO (4.865 [3.635; 6.497]) than in WT (2.749 [2.432; 3.321]) ($p < 0.001$, Dunn's test) (Figure 44c).

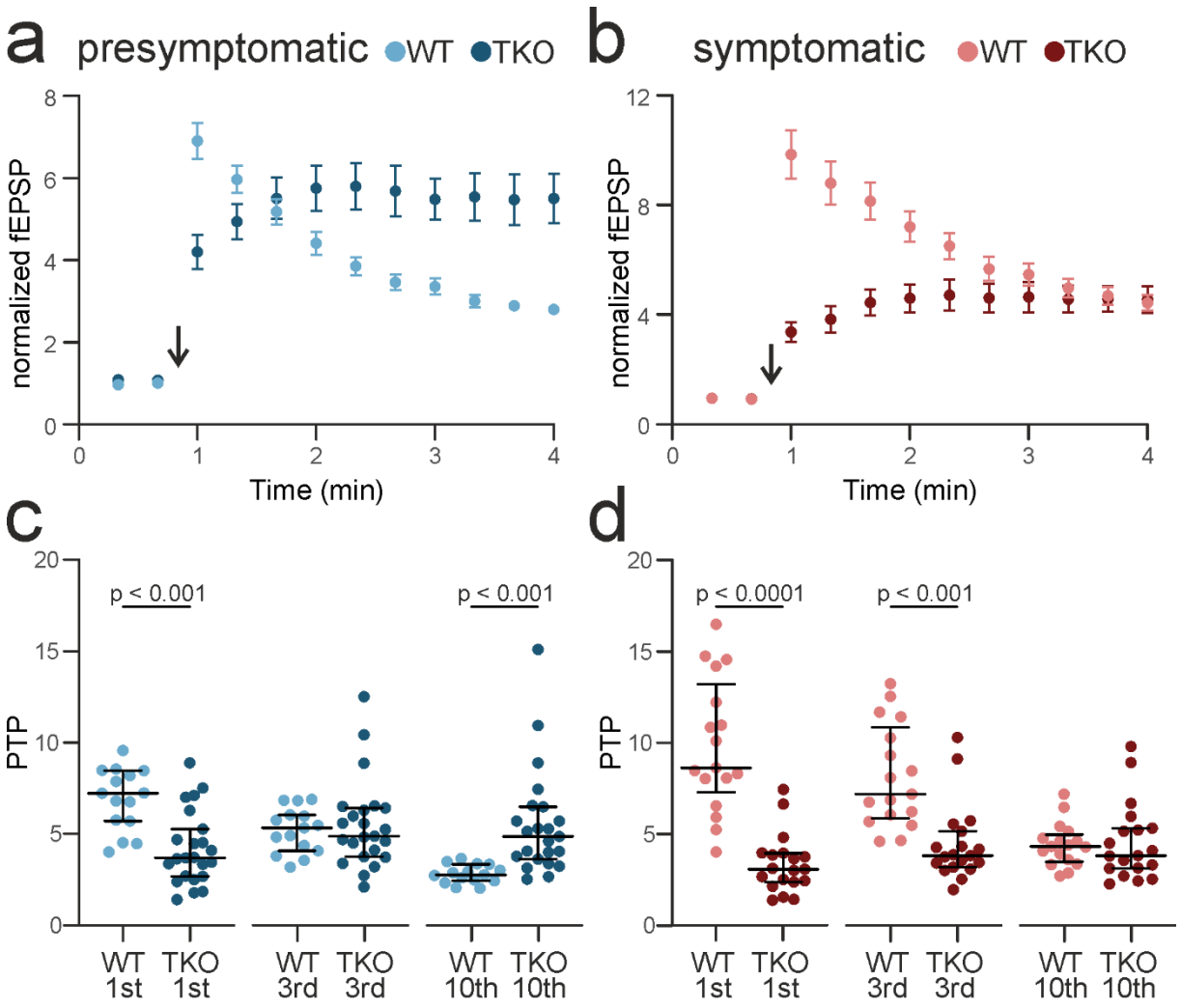

Figure 44: Post-tetanic potentiation is reduced in SynTKO animals in both age-groups. a) *In presymptomatic SynTKO animals early PTP is reduced while the second phase of PTP is increased compared to age-matched WT animals. Averaged normalized fEPSPs of WT (light blue) and SynTKO animals (dark blue) are plotted against time. The black arrow indicates the time point of the high-frequency stimulation to induce potentiation (4 x 125 pulses at 25 Hz). This figure is a partial zoom in from the plot shown in Figure 33a. Data points and error bars show mean values ± SEM. Statistics are reported in Figure 33a.* ***b)*** *In symptomatic SynTKO animals early PTP is reduced compared to age-matched WT animals, but in a second phase the normalized amplitudes become alike with the amplitudes from WT animals. Averaged normalized fEPSPs of WT (dusky pink) and SynTKO animals (dark red) are plotted against time. The black arrow indicates the time point of the high-frequency stimulation to induce potentiation (4 x 125 pulses at 25 Hz). This figure is a partial zoom in from the plot shown in Figure 33c. Data points and error bars show mean values ± SEM. Statistics are reported in Figure 33c.* ***c)*** *Normalized post-tetanic potentiation (PTP) for individual recordings of WT and SynTKO animals of the presymptomatic age group at three different time points after high-frequency stimulation. At the first stimulus after the tetanus PTP is reduced in SynTKO, at the third stimulus it is at the same level as PTP from WT animals and at the tenth stimulus it is bigger than WT levels. Black lines indicate median values and interquartile ranges. Median values were significantly different ($p < 0.0001$) in a Kruskal-Wallis test. A post-hoc Dunn's test for multiple comparisons revealed significant differences for the first and tenth stimulus after high-frequency stimulation ($p < 0.001$ and $p = 0.001$), but no significant difference for the third stimulus ($p > 0.99$).* ***d)*** *Normalized post-tetanic potentiation (PTP) for individual recordings of WT and SynTKO animals of the symptomatic age group at three different time points after high-frequency stimulation. At the first and third stimulus*

after the tetanus PTP is reduced in SynTKO compared to WT recordings, but at the tenth stimulus it is at the same PTP level as for WT animals again. Black lines indicate median values and interquartile ranges. Median values were significantly different ($p < 0.0001$) in a Kruskal-Wallis test. A post-hoc Dunn's test for multiple comparisons revealed significant differences for the first and third stimulus after high-frequency stimulation ($p < 0.0001$ and $p < 0.001$), but no significant difference for the tenth stimulus ($p > 0.99$).

In symptomatic animals the Kruskal-Wallis test showed also significant differences for the three time points ($p < 0.0001$). At the first pulse after induction the fEPSP was significantly smaller in SynTKO recordings compared to WT with a median of 3.073 [2.386; 3.947] for SynTKO and 8.625 [7.288; 13.21] for WT ($p < 0.0001$, post-hoc Dunn's test). At the third pulse the median normalized fEPSP amplitude of SynTKO animals was still smaller than that of WT animals with a median amplitude of 3.811 [3.192; 5.151] for SynTKO and 7.186 [5.868; 10.85] for WT recordings ($p < 0.001$, Dunn's test). However, at the 10^{th} stimulus, amplitudes were at the same level again. In SynTKO it was at 3.822 [3.132; 5.319] and in WT at 4.322 [3.479; 4.967] ($p > 0.99$, Dunn's test) (Figure 44d).

These data indicate that in SynTKO animals the mechanisms leading to PTP are impaired. Furthermore, in presymptomatic mice, the second phase of PTP is elevated compared to WT animals, while it is at the same levels in symptomatic animals and their WT controls. This might indicate a compensation of mechanisms leading to the overshoot in secondary PTP in presymptomatic animals after the onset of epileptic seizures. Together, our data suggest that two different mechanisms control the first and the later part of PTP and that the onset of epileptic seizures potentially changes network dynamics.

Long-term Potentiation

The NMDA-independent (Harris and Cotman, 1986), presynaptic form of long-term potentiation at the mossy fiber bouton is not yet fully understood. What is known to date is that a Ca^{2+}-dependent elevation of presynaptic cyclic adenosine monophosphate (cAMP) levels leads to the activation of protein kinase-A (PKA) and results in increased transmitter release (Weisskopf et al., 1994). The precise downstream targets of PKA or potential parallel cascades are not known yet, although many presynaptic molecules have already been investigated (Shahoha et al., 2022), including synapsins I and II (Spillane et al., 1995). In SynDKO animals, mossy fiber LTP was shown to be at WT levels (Spillane et al., 1995). Since mossy fibers also express SynIII (Pieribone et al., 2002) and synapsin III contains a PKA phosphorylation site (Piccini et al., 2015), it could be a potential downstream target in the LTP cascade, adjusting release during potentiation. Thus, we aimed to investigate if the complete loss of synapsins, including synapsin III, might lead to impaired mossy fiber LTP.

We recorded LTP for 30 minutes after induction (4 trains of 125 pulses at 25 Hz) in both presymptomatic and symptomatic SynTKO animals as well as their age-matched WT controls. In presymptomatic animals we saw that the effect of elevated fEPSP amplitudes observed in PTP (Figure 45) was continued throughout the LTP recording. From one minute to thirty minutes after induction, the normalized fEPSPs were larger in SynTKO than in WT recordings (Figure 45a). When tested in a mixed-effects model, the factors time and genotype as well as their interaction were significant ($p < 0.0001$, $p < 0.01$, $p < 0.0001$, respectively). A post-hoc Sidak's test revealed significant differences for single time points as well ($p < 0.05$). The magnitude of LTP was quantified at the end of the recording by averaging the fEPSP amplitudes of the last ten minutes. The median fEPSP [interquartile ranges] from all individual recordings was also here bigger for SynTKO animals (Figure 33b). It was 2.452 [1.982; 3.117] compared to 1.6 [1.3; 1.92] in WT animals ($p < 0.0001$, Mann-Whitney *U* test). At the end of each recording we applied DCG-IV, a mossy fiber specific metabotropic glutamate receptor 2/3 agonist (Kamiya et al., 1996). If the fEPSP amplitudes were inhibited by 75 % or more compared to baseline levels, it was categorized as mossy fiber-specific (Figure 45a and c).

In symptomatic animals the time course of SynTKO and WT fEPSP amplitudes was similar from the 10^{th} stimulus post-induction onwards, leading also to a similar magnitude of LTP in symptomatic SynTKO and age-matched WT animals (Figure 45c and d). When tested in a mixed-effects model, the factor time (stimulus number) as well as its interaction with genotype were significant ($p < 0.0001$, respectively), while the factor genotype was not ($p = 0.5$). A post-hoc Sidak's test revealed significant differences for single time points ($p < 0.05$). When comparing the level of LTP at the end of the recording, there was no significant difference between ranks of genotypes ($p = 0.22$, Mann-Whitney *U* test). The median fEPSP of WT was 2.326 [1.996; 2.623] while it was 2.044 [1.607; 2.414] for SynTKO animals.

In conclusion, there might be an effect in presymptomatic SynTKO animals leading to an overshoot in LTP, which is balanced out in older, symptomatic animals.

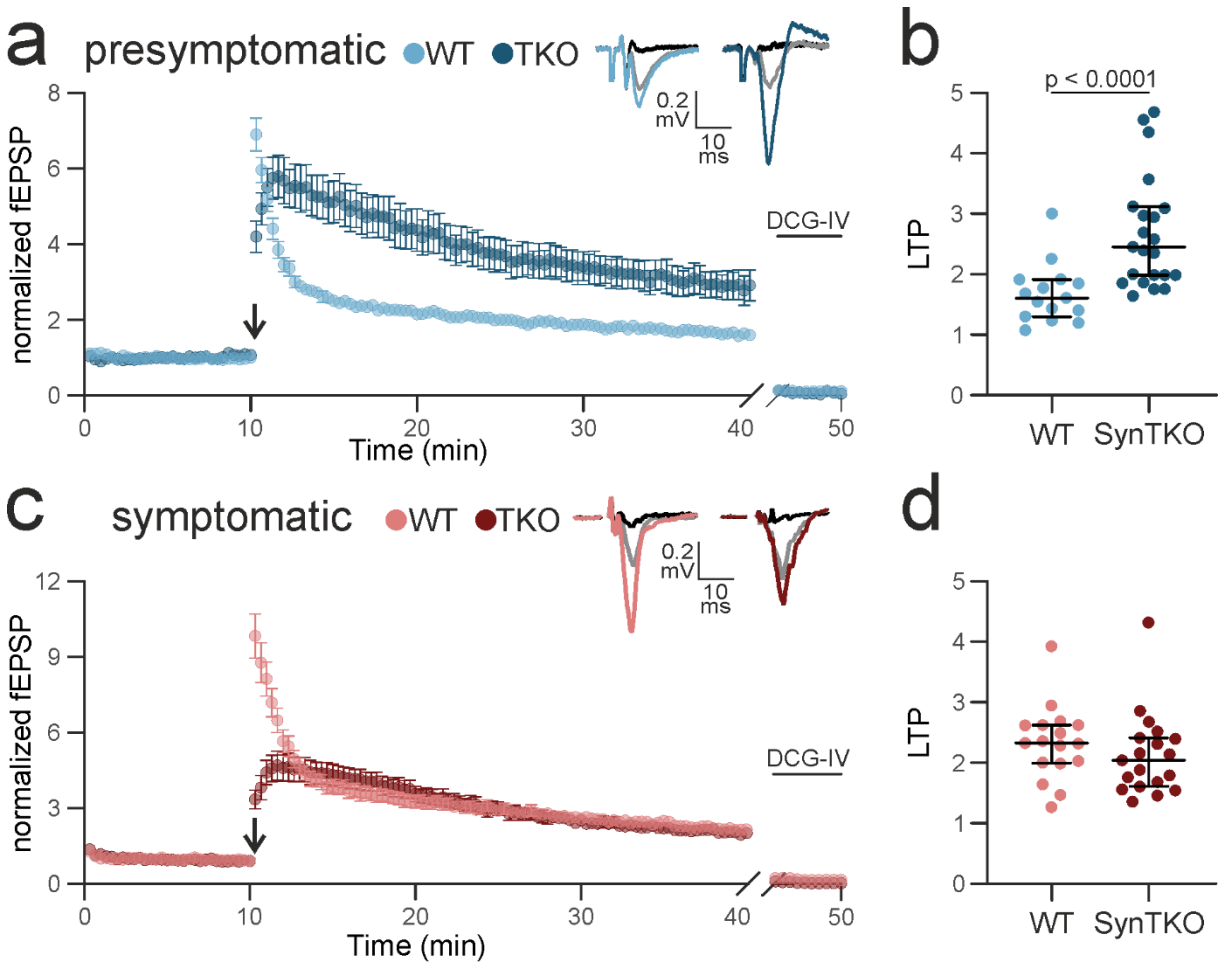

Figure 45: Long-term potentiation is elevated in presymptomatic but not symptomatic SynTKO animals. a) *Time course reveals elevated fEPSPs for presymptomatic SynTKO animals after high-frequency induction compared to age-matched controls. Averaged normalized fEPSP amplitudes are plotted against time for WT (light blue) and SynTKO (dark blue) animals. The black arrow shows the time point of high-frequency stimulation (4 x 125 pulses at 25 Hz) to induce potentiation. At the end of the recording, 1 µM DCG-IV is washed in to verify a mossy-fiber specific recording. Data points and error bars show mean values ± SEM. When tested in a mixed-effects analysis, there were significant differences for the factors time, genotype and the interaction of both ($p < 0.0001$, $p < 0.01$, $p < 0.0001$, respectively). A post-hoc Sidak's test for multiple comparisons revealed significant differences for single time points.* ***Inset on the top:*** *Example traces showing averaged fEPSP amplitudes after 30 minutes LTP recording for WT (left, light blue) and SynTKO (right, dark blue) animals. The grey traces show corresponding averaged baseline amplitudes and the black traces the signal after wash-in of DCG-IV, respectively.* ***b)*** *Long-term potentiation is increased in presymptomatic SynTKO compared to controls 30 minutes after high-frequency stimulation. Averaged level of LTP 20-30 minutes after induction from individual WT and SynTKO recordings. Black lines show median values and interquartile ranges. Ranks were significantly different between genotypes ($p < 0.0001$, Mann-Whitney* U *test).* ***c)*** *Adaptation of fEPSP amplitudes for symptomatic SynTKO animals compared to age-matched controls during the time course of LTP after initial drop in PTP. Averaged normalized fEPSP amplitudes are plotted against time for WT (dusky pink) and SynTKO (dark red) animals. The black arrow shows the time point of high-frequency stimulation (4 x 125 pulses at 25 Hz) to induce potentiation. At the end of the recording, 1 µM DCG-IV is washed in to verify a mossy-fiber specific recording. Data points and error bars show mean values ± SEM. When tested in a mixed-effects analysis, there were significant differences for the factors time, and the interaction of time and genotype ($p < 0.0001$, respectively), but not for the factor genotype ($p > 0.05$). A post-hoc Sidak's test for multiple comparisons revealed significant differences for*

single time points. ***Inset on the top:*** *Example traces showing averaged fEPSP amplitudes after 30 minutes LTP recording for WT (left, dusky pink) and SynTKO (right, dark red) animals. The grey traces show corresponding averaged baseline amplitudes and the black traces the signal after wash-in of DCG-IV, respectively.* ***d)*** *Long-term potentiation is unchanged between symptomatic SynTKO and WT animals 30 minutes after high-frequency stimulation. Averaged level of LTP 30 minutes after induction for individual WT and SynTKO recordings. Black lines show median values and interquartile ranges. Ranks were not significantly different between genotypes (p > 0.05, Mann-Whitney* U *test).*

Conclusion

In summary, we found that in mice lacking synapsins, hippocampal mossy fiber bouton transmission and presynaptic plasticity were changed. The input-output ratio was clearly enhanced in knockout animals, while 1 Hz facilitation was reduced with a stronger effect in symptomatic animals. Trains with higher stimulation frequency led to earlier and stronger reduction in field potentials of SynTKO animals, again with stronger effects in symptomatic animals. Post-tetanic potentiation was also strongly reduced in SynTKO animals, as suggested by a publication from the Peter Jonas group (Vandael et al., 2020). While the amplitude from the first stimulus after high-frequency stimulation was reduced in both age groups of SynTKO, an elevated late PTP and increased LTP was observed in presymptomatic animals.

Discussion

In this thesis I investigated the mechanisms underlying different forms of presynaptic potentiation at the hippocampal mossy fiber bouton. In particular, I was interested in presynaptic long-term potentiation at the mossy fiber to CA3 pyramidal cell synapse, which is known to be accompanied by an increase in release probability (Xiang et al., 1994; Weisskopf and Nicoll, 1995; Maeda et al., 1997) and involves phosphorylation of different substrates by PKA (Weisskopf et al., 1994; Nicoll and Schmitz, 2005). I tested three main hypotheses, each with the focus on a presynaptic protein that is expressed at mossy fiber boutons. (1) Release probability during presynaptic mossy fiber potentiation might increase due to a tightening between calcium channels and release sites. (2) During presynaptic mossy fiber potentiation, an increase in the vesicular priming molecule and release site marker Munc13-1 could lead to an increase in synaptic strength. (3) The lack of synapsins as putative downstream targets of PKA during mossy fiber presynaptic plasticity might lead to impaired mossy fiber LTP and changes in short-term plasticity.

Measuring Coupling Distances at Hippocampal Mossy Fiber Boutons

The first hypothesis was addressed by comparing calcium channel and release site coupling distances between control and chemically potentiated slices, using a super-resolution imaging approach. Distances were measured between immunolabeled Munc13-1, that was shown to be a marker for release sites (Sakamoto et al., 2018) and immunolabeled calcium channels from the Ca_V2 VGCC family. In summary, I saw no change in the distance between release sites and any of the three Ca_V2 channel types. However, the coupling distance between Munc13-1 and the calcium channel $Ca_V2.3$ was substantially shorter than between Munc13-1 and the other two calcium channels, $Ca_V2.1$ and $Ca_V2.2$.

During presynaptic LTP at hippocampal mossy fiber boutons, release probability increases (Xiang et al., 1994; Weisskopf and Nicoll, 1995; Maeda et al., 1997). Many factors can influence this variable, amongst others presynaptic Ca^{2+} dynamics (Atwood and Karunanithi, 2002). It has been shown that the number of calcium channels (Fukaya et al., 2023a; Kim et al., 2023) as well as the amount of Ca^{2+} influx (Regehr and Tank, 1991; Kamiya et al., 2002) do not change in mossy fiber boutons after presynaptic potentiation. However, the coupling distance between calcium channels and release sites could be dynamically modulated and thereby regulate release probability in an activity-dependent manner (Zhang et al., 2022). VGCC are loosely coupled to release sites in mature mossy fiber boutons, making it possible for slow calcium buffers to interfere with release (Vyleta and Jonas, 2014; Eggermann et al., 2012). A change from this loose to a tight coupling could lead to nanodomain instead of microdomain calcium arrangements with the possibility of a tremendous increase in the peak calcium concentration at release sites (Dittman and Ryan, 2019). Elevated calcium levels as well as the close proximity of the calcium source to the calcium sensor on synaptic vesicles would increase the probability for release in a non-linear fashion and slow calcium buffers

would be limited in their ability to interfere (Eggermann et al, 2012). For instance, a tightening of 20 nm leads to a tenfold increase in release at basket cell synapses in the dentate gyrus (Bucurenciu et al., 2008). Indeed, a tightening has also been suggested for hippocampal mossy fiber boutons: The inhibitory effects of the slow calcium buffer EGTA on release were occluded when dissociated mossy fiber boutons were chemically potentiated with cAMP, suggesting that cAMP-dependent potentiation likely modulates the coupling distance between calcium channels and synaptic vesicles (Midorikawa and Sakaba, 2017). The fact that $Ca_v2.1$ are mobile within presynaptic membranes (Schneider et al., 2015) supports the possibility of a tightening in coupling distance.

Methodological Approach

In acute mouse brain slices I measured the distance between Munc13-1, a marker for release sites (Sakamoto et al., 2018) and all members of the VGCC family Ca_v2 that are expressed at mossy fiber boutons (Li et al., 2007). Importantly, maximal distances from all sets of experiments were below 250 nm, indicating that I restricted my measurements to molecules from the same active zone. In mossy fiber boutons, active zones are approximately 500 nm apart (Rollenhagen et al., 2007) and have an area around 0.2 μm^2 (Orlando et al., 2021). The measurements were confined to ZnT-3 positive regions of hippocampal area CA3. Mossy fibers show enriched levels of zinc (Palmiter et al., 1996; Cole et al., 1999; Pan et al., 2011) and its vesicular transporter ZnT-3 (Palmiter et al., 1996; Wenzel et al., 1997; Cole et al., 1999), which can therefore be used as mossy fiber markers (Wenzel et al., 1997). I imaged the ZnT-3 signal in the confocal mode at the STED microscope for the $Ca_v2.2$ and $Ca_v2.3$ datasets. For the $Ca_v2.1$ dataset the ZnT-3 signal could only be obtained at low magnification with a 20x objective, due to a weak secondary antibody. Nevertheless, composite images from the $Ca_v2.2$ and $Ca_v2.3$ datasets revealed that most of the fluorescent markers for Munc13-1, calcium channels and Homer1 in *stratum lucidum* were situated within the ZnT-3-positive region (Figure 15b).

To measure the coupling distance only at functionally intact synapses, I restricted the measurements to Munc13-1 and Ca_v2 clusters juxtaposed to a Homer1 molecule, that is a postsynaptic marker for glutamatergic neurons (Imamura et al., 2011; Gutierrez-Mecinas et al., 2016). By this, I likely also excluded measurements from active zones of filopodial extentensions, which are protrusions from the mossy fiber bouton, contacting interneurons in the *stratum lucidum* (Acsády et al., 1998). Although filopodial extensions arise from the mossy fiber bouton (Amaral, 1979), their connections show markedly different plasticity mechanisms compared to the connections between the bouton and CA3 pyramidal cells (Maccaferri et al., 1998; Toth et al., 2000). Thus, it could be that also the spatial arrangement of active zone proteins is different, as suggested by publications showing arrangements of calcium channels dependent on synaptic strength (Rebola et al., 2019) and target cell (Éltes et al., 2017).

Measured Coupling Distances in Context

I found that the average distance between Munc13-1 and the most abundant Ca_v2 channel $Ca_v2.1$ was 64.62 ± 34.65 nm, in a total of 584 measurements from 11 control slices (Figure 19). This distance is in agreement with the loose coupling configuration proposed by Vyleta and colleagues (Vyleta and Jonas, 2014). Their functional readout suggested a distance of 75 nm from a single calcium channel to release site and 65 nm from the center of a calcium channel cluster. Thus, my data are in line with the proposed distance for a channel cluster (Vyleta and Jonas, 2014). A previous study investigated spatial relations between active zone proteins in hippocampal mossy fiber boutons (Brockmann et al., 2019). The authors also used STED microscopy and reported the nearest neighbor distance between $Ca_v2.1$ and Munc13-1 to be 106 nm (Brockmann et al., 2019). While this is also in line with a loose coupling configuration (Eggermann et al., 2012), the authors did not stain for a postsynaptic marker like Homer1. This might have led them to measure distances between molecules that were not part of a functional synapse or that belonged to another synapse type in the *stratum lucidum*. These factors might explain the discrepancy between their distance and the modeled distance (Vyleta and Jonas, 2014) as well as my results.

I compared the average control distance of approximately 65 nm to the average distance in forskolin-treated slices. Forskolin is a chemical activator of adenylyl cyclases (Hanoune and Defer, 2001) and thereby likely an activator of the cascade underlying mossy fiber LTP (Huang et al., 1994; Weisskopf et al., 1994). After chemical potentiation, the average distance between Munc13-1 and $Ca_v2.1$ was 63.62 ± 32.77 nm, which was not significantly different to the average distance from control slices in a GLMM. Thus, there is probably no change in coupling distance after chemical potentiation. However, it could be that the resolution at the gSTED microscope is not high enough to obtain relatively small changes in the coupling distance.

As a control, I measured distances in the *stratum radiatum* of hippocampal area CA1, in which Schaffer collaterals terminate (Amaral and Witter, 1989; Ishizuka et al., 1990; Li et al., 1994; Kajiwara et al., 2008). Modeling proposed a tighter coupling distance at these synapses (Scimemi and Diamond, 2012) compared to mossy fiber boutons (Vyleta and Jonas, 2014). Indeed, 491 measurements in area CA1 of 11 untreated control slices revealed an average coupling distance of 54.87 ± 32.49 nm, that was significantly shorter than the average coupling distance in CA3 from control slices (Figure 21). Scimemi and Diamond modeled several scenarios of possible vesicle and calcium channel arrangements for the CA3-CA1 synapse (Scimemi and Diamond, 2012). Summarized, they proposed a likely arrangement of 10 vesicles per active zone, accompanied by one to three calcium channels. In such scenarios the distances between vesicle and channel were in the range of 10 to 30 nm (Scimemi and Diamond, 2012).

Assuming a tight average coupling distances of 20 nm for CA1 (Scimemi and Diamond, 2012) compared to the predicted coupling distance of 70 nm for the mossy fiber synapse in CA3 (Vyleta and Jonas., 2014), would indicate a 50 nm tighter coupling at the Schaffer collateral compared to mossy fiber synapse.

However, my imaging experiments resulted in an interregional difference of only 10 nm (~65 nm vs. ~55 nm, Figure 21). Thus, it could be that only large shifts in coupling distance are detectable at the STED microscope, given limitations like the resolution (Sahl et al., 2017) and the so-called linkage error. This error describes the difference between the fluorescent probe and the actual target molecule, given the size of the primary-secondary antibody constructs. Such a construct has likely a size around 20 nm (Weber et al., 1978; Pauli et al., 2021) and can rotate freely around the epitope. Thus, the distance between the fluorescent probes labeling the target molecule will always be an indirect convergence to the true distance – not least because the use of polyclonal antibodies will result in a mixed labeling of epitopes. Nonetheless, due to the high number of individual measurements from 11 animals (Appendix, Tables 15 + 16) and the comparison of two conditions with the same average error, this inaccuracy should statistically be negligible.

Several recent publications from the lab of Takeshi Sakaba also found that the coupling distance at the hippocampal mossy fiber bouton was unchanged after chemical potentiation. With the same experimental approach, they saw no change in coupling distance between Munc13-1 and $Ca_V2.1$ in area CA3 of rat brain slices (Fukaya et al., 2021). Also, when they repeated these measurements with optogenetic induction of mossy fiber LTP, they again found no change in coupling distance (Fukaya et al., 2023a). However, a very recent preprint from the lab of Peter Jonas did measurements in labeled freeze fracture replica of mossy fiber boutons and found a tighter coupling distance between $Ca_V2.1$ and Munc13-1 in potentiated slices (Kim et al., 2023). The distance was on average 6 nm closer in boutons treated with forskolin than in untreated boutons. Importantly, Kim and coworkers also showed that when they added a PKA inhibitor together with forskolin, they could occlude the forskolin effect on the coupling distance, while the PKA inhibitor alone led even to longer distances compared to control (Kim et al., 2023). PKA is thought to be necessary in the mossy fiber LTP pathway (Huang et al., 1994, 1995; Weisskopf et al., 1994). Thus, these additional findings indicate that the change in coupling distance between Munc13-1 and $Ca_V2.1$ might be bi-directionally regulated via the AC-PKA pathway.

Although a shift of 6 nm seems small, it can increase the release approximately threefold, due to the nonlinear relation between Ca^{2+} and release (Bucurenciu et al., 2008) and the localized Ca^{2+} peaks at the calcium channel (Simon and Llinás, 1985) (Figure 5). Such a shift might already be sufficient to suppress release interference of slow calcium chelators, as suggested in previous experiments (Midorikawa and Sakaba, 2017). The labeling of freeze fracture replica can achieve a higher resolution than STED microscopy, reaching 15 nm or less (Da Silva and Kan, 1984) while the resolution of STED is on the order of tens of nanometers (Sahl et al., 2017). Thus, such a small shift is likely not detectable at the STED microscope, leading to the unchanged coupling distances reported by me and Fukaya et al. (Fukaya et al., 2021, 2023a). Interestingly, when comparing different configurations of Munc13-1 and $Ca_V2.1$ clusters (open versus strict), I found a smaller distance in forskolin-treated samples in the open configuration

(Figure 18). The average distance of only open configurations was 64.68 ± 32.13 nm in control conditions and 58.82 ± 29.19 nm in forskolin condition, leading to the same shift of 6 nm as described by Kim and coworkers (Kim et al., 2023). However, when compared in a GLMM, there was no significant difference between conditions, likely due to the smaller number of configurations categorized as "open". One could speculate that the configurations that I defined as open and strict could underlie different molecular conformational states at the release site, that might be associated with different channel-sensor distances. It could be that the labeled Munc13-1 moelcules in the experiments from Kim and colleagues were biased towards a Munc13-1 subset in a specific conformational state (Neher and Brose, 2018; Quade et al., 2019). Munc13-1 has no transmembrane domain and has therefore to be associated very tightly with the membrane to be detectable in freeze fracture labeling. Indeed, Kim et al. mention the possibility that recently primed (= not so tightly associated) Munc13-1 might have dissociated during their experimental procedure (Kim et al., 2023).

Limitations and Open Questions

While my measurements were repeated in several samples and included several controls, superresolution microscopy was not sufficient to measure a possible tightening of the coupling distance as observed by Kim et al. (Kim et al., 2023). There are several limitations in my approach. First of all, while the resolution of a STED microscope is very good, it is still lower that of an electron microscope or other nanoscopic techniques (Sahl et al., 2017). For instance, I measured a coupling distance of approximately 55 nm in area CA1, although modeling predicted a distance of 10 to 30 nm. However, findings regarding the coupling distance at Schaffer collateral synapses are diverse and also include propositions of over 130 up to 300 nm (Nadkarni et al., 2012; Brockmann et al., 2019), so further experiments might be needed to clarify discrepancies. Second, while I restricted my imaging to ZnT-3 positive regions, which are likely mossy fiber boutons, I cannot differentiate between individual boutons and synaptic contacts, which is decreasing the statistical power. Here, an approach of individual mossy fiber boutons as described by Pauli et al. might be useful (Pauli et al., 2021). Third, I am not able to differentiate individual active zones and also cannot resolve individual Munc13-1 molecules or calcium channels. This prevents the analysis of other parameters like clustering of molecules or the type of active zone topography, which would help to understand possible changes in synaptic strength (Rebola et al., 2019; Kim et al., 2023).

However, although a small shift as described by Kim et al. might be possible, several questions remain. These include the type of induction method for presynaptic potentiation as well as the time points after induction, at which structural changes occur. It remains to be elucidated if the shift described by Kim et al. is reproducible with other modes of mossy fiber activation like "flash and freeze" (Vandael et al., 2020) or electrical stimulation with natural activity patterns (Gundlfinger et al., 2010; Vandael et al., 2020) and if

such a shift could also be detected at later time points compatible with LTP after induction of potentiation in combination with freeze fracture replica labeling.

It has been suggested that forskolin does not activate the same presynaptic cascade as does the induction of mossy fiber LTP with high-frequency electrical stimulation (Shahoha et al., 2022; Fukaya et al., 2023b). Forskolin is a non-selective adenylyl cyclase activator (Hanoune and Defer, 2001) and could activate several presynaptic ACs in mossy fibers, including those that are not Ca^{2+}-dependent and would maybe not be activated during Ca^{2+}-dependent plasticity mechanisms (see Introduction). Furthermore, forskolin could induce AC-dependent cascades in other cells of the network, including postsynaptic CA3 pyramidal cells and glia cells (Jard et al., 1972), although early results suggested that associational-commissural fibers were not affected by forskolin application (Weisskopf et al., 1994). Such potential off-target effects could also explain differential results in mossy fiber studies of knockout animals in which both electrical and chemical potentiation were compared (Castillo et al., 1997, 2002; Shahoha et al., 2022). Fukaya and coworkers use such a line of arguments to explain their different findings in mossy fiber boutons in subsequent publications (Fukaya et al., 2023a, 2023b). In their first paper they reported no change in the coupling distance between Munc13-1 and $Ca_V2.1$, no change in Munc13-1 cluster number or size, but a change in the width of the calcium channel cluster (Fukaya et al., 2021). Two years later, they published an optogenetic induction approach, that allowed them to compare potentiated to non-potentiated boutons in the same slice (Fukaya et al., 2023a). Here, they found no change in the coupling distance, no change in the calcium channel cluster number, but a change in the number of Munc13-1 cluster after potentiation. While parts of these mixed findings might be attributable to the induction methodology, it is noteworthy that Kim et al. also used forskolin to induce potentiation and were able to measure a shift in the distance between Munc13-1 and $Ca_V2.1$ and an increase in the Munc13-1 cluster number (Kim et al., 2023). Thus, the results regarding number and positioning of Munc13-1 and $Ca_V2.1$ are highly variable across studies and the induction method is likely only a small puzzle piece alongside other contributing factors. Taken together, this is rather suggesting that the resolution of the technique and not the mode of induction are responsible for the divergent results.

Another interesting aspect is the temporal sequence of potentially parallel mechanisms orchestrating potentiation at the hippocampal mossy fiber bouton. Kim et al. incubated their samples for only five minutes (Kim et al., 2023), while I incubated brain slices for 15 minutes, comparable to the time frame of forskolin wash-in during electrophysiological recordings in the slice (Huang et al., 1994). In general, it is unknown when PTP blends into LTP and whether these types of potentiation share common mechanisms. An initial shift in channel-sensor distance as detected by Kim et al., could be superseded by other changes in the longer term. Structural changes have been reported at the mossy fiber boutons after potentiation and suggest an increase in the RRP and the insertion of new active zones after 15 minutes (Orlando et al., 2021). Similar

changes in the RRP size have also been reported 20 seconds (Vandael et al., 2020) and 5 minutes (Kim et al., 2023) after the induction of potentiation, probably depending on an enhanced recruitment of vesicles (Vandael et al., 2020), that occurs on short time scales (Neher and Sakaba, 2008). However, larger structural remodeling of synapses might need more time, including the potential insertion of new active zones (Orlando et al., 2021). Taking all these indications together, a possible model could include an initial tightening in calcium channel to release site coupling, facilitating intial increase in release. In turn, that could trigger additional mechanisms like the insertion of active zones and new release sites. Thus, several open questions remain and the mixed findings reported on this issue need to be reconciled. Preferentially, a high-resolution approach – for example freeze fracture replica labeling or Minflux (Eilers et al., 2018) with primarily labeled nanobodies – at different time points, for individual mossy fiber boutons and with different induction protocols.

Coupling Distances of Different Ca_v2 Calcium Channels

In my initial experiments, distance measurements between $Ca_v2.1$ and Munc13-1 indicated no change in the coupling distance at hippocampal mossy fiber boutons after chemical potentiation. However, mossy fiber boutons also express $Ca_v2.2$ channels (Li et al., 2007), that are involved in synaptic transmission at this synapse (Camillo et al., 1994; Breustedt et al., 2003). Thus, I also sought to investigate a potential shift in the coupling distance between $Ca_v2.2$ and Munc13-1 after potentiation. When comparing the average distance between control and forskolin-treated slices, I measured average distances of 61.26 ± 29.83 nm for control and 64.23 ± 33.55 nm for forskolin-treated slices (Figure 24). Thus, my results might indicate that there is no change in coupling distance after 15 minutes of chemical potentiation. Potentially, also here the shift could be as small as between $Ca_v2.1$ and Munc13-1 and therefore may not be detectable with gSTED. While the average coupling distance fits with the predicted loose coupling configuration of a channel cluster (Vyleta and Jonas, 2014), they contradict findings from a recent study, in which N-type channels were suggested to work via nanodomains in the range of 20 nm (Chamberland et al., 2017). In control slices, distances were also measured in area CA1. Here, I found an average coupling distance of 56.84 ± 31.25 nm (Figure 25), which was not significantly different to the distance in CA3. In summary, methods with a higher lateral resolution might be needed to shed light on exact distances and topography of this channel type, as for $Ca_v2.1$.

The last member of the Ca_v2 family is the R-type current mediating channel $Ca_v2.3$, also present at mossy fiber boutons (Li et al., 2007). While this channel type is probably not contributing to basal release (Castillo et al., 1994; Breustedt et al., 2003), it is involved in the induction of mossy fiber LTP (Breustedt et al., 2003; Dietrich et al., 2003). Therefore, also this channel could be an interesting candidate for a potential shift towards the release machinery. It had been proposed that $Ca_v2.3$ is rather located at remote locations in mossy fiber boutons, with primary access to the adenylyl cyclases (Dietrich et al., 2003). However, later

studies presented labeling of $Ca_V2.3$ at mossy fiber active zones (Parajuli et al., 2012) and from nonstationary fluctuation analyses of mossy fiber boutons an average number of five R-type channels was suggested to be present in each active zone (Li et al., 2007). Distance measurements from seven animals revealed a coupling distance to Munc13-1 of 50.01 ± 28.55 nm in control conditions and 48.72 ± 28.96 nm in forskolin-treated slices. The measurements were not significantly different when tested in a GLMM (Figure 28). Thus, also $Ca_V2.3$ might not move substantially closer to release sites during chemical potentiation at mossy fiber boutons, in a range that could be detected with STED microscopy. When measuring the average coupling distance in area CA1 of control slices, I found an average distance of 51.95 ± 31.1 nm (Figure 29). Compared to the distance measured in CA3 there was no significant difference, indicating that $Ca_V2.3$ has similar coupling distances in these two synapse types.

Potential Roles of $Ca_V2.3$ in Hippocampal Mossy Fiber Boutons

The measurements between $Ca_V2.3$ and Munc13-1 revealed significantly shorter distances (ca. 50 nm) than between Munc13-1 and the other two Ca_V2 family members (ca. 65 nm) (Figure 30). Notably, I used two different primary antibodies for $Ca_V2.3$ and found the same shorter coupling distance in both sets (Figure 26). In area CA1 all three Ca_V2 channels had similar coupling distances to Munc13-1 (Figure 31), indicating that the proximity of $Ca_V2.3$ to Munc13-1 at the mossy fiber bouton might have a special role. Indeed, granule cells express high levels of this calcium channel type (Soong et al., 1993; Day et al., 1996) and the distribution of $Ca_V2.3$ channels across the brain correlates with synapses expressing presynaptic forms of LTP (Myoga and Regehr, 2011). However, $Ca_V2.3$ was shown to not participate in basal mossy fiber transmission (Castillo et al., 1994; Breustedt et al., 2003; Pelkey et al., 2006). Why would especially this channel need a position closer to the release sites? When blocking the two principal Ca_V2 calcium channels for transmission ($Ca_V2.1$ and $Ca_V2.2$), mossy fiber LTP could still be induced (Castillo et al., 1994), indicating a role for another VGCC. Indeed, two publications demonstrated a role of $Ca_V2.3$ in the induction of mossy fiber LTP in induction paradigms using moderate electrical stimulation (Breustedt et al., 2003; Dietrich et al., 2003). This channel type is preferentially recruited during action potential broadening (Li et al., 2007), that occurs during high-frequency activity of granule cells (Geiger and Jonas, 2000b). At the same time, it is activated at lower membrane potentials than $Ca_V2.1$ and $Ca_V2.2$ (Li et al., 2007), thus participating in calcium influx earlier.

It has been suggested that endogenous buffers play a role in the regulation of mossy fiber presynaptic plasticity mechanisms (Blatow et al., 2003; Vyleta and Jonas, 2014). It might be that some residual influx below the thresholds of $Ca_V2.1$ and $Ca_V2.2$ channels could already prepare for an increase in free local Ca^{2+} concentration by saturating endogenous buffers. Other effects, like the potential tightening of coupling distances between $Ca_V2.1$ and Munc13-1 (Kim et al., 2023) could then build on this foundation by increasing the calcium concentration in vicinity to the release site and thereby enhancing the release probability. Such

$Ca_v2.3$-mediated Ca^{2+} influx could be modulated by divalent cations such as Zn^{2+} (Neumaier et al., 2020b). Zn^{2+} is abundant in mossy fibers (Wenzel et al., 1997) and might play a role in the induction of mossy fiber long-term potentiation (Lu et al., 2000). $Ca_v2.3$ is one of the most sensitive targets for Zn^{2+} modulation (Magistretti et al., 2003; Kang et al., 2007; Shcheglovitov et al., 2012; Neumaier et al., 2020a), that occurs in a concentration-dependent manner (Neumaier et al., 2020b). Thus, the R-type calcium current might be regulated depending on previous activity at the mossy fiber to CA3 pyramidal cell synapse.

Another factor could be the position of $Ca_v2.3$ within the active zone. It was proposed in a recent paper that release sites of hippocampal synapses participating in asynchronous release are rather situated at the center of active zones, while release sites for synchronous release are situated at the active zone edges (Kusick et al., 2020; Li et al., 2021). Li et al. described that a similar organization could be observed at the postsynaptic density. There, NMDA receptors are located more towards the middle, leading to a transsynaptic column with asynchronous release sites, while AMPA receptors are opposing synchronous release sites (Li et al., 2021). Intriguingly, it was proposed that $Ca_v2.3$ channels participate in asynchronous release at some synapses (Ermolyuk et al., 2013). While I cannot differentiate between different release sites within one active zone, it could be that $Ca_v2.3$ is coupled closer to specific release sites, implicated in asynchronous release. The same release sites might also be activated during weak tetani (Breustedt et al., 2003; Dietrich et al., 2003). Experiments using freeze fracture replica labeling for $Ca_v2.3$ and Munc13-1 could reveal such a potential centering within mossy fiber bouton active zones.

Summary of Coupling Distance Measurements

In summary, my data indicate that none of the voltage-gated calcium channels of family Ca_v2 change their relative position to the release site marker Munc13-1 after chemical potentiation at the hippocampal mossy fiber bouton. While the measured distances are in line with predicted loose coupling configurations (Vyleta and Jonas, 2014), it remains to be elucidated if small shifts in coupling distance occur (Kim et al., 2023), that might not be detectable with STED microscopy. Interestingly, the $Ca_v2.3$-containing R-type calcium channel seems to be situated closer to release sites than the other two calcium channels. This channel type might have special functions at the mossy fiber bouton, for example during the induction of LTP, during asynchronous release or as a target for modulators.

Number of Release Sites at the Hippocampal Mossy Fiber Bouton

In another set of experiments, I investigated if chemical potentiation leads to an increase in Munc13-1 signal in *stratum lucidum* of hippocampal area CA3, where mossy fibers terminate. To this end, Munc13-1 signal intensities were compared between confocal stacks of stained brain tissue, preincubated with control or forskolin solution for either 15 minutes or one hour. The different incubation times were aimed to differentiate short term-effects versus possible translational changes in the bouton, which need more time (Monday et al., 2022). Furthermore, I acquired confocal stacks in three subregions of area CA3, namely CA3a, CA3b and CA3c. In summary, I found no difference in Munc13-1 intensities between control and potentiated slices for either incubation time. However, I found intensity differences within the subregions of hippocampal area CA3 irrespective of the treatment.

The strength of a synapse is influenced by many factors, among them also the number of functional release sites (Katz and Miledi, 1969; Redman, 1990; Tong et al., 1996; Reid et al., 2004). It has been shown that during presynaptic potentiation, structural changes occur at the hippocampal mossy fiber bouton (Orlando et al., 2021), that might underlie increase in release site numbers. These include an increase in the density of active zones as well as an increase in the number of docked and tethered vesicles at individual active zones (Orlando et al., 2021), suggestive of an increase in the number of Munc13-1 molecular bridges (Quade et al., 2019; Papantoniou et al., 2023). Furthermore, imaging with the glutamate sensor iGluSnFR indicated increased active release area after potentiation and a more synchronous release kinetic (Orlando et al., 2021), in line with the insertion of new release sites together with an unsilencing of already existing release sites (Reid et al., 2004).

Munc13-1 is an important active zone protein, that is known as a docking and priming factor for synaptic vesicle release (Augustin et al., 1999b; Varoqueaux et al., 2002; Imig et al., 2014) and proposed to be a marker for individual release sites (Sakamoto et al., 2018): indeed, Munc13-1 precisely co-localizes with syntaxin-1 – an essential protein in the fusion machinery (Südhof, 2013) – and it correlates with the number of readily-releasable vesicles in hippocampal neurons (Sakamoto et al., 2018). To elucidate if mossy fiber presynaptic potentiation is accompanied by an increase in Munc13-1, I compared fluorescent intensities of immunolabeled Munc13-1 in confocal stacks acquired in *stratum lucidum* of hippocampal area CA3. I used the chemical activator for adenylyl cyclases forskolin (Hanoune and Defer, 2001) to chemically potentiate mossy fiber boutons and compared intensities between chemically potentiated and control slices. Two different incubation times were compared: A shorter one of 15 minutes, as in previous experiments (Orlando et al., 2021) and a longer one of one hour. The longer incubation time was chosen, because recent findings suggest local protein synthesis during the expression of mossy fiber LTP in similar time frames (Monday et al., 2022). Mossy fibers were defined by staining for ZnT-3 (Wenzel et al., 1997) and regions of interest (ROIs) for intensity measurement were defined via the ZnT-3 signal.

Measurement of ZnT-3 Positive Area

At first, I was interested in the area of ZnT-3 positive regions, as an indicator for possible changes in mossy fibers boutons after forskolin treatment. Furthermore, the size of ZnT-3 positive ROIs could also influence the integrated density measure for intensity, which factors in the ROI area. To exclude unspecificly stained blood vessels and small ROIs outside the *stratum lucidum*, I defined a threshold of 50 μm^2 as the minimal area. The analysis revealed larger average ROI areas after the treatment with forskolin (Figure 34). This observation indicates that the ZnT-3 signal is more distributed after potentiation, leading to larger automatically-detected signal clusters. A possible explanation might arise from the fact that ZnT-3 is located in vesicular membranes (Wenzel et al., 1997) and that synaptic vesicles are more dispersed in potentiated mossy fiber boutons (Orlando et al., 2021). However, the number of ROIs decreased after forskolin treatment, indicating that the overall ZnT-3 positive area might not change. Indeed, when analyzing the total ZnT-3 positive area per image, I found no difference between conditions. This is again in line with findings from mossy fiber boutons, in which the synaptic vesicle density is not changed after chemical potentiation (Orlando et al., 2021). Together, such an increase in the single ROI area could be due to more dispersed vesicles and increased size and structural complexity of mossy fiber boutons after potentiation (Galimberti et al., 2006; Zhao et al., 2012; Maruo et al., 2016; Orlando et al., 2021). For example, bouton volume is increased in mice that are kept in an enriched environment (Monday et al., 2022).

Munc13-1 Intensity Measurements

Next, I compared the intensity of labeled Munc13-1 in *stratum lucidum* of hippocampal area CA3. I analyzed the mean intensity, which is an area-independent parameter. For slices incubated either in control or forskolin solution, I found no difference in the fluorescence intensity between treatments (Figure 36). This finding indicates that there is no overall change in the intensity of Munc13-1 after potentiation. However, Munc13-1 content could vary at the individual bouton level. In my approach, imaging areas comprised relatively large parts of CA3 *stratum lucidum*, roughly subdivided into CA3a, CA3b and CA3c, to investigate large scale changes in the Munc13-1 content upon potentiation. This approach prevented the investigation of individual Munc13-1 content at the bouton or even active zone level. An additional caveat in my experiments could be the comparison of slices from different septotemporal portions of the hippocampus. Different subpopulations of cells or synapses might exist along this axis due to variation in hippocampal circuitry (Dalton et al., 2022) and variations in packing number and ratios between granule cells and CA3 pyramidal cells (Amaral et al., 2007), which might also influence the molecular content. Indeed, a recent study demonstrated changes in Bassoon clusters of mossy fiber boutons along this axis (Pauli et al., 2021).

In their study, Pauli and coworkers developed a technique to image individual mossy fiber boutons at specific locations along the septotemporal axis of the hippocampus (Pauli et al., 2021). They combined a

mouse line that sparsely labels mossy fibers with so-called targeted cutting, to investigate molecular active zone content along the septotemporal axis. They found that the number and size of Bassoon clusters – an active zone scaffolding protein (Dieck et al., 1998) which size correlates with transmitter release (Matz et al., 2010) – varied along the septotemporal axis. This could mean that also other mossy fiber components could vary along this axis, including core active zone proteins like Munc13-1. The study by Pauli et al. also investigated possible changes in Bassoon clusters after application of forskolin, but did not see significant changes, indicating no plasticity-related adjustment of this structural active zone protein in the framework of their experiments (Pauli et al., 2021). A co-author of the study investigated Munc13-1 clusters in his doctoral thesis in a similar way and found no change in Munc13-1 clusters after treatment with 50 µM forskolin for 30 minutes (Sharifi, 2021). These data strengthen my finding that the net mossy fiber Munc13-1 content does probably not change after chemical potentiation.

However, two even more recent studies reported potentiation-related increases in Munc13-1 clusters in mossy fiber boutons (Fukaya et al., 2023a; Kim et al., 2023), supporting our previous finding of increased active zone densities (Orlando et al., 2021). The first study used STED microscopy and imaged Munc13-1 in individual mossy fiber boutons (Fukaya et al., 2023a). They induced LTP with an optogenetic tool, by expressing a fast version of the light-activatable and cation-conducting channel Channelrhodopsin 2, called Chronos (Klapoetke et al., 2014). Light at specific wavelengths activates Chronos, leading to the opening of the channel, the influx of cations (Rost et al., 2022) and the depolarization of the cell. Importantly, light-induced potentiation led to increased field excitatory postsynaptic potentials as observed during electrically induced mossy fiber LTP (Fukaya et al., 2023a). After potentiation, the molecular content of individual boutons in the *stratum lucidum* of area CA3 was analyzed. Fukaya and coworkers compared Chronos-positive to Chronos-negative boutons, accessing both potentiated and non-potentiated boutons from the same slice. The authors report a significant increase in Munc13-1 and RIM1 fluorescent signal intensity at optogenetically potentiated individual mossy fiber active zones (Fukaya et al., 2023a). The second study used a different technique but achieved similar results. Kim and colleagues made use of freeze fracture replica labeling, thereby achieving resolutions of 15 nm or less (Da Silva and Kan, 1984). Furthermore, this technique allows to access the whole active zone area without limitations from slicing, that characterize immunohistochemial experiments. Kim and colleagues compared individual active zones of mossy fiber boutons for their content of Munc13-1 clusters between untreated control boutons and chemically potentiated boutons. They found an increase in the number of Munc13-1 clusters after potentiation with forskolin. This increase was blocked upon additional treatment with the PKA blocker H-89, indicating a PKA-dependent pathway, that underpins their finding (Kim et al., 2023).

The differences in the findings reported by Kim, Fukaya, Scharifi and me are potentially due to the choice of method as well as the angle of vision. Fukaya et al. compared potentiated versus non-potentiated boutons

from the same slice, which reduces variability substantially, because the compared mossy fibers are from the same septotemporal location, the same subregion within the *stratum lucidum* and underwent the same experimental procedures. In contrast, Kim et al. used a high-resolution method, which allows analysis of the active zone topography. Importantly, they report that the staining density for Munc13-1 and the average distance to the nearest Munc13-1 neighbor did not change after forskolin treatment (Figure S4, Kim et al., 2023). The observed changes referred solely to a change in cluster number of Munc13-1, i.e. regions with closely arranged Munc13-1 molecules within active zones, which were referred to as nanoassemblies before (Sakamoto et al., 2018). These indications rather point to an adjustment of molecular arrangements within active zones than to actual changes in the Munc13-1 number (Kim et al., 2023). Of note, Kim et al. might primarily detect Munc13-1 in a conformational state associated with tightly docked vesicles (Quade et al., 2019; Rizo, 2022), meaning that especially those Munc13-1 molecules might be labeled that are close to the membrane (Kim et al., 2023). Thus, the overall Munc13-1 content within boutons might not change, while conformation and topography of individual molecules might do, potentially promoting fusion competence of vesicles.

These results all point to high variability within single synapses and therein individual active zones. Indeed, it has been suggested that individual active zones from the same synapse show high variability in their Munc13-1 content and number of release sites (Karlocai et al., 2021). Active zones in synapses between CA1 pyramidal cells and fast-spiking interneurons displayed a threefold variability in their individual Munc13-1 content while the variability in size and density of Munc13-1 clusters was even higher (Karlocai et al., 2021). Such variability could promote individual synaptic strength between the same types of neurons (Holderith et al., 2012; Karlocai et al., 2021) or different synapse types (Rebola et al., 2019). Release sites in cultured hippocampal neurons were also found to be functionally heterogeneous (Maschi and Klyachko, 2020). Such fluctuations in Munc13-1 content at the active zone level increase variability and potentially hinder the detection of small Munc13-1 changes at a larger scale.

Comparison of Different Incubation Times

Recent findings reported local protein translation in mossy fiber boutons (Monday et al., 2022). To allow for possible potentiation-induced translation of Munc13-1, I incubated some of the slices for one hour instead of 15 minutes. However, a generalized linear mixed model revealed no changes in intensity between conditions after one hour or between different incubation times (Figure 36). These data indicate that there is probably no substantial potentiation-induced increase in translation of Munc13-1 in mossy fiber boutons in contrast to β-actin (Monday et al., 2022). The low magnification at the confocal microscope and the less specific labeling technique compared to Monday et al. could hinder the detection of such changes. However, my results could also indicate that Munc13-1 levels within the whole bouton do not change, and that supplies of Munc13-1 might be stored within the bouton. It has been suggested that active zone components are

stored in vesicles (Maas et al., 2012). Thus, the increase in active zone density after 15 minutes of potentiation (Orlando et al., 2021), might be realized by the fusion of dense-core vesicles comprising active zone components (Ziv and Garner, 2004) and their cargo might also comprise Munc13-1, as a core component of the active zone protein complex (Maas et al., 2012; Südhof, 2012). Thus, the net Munc13-1 content might not change within mossy fiber boutons.

Comparison Along the Transversal Axis of CA3

Variability does not only exist along the septotemporal axis, but also along the transversal axis within area CA3. For instance, proximal parts of CA3 may primarily receive inputs from granule cells of the supra-pyramidal blade of the dentate gyrus while distal CA3 pyramidal cells might receive mixed inputs from all mossy fiber tracts within the transversal axis as well as potential input from mossy fibers originating in other transversal lamellae (Amaral et al., 2007; Witter, 2007a). To account for possible differences within CA3, I roughly differentiated subareas CA3a, CA3b and CA3c within the *stratum lucidum* and compared the Munc13-1 intensity among them. I found a significant difference in the Munc13-1 intensity between areas CA3a and CA3c, with higher intensities in area CA3c (Figure 36). These findings were true for both treatment conditions, indicating a general decrease in Munc13-1 intensity along the proximal-distal axis of CA3. Interestingly, it has been reported that different populations of CA3 pyramidal cells exist (Cembrowski and Spruston, 2019) and that there might be a subpopulation that does not receive inputs from mossy fibers (Hunt et al., 2018). These pyramidal cells were found more in distal parts, i.e. CA3a (Hunt et al., 2018). Thus, reduced Munc13-1 intensity in CA3a could maybe be attributed to less connectivity onto CA3 pyramidal cells in that subregion. Of note, ZnT-3 intensity was unchanged between subregions (Figure 38), indicating that the density of ZnT-3 containing fibers is similar throughout CA3.

Summary of Confocal Data

In summary, I saw no change in Munc13-1 intensity between potentiated and control mossy fibers within the CA3 *stratum lucidum*, indicating that the net Munc13-1 content does neither change after 15 minutes nor after one hour of chemical potentiation. Furthermore, I observed a gradient in Munc13-1 intensity along the transversal axis of CA3 *stratum lucidum*, with least intensity in area CA3a. Such a gradient could indicate less synaptic connections in proximal parts of CA3, which might be correlated to the distribution of CA3 pyramidal cell subtypes (Hunt et al., 2018). Interestingly, the area of individual automatically-retrieved ZnT-3 ROIs was on average larger after forskolin treatment, which might be explained by structural changes in mossy fiber boutons such as vesicle dispersion (Orlando et al., 2021).

Presynaptic Plasticity in Mossy Fibers Lacking Synapsins

We aimed to investigate the role of synapsins in presynaptic plasticity mechanisms at mossy fiber boutons in a mouse model lacking all synapsins. To this end, we performed electrophysiological field recordings in acute brain slices of SynTKO and WT mice from two age groups: before and after the onset of epileptic seizures in SynTKO animals (Gitler 2004, Ketzef 2011). This allowed us to compare mossy fiber transmission and plasticity in two potentially different network states (Ketzef 2011). Notably, in mossy fiber boutons synapsin III expression is retained in mature synapses (Pieribone 2002) in contrast to most other synapses. We found that SynTKO showed increased excitability and synaptic depression, while frequency facilitation and post-tetanic potentiation were reduced. In presymptomatic SynTKO animals LTP was increased, in contrast to symptomatic animals, in which LTP had the same magnitude as in WT animals.

Increased Excitability

The genetic ablation of all synapsins resulted in increased excitability, measured by a change in the input-output relation of local field potentials (Figure 39). With the same amount of stimulated fibers, the excitatory postsynaptic potential was significantly enhanced in the knockout animals of both age groups. Similar enhancement has been described before in SynTKO animals (Ketzef et al., 2011) and upon the knockdown of synapsins in the land snail *Helix*, cellular excitability was increased in serotonergic neurons (Brenes et al., 2015). There is a plethora of possible underlying reasons for the enhanced excitability, some of which are linked to the epileptic phenotype of SynTKO animals. The dentate gyrus is thought to play a key role in temporal lobe epilepsy (Nadler, 2003). For example, it has been shown that status epilepticus leads to the loss of hilar cell types (Buckmaster and Edward Dudek, 1997), to the growth of recurrent mossy fibers onto granule cells (Nadler, 2003), and to an increase in granule cell neurogenesis (Parent et al., 1997). Together, these adaptations culminate in a changed local circuitry of the dentate gyrus, leading to a higher excitability of granule cells and to the breakdown of the dentate gyrus filter function (Heinemann et al., 1992; Nadler, 2003). However, such network changes might be especially important in progressing epilepsy (Gorter et al., 2001) and gross morphology as well as the number of inhibitory neurons were unchanged in SynTKO animals (Gitler et al., 2004; Ketzef et al., 2011). Thus, such contributions might not primarly cause the increased excitability in our experiments.

Other factors that might promote the increased excitability are the differential properties of mature versus newborn granule cells, i.e. higher excitability of newborn cells (Marín-Burgin et al., 2012; Dieni et al., 2013). With increased numbers of newborn granule cells – as reported for status epilepticus (Parent et al., 1997) – the network excitability might be enhanced (Lopez-Rojas and Kreutz, 2016). Notably, the onset of epileptic seizures is around two months after birth (Li et al., 1995; Gitler et al., 2004; Ketzef et al., 2011), but we already observed high excitability in presymptomatic mice. However, also the younger SynTKO animals might already exhibit nerwork changes, increasing the susceptibility for enhanced excitatory inputs

and promoting the development of seizures (Toader et al., 2013). Other reasons for increased excitability might include molecular composition of pre- and postsynaptic partners and changes in quantal parameters of neurotransmission (Redman, 1990; Jackman and Regehr, 2017). Indeed, immunogold experiments suggested an increase of postsynaptic AMPA receptor subunits in SynDKO animals (Gylterud Owe et al., 2005), which would contribute to an increased quantal response.

Increased excitability could also be associated with an increase in release probability, that is usually low at the hippocampal mossy fiber bouton (Jonas et al., 1993). The paired pulse ratio is an indicator for release probability (Thomson, 2000; Zucker and Regehr, 2002) and a change in that ratio is suggestive of presynaptic changes (Dobrunz and Stevens, 1997). However, in electrophysiological field recordings, this measure has to be taken with caution, because many factors can influence its outcome, like changes in the RRP size, alterations in residual Ca^{2+} clearance, rapid clearance of neurotransmitters from the synaptic cleft or changes at postsynaptic receptors (Hanse and Gustafsson, 2001; Sun et al., 2005; Glasgow et al., 2019). Consequently, we observed large variability when measuring the paired pulse facilitation in mossy fibers from WT and SynTKO animals. We found that paired-pulse facilitation was on average 2.8 in young wildtype animals, which is comparable to previous results (Salin et al., 1996b). In SynTKO animals of the same age, the average value was higher, around 3.7, but not significantly different from the wildtype ratio (Figure 40). This trend was also observed with a shortened inter-stimulus interval and in older SynTKO animals. While these results have to be treated with caution, they might indicate a decrease in release probability and would rather not explain the increased excitability.

While several of the aforementioned factors might contribute to the observed increase in excitability, a likely explanation is based on the differential effect of synapsins on excitatory and inhibitory neurons (Song and Augustine, 2015). While excitatory transmission is largely unaffected by the lack of synapsins, the basal transmission of cultured inhibitory neurons is impaired upon the knockout of SynI, SynIII or all three synapsins (Terada et al., 1999; Feng et al., 2002; Gitler et al., 2004; Baldelli et al., 2007; Chiappalone et al., 2009). Additionally, the knockout of Syn II leads to impaired tonic inhibition in hippocampal slices (Medrihan et al., 2013, 2015). Mossy fibers activate at least four times more inhibitory neurons than pyramidal cells in the area CA3 (Acsády et al., 1998), regulating CA3 excitability via feedforward inhibition (Acsády and Káli, 2007; Torborg et al., 2010). Reduced feedforward inhibitory transmission at a cellular level would thus mean reduced feedforward inhibition at the network level, possibly leading to increased excitability. Indeed, while in SynTKO the input-output ratio is increased in excitatory Schaffer collaterals, it is decreased in inhibitory fibers from CA1 (Farisello et al., 2013) likely due to the reduced $GABA_B$-mediated inhibition (Valente et al., 2017). This excitatory/inhibitory imbalance in synapsin knockout animals was suggested to support the breakthrough of epileptic seizures after two months (Rosahl et al., 1995; Chiappalone et al., 2009; Boido et al., 2010; Farisello et al., 2013).

Frequency Facilitation

We were interested to test whether the loss of all synapsins would also change presynaptic plasticity at the hippocampal mossy fiber bouton. The astonishing ability of these synapses to facilitate in response to increased presynaptic activity (Salin et al., 1996b; Toth et al., 2000) can reliably recruit CA3 pyramidal cells (Henze et al., 2002b; Vyleta et al., 2016) and is therefore thought to be an important mechanism for information transfer within the hippocampus (Henze et al., 2002b; Mori et al., 2004). A study in mossy fibers lacking synapsin I and II reported that frequency facilitation was reduced in knockout animals during 2 Hz trains (Owe et al., 2009). The authors of the study suggested that the remaining isoform, synapsin III, might be responsible for this decreased facilitation, because synapsin III co-localized with the RRP (Owe et al., 2009) and hippocampal neurons lacking synapsin III showed less depression (Feng et al., 2002). However, even in the absence of all synapsins, we still observed reduced facilitation in both presymptomatic and symptomatic animals (Figure 41). Our results indicate that the absence of synapsin, rather than the presence of synapsin III, is responsible for the decreased facilitation.

Frequency facilitation is a presynaptic mechanism dependent on changes in presynaptic Ca^{2+} dynamics and on the increase of release probability (Atluri and Regehr, 1996; Chamberland et al., 2017; Jackman and Regehr, 2017). However, possible reasons for reduced facilitation are diverse and could also include postsynaptic effects like the saturation of glutamatergic receptors (Neher and Sakaba, 2008). Other possible reasons comprise enhanced basal release probability, depletion of the RRP, changes in vesicle recruitment and priming rates (Neher and Sakaba, 2008). Interestingly, structural investigations of mossy fiber boutons from SynTKO animals indicated a decrease in the RRP correlate in knockout animals (Bruentgens et al., 2023, under revision). Potentially, a reduced RRP could limit the facilitation. Additionally, the reduced reserve pool (Gitler et al., 2004) probably hinders or slows down vesicle replenishment during facilitation, potentially limiting the enhancement. In summary, changes in vesicle pool size and dynamics are most likely underlying the decrease in frequency facilitation measured at SynTKO mossy fiber boutons, supporting synapsins role in vesicle organization.

Synaptic Depression

When stimulating mossy fibers with higher frequency trains (25 Hz) and for longer time intervals (5 seconds) we observed depression of fEPSPs during the train in both genotypes, but depression was stronger in SynTKO animals and especially prominent in symptomatic mice (Figures 42 and 43). In general, synaptic depression is linked to the depletion of the RRP (Zucker and Regehr, 2002) and to the slow replenishment of the RRP from the reserve pool (Wesseling and Lo, 2002). Indeed, increased depression at the calyx of Held of SynTKO animals has been attributed to the missing reserve pool observed in this genotype (Vasileva et al., 2012). The reserve pool is reduced in many synapses from synapsin knockout models (Chi et al., 2001, 2003; Fornasiero et al., 2012), including the mossy fiber bouton lacking

synapsins I and II (Takei et al., 1995; Owe et al., 2009) and cultured hippocampal neurons from SynTKO animals (Gitler et al., 2004; Siksou et al., 2007). Mossy fiber boutons from SynTKO animals also have a reduced density of synaptic vesicles and an increased average distance between vesicles (Bruentgens et al., under revision). Taken together, the increase in synaptic depression during high-frequency stimulation at the mossy fiber bouton can likely be attributed to reduced vesicle pools and impaired vesicle replenishment.

Post-tetanic Potentiation

After high-frequency stimulation and recovery from depression, post-tetanic potentiation is observed. This form of short-term plasticity has recently been linked to short-term memory in the hippocampus (Vandael et al., 2020). The authors of the study observed a so-called "pool engram" at the hippocampal mossy fiber bouton, i.e. an increased RRP after natural PTP-inducing stimulation patterns (Vandael et al., 2020). It has been proposed before that high-frequency stimulation leads to increased replenishment rates (Wang and Kaczmarek, 1998) and might result in an over-filling of the RRP at some synapses (Neher and Sakaba, 2008). Vandael and coworkers suggested that the increase in the RRP at the mossy fiber bouton depends on the synapsin-dependent enhanced refilling rate from the reserve pool (Vandael et al., 2020). Indeed, we observed a reduced PTP in mossy fibers lacking synapsins from both age groups (Figure 44), in line with the hypothesis of Vandael and colleagues (Vandael et al., 2020).

Reduced PTP has been described before in animal models lacking synapsins, including several preparations from invertebrates (Humeau et al., 2011), Schaffer collaterals (Rosahl et al., 1995; Farisello et al., 2013), cultured hippocampal neurons (Valente et al., 2012; Cheng et al., 2018), corticothalamic synapses (Nikolaev and Heggelund, 2015) and mossy fiber boutons from SynDKO mice (Spillane et al., 1995). While the absence of synapsin I and II reduced PTP at the mossy fiber bouton to 73 % of the control (Spillane et al., 1995), we observed a more drastic reduction to approximately 61 % of the control in animals of a similar age (Figure 44). This might indicate that the additional deletion of synapsin III exacerbates the impaired PTP phenotype in mossy fiber boutons. Interestingly, in cultured hippocampal neurons, only the splice variant SynIIIa could rescue a phenotype with reduced PTP (Cheng et al., 2018). In mossy fiber boutons, synapsin III could either be involved in the replenishment mechanism from the reserve pool and/or play an additional role at the RRP. As already mentioned, the RRP correlate in SynTKO mossy fiber boutons was decreased (Bruentgens et al., under revision), in line with the suggested synapsin-dependent replenishment at the mossy fiber bouton (Vandael et al., 2020) and putative further functions of specific synapsin isoforms.

Interestingly, the initial drop in PTP was followed by an increased second phase in young SynTKO compared to WT animals (Figure 44). Not only the RRP, but also release probability and quantal size were reported to be increased during mossy fiber PTP (Vandael et al., 2020). Quantal components, like the number of release sites, could be elevated by default in the SynTKO mossy fiber synapse, leading to the observed increase in PTP in the second phase. In fact, the number of release sites might be elevated in

SynTKO boutons, because the active zone density was increased in the knockout synapses (Bruentgens et al., under revision). Such an increase has been described before in potentiated WT mossy fiber boutons (Orlando et al., 2021). Thus, mossy fiber boutons from SynTKO animals could be in a preset potentiated state, leading to the enhanced fEPSPs. Similar structural changes in the form of increased active zone areas have been observed at the Calyx of Held of SynTKO animals (Vasileva et al., 2012).

LTP in Presymptomatic Animals

The increased fEPSP size in SynTKO recordings was still present half an hour after the high-frequency stimulation, indicating an increased LTP in young SynTKO animals (Figure 45). Interestingly, mossy fiber LTP in synapsin knockout models lacking synapsin I or synapsin I and II was unchanged (Takei et al., 1995; Spillane et al., 1995). Thus, it is tempting to speculate that especially the lack of synapsin III is unleashing processes, that lead to increased LTP in SynTKO animals. Indeed, in the striatum, knockout of synapsin III or all three synapsins leads to an increased release of dopamine (Kile et al., 2010). Notably, a colleague found that the preset elevated density in active zones of SynTKO mossy fiber boutons was further increased after chemical potentiation. Furthermore, also the RRP correlate was increased after chemical potentiation in mossy fiber boutons (Bruentgens et al., under revision). Both mechanisms have been observed before after chemical potentiation of WT mossy fiber boutons (Orlando 2021), indicating that those structural changes during presynaptic potentiation might be synapsin-independent. Since the active zone density is already elevated in non-potentiated mossy fiber boutons from SynTKO animals, additional insertion of active zones, together with an alternative vesicle recruitment pathway to the RRP might underlie the increased LTP in young SynTKO animals.

This alternative pathway could result from an increased vesicle recycling instead of an increased replenishment from the reserve pool. Interestingly, increased vesicle recycling has been observed in cultured synapsin III knockout neurons (Feng et al., 2002) and vesicles from the recycling pool can feed the RRP (Rizzoli and Betz, 2005; Denker and Rizzoli, 2010). In line with this argument, increased vesicle-turnover has been described in cultured hippocampal neurons after induction of potentiation (Ryan et al., 1996b) and has been proposed as a mechanism for LTP at other hippocampal synapses (Rey et al., 2020). Thus, increased recycling might be present both in synapses lacking synapsin III and potentiated WT boutons, indicating that the RRP might be regulated by synapsin III. However, synapsin III is also implicated in growth cone regulation (Ferreira et al., 2000) and the co-localization of synapsin III with the RRP (Owe et al., 2009) could also arise from this role. Future studies are needed to disentangle these roles at the mossy fiber bouton, since adult neurogenesis could lead to pre-mature, growth-cone like mossy fibers, in which synapsin III could have another role than in mature mossy fibers.

To date it is unclear if and how we can differentiate between the mechanisms underlying PTP and LTP at the hippocampal mossy fiber bouton. Ultrastructural analyses implicate that an increase in the RRP is

important for both processes and was observed at several time points after high frequency or chemical induction: after 20 seconds (Vandael et al., 2020), after 5 minutes (Kim et al., 2023) and after 15 minutes (Orlando et al., 2021). Potentially, synapsins are implicated in the initial increase in the RRP via replenishment from the reserve pool during or right after high-frequency stimulation, although also parallel synapsin-independent vesicle recruitment mechanisms might be in place at the mossy fiber bouton (Bruentgens et al., under revision). Further mechanisms, like the incorporation of new active zones, together with a speculative synapsin III-regulated increased vesicle recycling might stabilize long-term increase in release. Hence, while the initial drop in PTP at SynTKO animals is likely mediated by an impaired reserve pool and deficient vesicle recruitment, the secondary enhancement might have other sources, resulting in a stabilized increased number of active zones with a larger RRP.

LTP in Symptomatic Animals

In contrast to presymptomatic SynTKO mice, late PTP and LTP were unchanged in symptomatic SynTKO animals compared to their age-matched controls (Figure 45). This could indicate that after the onset of epileptic seizures, structural and other changes are balanced out by compensatory effects, leading to a normal phenotype in potentiation. Indeed, it has been suggested that the onset of epileptic seizures in SynTKO mice is accompanied by an increased inhibitory component, as suggested from field recordings in young and adult SynTKO animals (Ketzef et al., 2011). The authors additionally observed increased levels of GAD67 in adult compared to young SynTKO brains (Ketzef et al., 2011), a protein which is involved in the synthesis of GABA (Houser and Esclapez, 1994). An increase in inhibitory transmission in an epileptic phenotype might help to control seizures and was also observed in other epileptic models before (Engel, 1996). However, it might counter-intuitively also contribute to epileptogenesis (Khalilov et al., 2005), network hypersynchronicity and seizures (Staley et al., 1995; Avoli et al., 1996). Ketzef et al. proposed that the excitatory/inhibitory imbalance in networks lacking synapsins may serve as the initiator of epileptogenic activity, but that the increased inhibitory components in adult SynTKO are underlying the epileptic phenotype (Ketzef et al., 2011). Thus, normal LTP at the mossy fiber bouton might be due to a more balanced excitatory versus inhibitory transmission in adult animals, probably via increased inhibitory recurrent connections (Ketzef et al., 2011).

Summary of Synapsin-Dependent Transmission and Plasticity

In summary, we observed increased excitability and reduced short-term plasticity at mossy fiber to CA3 pyramidal cell synapses of SynTKO animals. These changes can likely be attributed to differential roles of synapsins in excitatory and inhibitory neurons as well as to impaired synaptic vesicle pools and vesicle recruitment. Long-term potentiation was increased in young SynTKO animals while it was normal in older SynTKO after the onset of epileptic seizures. It has been suggested that an increased inhibitory component exists in older SynTKO after the onset of epileptic seizures (Ketzef et al., 2011), which might explain these

differences. The increased potentiation in presymptomatic animals might be specifically caused by the absence of synapsin III, that could act as a regulator of vesicular release during long-term potentiation.

Perspective

In this thesis, I investigated the possible involvement of the presynaptic proteins Munc13-1, Ca_v2 calcium channels and synapsins in hippocampal mossy fiber presynaptic plasticity. While the complete cascade underlying long-term increase in transmitter release remains enigmatic, my work contributes to a better understanding of the involved molecules.

A tightening in the coupling distance between voltage-gated calcium channels and release sites could lead to strong increases in the release probability. However, I found an unchanged distance between voltage-gated calcium channels and release sites after chemical potentiation, suggesting no major changes in the coupling distance. In contrast, a recent preprint reports a tightening of 6 nm after mossy fiber potentiation (Kim et al., 2023). While technical limitations in my approach might explain this discrepancy, many questions remain to be clarified, including the temporal deciphering of mechanisms. It is unclear when post-tetanic potentiation transitions into long-term potentiation and which molecular mechanisms support the individual steps. It might be that only early changes include a tightening in the coupling distance between voltage-gated calcium channels and release sites, that are later on supplemented or exchanged by other mechanisms. Detailed experiments with high-resolution techniques at different time points after induction and with different induction methods are needed, to unravel the course of action after induction of long-term plasticity. Such experiments should also include a detailed topographic analysis of the distribution of all Ca_v2 channel types. My experiments revealed, that the $Ca_v2.3$ calcium channel is situated closer to release sites than the other two Ca_v2 calcium channels, implicating a special role of this channel, that might reach beyond its role in the induction of mossy fiber long-term potentiation (Breustedt et al., 2003).

It has been suggested that mossy fiber potentiation is accompanied by increased numbers of functional release sites (Tong et al., 1996; Orlando et al., 2021). I showed that the net content of Munc13-1 is likely not changing in mossy fibers after chemical potentiation. In contrast to cytomatrix components (Monday et al., 2022), Munc13-1 might not be translated locally during mossy fiber potentiation, but the insertion of new active zones might be fed from existing supplies. A recent publication suggests an increase in Munc13-1 clusters within individual mossy fiber active zones after potentiation (Kim et al., 2023). Possibly, the number of single Munc13-1 molecules within one active zone does not increase, but Munc13-1 rearranges spatially instead. This could include a clustering within active zones (Kim et al., 2023) as well as conformational changes of individual Munc13-1 molecules into tight docking and priming states (Neher and Brose, 2018;

Quade et al., 2019). In sum, such changes might increase the fusion competence of individual vesicles in concert with an increase in the total number of functional release sites.

Notably, I observed a gradient of Munc13-1 content along the proximal-distal axis of hippocampal area CA3, suggesting differential synaptic connectivity between mossy fibers and their postsynaptic partners along that axis. This would be in line with a recent publication showing that a subpopulation of “athorny” CA3 pyramidal cells is more abundant in the distal CA3, that might not be targeted by mossy fibers (Hunt et al., 2018). On a functional level, such differences in connectivity of mossy fibers onto CA3 pyramidal cells might promote pattern completion in an interplay with CA3 recurrent activity (Hunt et al., 2018; Sammons et al., 2024).

Upon increased demands of vesicle fusion, enhanced vesicle replenishment into the readily releasable pool is needed. We showed that the complete loss of synapsins leads to increased synaptic depression during high-frequency stimulation as well as to a reduced post-tetanic potentiation. Both effects can likely be attributed to reduced synaptic vesicle pools and therefore an impaired replenishment, highlighting synapsins role in the provision of vesicles also at the mossy fiber bouton. These synapsin-dependent mechanisms might be directly linked to short-term memory mechanisms (Vandael et al., 2020). Long-term potentiation was not reduced in SynTKO mice, suggesting that synapsin-dependent replenishment is especially important during and right after high-frequency induction. However, the magnitude of long-term potentiation was increased in presymptomatic SynTKO animals. With respect to previous literature (Spillane et al., 1995) one could speculate about a mossy fiber-specific role for synapsin III in the fine-tuning of release dynamics, as it has been proposed for other synapses before (Kile et al., 2010). Future experiments at mossy fiber boutons lacking only synapsin III are needed to elucidate the exact role of this isoform in mossy fiber presynaptic plasticity in health and disease.

In summary, the results of my thesis provide insight into mechanisms underlying presynaptic potentiation at the hippocampal mossy fiber bouton. While many questions about the physiology of this synapse remain, every little step helps to shed new light on its function. The understanding of this unique synapse will lead to a deeper understanding of the hippocampal circuitry and eventually to a better understanding of processes underlying learning and memory formation. In the long term, this will help to understand some of the most enigmatic brain functions and might contribute to curing neurological diseases.

References

Aarts E, Verhage M, Veenvliet J V., Dolan C V., Van Der Sluis S (2014) A solution to dependency: Using multilevel analysis to accommodate nested data. Nat Neurosci 17:491–496.

Abbe PE (1882) The Relation of Aperture and Power in the Microscope (continued). :460–473.

Acsády L, Káli S (2007) Models, structure, function: the transformation of cortical signals in the dentate gyrus. Prog Brain Res 163:577–599.

Acsády L, Kamondi A, Sík A, Freund T, Buzsáki G (1998) GABAergic cells are the major postsynaptic targets of mossy fibers in the rat hippocampus. J Neurosci 18:3386–3403.

Addis DR, Wong AT, Schacter DL (2007) Remembering the past and imagining the future: Common and distinct neural substrates during event construction and elaboration. Neuropsychologia 45:1363–1377.

Adler EM, Augustine GJ, Duffy SN, Charlton MP (1991) Alien intracellular calcium chelators attenuate neurotransmitter release at the squid giant synapse. J Neurosci 11:1496 LP – 1507.

Agster KL, Burwell RD (2013) Hippocampal and subicular efferents and afferents of the perirhinal, postrhinal, and entorhinal cortices of the rat. Behav Brain Res 254:50–64.

Altman J, Bayer SA (1990) Migration and distribution of two populations of hippocampal granule cell precursors during the perinatal and postnatal periods. J Comp Neurol 301:365–381.

Altman J, Das GD (1965) Autoradiographic and histological evidence of postnatal hippocampal neurogenesis in rats. J Comp Neurol 124:319–335.

Amaral DG (1979) Synaptic extensions from the mossy fibers of the fascia dentata. Anat Embryol (Berl) 155:241–251.

Amaral DG, Dent JA (1981) Development of the mossy fibers of the dentate gyrus: I. A light and electron microscopic study of the mossy fibers and their expansions. J Comp Neurol 195:51–86.

Amaral DG, Ishizuka N, Claiborne B (1990) Chapter Neurons, numbers and the hippocampal network. Prog Brain Res 83:1–11.

Amaral DG, Scharfman HE, Lavenex P (2007) The dentate gyrus: fundamental neuroanatomical organization (dentate gyrus for dummies). Prog Brain Res 163.

Amaral DG, Witter MP (1989) The three-dimensional organization of the hippocampal formation: A review of anatomical data. Neuroscience 31:571–591.

Andersen P, Bliss TVP, Skrede KK (1971) Lamellar organization of hippocampal excitatory pathways. Exp Brain Res 13:222–238.

Andersen P, Morris R, Amaral D, Bliss T, O'Keefe J (2007) The Hippocampus Book, First. New York: Oxford University Press.

Ando M, Oku N, Takeda A (2010) Zinc-mediated attenuation of hippocampal mossy fiber long-term potentiation induced by forskolin. Neurochem Int 57:608–614.

Aravamudan B, Fergestad T, Davis WS, Rodesch CK, Broadie K (1999) Drosophila UNC-13 is essential for synaptic transmission. Nat Neurosci 2:965–971.

Armstrong JN, Saganich MJ, Xu NJ, Henkemeyer M, Heinemann SF, Contractor A (2006) B-ephrin reverse signaling is required for NMDA-independent long-term potentiation of mossy fibers in the hippocampus. J Neurosci 26:3474–3481.

Atluri PP, Regehr WG (1996) Determinants of the time course of facilitation at the granule cell to Purkinje cell synapse. J Neurosci 16:5661–5671.

Atluri PP, Regehr WG (1998) Delayed release of neurotransmitter from cerebellar granule cells. J Neurosci 18:8214–8227.

Atwood HL, Karunanithi S (2002) Diversification of synaptic strength: Presynaptic elements. Nat Rev Neurosci 3:497–516.

Augustin I, Betz A, Herrmann C, Jo T, Brose N (1999a) Differential expression of two novel Munc13 proteins in rat brain. Biochem J 337:363–371.

Augustin I, Rosenmund C, Su TC, Brose N (1999b) Munc13-1 is essential for fusion competence of glutamatergic synaptic vesicles. 263:457–461.

Augustine GJ, Santamaria F, Tanaka K (2003) Local calcium signaling in neurons. Neuron 40:331–346.

Avoli M, Barbarosle M, Lücke A, Nagao T, Lopantsev V, Köhling R (1996) Synchronous GABA-mediated potentials and epileptiform discharges in the rat limbic system in vitro. J Neurosci 16:3912–3924.

Bacaj T, Wu D, Yang X, Morishita W, Zhou P, Xu W, Malenka RC, Südhof TC (2013) Synaptotagmin-1 and Synaptotagmin-7 Trigger Synchronous and Asynchronous Phases of Neurotransmitter Release. Neuron 80:947–959.

Baldelli P, Fassio A, Valtorta F, Benfenati F (2007) Lack of synapsin I reduces the readily releasable pool of synaptic vesicles at central inhibitory synapses. J Neurosci 27:13520–13531.

Barr DJ, Levy R, Scheepers C, Tily HJ (2013) Random effects structure for confirmatory hypothesis testing: Keep it maximal. J Mem Lang 68:255–278.

Basu J, Betz A, Brose N, Rosenmund C (2007) Munc13-1 C1 domain activation lowers the energy barrier for synaptic vesicle fusion. J Neurosci 27:1200–1210.

Basu J, Shen N, Dulubova I, Lu J, Guan R, Guryev O, Grishin N V., Rosenmund C, Rizo J (2005) A minimal domain responsible for Munc13 activity. Nat Struct Mol Biol 12:1017–1018.

Bates D, Mächler M, Bolker B, Walker S (2015) Fitting Linear Mixed-Effects Models Using lme4. J Stat Softw 67.

Bear MF, Malenka RC (1994) Synaptic plasticity: LTP and LTD. Curr Opin Neurobiol 4:389–399.

Beltrán JQ, Gutiérrez R (2012) Co-release of glutamate and GABA from single, identified mossy fibre giant boutons. J Physiol 590:4789–4800.

Ben-Simon Y, Rodenas-Ruano A, Alviña K, Lam AD, Stuenkel EL, Castillo PE, Ashery U (2015) A Combined Optogenetic-Knockdown Strategy Reveals a Major Role of Tomosyn in Mossy Fiber Synaptic Plasticity. Cell Rep 12:396–404.

Benfenati F, Bahler M, Jahn R, Greengard P (1989) Interactions of synapsin I with small synaptic vesicles: Distinct sites in synapsin I bind to vesicle phospholipids and vesicle proteins. J Cell Biol 108:1863–1872.

Benjamini Y, Hochberg Y (1995) Controlling the False Discovery Rate: A Practical and Powerful Approach to Multiple Testing. J R Stat Soc Ser B 57:289–300.

Berridge MJ, Bootman MD, Roderick HL (2003) Calcium signalling: Dynamics, homeostasis and remodelling. Nat Rev Mol Cell Biol 4:517–529.

Betz A, Ashery U, Rickmann M, Augustin I, Neher E, Su TC, Rettig J, Brose N (1998) Munc13-1 Is a Presynaptic Phorbol Ester Receptor that Enhances Neurotransmitter Release. 21:123–136.

Betz A, Thakur P, Junge HJ, Ashery U, Rhee JS, Scheuss V, Rosenmund C, Rettig J, Brose N (2001) Functional interaction of the active zone proteins Munc13-1 and RIM1 in synaptic vesicle priming. Neuron 30:183–196.

Bhangu PS, Genever PG, Spencer GJ, Grewal TS, Skerry TM (2001) Evidence for targeted vesicular glutamate exocytosis in osteoblasts. Bone 29:16–23.

Biederer T, Kaeser PS, Blanpied TA (2017) Transcellular Nanoalignment of Synaptic Function. Neuron 96:680–696.

Bischofberger J, Engel D, Li L, Geiger JRP, Jonas P (2006) Patch-clamp recording from mossy fiber terminals in hippocampal slices. Nat Protoc 1:2075–2081.

Blackstad TW, Kjaerheim Å (1961) Special axo-dendritic synapses in the hippocampal cortex: Electron and light microscopic studies on the layer of mossy fibers. J Comp Neurol 117:133–159.

Blatow M, Caputi A, Burnashev N, Monyer H, Rozov A (2003) Ca2+ Buffer Saturation Underlies Paired Pulse Facilitation in Calbindin-D28k-Containing Terminals. Neuron 38:79–88.

Bliss TVP, Gardner-Medwin AR (1973) Long-lasting potentiation of synaptic transmission in the dentate area of the unanaesthetized rabbit following stimulation of the perforant path. J Physiol 232:357–374.

Bliss TVP, Lømo T (1973) Long-lasting potentiation of synaptic transmission in the dentate area of the anaesthetized rabbit following stimulation of the perforant path. J Physiol 232:331–356.

Blom H, Widengren J (2017) Stimulated Emission Depletion Microscopy. Chem Rev 117:7377–7427.

Bogen IL, Jensen V, Hvalby O, Walaas SI (2009) Synapsin-dependent development of glutamatergic synaptic vesicles and presynaptic plasticity in postnatal mouse brain. Neuroscience 158:231–241.

Böhme MA, Grasskamp AT, Walter AM (2018) Regulation of synaptic release-site Ca2+ channel coupling as a mechanism to control release probability and short-term plasticity. FEBS Lett 592:3516–3531.

Boido D, Farisello P, Cesca F, Ferrea E, Valtorta F, Benfenati F, Baldelli P (2010) Cortico-hippocampal hyperexcitability in synapsin I/II/III knockout mice: Age-dependency and response to the antiepileptic drug levetiracetam. Neuroscience 171:268–283.

Boldrini M, Fulmore CA, Tartt AN, Simeon LR, Pavlova I, Poposka V, Rosoklija GB, Stankov A, Arango V, Dwork AJ, Hen R, Mann JJ (2018) Human Hippocampal Neurogenesis Persists throughout Aging. Cell Stem Cell 22:589-599.e5.

Bornschein G, Schmidt H (2019) Synaptotagmin Ca2+ Sensors and Their Spatial Coupling to Presynaptic Cav Channels in Central Cortical Synapses. Front Mol Neurosci 11.

Borst JGG, Sakmann B (1996) Calcium influx and transmitter release in a fast CNS synapse. Nature 383:431–434.

Branco Tiago, Staras Kevin (2009) The probability of neurotransmitter release: variability and feedback control at single synapses. Nat Rev Neurosci 10:373–383.

Brenes O, Vandael DHF, Carbone E, Montarolo PG, Ghirardi M (2015) Knock-down of synapsin alters cell excitability and action potential waveform by potentiating BK and voltage-gated Ca2+ currents in Helix serotonergic neurons. Neuroscience 311:430–443.

Breustedt J, Gundlfinger A, Varoqueaux F, Reim K, Brose N, Schmitz D (2010) Munc13-2 differentially affects hippocampal synaptic transmission and plasticity. Cereb Cortex 20:1109–1120.

Breustedt J, Vogt KE, Miller RJ, Nicoll RA, Schmitz D (2003) Alpha1E-containing Ca2+ channels are involved in synaptic plasticity. Proc Natl Acad Sci U S A 100:12450–12455.

Brockmann MM, Maglione M, Willmes CG, Stumpf A, Bouazza BA, Velasquez LM, Grauel MK, Beed P, Lehmann M, Gimber N, Schmoranzer J, Sigrist SJ, Rosenmund C, Schmitz D (2019) RIM-BP2 primes synaptic vesicles via recruitment of Munc13-1 at hippocampal mossy fiber synapses. Elife 8:1–22.

Brose N, Petrenko AG, Südhof TC, Jahn R (1992) Synaptotagmin: a Calcium Sensor on the Synaptic Vesicle Surface. Science (80-) 256:1021–1025.

Bruentgens F, Velasquez LM, Stumpf A, Parthier D, Breustedt J, Benfenati F, Milovanovic D, Schmitz D, Orlando M (2023) The synapsin-dependent vesicle cluster is crucial for presynaptic plasticity at a glutamatergic synapse in male mice.

Buckmaster PS, Edward Dudek F (1997) Network properties of the dentate gyms in epileptic rats with hilar neuron loss and granule cell axon reorganization. J Neurophysiol 77:2685–2696.

Buckmaster PS, Wenzel HJ, Kunkel DD, Schwartzkroin PA (1996) Axon arbors and synaptic connections of hippocampal mossy cells in the rat in vivo. J Comp Neurol 366:270–292.

Bucurenciu I, Bischofberger J, Jonas P (2010) A small number of open Ca 2+ channels trigger transmitter release at a central GABAergic synapse. Nat Neurosci 13:19–21.

Bucurenciu I, Kulik A, Schwaller B, Frotscher M, Jonas P (2008) Nanodomain Coupling between Ca2+ Channels and Ca2+ Sensors Promotes Fast and Efficient Transmitter Release at a Cortical GABAergic Synapse. Neuron 57:536–545.

Bustos R, Kolen ER, Braiterman L, Baines AJ, Gorelick FS, Hubbard AL (2001) Synapsin I is expressed in epithelial cells: Localization to a unique trans-Golgi compartment. J Cell Sci 114:3695–3704.

Buzsáki G, Moser EI (2013) Memory, navigation and theta rhythm in the hippocampal-entorhinal system. Nat Neurosci 16:130–138.

Camacho M, Basu J, Trimbuch T, Chang S, Pulido-Lozano C, Chang SS, Duluvova I, Abo-Rady M, Rizo J, Rosenmund C (2017) Heterodimerization of Munc13 C2A domain with RIM regulates synaptic vesicle docking and priming. Nat Commun 8:1–13.

Candiani S, Moronti L, Pennati R, De Bernardi F, Benfenati F, Pestarino M (2010) The synapsin gene family in basal chordates: evolutionary perspectives in metazoans. BMC Evol Biol 10:32.

Carta M, Srikumar BN, Gorlewicz A, Rebola N, Mulle C (2018) Activity-dependent control of NMDA receptor subunit composition at hippocampal mossy fibre synapses. J Physiol 596:703–716.

Castillo PE (2012) Presynaptic LTP and LTD of Excitatory and Inhibitory Synapses.

Castillo PE, Janz R, Südhof TC, Tzounopoulos T, Malenka RC, Nicoll RA (1997) Rab3A is essential for mossy fibre long-term potentiation in the hippocampus. Nature 388:590–593.

Castillo PE, Jung H, Klann E, Riccio A (2023) Presynaptic Protein Synthesis in Brain Function and Disease. J Neurosci 43:7483–7488.

Castillo PE, Schoch S, Schmitz F, Südhof TC, Malenka RC (2002) RIM1α is required for presynaptic long-term potentiation. Nature 415:327–330.

Castillo PE, Weisskopf MG, Nicoll RA (1994) The role of Ca2+channels in hippocampal mossy fiber synaptic transmission and long-term potentiation. Neuron 12:261–269.

Catterall WA (2011) Voltage-Gated Calcium Channels. Cold Spring Harb Perspect Biol 3:a003947.

Cembrowski MS, Spruston N (2019) Heterogeneity within classical cell types is the rule: lessons from hippocampal pyramidal neurons. Nat Rev Neurosci 20:193–204.

Cesca F, Baldelli P, Valtorta F, Benfenati F (2010) The synapsins: Key actors of synapse function and plasticity. Prog Neurobiol 91:313–348.

Chamberland S, Evstratova A, Tóth K (2014) Interplay between synchronization of multivesicular release and recruitment of additional release sites support short-term facilitation at hippocampal mossy fiber to CA3 pyramidal cells synapses. J Neurosci 34:11032–11047.

Chamberland S, Evstratova A, Tóth K (2017) Short-term facilitation at a detonator synapse requires the distinct contribution of multiple types of voltage-gated calcium channels. J Neurosci 37:4913–4927.

Cheng Q, Song S, Augustine GJ (2018) Molecular Mechanisms of Short-Term Plasticity: Role of Synapsin Phosphorylation in Augmentation and Potentiation of Spontaneous Glutamate Release. Front Synaptic Neurosci 10:1–12.

Chi P, Greengard P, Ryan TA (2001) Synapsin dispersion and reclustering during synaptic activity. Nat Neurosci 4:1187–1193.

Chi P, Greengard P, Ryan TA (2003) Synaptic vesicle mobilization is regulated by distinct synapsin I phosphorylation pathways at different frequencies. Neuron 38:69–78.

Chiappalone M, Casagrande S, Tedesco M, Valtorta F, Baldelli P, Martinoia S, Benfenati F (2009) Opposite changes in glutamatergic and GABAergic transmission underlie the diffuse hyperexcitability of synapsin i-deficient cortical networks. Cereb Cortex 19:1422–1439.

Chicurel ME, Harris KM (1992) Three-dimensional analysis of the structure and composition of CA3 branched dendritic spines and their synaptic relationships with mossy fiber boutons in the rat hippocampus. J Comp Neurol 325:169–182.

Chierzi S, Stachniak TJ, Trudel E, Bourque CW, Murai KK (2012) Activity maintains structural plasticity of mossy fiber terminals in the hippocampus. Mol Cell Neurosci 50:260–271.

Claiborne BJ, Amaral DG, Cowan WM (1986) A light and electron microscopic analysis of the mossy fibers of the rat dentate gyrus. J Comp Neurol 246:435–458.

Clapham DE (2007) Calcium Signaling. Cell 131:1047–1058.

Cole TB, Wenzel HJ, Kafer KE, Schwartzkroin PA, Palmiter RD (1999) Elimination of zinc from synaptic vesicles in the intact mouse brain by disruption of the ZnT 3 gene. Proc Natl Acad Sci 96:1716–1721.

Coleman WL, Kulp AC, Venditti JJ (2015) Functional distribution of synapsin I in human sperm. FEBS Open Bio 5:801–808.

Contractor A, Rogers C, Maron C, Henkemeyer M, Swanson GT, Heinemann SF (2002) Trans-synaptic Eph receptor-ephrin signaling in hippocampal mossy fiber LTP. Science (80-) 296:1864–1869.

Contractor A, Swanson G, Heinemann SF (2001) Kainate receptors are involved in short- and long-term plasticity at mossy fiber synapses in the hippocampus. Neuron 29:209–216.

Corkin S (2002) What's new with the amnesic patient H.M.? Nat Rev Neurosci 3:153–160.

Cox DH, Dunlap K (1992) Pharmacological discrimination of N-type from L-type calcium current and its selective modulation by transmitters. J Neurosci 12:606–614.

Da Silva PP, Kan FWK (1984) Label-fracture: A method for high resolution labeling of cell surfaces. J Cell Biol 99:1156–1161.

Dalton MA, D'souza A, Lv J, Calamante F (2022) New insights into anatomical connectivity along the anterior–posterior axis of the human hippocampus using in vivo quantitative fibre tracking. Elife 11:1–29.

Day NC, Shaw PJ, McCormack AL, Craig PJ, Smith W, Beattie R, Williams TL, Ellis SB, Ince PG, Harpold MM, Lodge D, Volsen SG (1996) Distribution ofα1A, α1B andα1E voltage-dependent calcium channel subunits in the human hippocampus and parahippocampal gyrus. Neuroscience 71:1013–1024.

De Camilli P, Benfenati F, Valtorta F, Greengard P (1990) The synapsins. Annu Rev Cell Biol 6:433–460.

De Camilli P, Harris SM, Huttner WB, Greengard P (1983) Synapsin I (Protein I), a nerve terminal-specific phosphoprotein. II. Its specific association with synaptic vesicles demonstrated by immunocytochemistry in agarose-embedded synaptosomes. J Cell Biol 96:1355–1373.

De Lecea L, Criado JR, Rivera S, Wen W, Soriano E, Henriksen SJ, Taylor SS, Gall CM, Sutcliffe JG (1998) Endogenous protein kinase a inhibitor (PKIα) modulates synaptic activity. J Neurosci Res 53:269–278.

De Paola V, Arber S, Caroni P (2003) AMPA receptors regulate dynamic equilibrium of presynaptic terminals in mature hippocampal networks. Nat Neurosci 6:491–500.

Deng L, Kaeser PS, Xu W, Südhof TC (2011) RIM proteins activate vesicle priming by reversing autoinhibitory homodimerization of munc13. Neuron 69:317–331.

Denker A, Rizzoli SO (2010) Synaptic vesicle pools: An update. Front Synaptic Neurosci 2:1–12.

Diamantaki M, Frey M, Berens P, Preston-Ferrer P, Burgalossi A (2016) Sparse activity of identified dentate granule cells during spatial exploration. Elife 5:1–17.

Diamond JS, Jahr CE (1995) Asynchronous release of synaptic vesicles determines the time course of the AMPA receptor-mediated EPSC. Neuron 15:1097–1107.

Dieck S, Sanmartí-vila L, Langnaese K, Richter K, Kindler S, Soyke A, Wex H, Smalla K, Kämpf U, Fränzer J, Stumm M, Garner CC, Gundelfinger ED (1998) Bassoon, a Novel Zinc-finger CAG/Glutamine-repeat Protein Selectively Localized at the Active Zone of Presynaptic Nerve Terminals. 142:499–509.

Dieni S, Matsumoto T, Dekkers M, Rauskolb S, Ionescu MS, Deogracias R, Gundelfinger ED, Kojima M, Nestel S, Frotscher M, Barde Y-A (2012) BDNF and its pro-peptide are stored in presynaptic dense core vesicles in brain neurons. J Cell Biol 196:775–788.

Dieni C V., Nietz AK, Panichi R, Wadiche JI, Overstreet-Wadiche L (2013) Distinct determinants of sparse activation during granule cell maturation. J Neurosci 33:19131–19142.

Dietrich D, Kirschstein T, Kukley M, Pereverzev A, Von Der Brelie C, Schneider T, Beck H (2003) Functional specialization of presynaptic Cav2.3 Ca2+ channels. Neuron 39:483–496.

Dittman JS, Ryan TA (2019) The control of release probability at nerve terminals. Nat Rev Neurosci 20:177.

Dobrunz LE, Stevens CF (1997) Heterogeneity of release probability, facilitation, and depletion at central synapses. Neuron 18:995–1008.

Dolphin AC, Lee A (2020) Presynaptic calcium channels: specialized control of synaptic neurotransmitter release. Nat Rev Neurosci 21:213–229.

Dubel SJ, Starr TVB, Hell J, Ahlijanian MK, Enyeart JJ, Catterall WA, Snutch TP (1992) Molecular cloning of the alpha-1 subunit of an omega-conotoxin-sensitive calcium channel. Proc Natl Acad Sci 89:5058–5062.

Dulubova I, Sugita S, Hill S, Hosaka M, Fernandez I, Südhof TC, Rizo J (1999) A conformational switch in syntaxin during exocytosis: Role of munc18. EMBO J 18:4372–4382.

Dumenieu M, Senkov O, Mironov A, Bourinet E, Kreutz MR, Dityatev A, Heine M, Bikbaev A, Lopez-Rojas J (2018) The Low-Threshold Calcium Channel Cav3.2 Mediates Burst Firing of Mature Dentate Granule Cells. Cereb Cortex 28:2594–2609.

Edelmann E, Leßmann V, Brigadski T (2014) Pre- and postsynaptic twists in BDNF secretion and action in synaptic plasticity. Neuropharmacology 76:610–627.

Eggermann E, Bucurenciu I, Goswami SP, Jonas P (2012) Nanodomain coupling between Ca2+ channels and sensors of exocytosis at fast mammalian synapses. Nat Rev Neurosci 13:7–21.

Eichenbaum H (1997) Declarative Memory: Insights from Cognitive Neurobiology. Annu Rev Psychol 48:547–572.

Eichenbaum H (2017) The role of the hippocampus in navigation is memory. J Neurophysiol 117:1785–1796.

Eilers Y, Ta H, Gwosch KC, Balzarotti F, Hell SW (2018) MINFLUX monitors rapid molecular jumps with superior spatiotemporal resolution. Proc Natl Acad Sci 115:6117–6122.

Éltes T, Kirizs T, Nusser Z, Holderith N (2017) Target Cell Type-Dependent Differences in Ca2+ Channel Function Underlie Distinct Release Probabilities at Hippocampal Glutamatergic Terminals. J Neurosci 37:1910–1924.

Emptage NJ, Reid CA, Fine A (2001) Calcium stores in hippocampal synaptic boutons mediate short-term plasticity, store-operated Ca2+ entry, and spontaneous transmitter release. Neuron 29:197–208.

Engel J (1996) Excitation and inhibition in epilepsy. Can J Neurol Sci 23:167–174.

Ermolyuk YS, Alder FG, Surges R, Pavlov IY, Timofeeva Y, Kullmann DM, Volynski KE (2013) Differential triggering of spontaneous glutamate release by P/Q-, N- and R-type Ca2+ channels. Nat Neurosci 16:1754–1763.

Erwin SR, Sun W, Copeland M, Lindo S, Spruston N, Cembrowski MS (2020) A Sparse, Spatially Biased Subtype of Mature Granule Cell Dominates Recruitment in Hippocampal-Associated Behaviors. Cell Rep 31:107551.

Evergren E, Benfenati F, Shupliakov O (2007) The synapsin cycle: A view from the synaptic endocytic zone. J Neurosci Res 85:2648–2656.

Evstratova A, Chamberland S, Faundez V, Tóth K (2014) Vesicles derived via AP-3-dependent recycling contribute to asynchronous release and influence information transfer. Nat Commun 5:5530.

Farisello P, Boido D, Nieus T, Medrihan L, Cesca F, Valtorta F, Baldelli P, Benfenati F (2013) Synaptic and extrasynaptic origin of the excitation/inhibition imbalance in the hippocampus of synapsin I/II/III knockout mice. Cereb Cortex 23:581–593.

Fassio A, Raimondi A, Lignani G, Benfenati F, Baldelli P (2011) Synapsins: From synapse to network hyperexcitability and epilepsy. Semin Cell Dev Biol 22:408–415.

Fdez E, Hilfiker S (2006) Vesicle pools and synapsins: New insights into old enigmas. Brain Cell Biol 35:107–115.

Fedchyshyn MJ, Wang L-Y (2005) Developmental transformation of the release modality at the calyx of Held synapse. J Neurosci 25:4131–4140.

Feng J, Chi P, Blanpied TA, Xu Y, Magarinos AM, Ferreira A, Takahashi RH, Kao HT, McEwen BS, Ryan TA, Augustine GJ, Greengard P (2002) Regulation of Neurotransmitter Release by Synapsin III. J Neurosci 22:4372–4380.

Fernandes HB, Riordan S, Nomura T, Remmers CL, Kraniotis S, Marshall JJ, Kukreja L, Vassar R, Contractor A (2015) Epac2 mediates cAMP-dependent potentiation of neurotransmission in the hippocampus. J Neurosci 35:6544–6553.

Ferreira A, Kao HT, Feng J, Rapoport M, Greengard P (2000) Synapsin III: Developmental expression, subcellular localization, and role in axon formation. J Neurosci 20:3736–3744.

Ferry G (2019) Paul Greengard (1925–2019). Nature 569:488–488.

Fisher SA, Fischer TM, Carew TJ (1997) Multiple overlapping processes underlying short-term synaptic enhancement. Trends Neurosci 20:170–177.

Fornasiero EF, Raimondi A, Guarnieri FC, Orlando M, Fesce R, Benfenati F, Valtorta F (2012) Synapsins contribute to the dynamic spatial organization of synaptic vesicles in an activity-dependent manner. J Neurosci 32:12214–12227.

Frotscher M, Soriano E, Misgeld U (1994) Divergence of hippocampal mossy fibers. Synapse 16:148–160.

Fukaya R, Hirai H, Sakamoto H, Hashimotodani Y, Hirose K, Sakaba T (2023a) Increased vesicle fusion competence underlies long-term potentiation at hippocampal mossy fiber synapses. Sci Adv 9:1–14.

Fukaya R, Maglione M, Sigrist SJ, Sakaba T (2021) Rapid Ca 2+ channel accumulation contributes to cAMP-mediated increase in transmission at hippocampal mossy fiber synapses. Proc Natl Acad Sci 118:1–11.

Fukaya R, Miyano R, Hirai H, Sakaba T (2023b) Mechanistic insights into cAMP-mediated presynaptic potentiation at hippocampal mossy fiber synapses. Front Cell Neurosci 17:1–8.

Galbraith S, Daniel JA, Vissel B (2010) A study of clustered data and approaches to its analysis. J Neurosci 30:10601–10608.

Galimberti I, Gogolla N, Alberi S, Santos AF, Muller D, Caroni P (2006) Long-Term Rearrangements of Hippocampal Mossy Fiber Terminal Connectivity in the Adult Regulated by Experience. Neuron 50:749–763.

Gao Y, Zorman S, Gundersen G, Xi Z, Ma L, Sirinakis G, Rothman JE, Zhang Y (2012) Single Reconstituted Neuronal SNARE Complexes Zipper in Three Distinct Stages. Science (80-) 337:1340–1343.

Garcia CC, Blair HJ, Seager M, Coulthard A, Tennant S, Buddles M, Curtis A, Goodship JA (2004) Identification of a mutation in synapsin I, a synaptic vesicle protein, in a family with epilepsy. J Med Genet 41:183–186.

Ge S, Yang C hao, Hsu K sen, Ming G li, Song H (2007) A Critical Period for Enhanced Synaptic Plasticity in Newly Generated Neurons of the Adult Brain. Neuron 54:559–566.

Geiger JRP, Jonas P (2000a) Dynamic control of presynaptic Ca2+ inflow by fast-inactivating K+ channels in hippocampal mossy fiber boutons. Neuron 28:927–939.

Geiger JRP, Jonas P (2000b) Dynamic Control of Presynaptic Ca2+ Inflow by Fast-Inactivating K+ Channels in Hippocampal Mossy Fiber Boutons. Neuron 28:927–939.

Giocomo LM, Hasselmo ME (2007) Neuromodulation by glutamate and acetylcholine can change circuit dynamics by regulating the relative influence of afferent input and excitatory feedback. Mol Neurobiol 36:184–200.

Girault JA, Greengard P (2004) The Neurobiology of Dopamine Signaling. Arch Neurol 61:641–644.

Gitler D, Cheng Q, Greengard P, Augustine GJ (2008) Synapsin IIa controls the reserve pool of glutamatergic synaptic vesicles. J Neurosci 28:10835–10843.

Gitler D, Takagishi Y, Feng J, Ren Y, Rodriguiz RM, Wetsel WC, Greengard P, Augustine GJ (2004) Different presynaptic roles of synapsins at excitatory and inhibitory synapses. J Neurosci 24:11368–11380.

Glasgow SD, McPhedrain R, Madranges JF, Kennedy TE, Ruthazer ES (2019) Approaches and limitations in the investigation of synaptic transmission and plasticity. Front Synaptic Neurosci 11:1–16.

Gogolla N, Galimberti I, Deguchi Y, Caroni P (2009) Article Wnt Signaling Mediates Experience-Related Regulation of Synapse Numbers and Mossy Fiber Connectivities in the Adult Hippocampus. Neuron 62:510–525.

Goldman-Rakic PS (1984) The frontal lobes: Uncharted provinces of the brain. Trends Neurosci 7:425–429.

Gómez-Padilla E, Bello-Medina PC, León-Jacinto U, Orta-Salazar E, Quirarte GL, Ramírez-Amaya V, Prado-Alcalá RA, Díaz-Cintra S (2020) Morris water maze overtraining increases the density of thorny excrescences in the basal dendrites of CA3 pyramidal neurons. Behav Brain Res 379:112373.

Gómez-Palacio-Schjetnan A, Escobar ML (2008) In vivo BDNF modulation of adult functional and morphological synaptic plasticity at hippocampal mossy fibers. Neurosci Lett 445:62–67.

Gorter JA, Van Vliet EA, Aronica E, Lopes Da Silva FH (2001) Progression of spontaneous seizures after status epilepticus is associated with mossy fibre sprouting and extensive bilateral loss of hilar parvalbumin and somatostatin-immunoreactive neurons. Eur J Neurosci 13:657–669.

Grauel MK, Maglione M, Reddy-Alla S, Willmes CG, Brockmann MM, Trimbuch T, Rosenmund T, Pangalos M, Vardar G, Stumpf A, Walter AM, Rost BR, Eickholt BJ, Haucke V, Schmitz D, Sigrist SJ, Rosenmund C (2016) RIM-binding protein 2 regulates release probability by fine-tuning calcium channel localization at murine hippocampal synapses. Proc Natl Acad Sci 113:11615–11620.

Greengard P, Valtorta F, Czernik AJ, Benfenati F (1993) Synaptic vesicle phosphoproteins and regulation of synaptic function. Science (80-) 259:780–785.

Gross CG (2000) Neurogenesis in the adult brain: Death of a dogma. Nat Rev Neurosci 1:67–73.

Gundlfinger A, Breustedt J, Sullivan D, Schmitz D (2010) Natural spike trains trigger short- and long lasting dynamics at hippocampal mossy fiber synapses in rodents. PLoS One 5:1–9.

Gutierrez-Mecinas M, Kuehn ED, Abraira VE, Polgár E, Watanabe M, Todd AJ (2016) Immunostaining for Homer reveals the majority of excitatory synapses in laminae I-III of the mouse spinal dorsal horn. Neuroscience 329:171–181.

Gylterud Owe S, Bogen IL, Walaas SI, Storm-Mathisen J, Bergersen LH (2005) Ultrastructural quantification of glutamate receptors at excitatory synapses in hippocampus of synapsin I+II double knock-out mice. Neuroscience 136:769–777.

Habets RLP, Borst JGG (2007) Dynamics of the readily releasable pool during post-tetanic potentiation in the rat calyx of Held synapse. J Physiol 581:467–478.

Hainmueller T (2020) Dentate gyrus circuits for encoding , retrieval and discrimination of episodic memories. Nat Rev Neurosci 21:153–168.

Hainmueller T, Bartos M (2018) Parallel emergence of stable and dynamic memory engrams in the hippocampus. Nature 558:292–296.

Hajnóczky G, Davies E, Madesh M (2003) Calcium signaling and apoptosis. Biochem Biophys Res Commun 304:445–454.

Hallermann S, Pawlu C, Jonas P, Heckmann M (2003) A large pool of releasable vesicles in a cortical glutamatergic synapse. Proc Natl Acad Sci U S A 100:8975–8980.

Hamblin MW, Guthrie CR, Kohen R, Heidmann DEA (1998) Gs Protein-Coupled Serotonin Receptors: Receptor Isoforms and Functional Differences. Ann N Y Acad Sci 861:31–37.

Hanoune J, Defer N (2001) Regulation and Role of Adenylyl Cyclase Isoforms. Annu Rev Pharmacol Toxicol 41:145–174.

Hanse E, Gustafsson B (2001) Paired-pulse plasticity at the single release site level: An experimental and computational study. J Neurosci 21:8362–8369.

Hanson PI, Heuser JE, Jahn R (1997) Neurotransmitter release - four years of SNARE complexes. Curr Opin Neurobiol 7:310–315.

Harris EW, Cotman CW (1986) Long-term potentiation of guinea pig mossy fiber responses is not blocked by N-methyl d-aspartate antagonists. Neurosci Lett 70:132–137.

Harte-Hargrove LC, MacLusky NJ, Scharfman HE (2013) Brain-derived neurotrophic factor-estrogen interactions in the hippocampal mossy fiber pathway: Implications for normal brain function and disease. Neuroscience 239:46–66.

Hashimotodani Y, Nasrallah K, Jensen KR, Chávez AE, Carrera D, Castillo PE (2017) LTP at Hilar Mossy Cell-Dentate Granule Cell Synapses Modulates Dentate Gyrus Output by Increasing Excitation/Inhibition Balance. Neuron 95:928-943.e3.

Hassabis D, Kumaran D, Maguire EA (2007) Using imagination to understand the neural basis of episodic memory. J Neurosci 27:14365–14374.

Hayashi Y, Shi SH, Esteban JA, Piccini A, Poncer JC, Malinow R (2000) Driving AMPA receptors into synapses by LTP and CaMKII: Requirement for GluR1 and PDZ domain interaction. Science (80-) 287:2262–2267.

Hebb DO (1949) The Organization of Behavior, First. John Wiley & Sons, Inc.

Heck J, Parutto P, Ciuraszkiewicz A, Bikbaev A, Freund R, Mitlöhner J, Andres-Alonso M, Fejtova A, Holcman D, Heine M (2019) Transient Confinement of CaV2.1 Ca2+-Channel Splice Variants Shapes Synaptic Short-Term Plasticity. Neuron:1–14.

Heinemann U, Beck H, Dreier JP, Ficker E, Stabel J, Zhang CL (1992) The dentate gyrus as a regulated gate for the propagation of epileptiform activity. Epilepsy Res Suppl 7:273–280.

Heintzmann R, Ficz G (2006) Breaking the resolution limit in light microscopy. Briefings Funct Genomics Proteomics 5:289–301.

Hell SW, Wichmann J (1994) Breaking the diffraction resolution limit by stimulated emission: stimulated-emission-depletion fluorescence microscopy. Opt Lett 19:780.

Henze DA, McMahon DBT, Harris KM, Barrionuevo G (2002a) Giant Miniature EPSCs at the Hippocampal Mossy Fiber to CA3 Pyramidal Cell Synapse Are Monoquantal. J Neurophysiol 87:15–29.

Henze DA, Wittner L, Buzsáki G (2002b) Single granule cells reliably discharge targets in the hippocampal CA3 network in vivo. Nat Neurosci 5:790–795.

Hess SD, Doroshenko PA, Augustine GJ (1993) A functional role for GTP-binding proteins in synaptic vesicle cycling. Science (80-) 259:1169–1172.

Hirokawa N, Sobue K, Kanda K, Harada A, Yorifuji H (1989) The cytoskeletal architecture of the presynaptic terminal and molecular structure of synapsin 1. J Cell Biol 108:111–126.

Hjorth-Simonsen A, Jeune B (1972) Origin and termination of the hippocampal perforant path in the rat studied by silver impregnation. J Comp Neurol 144:215–231.

Holahan MR, Rekart JL, Sandoval J, Routtenberg A (2006) Spatial learning induces presynaptic structural remodeling in the hippocampal mossy fiber system of two rat strains. Hippocampus 16:560–570.

Holderith N, Lorincz A, Katona G, Rózsa B, Kulik A, Watanabe M, Nusser Z (2012) Release probability of hippocampal glutamatergic terminals scales with the size of the active zone. Nat Neurosci 15:988–997.

Hosaka M, Hammer RE, Südhof TC (1999) A phospho-switch controls the dynamic association of synapsins with synaptic vesicles. Neuron 24:377–387.

Hosaka M, Südhof TC (1998) Synapsin III, a novel synapsin with an unusual regulation by Ca2+. J Biol Chem 273:13371–13374.

Houser CR, Esclapez M (1994) Localization of mRNAs encoding two forms of glutamic acid decarboxylase in the rat hippocampal formation. Hippocampus 4:530–545.

Hsu D (2007) The dentate gyrus as a filter or gate: a look back and a look ahead. Prog Brain Res 163:601–613.

Huang YY, Kandel ER (1996) Modulation of both the early and the late phase of mossy fiber LTP by the activation of β-adrenergic receptors. Neuron 16:611–617.

Huang YY, Kandel ER, Varshavsky L, Brandont EP, Qi M, Idzerda RL, Stanley McKnight G, Bourtchouladz R (1995) A genetic test of the effects of mutations in PKA on mossy fiber ltp and its relation to spatial and contextual learning. Cell 83:1211–1222.

Huang YY, Li XC, Kandel ER (1994) cAMP contributes to mossy fiber LTP by initiating both a covalently mediated early phase and macromolecular synthesis-dependent late phase. Cell 79:69–79.

Huang YZ, Pan E, Xiong ZQ, McNamara JO (2008) Zinc-Mediated Transactivation of TrkB Potentiates the Hippocampal Mossy Fiber-CA3 Pyramid Synapse. Neuron 57:546–558.

Humeau Y, Candiani S, Ghirardi M, Poulain B, Montarolo P (2011) Functional roles of synapsin: Lessons from invertebrates. Semin Cell Dev Biol 22:425–433.

Hunt DL, Linaro D, Si B, Romani S, Spruston N (2018) A novel pyramidal cell type promotes sharp-wave synchronization in the hippocampus. Nat Neurosci 21:985–995.

Hurst JL, West RS (2010) Taming anxiety in laboratory mice. Nat Methods 7:825–826.

Huson V, Regehr WG (2020) Diverse roles of Synaptotagmin-7 in regulating vesicle fusion. Curr Opin Neurobiol 63:42–52.

Huttner WB, Schiebler W, Greengard P, De Camilli P (1983) Synapsin I (protein I), a nerve terminal-specific phosphoprotein. III. Its association with synaptic vesicles studied in a highly purified synaptic vesicle preparation. J Cell Biol 96:1374–1388.

Hvalby Ø, Jensen V, Kao HT, Walaas SI (2006) Synapsin-regulated synaptic transmission from readily releasable synaptic vesicles in excitatory hippocampal synapses in mice. J Physiol 571:75–82.

Ikegaya Y, Nishiyama N, Matsuki N (2000) L-type Ca2+ channel blocker inhibits mossy fiber sprouting and cognitive deficits following pilocarpine seizures in immature mice. Neuroscience 98:647–659.

Imamura N, Nonaka A, Yamamoto H, Matsuki N, Nomura H (2011) Experience-dependent Homer1a expression in excitatory and inhibitory neurons. Neuroreport 22:353–357.

Imayoshi I, Sakamoto M, Ohtsuka T, Takao K, Miyakawa T, Yamaguchi M, Mori K, Ikeda T, Itohara S, Kageyama R (2008) Roles of continuous neurogenesis in the structural and functional integrity of the adult forebrain. Nat Neurosci 11:1153–1161.

Imig C, Min SW, Krinner S, Arancillo M, Rosenmund C, Südhof TC, Rhee JS, Brose N, Cooper BH (2014) The Morphological and Molecular Nature of Synaptic Vesicle Priming at Presynaptic Active Zones. Neuron 84:416–431.

Ingaramo M, York AG, Hoogendoorn E, Postma M, Shroff H, Patterson GH (2014) Richardson-Lucy deconvolution as a general tool for combining images with complementary strengths. ChemPhysChem 15:794–800.

Ishizuka N, Weber J, Amaral DG (1990) Organization of intrahippocampal projections originating from CA3 pyramidal cells in the rat. J Comp Neurol 295:580–623.

Jackman SL, Regehr WG (2017) The Mechanisms and Functions of Synaptic Facilitation. Neuron 94:447–464.

Jahr W, Velicky P, Danzl JG (2020) Strategies to maximize performance in STimulated Emission Depletion (STED) nanoscopy of biological specimens. Methods 174:27–41.

Jard S, Premont J, Benda P (1972) Adenylate cyclase, phosphodiesterases and protein kinase of rat glial cells in culture. FEBS Lett 26:344–348.

Ji Z, Stäubli U (2002) Presynaptic kainate receptors play different physiological roles in mossy fiber and associational-commissural synapses in CA3 of hippocampus from adult rats. Neurosci Lett 331:71–74.

Johnson M (2006) Molecular mechanisms of β2-adrenergic receptor function, response, and regulation. J Allergy Clin Immunol 117:18–24.

Jonas P, Major G, Sakmann B (1993) Quantal components of unitary EPSCs at the mossy fibre synapse on CA3 pyramidal cells of rat hippocampus. J Physiol 472:615–663.

Jones BW, Deem J, Younts TJ, Weisenhaus M, Sanford CA, Slack MC, Chin J, Nachmanson D, McKennon A, Castillo PE, McKnight GS (2016) Targeted deletion of AKAP7 in dentate granule cells impairs spatial discrimination. Elife 5:1–19.

Jung MW, McNaughton BL (1993) Spatial selectivity of unit activity in the hippocampal granular layer. Hippocampus 3:165–182.

Junge HJ, Rhee JS, Jahn O, Varoqueaux F, Spiess J, Waxham MN, Rosenmund C, Brose N (2004) Calmodulin and Munc13 form a Ca2+ sensor/effector complex that controls short-term synaptic plasticity. Cell 118:389–401.

Kaeser-Woo YJ, Younts TJ, Yang X, Zhou P, Wu D, Castillo PE, Südhof TC (2013) Synaptotagmin-12 phosphorylation by cAMP-dependent protein kinase is essential for hippocampal mossy fiber LTP. J Neurosci 33:9769–9780.

Kaeser PS, Deng L, Wang Y, Dulubova I, Liu X, Rizo J, Südhof TC (2011) RIM proteins tether Ca2+ channels to presynaptic active zones via a direct PDZ-domain interaction. Cell 144:282–295.

Kaeser PS, Regehr WG (2014) Molecular mechanisms for synchronous, asynchronous, and spontaneous neurotransmitter release. Annu Rev Physiol 76:333–363.

Kajiwara R, Wouterlood FG, Sah A, Boekel AJ, Baks-Te Bulte LTG, Witter MP (2008) Convergence of entorhinal and CA3 inputs onto pyramidal neurons and interneurons in hippocampal area CA1 - An anatomical study in the rat. Hippocampus 18:266–280.

Kamiya H, Shinozaki H, Yamamoto C (1996) Activation of metabotropic glutamate receptor type 2/3 suppresses transmission at rat hippocampal mossy fibre synapses. J Physiol 493:447–455.

Kamiya H, Umeda K, Ozawa S, Manabe T (2002) Presynaptic Ca2+ entry is unchanged during hippocampal mossy fiber long-term potentiation. J Neurosci 22:10524–10528.

Kandel ER (2001) The Molecular Biology of Memory Storage: A Dialogue Between Genes and Synapses. Science (80-) 294:1030–1038.

Kandel ER, Schwartz JH, Jessel TM, Siegelbaum SA, Hudspeth AJ (2013) Principles of Neural Science, Fifth Edit.

Kang HW, Moon HJ, Joo S hee, Lee JH (2007) Histidine residues in the IS3-IS4 loop are critical for nickel-sensitive inhibition of the Cav2.3 calcium channel. FEBS Lett 581:5774–5780.

Kao H-T, Porton B, Czernik AJ, Feng J, Yiu G, Häring M, Benfenati F, Greengard P (1998) A third member of the synapsin gene family. Proc Natl Acad Sci 95:4667–4672.

Kao H-T, Porton B, Hilfiker S, Stefani G, Pieribone VA, DeSalle R, Greengard P (1999) Molecular evolution of the synapsin gene family. J Exp Zool 285:360–377.

Karlocai MR, Heredi J, Benedek T, Holderith N, Lorincz A, Nusser Z (2021) Variability in the Munc13-1 content of excitatory release sites. Elife 10:1–25.

Katz B, Miledi R (1967) Ionic Requirements of Synaptic Transmitter Release. Nature 215:651–651.

Katz B, Miledi R (1968) The role of calcium in neuromuscular facilitation. J Physiol 195:481–492.

Katz B, Miledi R (1969) Spontaneous and evoked activity of motor nerve endings in calcium Ringer. J Physiol 203:689–706.

Kavalali ET (2015) The mechanisms and functions of spontaneous neurotransmitter release. Nat Rev Neurosci 16:5–16.

Kawamura Y, Manita S, Nakamura T, Inoue M, Kudo Y, Miyakawa H (2004) Glutamate release increases during mossy-CA3 LTP but not during Schaffer-CA1 LTP. Eur J Neurosci 19:1591–1600.

Kawasaki H, Springett GM, Mochizuki N, Toki S, Nakaya M, Matsuda M, Housman DE, Graybiel AM (1998) A family of cAMP-binding proteins that directly activate Rap1. Science (80-) 282:2275–2279.

Kempermann G, Gage FH (2000) Neurogenesis in the adult hippocampus. Novartis Found Symp 231:220–235; discussion 235-41, 302–306.

Ketzef M, Kahn J, Weissberg I, Becker AJ, Friedman A, Gitler D (2011) Compensatory network alterations upon onset of epilepsy in synapsin triple knock-out mice. Neuroscience 189:108–122.

Khalilov I, Le Van Quyen M, Gozlan H, Ben-Ari Y (2005) Epileptogenic actions of GABA and fast oscillations in the developing hippocampus. Neuron 48:787–796.

Kielland A, Erisir A, Walaas SI, Heggelund P (2006) Synapsin utilization differs among functional classes of synapses on thalamocortical cells. J Neurosci 26:5786–5793.

Kile BM, Guillot TS, Venton BJ, Wetsel WC, Augustine GJ, Wightman RM (2010) Synapsins differentially control dopamine and serotonin release. J Neurosci 30:9762–9770.

Kim O, Okamoto Y, Brose N, Shigemoto R, Jonas P (2023) Presynaptic cAMP-PKA-mediated potentiation induces reconfiguration of synaptic vesicle pools and channel-vesicle coupling at hippocampal mossy fiber boutons. bioRxiv.

Kitamura T, MacDonald CJ, Tonegawa S (2015) Entorhinal-hippocampal neuronal circuits bridge temporally discontiguous events. Learn Mem 22:438–443.

Klapoetke NC et al. (2014) Independent optical excitation of distinct neural populations. Nat Methods 11:338–346.

Klausnitzer J, Manahan-Vaughan D (2008) Frequency facilitation at mossy fiber-CA3 synapses of freely behaving rats is regulated by adenosine A1 receptors. J Neurosci 28:4836–4840.

Kochubey O, Schneggenburger R (2011) Synaptotagmin Increases the Dynamic Range of Synapses by Driving Ca2+-Evoked Release and by Clamping a Near-Linear Remaining Ca2+ Sensor. Neuron 69:736–748.

Kokaia M (2000) Long-term potentiation of single subicular neurons in mice. Hippocampus 10:684–692.

Kusick GF, Chin M, Raychaudhuri S, Lippmann K, Adula KP, Hujber EJ, Vu T, Davis MW, Jorgensen EM, Watanabe S (2020) Synaptic vesicles transiently dock to refill release sites. Nat Neurosci 23:1329–1338.

Kwon HB, Castillo PE (2008) Long-Term Potentiation Selectively Expressed by NMDA Receptors at Hippocampal Mossy Fiber Synapses. Neuron 57:108–120.

Larimer P, Strowbridge BW (2008) Nonrandom local circuits in the dentate gyrus. J Neurosci 28:12212–12223.

Lauri SE, Bortolotto ZA, Nistico R, Bleakman D, Ornstein PL, Lodge D, Isaac JTR, Collingridge GL (2003) A role for Ca2+ stores in kainate receptor-dependent synaptic facilitation and LTP at mossy fiber synapses in the hippocampus. Neuron 39:327–341.

Lavoie N, Jeyaraju D V., Peralta MR, Seress L, Pellegrini L, Tóth K (2011) Vesicular zinc regulates the Ca 2+ sensitivity of a subpopulation of presynaptic vesicles at hippocampal mossy fiber terminals. J Neurosci 31:18251–18265.

Lawrence JJ, Grinspan ZM, McBain CJ (2004) Quantal transmission at mossy fibre targets in the CA3 region of the rat hippocampus. J Physiol 554:175–193.

Le Duigou C, Simonnet J, Teleñczuk MT, Fricker D, Miles R (2014) Recurrent synapses and circuits in the CA3 region of the hippocampus: An associative network. Front Cell Neurosci 7:1–13.

Lee ACH, Yeung LK, Barense MD (2012) The hippocampus and visual perception. Front Hum Neurosci 6:1–17.

Lee JW, Jung MW (2017) Separation or binding? Role of the dentate gyrus in hippocampal mnemonic processing. Neurosci Biobehav Rev 75:183–194.

Leutgeb JK, Leutgeb S, Moser MB, Moser EI (2007) Pattern separation in the dentate gyrus and CA3 of the hippocampus. Science (80-) 315:961–966.

Li L, Bischofberger J, Jonas P (2007) Differential Gating and Recruitment of P/Q-, N-, and R-Type Ca 2+ Channels in Hippocampal Mossy Fiber Boutons. J Neurosci 27:13420–13429.

Li L, Chin LS, Shupliakov O, Brodin L, Sihra TS, Hvalby O, Jensen V, Zheng D, McNamara JO, Greengard P (1995) Impairment of synaptic vesicle clustering and of synaptic transmission, and increased seizure propensity, in synapsin I-deficient mice. Proc Natl Acad Sci 92:9235–9239.

Li S, Raychaudhuri S, Lee SA, Brockmann MM, Wang J, Kusick G, Prater C, Syed S, Falahati H, Ramos R, Bartol TM, Hosy E, Watanabe S (2021) Asynchronous release sites align with NMDA receptors in mouse hippocampal synapses. Nat Commun 12:1–13.

Li X -G, Somogyi P, Ylinen A, Buzsáki G (1994) The hippocampal CA3 network: An in vivo intracellular labeling study. J Comp Neurol 339:181–208.

Li Y, Hough CJ, Frederickson CJ, Sarvey JM (2001) Induction of mossy fiber→CA3 long-term potentiation requires translocation of synaptically released Zn2+. J Neurosci 21:8015–8025.

Li YX, Zhang Y, Lester HA, Schuman EM, Davidson N (1998) Enhancement of neurotransmitter release induced by brain-derived neurotrophic factor in cultured hippocampal neurons. J Neurosci 18:10231–10240.

Liang Y, Yuan LL, Johnston D, Gray R (2002) Calcium signaling at single mossy fiber presynaptic terminals in the rat hippocampus. J Neurophysiol 87:1132–1137.

Lipstein N, Chang S, Lin K-H, López-Murcia FJ, Neher E, Taschenberger H, Brose N (2021) Munc13-1 is a Ca2+-phospholipid-dependent vesicle priming hub that shapes synaptic short-term plasticity and enables sustained neurotransmission. Neuron 109:3980-4000.e7.

Lituma PJ, Kwon H-B, Alviña K, Luján R, Castillo PE (2021) Presynaptic NMDA receptors facilitate short-term plasticity and BDNF release at hippocampal mossy fiber synapses. Elife 10:1–26.

Liu X, Seven AB, Camacho M, Esser V, Xu J, Trimbuch T, Quade B, Su L, Ma C, Rosenmund C, Rizo J (2016) Functional synergy between the Munc13 C-terminal C1 and C2 domains. Elife 5:1–27.

Lopez-Rojas J, Kreutz MR (2016) Mature granule cells of the dentate gyrus-Passive bystanders or principal performers in hippocampal function? Neurosci Biobehav Rev 64:167–174.

Lorente De Nó R (1934) Studies on the structure of the cerebral cortex. II. Continuation of the study of the ammonic system. J für Psychol und Neurol:113–117.

Lu T, Trussell LO (2000) Inhibitory transmission mediated by asynchronous transmitter release. Neuron 26:683–694.

Lu Y-M, Taverna FA, Tu R, Ackerley CA, Wang Y-T, Roder J (2000) Endogenous Zn2+ is required for the induction of long-term potentiation at rat hippocampal mossy fiber-CA3 synapses. Synapse 38:187–197.

Lucy LB (1974) An iterative technique for the rectification of observed distributions. Astron J 79:745.

Luttmann W, Bratke K, Küpper M, Myrtek D (2014) Der Experimentator: Immunologie, Fourth Ed. Berlin, Heidelberg: Springer Berlin Heidelberg.

Lynch M (2004) Long-Term Potentiation and Memory. Physiol Rev 84:87–136.

Lysetskiy M, Földy C, Soltesz I (2005) Long- and short-term plasticity at mossy fiber synapses on mossy cells in the rat dentate gyrus. Hippocampus 15:691–696.

Ma C, Li W, Xu Y, Rizo J (2011) Munc13 mediates the transition from the closed syntaxin-Munc18 complex to the SNARE complex. Nat Struct Mol Biol 18:542–549.

Ma L, Rebane AA, Yang G, Xi Z, Kang Y, Gao Y, Zhang Y (2015) Munc18-1-regulated stage-wise SNARE assembly underlying synaptic exocytosis. Elife 4:1–30.

Maas C, Torres VI, Altrock WD, Leal-ortiz S, Wagh D, Terry-lorenzo RT, Fejtova A, Gundelfinger ED, Ziv NE, Garner CC (2012) Formation of Golgi-Derived Active Zone Precursor Vesicles. 32:11095–11108.

Maccaferri G, Tóth K, McBain CJ (1998) Target-specific expression of presynaptic mossy fiber plasticity. Science (80-) 279:1368–1370.

Maeda T, Kaneko S, Akaike A, Satoh M (1997) Direct evidence for increase in excitatory amino acids release during mossy fiber LTP in rat hippocampal slices as revealed by the patch sensor methods. Neurosci Lett 224:103–106.

Magistretti J, Castelli L, Taglietti V, Tanzi F (2003) Dual effect of Zn2+ on multiple types of voltage-dependent Ca2+ currents in rat palaeocortical neurons. Neuroscience 117:249–264.

Maglione M, Sigrist SJ (2013) Seeing the forest tree by tree: Super-resolution light microscopy meets the neurosciences. Nat Neurosci 16:790–797.

Maiole F, Tedeschi G, Candiani S, Maragliano L, Benfenati F, Zullo L (2019) Synapsins are expressed at neuronal and non-neuronal locations in Octopus vulgaris. Sci Rep 9:1–13.

Malenka RC, Bear MF (2004) LTP and LTD: An embarrassment of riches. Neuron 44:5–21.

Malenka RC, Kauer JA, Perkel DJ, Nicoll RA (1989) The impact of postsynaptic calcium on synaptic transmission — its role in long-term potentiation. Trends Neurosci 12:444–450.

Mangoni ME, Couette B, Marger L, Bourinet E, Striessnig J, Nargeot J (2006) Voltage-dependent calcium channels and cardiac pacemaker activity: From ionic currents to genes. Prog Biophys Mol Biol 90:38–63.

Manns JR, Eichenbaum H (2006) Evolution of declarative memory. Hippocampus 16:795–808.

Marín-Burgin A, Mongiat LA, Pardi MB, Schinder AF (2012) Unique processing during a period of high excitation/inhibition balance in adult-born neurons. Science (80-) 335:1238–1242.

Markram H, Tsodyks M (1996) Redistribution of synaptic efficacy between neocortical pyramidal neurons. Nature 382:807–810.

Martín R, García-Font N, Suárez-Pinilla AS, Bartolomé-Martín D, Ferrero JJ, Luján R, Torres M, Sánchez-Prieto J (2020) β-Adrenergic Receptors/Epac Signaling Increases the Size of the Readily Releasable Pool of Synaptic Vesicles Required for Parallel Fiber LTP. J Neurosci 40:8604–8617.

Martínez-Moreno A, Rivera-Olvera A, Escobar ML (2020) BDNF induces in vivo long-lasting enhancement of synaptic transmission and structural reorganization at the hippocampal mossy fibers in a transcription and translation-independent manner. Neurobiol Learn Mem 167:107125.

Maruo T, Mandai K, Takai Y, Mori M (2016) Activity-dependent alteration of the morphology of a hippocampal giant synapse. Mol Cell Neurosci 71:25–33.

Maschi D, Klyachko VA (2020) Spatiotemporal dynamics of multi-vesicular release is determined by heterogeneity of release sites within central synapses. Elife 9:65-73.e3.

Matsumoto K, Ebihara K, Yamamoto H, Tabuchi H, Fukunaga K, Yasunami M, Ohkubo H, Shichiri M, Miyamoto E (1999) Cloning from insulinoma cells of synapsin I associated with insulin secretory granules. J Biol Chem 274:2053–2059.

Matz J, Gilyan A, Kolar A, McCarvill T, Krueger SR (2010) Rapid structural alterations of the active zone lead to sustained changes in neurotransmitter release. Proc Natl Acad Sci 107:8836–8841.

Maximov A, Südhof TC (2005) Autonomous function of synaptotagmin 1 in triggering synchronous release independent of asynchronous release. Neuron 48:547–554.

McAllister BB, Dyck RH (2017) Zinc transporter 3 (ZnT3) and vesicular zinc in central nervous system function. Neurosci Biobehav Rev 80:329–350.

McCormick C, Dalton MA, Zeidman P, Maguire EA (2021) Characterising the hippocampal response to perception, construction and complexity. Cortex 137:1–17.

McCormick C, Rosenthal CR, Miller TD, Maguire EA (2016) Hippocampal damage increases deontological responses during moral decision making. J Neurosci 36:12157–12167.

Medrihan L, Cesca F, Raimondi A, Lignani G, Baldelli P, Benfenati F (2013) Synapsin II desynchronizes neurotransmitter release at inhibitory synapses by interacting with presynaptic calcium channels. Nat Commun 4:1512.

Medrihan L, Ferrea E, Greco B, Baldelli P, Benfenati F (2015) Asynchronous GABA release is a key determinant of tonic inhibition and controls neuronal excitability: A study in the synapsin II-/- mouse. Cereb Cortex 25:3356–3368.

Meinrenken CJ, Borst JGG, Sakmann B (2002) Calcium secretion coupling at calyx of Held governed by nonuniform channel-vesicle topography. J Neurosci 22:1648–1667.

Meir A, Ginsburg S, Butkevich A, Kachalsky SG, Kaiserman I, Ahdut R, Demirgoren S, Rahamimoff R (1999) Ion channels in presynaptic nerve terminals and control of transmitter release. Physiol Rev 79:1019–1088.

Mellor J, Nicoll RA (2001) Hippocampal mossy fiber LTP is independent of postsynaptic calcium. Nat Neurosci 4:125–126.

Mendonça PRF, Tagliatti E, Langley H, Kotzadimitriou D, Zamora-Chimal CG, Timofeeva Y, Volynski KE (2022) Asynchronous glutamate release is enhanced in low release efficacy synapses and dispersed across the active zone. Nat Commun 13:3497.

Midorikawa M, Sakaba T (2017) Kinetics of Releasable Synaptic Vesicles and Their Plastic Changes at Hippocampal Mossy Fiber Synapses. Neuron 96:1033-1040.e3.

Milner B, Squire LR, Kandel ER (1998) Cognitive neuroscience and the study of memory. Neuron 20:445–468.

Milovanovic D, Wu Y, Bian X, De Camilli P (2018) A liquid phase of synapsin and lipid vesicles. Science (80-) 361:604–607.

Mintz IM, Venema VJ, Swiderek KM, Lee TD, Bean BP, Adams ME (1992) P-type calcium channels blocked by the spider toxin ω-Aga-IVA. Nature 355:827–829.

Mirza FJ, Zahid S (2018) The Role of Synapsins in Neurological Disorders. Neurosci Bull 34:349–358.

Misura KMS, Scheller RH, Weis WI (2000) Three-dimensional structure of the neuronal-Sec1-syntaxin 1a complex. Nature 404:355–362.

Monday HR, Kharod SC, Yoon YJ, Singer RH, Castillo PE (2022) Presynaptic FMRP and local protein synthesis support structural and functional plasticity of glutamatergic axon terminals. Neuron 110:1–19.

Mongillo G, Barak O, Tsodyks M (2008) Synaptic Theory of Working Memory. Science (80-) 319:1543–1546.

Montagrin A, Saiote C, Schiller D (2018) The social hippocampus. Hippocampus 28:672–679.

Moore KA, Nicoll RA, Schmitz D (2003) Adenosine gates synaptic plasticity at hippocampal mossy fiber synapses. Proc Natl Acad Sci 100:14397–14402.

Mori M, Abegg MH, Gähwiler BH, Gerber U (2004) A frequency-dependent switch from inhibition to excitation in a hippocampal unitary circuit. Nature 431:453–456.

Mori Y, Friedrich T, Kim MS, Mikami A, Nakai J, Ruth P, Bosse E, Hofmann F, Flockerzi V, Furuichi T, Mikoshiba K, Imoto K, Tanabe T, Numa S (1991) Primary structure and functional expression from complementary DNA of a brain calcium channel. Nature 350:398–402.

Morris RGM (2003) Long-term potentiation and memory. Philos Trans R Soc B Biol Sci 358:643–647.

Müller CS, Haupt A, Bildl W, Schindler J, Knaus H-G, Meissner M, Rammner B, Striessnig J, Flockerzi V, Fakler B, Schulte U (2010) Quantitative proteomics of the Cav2 channel nano-environments in the mammalian brain. Proc Natl Acad Sci 107:14950–14957.

Murphy DB, Davidson MW (2013) Fundamentals of Light Microscopy and Electronic Imaging, Second Ed. John Wiley & Sons, Inc.

Myoga MH, Regehr WG (2011) Calcium microdomains near r-type calcium channels control the induction of presynaptic long-term potentiation at parallel fiber to purkinje cell synapses. J Neurosci 31:5235–5243.

Nadkarni S, Bartol TM, Stevens CF, Sejnowski TJ, Levine H (2012) Short-term plasticity constrains spatial organization of a hippocampal presynaptic terminal. Proc Natl Acad Sci 109:14657–14662.

Nadler JV (2003) The Recurrent Mossy Fiber Pathway of the Epileptic Brain. Neurochem Res 28:1649–1658.

Nakamura Y, Harada H, Kamasawa N, Matsui K, Rothman JS, Shigemoto R, Silver RA, DiGregorio DA, Takahashi T (2015) Nanoscale Distribution of Presynaptic Ca2+Channels and Its Impact on Vesicular Release during Development. Neuron 85:145–159.

Nakashiba T, Cushman JD, Pelkey KA, Renaudineau S, Buhl DL, McHugh TJ, Barrera VR, Chittajallu R, Iwamoto KS, McBain CJ, Fanselow MS, Tonegawa S (2012) Young dentate granule cells mediate pattern separation, whereas old granule cells facilitate pattern completion. Cell 149:188–201.

Narita K, Akita T, Osanai M, Shirasaki T, Kijima H, Kuba K (1998) A Ca2+-induced Ca2+ release mechanism involved in asynchronous exocytosis at frog motor nerve terminals. J Gen Physiol 112:593–609.

Neher E, Brose N (2018) Perspective Dynamically Primed Synaptic Vesicle States : Key to Understand Synaptic Short-Term Plasticity. Neuron 100:1283–1291.

Neher E, Sakaba T (2008) Multiple Roles of Calcium Ions in the Regulation of Neurotransmitter Release. Neuron 59:861–872.

Neumaier F, Akhtar-Schäfer I, Lüke JN, Dibué-Adjei M, Hescheler J, Schneider T (2018) Reciprocal modulation of Cav2.3 voltage-gated calcium channels by copper(II) ions and kainic acid. J Neurochem 147:310–322.

Neumaier F, Alpdogan S, Hescheler J, Schneider T (2020a) Zn2+-induced changes in Cav2.3 channel function: An electrophysiological and modeling study. J Gen Physiol 152:1–25.

Neumaier F, Schneider T, Albanna W (2020b) Cav2.3 channel function and Zn2+-induced modulation: potential mechanisms and (patho)physiological relevance. Channels 14:362–379.

Neunuebel JP, Knierim JJ (2014) CA3 retrieves coherent representations from degraded input: Direct evidence for CA3 pattern completion and dentate gyrus pattern separation. Neuron 81:416–427.

Newcomb R, Szoke B, Palma A, Wang G, Chen XH, Hopkins W, Cong R, Miller J, Urge L, Tarczy-Hornoch K, Loo JA, Dooley DJ, Nadasdi L, Tsien RW, Lemos J, Miljanich G (1998) Selective peptide antagonist of the class E calcium channel from the venom of the tarantula Hysterocrates gigas. Biochemistry 37:15353–15362.

Nicoll RA (2017) A Brief History of Long-Term Potentiation. Neuron 93:281–290.

Nicoll RA, Malenka RC (1995) Contrasting properties of two forms of long-term potentiation in the hippocampus. Nature 377:115–118.

Nicoll RA, Schmitz D (2005) Synaptic plasticity at hippocampal mossy fibre synapses. Nat Rev Neurosci 6:863–876.

Nikolaev M, Heggelund P (2015) Functions of synapsins in corticothalamic facilitation: Important roles of synapsin I. J Physiol 593:4499–4510.

O'Keefe, J., and Nadel L (1978) The hippocampus as a cognitive map.

Oldani S, Moreno-Velasquez L, Faiss L, Stumpf A, Rosenmund C, Schmitz D, Rost BR (2021) SynaptoPAC, an optogenetic tool for induction of presynaptic plasticity. J Neurochem 156:324–336.

Oren I, Nissen W, Kullmann DM, Somogyi P, Lamsa KP (2009) Role of ionotropic glutamate receptors in long-term potentiation in rat hippocampal CA1 oriens-lacunosum moleculare interneurons. J Neurosci 29:939–950.

Orlando M, Dvorzhak A, Bruentgens F, Maglione M, Rost BR, Sigrist SJ, Breustedt J, Schmitz D (2021) Recruitment of release sites underlies chemical presynaptic potentiation at hippocampal mossy fiber boutons. PLoS Biol 19:1–29.

Orlando M, Lignani G, Maragliano L, Fassio A, Onofri F, Baldelli P, Giovedí S, Benfenati F (2014) Functional role of ATP binding to synapsin I in synaptic vesicle trafficking and release dynamics. J Neurosci 34:14752–14768.

Ortega-de San Luis C, Ryan TJ (2022) Understanding the physical basis of memory: Molecular mechanisms of the engram. J Biol Chem 298:1–23.

Owe SG, Jensen V, Evergren E, Ruiz A, Shupliakov O, Kullmann DM, Storm-Mathisen J, Walaas SI, Hvalby O, Bergersen LH (2009) Synapsin- and Actin-Dependent Frequency Enhancement in Mouse Hippocampal Mossy Fiber Synapses. Cereb Cortex 19:511–523.

Palmiter RD, Cole TB, Quaife CJ, Findley SD (1996) ZnT-3, a putative transporter of zinc into synaptic vesicles. Proc Natl Acad Sci 93:14934–14939.

Pan E, Zhang X an, Huang Z, Krezel A, Zhao M, Tinberg CE, Lippard SJ, McNamara JO (2011) Vesicular Zinc Promotes Presynaptic and Inhibits Postsynaptic Long-Term Potentiation of Mossy Fiber-CA3 Synapse. Neuron 71:1116–1126.

Paoletti P, Bellone C, Zhou Q (2013) NMDA receptor subunit diversity: Impact on receptor properties, synaptic plasticity and disease. Nat Rev Neurosci 14:383–400.

Papantoniou C, Laugks U, Betzin J, Capitanio C, Ferrero JJ, Sánchez-Prieto J, Schoch S, Brose N, Baumeister W, Cooper BH, Imig C, Lučić V (2023) Munc13- and SNAP25-dependent molecular bridges play a key role in synaptic vesicle priming. Sci Adv 9:1–21.

Parajuli LK, Nakajima C, Kulik A, Matsui K, Schneider T, Shigemoto R, Fukazawa Y (2012) Quantitative regional and ultra structural localization of the Ca v2.3 subunit of R-type calcium channel in mouse brain. J Neurosci 32:13555–13567.

Parent JM, Yu TW, Leibowitz RT, Geschwind DH, Sloviter RS, Lowenstein DH (1997) Dentate granule cell neurogenesis is increased by seizures and contributes to aberrant network reorganization in the adult rat hippocampus. J Neurosci 17:3727–3738.

Park H, Popescu A, Poo M ming (2014) Essential role of presynaptic NMDA receptors in activity-dependent BDNF secretion and corticostriatal LTP. Neuron 84:1009–1022.

Pauli M, Paul MM, Proppert S, Mrestani A, Sharifi M, Repp F, Kürzinger L, Kollmannsberger P, Sauer M, Heckmann M, Sirén AL (2021) Targeted volumetric single-molecule localization microscopy of defined presynaptic structures in brain sections. Commun Biol 4:1–13.

Pelkey KA, McBain CJ (2005) How to dismantle a detonator synapse. Neuron 45:327–329.

Pelkey KA, Topolnik L, Lacaille JC, McBain CJ (2006) Compartmentalized Ca2+ Channel Regulation at Divergent Mossy-Fiber Release Sites Underlies Target Cell-Dependent Plasticity. Neuron 52:497–510.

Pelkey KA, Vargish GA, Pellegrini L V, Calvigioni D, Chapeton J, Yuan X, Hunt S, Cummins AC, Eldridge MAG, Pickel J, Chittajallu R, Averbeck BB, Tóth K, Zaghloul K, McBain CJ (2023) Evolutionary conservation of hippocampal mossy fiber synapse properties. Neuron 111:3802-3818.e5.

Perez-Reyes E, Cribbs LL, Daud A, Lacerda AE, Barclays J, Williamson MP, Fox M, Rees M, Lee JH (1998) Molecular characterization of a neuronal low-voltage-activated T-type calcium channel. Nature 391:896–900.

Perin MS, Brose N, Jahn R, Südhof TC (1991) Domain structure of synaptotagmin (p65). J Biol Chem 266:623–629.

Perin MS, Fried VA, Mignery GA, Jahn R, Südhof TC (1990) Phospholipid binding by a synaptic vesicle protein homologous to the regulatory region of protein kinase C. Nature 345:260–263.

Piccini A, Perlini LE, Cancedda L, Benfenati F, Giovedì S (2015) Phosphorylation by PKA and Cdk5 mediates the early effects of synapsin III in neuronal morphological maturation. J Neurosci 35:13148–13159.

Pieribone VA, Porton B, Rendon B, Feng J, Greengard P, Kao HT (2002) Expression of synapsin III in nerve terminals and neurogenic regions of the adult brain. J Comp Neurol 454:105–114.

Pieribone VA, Shupliakov O, Brodin L, Hilfiker-Rothenfluh S, Czernik AJ, Greengard P (1995) Distinct pools of synaptic vesicles in neurotransmitter release. Nature 375:493–497.

Porton B, Wetsel WC, Kao HT (2011) Synapsin III: Role in neuronal plasticity and disease. Semin Cell Dev Biol 22:416–424.

Quade B, Camacho M, Zhao X, Orlando M, Trimbuch T, Xu J, Li W, Nicastro D, Rosenmund C, Rizo J (2019) Membrane bridging by Munc13-1 is crucial for neurotransmitter release. Elife 8:1–30.

Ramón y Cajal S (1911) Histologie du Système Nerveux de l'Homme et des Vertébrés.

Rao YL, Ganaraja B, Murlimanju B V., Joy T, Krishnamurthy A, Agrawal A (2022) Hippocampus and its involvement in Alzheimer's disease: a review. 3 Biotech 12:55.

Rebola N, Carta M, Lanore F, Blanchet C, Mulle C (2011) NMDA receptor-dependent metaplasticity at hippocampal mossy fiber synapses. Nat Neurosci 14:691–693.

Rebola N, Reva M, Kirizs T, Szoboszlay M, Lőrincz A, Moneron G, Nusser Z, DiGregorio DA (2019) Distinct Nanoscale Calcium Channel and Synaptic Vesicle Topographies Contribute to the Diversity of Synaptic Function. Neuron 104:1–18.

Redman S (1990) Quantal analysis of synaptic potentials in neurons of the central nervous system. Physiol Rev 70:165–198.

Regehr WG, Abbott LF (2004) Synaptic computation. Nature 431:796–803.

Regehr WG, Delaney KR, Tank DW (1994) The role of presynaptic calcium in short-term enhancement at the hippocampal mossy fiber synapse. J Neurosci 14:523–537.

Regehr WG, Tank DW (1991) The maintenance of LTP at hippocampal mossy fiber synapses is independent of sustained presynaptic calcium. Neuron 7:451–459.

Reid CA, Dixon DB, Takahashi M, Bliss TVP, Fine A (2004) Optical Quantal Analysis Indicates that Long-Term Potentiation at Single Hippocampal Mossy Fiber Synapses is Expressed through Increased Release Probability, Recruitment of New Release Sites, and Activation of Silent Synapses. J Neurosci 24:3618–3626.

Rey S, Marra V, Smith C, Staras K (2020) Nanoscale Remodeling of Functional Synaptic Vesicle Pools in Hebbian Plasticity. Cell Rep 30:2006–2017.

Reyes A, Lujan R, Rozov A, Burnashev N, Somogyi P, Sakmann B (1998) Target-cell-specific facilitation and depression in neocortical circuits. Nat Neurosci 1:279–284.

Ribak CE, Shapiro LA (2007) Ultrastructure and synaptic connectivity of cell types in the adult rat dentate gyrus. Prog Brain Res 163:155–166.

Richardson WH (1972) Bayesian-Based Iterative Method of Image Restoration*. J Opt Soc Am 62:55–59.

Richmond JE, Davis WS, Jorgensen EM (1999) Unc-13 is required for synaptic vesicle fusion for neurotransmission. Nat Neuros 2:959–964.

Ricoy UM, Frerking ME (2014) Distinct roles for Cav2.1-2.3 in activity-dependent synaptic dynamics. J Neurophysiol 111:2404–2413.

Rizo J (2012) Staging Membrane Fusion. Science (80-) 337:1300–1301.

Rizo J (2022) Molecular Mechanisms Underlying Neurotransmitter Release. Annu Rev Biophys 51:377–408.

Rizzoli SO, Betz WJ (2005) Synaptic vesicle pools. Nat Rev Neurosci 6:57–69.

Robinson JM, Takizawa T, Vandré DD (2000) Enhanced labeling efficiency using ultrasmall immunogold probes: Immunocytochemistry. J Histochem Cytochem 48:487–492.

Rockland KS, Van Hoesen GW (1999) Some temporal and parietal cortical connections converge in CA1 of the primate hippocampus. Cereb Cortex 9:232–237.

Rodríguez F, López JC, Vargas JP, Broglio C, Gómez Y, Salas C (2002) Spatial memory and hippocampal pallium through vertebrate evolution: Insights from reptiles and teleost fish. Brain Res Bull 57:499–503.

Rollenhagen A, Sätzler K, Rodríguez EP, Jonas P, Frotscher M, Lübke JHR (2007) Structural Determinants of Transmission at Large Hippocampal Mossy Fiber Synapses. J Neurosci 27:10434–10444.

Rolls ET (2017) Limbic Structures, Emotion, and Memory. In: Reference Module in Neuroscience and Biobehavioral Psychology, pp 1–37. Elsevier.

Rolls ET, Treves A (1994) Neural networks in the brain involved in memory and recall. Prog Brain Res 102:335–341.

Römer B, Krebs J, Overall RW, Fabel K, Babu H, Overstreet-Wadiche L, Brandt MD, Williams RW, Jessberger S, Kempermann G (2011) Adult hippocampal neurogenesis and plasticity in the infrapyramidal bundle of the mossy fiber projection: I. Co-regulation by activity. Front Neurosci 5:1–8.

Rosahl TW, Spillane D, Missler M, Herz J, Selig DK, Wolff JR, Hammer RE, Malenka RC, Südhof TC (1995) Essential functions of synapsins I and II in synaptic vesicle regulation. Nature 375:488–493.

Rosenbaum R, Rubin J, Doiron B (2012) Short Term Synaptic Depression Imposes a Frequency Dependent Filter on Synaptic Information Transfer Sporns O, ed. PLoS Comput Biol 8:1–18.

Rosenmund C, Stevens CF (1996) Definition of the readily releasable pool of vesicles at hippocampal synapses. Neuron 16:1197–1207.

Rost BR, Wietek J, Yizhar O, Schmitz D (2022) Optogenetics at the presynapse. Nat Neurosci 25:984–998.

Rothman JS, Silver RA (2018) Neuromatic: An integrated open-source software toolkit for acquisition, analysis and simulation of electrophysiological data. Front Neuroinform 12:1–21.

Routtenberg A (2010) Adult learning and remodeling of hippocampal mossy fibers: Unheralded participant in circuitry for long-lasting spatial memory. Hippocampus 20:44–45.

Rozov A, Burnashev N, Sakmann B, Neher E (2001) Transmitter release modulation by intracellular Ca^{2+} buffers in facilitating and depressing nerve terminals of pyramidal cells in layer 2/3 of the rat neocortex indicates a target cell-specific difference in presynaptic calcium dynamics. J Physiol 531:807–826.

Rudolph S, Tsai M-C, von Gersdorff H, Wadiche JI (2015) The ubiquitous nature of multivesicular release. Trends Neurosci 38:428–438.

Ruediger S, Vittori C, Bednarek E, Genoud C, Strata P, Sacchetti B, Caroni P (2011) Learning-related feedforward inhibitory connectivity growth required for memory precision. Nature 473:514–518.

Ruiz A, Campanac E, Scott RS, Rusakov DA, Kullmann DM (2010) Presynaptic GABA A receptors enhance transmission and LTP induction at hippocampal mossy fiber synapses. Nat Neurosci 13:431–438.

Ryan TA, Li L, Chin LS, Greengard P, Smith SJ (1996a) Synaptic vesicle recycling in synapsin I knock-out mice. J Cell Biol 134:1219–1227.

Ryan TA, Ziv NE, Smith SJ (1996b) Potentiation of evoked vesicle turnover at individually resolved synaptic boutons. Neuron 17:125–134.

Ryan TJ, Roy DS, Pignatelli M, Arons A, Tonegawa S (2015) Engram cells retain memory under retrograde amnesia. Science (80-) 348:1007–1013.

Sabatini BL, Regehr WG (1999) Timing of Synaptic Transmission. Annu Rev Physiol 61:521–542.

Sahl SJ, Hell SW, Jakobs S (2017) Fluorescence nanoscopy in cell biology. Nat Rev Mol Cell Biol 18:685–701.

Sakamoto H, Ariyoshi T, Kimpara N, Sugao K, Taiko I, Takikawa K, Asanuma D, Namiki S, Hirose K (2018) Synaptic weight set by Munc13-1 supramolecular assemblies. Nat Neurosci 21:41–49.

Salin PA, Malenka RC, Nicoll RA (1996a) Cyclic AMP mediates a presynaptic form of LTP at cerebellar parallel fiber synapses. Neuron 16:797–803.

Salin PA, Scanziani M, Malenka RC, Nicoll RA (1996b) Distinct short-term plasticity at two excitatory synapses in the hippocampus. Proc Natl Acad Sci 93:13304–13309.

Salio C, Lossi L, Ferrini F, Merighi A (2006) Neuropeptides as synaptic transmitters. Cell Tissue Res 326:583–598.

Sammons RP, Vezir M, Moreno-velasquez L, Cano G, Orlando M, Sievers M (2024) Structure and function of the hippocampal CA3 module. 121:1–9.

Sansevrino R, Hoffmann C, Milovanovic D (2023) Condensate biology of synaptic vesicle clusters. Trends Neurosci 46:293–306.

Saunders A, Macosko EZ, Wysoker A, Goldman M, Krienen FM, de Rivera H, Bien E, Baum M, Bortolin L, Wang S, Goeva A, Nemesh J, Kamitaki N, Brumbaugh S, Kulp D, McCarroll SA (2018) Molecular Diversity and Specializations among the Cells of the Adult Mouse Brain. Cell 174:1015-1030.e16.

Schacter DL (2022) On the evolution of a functional approach to memory. Learn Behav 50:11–19.

Schaffer K (1892) Beitrag zur Histologie der Ammonshornformation. Arch für Mikroskopische Anat 39:611–632.

Scharfman HE (2007) The CA3 “backprojection” to the dentate gyrus. Prog Brain Res 163:627–637.

Schikorski T, Stevens CF (2001) Morphological correlates of functionally defined synaptic vesicle populations. Nat Neurosci 4:391–395.

Schildt S, Endres T, Lessmann V, Edelmann E (2013) Acute and chronic interference with BDNF/TrkB-signaling impair LTP selectively at mossy fiber synapses in the CA3 region of mouse hippocampus. Neuropharmacology 71:247–254.

Schindelin J, Arganda-Carreras I, Frise E, Kaynig V, Longair M, Pietzsch T, Preibisch S, Rueden C, Saalfeld S, Schmid B, Tinevez JY, White DJ, Hartenstein V, Eliceiri K, Tomancak P, Cardona A (2012) Fiji: An open-source platform for biological-image analysis. Nat Methods 9:676–682.

Schjetnan AGP, Escobar ML (2012) In vivo BDNF modulation of hippocampal mossy fiber plasticity induced by high frequency stimulation. Hippocampus 22:1–8.

Schlessinger AR, Cowan WM, Gottlieb DI (1975) An autoradiographic study of the time of origin and the pattern of granule cell migration in the dentate gyrus of the rat. J Comp Neurol 159:149–175.

Schmidt-Hieber C, Jones P, Bischofberger J (2004) Enhanced synaptic plasticity in newly generated granule cells of the adult hippocampus. Nature 429:184–187.

Schmitz D, Frerking M, Nicoll RA (2000) Synaptic Activation of Presynaptic Kainate Receptors on Hippocampal Mossy Fiber Synapses. Neuron 27:327–338.

Schmitz D, Mellor J, Nicoll RA (2001) Presynaptic kainate receptor mediation of frequency facilitation at hippocampal mossy fiber synapses. Science 291:1972–1976.

Schmitz S, Desel C (2018) Der Experimentator - Zellbiologie, First Ed.

Schneider R, Hosy E, Kohl J, Klueva J, Choquet D, Thomas U, Voigt A, Heine M (2015) Mobility of Calcium Channels in the Presynaptic Membrane. Neuron 86:672–680.

Scimemi A, Diamond JS (2012) The number and organization of Ca2+ channels in the active zone shapes neurotransmitter release from Schaffer collateral synapses. J Neurosci 32:18157–18176.

Scott R, Rusakov DA (2006) Main determinants of presynaptic Ca2+ dynamics at individual mossy fiber-CA3 pyramidal cell synapses. J Neurosci 26:7071–7081.

Scoville WB, Milner B (1957) Loss of recent memory after bilateral hippocampal lesions. J Neurol Neurosurg Psychiatry 20:11–21.

Sendrowski K, Sobaniec W (2013) Hippocampus, hippocampal sclerosis and epilepsy. Pharmacol Reports 65:555–565.

Senzai Y, Buzsáki G (2017) Physiological Properties and Behavioral Correlates of Hippocampal Granule Cells and Mossy Cells. Neuron 93:691-704.e5.

Shahoha M, Cohen R, Ben-Simon Y, Ashery U (2022) cAMP-Dependent Synaptic Plasticity at the Hippocampal Mossy Fiber Terminal. Front Synaptic Neurosci 14:1–15.

Sharifi M (2021) Structural Plasticity of Active Zones in Mouse Hippocampal Mossy Fiber Synapses.

Shcheglovitov A, Vitko I, Lazarenko RM, Orestes P, Todorovic SM, Perez-Reyes E (2012) Molecular and biophysical basis of glutamate and trace metal modulation of voltage-gated Cav2.3 calcium channels. J Gen Physiol 139:219–234.

Sheng M, Hoogenraad CC (2007) The postsynaptic architecture of excitatory synapses: A more quantitative view. Annu Rev Biochem 76:823–847.

Shin OH, Lu J, Rhee JS, Tomchick DR, Pang ZP, Wojcik SM, Camacho-Perez M, Brose N, MacHius M, Rizo J, Rosenmund C, Südhof TC (2010) Munc13 C 2 B domain is an activity-dependent Ca 2+ regulator of synaptic exocytosis. Nat Struct Mol Biol 17:280–288.

Shors TJ, Miesegaes G, Beylin A, Zhao M, Rydel T, Gould E (2001) Neurogenesis in the adult is involved in the formation of trace memories. Nature 414:938–938.

Shu T, Jin H, Rothman JE, Zhang Y (2020) Munc13-1 MUN domain and Munc18-1 cooperatively chaperone SNARE assembly through a tetrameric complex. Proc Natl Acad Sci 117:1036–1041.

Shupliakov O, Haucke V, Pechstein A (2011) How synapsin I may cluster synaptic vesicles. Semin Cell Dev Biol 22:393–399.

Sigrist SJ, Schmitz D (2011) Structural and functional plasticity of the cytoplasmic active zone. Curr Opin Neurobiol 21:144–150.

Sihra TS, Wang JKT, Gorelick FS, Greengard P (1989) Translocation of synapsin I in response to depolarization of isolated nerve terminals. Proc Natl Acad Sci 86:8108–8112.

Siksou L, Rostaing P, Lechaire J-P, Boudier T, Ohtsuka T, Fejtová A, Kao H-T, Greengard P, Gundelfinger ED, Triller A, Marty S (2007) Three-dimensional architecture of presynaptic terminal cytomatrix. J Neurosci 27:6868–6877.

Simon SM, Llinás RR (1985) Compartmentalization of the submembrane calcium activity during calcium influx and its significance in transmitter release. Biophys J 48:485–498.

Snyder JS, Hong NS, McDonald RJ, Wojtowicz JM (2005) A role for adult neurogenesis in spatial long-term memory. Neuroscience 130:843–852.

Sochivko D, Pereverzev A, Smyth N, Gissel C, Schneider T, Beck H (2002) The Cav2.3 Ca2+ channel subunit contributes to R-type Ca2+ currents in murine hippocampal and neocortical neurones. J Physiol 542:699–710.

Söllner T, Whiteheart SW, Brunner M, Erdjument-Bromage H, Geromanos S, Tempst P, Rothman JE (1993) SNAP receptors implicated in vesicle targeting and fusion. Nature 362:318–324.

Song S, Augustine GJ (2023) Different mechanisms of synapsin-induced vesicle clustering at inhibitory and excitatory synapses. Cell Rep 42:113004.

Song SH, Augustine GJ (2015) Synapsin isoforms and synaptic vesicle trafficking. Mol Cells 38:936–940.

Soong TW, Stea A, Hodson CD, Dubel SJ, Vincent SR, Snutch TP (1993) Structure and Functional Expression of a Member of the Low Voltage-Activated Calcium Channel Family. Science (80-) 260:1133–1136.

Sotelo C (2003) Viewing the brain through the master hand of Ramon y Cajal. Nat Rev Neurosci 4:71–77.

Spillane DM, Rosahl TW, Südhof TC, Malenka RC (1995) Long-term potentiation in mice lacking synapsins. Neuropharmacology 34:1573–1579.

Squire LR, Zola-Morgan S (1991) The medial temporal lobe memory system. Science (80-) 253:1380–1386.

Staley KJ, Soldo BL, Proctor WR (1995) Ionic mechanisms of neuronal excitation by inhibitory GABAA receptors. Science (80-) 269:977–981.

Starr TVB, Prystay W, Snutch TP (1991) Primary structure of a calcium channel that is highly expressed in the rat cerebellum. Proc Natl Acad Sci 88:5621–5625.

Steward O, Scoville SA (1976) Cells of origin of entorhinal cortical afferents to the hippocampus and fascia dentata of the rat. J Comp Neurol 169:347–370.

Storm-Mathisen J, Leknes AK, Bore AT, Vaaland JL, Edminson P, Haug F-MŠ, Ottersen OP (1983) First visualization of glutamate and GABA in neurones by immunocytochemistry. Nature 301:517–520.

Südhof TC (2012) The Presynaptic Active Zone. Neuron 75:11–25.

Südhof TC (2013) Neurotransmitter release: The last millisecond in the life of a synaptic vesicle. Neuron 80:675–690.

Südhof TC, Czernik AJ, Kao HT, Takei K, Johnston PA, Horiuchi A, Kanazir SD, Wagner MA, Perin MS, De Camilli P, Greengard P (1989) Synapsins: Mosaics of shared and individual domains in a family of synaptic vesicle phosphoproteins. Science (80-) 245:1474–1480.

Sugiyama Y, Kawabata I, Sobue K, Okabe S (2005) Determination of absolute protein numbers in single synapses by a GFP-based calibration technique. Nat Methods 2:677–684.

Sun HY, Lyons SA, Dobrunz LE (2005) Mechanisms of target-cell specific short-term plasticity at Schaffer collateral synapses onto interneurones versus pyramidal cells in juvenile rats. J Physiol 568:815–840.

Sun Y, Grieco SF, Holmes TC, Xu X (2017) Local and Long-Range Circuit Connections to Hilar Mossy Cells in the Dentate Gyrus. eNeuro 4:1–21.

Swanson LW, Wyss JM, Cowan WM (1978) An autoradiographic study of the organization of intrahippocampal association pathways in the rat. J Comp Neurol 181:681–715.

Swedlow JR (2013) Quantitative fluorescence microscopy and image deconvolution, Fourth Ed. Elsevier Inc.

Szabadics J, Soltesz I (2009) Functional Specificity of Mossy Fiber Innervation of GABAergic Cells in the Hippocampus. J Neurosci 29:4239–4251.

Takamori S et al. (2006) Molecular Anatomy of a Trafficking Organelle. Cell 127:831–846.

Takei Y, Harada A, Takeda S, Kobayashi K, Terada S, Noda T, Takahashi T, Hirokawa N (1995) Synapsin I deficiency results in the structural change in the presynaptic terminals in the murine nervous system. J Cell Biol 131:1789–1800.

Takeuchi T, Duszkiewicz AJ, Morris RGM (2014) The synaptic plasticity and memory hypothesis: encoding, storage and persistence. Philos Trans R Soc B Biol Sci 369:20130288.

Takeuchi T, Duszkiewicz AJ, Sonneborn A, Spooner PA, Yamasaki M, Watanabe M, Smith CC, Fernández G, Deisseroth K, Greene RW, Morris RGM (2016) Locus coeruleus and dopaminergic consolidation of everyday memory. Nature 537:357–362.

Tan C, Wang SSH, de Nola G, Kaeser PS (2022) Rebuilding essential active zone functions within a synapse. Neuron 110:1498–1515.

Tang W-J, Hurley JH (1998) Catalytic Mechanism and Regulation of Mammalian Adenylyl Cyclases. Mol Pharmacol 54:231–240.

Tayler KK, Tanaka KZ, Reijmers LG, Wiltgen BJ (2013) Reactivation of neural ensembles during the retrieval of recent and remote memory. Curr Biol 23:99–106.

Terada S, Tsujimoto T, Takei Y, Takahashi T, Hirokawa N (1999) Impairment of inhibitory synaptic transmission in mice lacking synapsin I. J Cell Biol 145:1039–1048.

Terreros-Roncal J, Moreno-Jiménez EP, Flor-García M, Rodríguez-Moreno CB, Trinchero MF, Cafini F, Rábano A, Llorens-Martín M (2021) Impact of neurodegenerative diseases on human adult hippocampal neurogenesis. Science (80-) 374:1106–1113.

Terrian DM, Gannon RL, Rea MA (1990) Glutamate is the endogenous amino acid selectively released by rat hippocampal mossy fiber synaptosomes concomitantly with prodynorphin-derived peptides. Neurochem Res 15:1–5.

Thomson AM (2000) Facilitation, augmentation and potentiation at central synapses. Trends Neurosci 23:305–312.

Tippens AL, Pare J, Langwieser N, Moosmang S, Milner TA, Smith Y, Lee A (2008) Ultrastructural evidence for pre- and postsynaptic localization of Ca v 1.2 L-type Ca 2+ channels in the rat hippocampus. J Comp Neurol 506:569–583.

Toader O, Forte N, Orlando M, Ferrea E, Raimondi A, Baldelli P, Benfenati F, Medrihan L (2013) Dentate gyrus network dysfunctions precede the symptomatic phase in a genetic mouse model of seizures. Front Cell Neurosci 7:1–15.

Tokunaga T, Miyazaki K, Koseki M, Mobarakeh JI, Ishizuka T, Yawo H (2004) Pharmacological dissection of calcium channel subtype-related components of strontium inflow in large mossy fiber boutons of mouse hippocampus. Hippocampus 14:570–585.

Tonegawa S, Liu X, Ramirez S, Redondo R (2015) Memory Engram Cells Have Come of Age. Neuron 87:918–931.

Tong G, Malenka RC, Nicoll RA (1996) Long-term potentiation in cultures of single hippocampal granule cells: A presynaptic form of plasticity. Neuron 16:1147–1157.

Torborg CL, Nakashiba T, Tonegawa S, McBain CJ (2010) Control of CA3 Output by Feedforward Inhibition Despite Developmental Changes in the Excitation–Inhibition Balance. J Neurosci 30:15628–15637.

Toth K, Suares G, Lawrence JJ, Philips-Tansey E, McBain CJ (2000) Differential mechanisms of transmission at three types of mossy fiber synapse. J Neurosci 20:8279–8289.

Trommershäuser J, Schneggenburger R, Zippelius A, Neher E (2003) Heterogeneous presynaptic release probabilities: Functional relevance for short-term plasticity. Biophys J 84:1563–1579.

Tsodyks M V., Markram H (1997) The neural code between neocortical pyramidal neurons depends on neurotransmitter release probability. Proc Natl Acad Sci 94:719–723.

Ueda T, Maeno H, Greengard P (1973) Regulation of endogenous phosphorylation of specific proteins in synaptic membrane fractions from rat brain by adenosine 3':5' monophosphate. J Biol Chem 248:8295–8305.

Valente P, Casagrande S, Nieus T, Verstegen AMJ, Valtorta F, Benfenati F, Baldelli P (2012) Site-specific synapsin I phosphorylation participates in the expression of post-tetanic potentiation and its enhancement by BDNF. J Neurosci 32:5868–5879.

Valente P, Farisello P, Valtorta F, Baldelli P, Benfenati F (2017) Impaired GABAB-mediated presynaptic inhibition increases excitatory strength and alters short-term plasticity in synapsin knockout mice. Oncotarget 8:90061–90076.

van de Bospoort R, Farina M, Schmitz SK, de Jong A, de Wit H, Verhage M, Toonen RF (2012) Munc13 controls the location and efficiency of dense-core vesicle release in neurons. J Cell Biol 199:883–891.

van den Pol AN (2012) Neuropeptide Transmission in Brain Circuits. Neuron 76:98–115.

Vandael D, Borges-Merjane C, Zhang X, Jonas P (2020) Short-Term Plasticity at Hippocampal Mossy Fiber Synapses Is Induced by Natural Activity Patterns and Associated with Vesicle Pool Engram Formation. Neuron 107:1–13.

Varoqueaux F, Sigler A, Rhee J-S, Brose N, Enk C, Reim K, Rosenmund C (2002) Total arrest of spontaneous and evoked synaptic transmission but normal synaptogenesis in the absence of Munc13-mediated vesicle priming. Proc Natl Acad Sci 99:9037–9042.

Vasileva M, Horstmann H, Geumann C, Gitler D, Kuner T (2012) Synapsin-dependent reserve pool of synaptic vesicles supports replenishment of the readily releasable pool under intense synaptic transmission. Eur J Neurosci 36:3005–3020.

Vicidomini G, Schönle A, Ta H, Han KY, Moneron G, Eggeling C, Hell SW (2013) STED Nanoscopy with Time-Gated Detection: Theoretical and Experimental Aspects Chirico G, ed. PLoS One 8:e54421.

Villacres EC, Wong ST, Chavkin C, Storm DR (1998) Type I adenylyl cyclase mutant mice have impaired mossy fiber long-term potentiation. J Neurosci 18:3186–3194.

Vogt K, Mellor J, Tong G, Nicoll R (2000) The actions of synaptically released zinc at hippocampal mossy fiber synapses. Neuron 26:187–196.

Vyleta NP, Borges-Merjane C, Jonas P (2016) Plasticity-dependent, full detonation at hippocampal mossy fiber-CA3 pyramidal neuron synapses. Elife 5:1–12.

Vyleta NP, Jonas P (2014) Loose Coupling Between Ca 2+ Channels and Release Sensors at a Plastic Hippocampal Synapse. Science (80-) 343:665–670.

Wadel K, Neher E, Sakaba T (2007) The Coupling between Synaptic Vesicles and Ca2+ Channels Determines Fast Neurotransmitter Release. Neuron 53:563–575.

Wagatsuma A, Okuyama T, Sun C, Smith LM, Abe K, Tonegawa S (2018) Locus coeruleus input to hippocampal CA3 drives single-trial learning of a novel context. Proc Natl Acad Sci 115:E310–E316.

Walker MC, Ruiz A, Kullmann DM (2002) Do mossy fibers release GABA? Epilepsia 43:196–202.

Wang H, Pineda V V., Chan GCK, Wong ST, Muglia LJ, Storm DR (2003) Type 8 Adenylyl Cyclase Is Targeted to Excitatory Synapses and Required for Mossy Fiber Long-Term Potentiation. J Neurosci 23:9710–9718.

Wang L-Y, Kaczmarek LK (1998) High-frequency firing helps replenish the readily releasable pool of synaptic vesicles. Nature 394:384–388.

Weber K, Rathke PC, Osborn M (1978) Cytoplasmic microtubular images in glutaraldehyde-fixed tissue culture cells by electron microscopy and by immunofluorescence microscopy. Proc Natl Acad Sci 75:1820–1824.

Weiergräber M, Kamp MA, Radhakrishnan K, Hescheler J, Schneider T (2006) The Cav2.3 voltage-gated calcium channel in epileptogenesis-Shedding new light on an enigmatic channel. Neurosci Biobehav Rev 30:1122–1144.

Weisskopf MG, Castillo PE, Zalutsky RA, Nicoll RA (1994) Mediation of hippocampal mossy fiber long-term potentiation by cyclic AMP. Science 265:1878–1882.

Weisskopf MG, Nicoll RA (1995) Presynaptic changes during mossy fibre LTP revealed by NMDA receptor-mediated synaptic responses. Nature 376:256–259.

Wenzel HJ, Cole TB, Born DE, Schwartzkroin PA, Palmiter RD (1997) Ultrastructural localization of zinc transporter-3 (ZnT-3) to synaptic vesicle membranes within mossy fiber boutons in the hippocampus of mouse and monkey. Proc Natl Acad Sci 94:12676–12681.

Wesseling JF, Lo DC (2002) Limit on the role of activity in controlling the release-ready supply of synaptic vesicles. J Neurosci 22:9708–9720.

Williams ME, Brust PF, Feldman DH, Patthi S, Simerson S, Maroufi A, McCue AF, Veliçelebi G, Ellis SB, Harpold MM (1992) Structure and functional expression of an ω-conotoxin-sensitive human N-type calcium channel. Science (80-) 257:389–395.

Williams PA, Larimer P, Gao Y, Strowbridge BW (2007) Semilunar granule cells: Glutamatergic neurons in the rat dentate gyrus with axon collaterals in the inner molecular layer. J Neurosci 27:13756–13761.

Witter MP (2007a) The perforant path: projections from the entorhinal cortex to the dentate gyrus. Prog Brain Res 163:43–61.

Witter MP (2007b) Intrinsic and extrinsic wiring of CA3: Indications for connectional heterogeneity. Learn Mem 14:705–713.

Witter MP, Doan TP, Jacobsen B, Nilssen ES, Ohara S (2017) Architecture of the Entorhinal Cortex A Review of Entorhinal Anatomy in Rodents with Some Comparative Notes. Front Syst Neurosci 11:1–12.

Worley PF, Baraban JM, De Souza EB, Snyder SH (1986) Mapping second messenger systems in the brain: differential localizations of adenylate cyclase and protein kinase C. Proc Natl Acad Sci 83:4053–4057.

Wozny C, Maier N, Schmitz D, Behr J (2008) Two different forms of long-term potentiation at CA1-subiculum synapses. J Physiol 586:2725–2734.

Xiang Z, Greenwood AC, Kairiss EW, Brown TH (1994) Quantal mechanism of long-term potentiation in hippocampal mossy-fiber synapses. J Neurophysiol 71:2552–2556.

Xie W, Cappiello M, Yassa MA, Ester E, Zaghloul KA, Zhang W (2023) The entorhinal-DG/CA3 pathway in the medial temporal lobe retains visual working memory of a simple surface feature. Elife 12:1–20.

Xie X, Smart TG (1994) Modulation of long-term potentiation in rat hippocampal pyramidal neurons by zinc. Pflügers Arch Eur J Physiol 427:481–486.

Xu J, Mashimo T, Südhof TC (2007) Synaptotagmin-1, -2, and -9: Ca2+ Sensors for Fast Release that Specify Distinct Presynaptic Properties in Subsets of Neurons. Neuron 54:567–581.

Yang HJ, Chen PC, Huang CT, Cheng TL, Hsu SP, Chen CY, Lu JC, Wang CT (2021) The phosphoprotein synapsin ia regulates the kinetics of dense-core vesicle release. J Neurosci 41:2828–2841.

Yang X, Wang S, Sheng Y, Zhang M, Zou W, Wu L, Kang L, Rizo J, Zhang R, Xu T, Ma C (2015) Syntaxin opening by the MUN domain underlies the function of Munc13 in synaptic-vesicle priming. Nat Struct Mol Biol 22:547–554.

Yeckel MF, Berger TW (1990) Feedforward excitation of the hippocampus by afferents from the entorhinal cortex: redefinition of the role of the trisynaptic pathway. Proc Natl Acad Sci 87:5832–5836.

Yu SC, Liewald JF, Shao J, Costa WS, Gottschalk A (2021) Synapsin is required for dense core vesicle capture and cAMP-dependent neuropeptide release. J Neurosci 41:4187–4201.

Zakharenko SS, Zablow L, Siegelbaum SA (2001) Visualization of changes in presynaptic function during long-term synaptic plasticity. Nat Neurosci 4:711–717.

Zalutsky RA, Nicoll RA (1990) Comparison of Two Forms of Long-Term Potentiation in Single Hippocampal Neurons. Science (80-) 248:1619–1624.

Zhang M, Augustine GJ (2021) Synapsins and the Synaptic Vesicle Reserve Pool: Floats or Anchors? Cells 10:658.

Zhang W, Jiang HH, Luo F (2022) Diverse organization of voltage-gated calcium channels at presynaptic active zones. Front Synaptic Neurosci 14:1–10.

Zhao S, Studer D, Chai X, Graber W, Brose N, Nestel S, Young C, Rodriguez EP, Saetzler K, Frotscher M (2012) Structural plasticity of hippocampal mossy fiber synapses as revealed by high-pressure freezing. J Comp Neurol 520:2340–2351.

Zhou Z, Ikegaya Y, Koyama R (2019) The astrocytic cAMP pathway in health and disease. Int J Mol Sci 20:1–27.

Ziv NE, Garner CC (2004) Cellular and molecular mechanisms of presynaptic assembly. Nat Rev Neurosci 5:385–399.

Zucca S, Griguoli M, Malézieux M, Grosjean N, Carta M, Mulle C (2017) Control of spike transfer at hippocampal mossy fiber synapses in vivo by GABAA and GABAB receptor-mediated inhibition. J Neurosci 37:587–598.

Zucker RS (1989) Short-Term Synaptic Plasticity. Annu Rev Neurosci 12:13–31.

Zucker RS, Regehr WG (2002) Short-Term Synaptic Plasticity. Annu Rev Physiol 64:355–405.

Appendix

Additional Tables

Part I: Distance Measurements

Table 15: Summary statistics for coupling distances.

Munc13-1 coupling partner	Area	Condition	Nr. of animals	Nr. of measure-ments	Mean (nm)	SD (nm)	Median (nm)	Interquartile range (nm)
$Ca_V2.1$	CA3	Control	11	584	64.62	34.65	60	[40; 80]
$Ca_V2.1$	CA3	Forskolin	11	525	63.62	32.77	60	[40; 80]
$Ca_V2.1$	CA1	Control	11	491	54.87	32.49	60	[40; 80]
$Ca_V2.2$	CA3	Control	8	376	61.26	29.83	58.99	[37.28; 78.48]
$Ca_V2.2$	CA3	Forskolin	8	363	64.23	33.55	60.13	[40.52; 79.98]
$Ca_V2.2$	CA1	Control	9	424	56.84	31.25	52.84	[33.85; 76.1]
$Ca_V2.3$	CA3	Control	7	344	50.01	28.55	44.01	[27.66; 68.66]
$Ca_V2.3$	CA3	Forskolin	7	336	48.73	28.96	43.32	[26.5; 65.65]
$Ca_V2.3$	CA1	Control	6	288	51.95	31.1	44.88	[29.61; 68.51]

Table 16: Overview of included/ excluded images for the $Ca_V2.1$ dataset.

Animal	Area	Condition	Nr. of Images	Nr. of Excluded images	Exclusion reason	Nr. of included measurements
1	CA3	Control	6			57
		Forskolin	7			53
	CA1	Control	6	1	imaging artefact	22
2	CA3	Control	6			46
		Forskolin	6	3	outside ZnT-positive region	24
	CA1	Control	6	1	no deconvolution	56
3	CA3	Control	6			69
		Forskolin	6			72
	CA1	Control	6			52
4	CA3	Control	6			50
		Forskolin	6			80
	CA1	Control	6			47
5	CA3	Control	6			81
		Forskolin	6			49
	CA1	Control	6			47
6	CA3	Control	6	6	unclear condition	0
		Forskolin	6	6	unclear condition	0
	CA1	Control	not imaged	-	-	0
7	CA3	Control	6			48
		Forskolin	6			42
	CA1	Control	6			48
8	CA3	Control	6			48
		Forskolin	6	2	not in ZnT-positive region	23
	CA1	Control	6			48
9	CA3	Control	6			45
		Forskolin	6			39
	CA1	Control	6			45

10	CA3	Control	6			48
		Forskolin	6			47
	CA1	Control	6			36
11	CA3	Control	6			48
		Forskolin	6			48
	CA1	Control	6			42
12	CA3	Control	6			44
		Forskolin	6			48
	CA1	Control	6			48

Table 17: Overview of included/ excluded images for the $Ca_V2.2$ dataset.

Animal	**Area**	**Condition**	**Nr. of Images**	**Nr. of excluded images**	**Exclusion reason**	**Nr. of included measurements**
13	CA3	Control	6	1	imaging in CA2	40
		Forskolin	6			43
	CA1	Control	6			48
14	CA3	Control	6			48
		Forskolin	6	2	imaging in CA2	32
	CA1	Control	6			48
15	CA3	Control	6	6	imaging in CA2	0
		Forskolin	6			48
	CA1	Control	6	1	Alexa594 scan missing	40
16	CA3	Control	6			48
		Forskolin	6			48
	CA1	Control	6			48
17	CA3	Control	6			48
		Forskolin	6			48
	CA1	Control	6			48
18	CA3	Control	6			48

		Forskolin	6			48
	CA1	Control	6			48
19	CA3	Control	6			48
		Forskolin	6			48
	CA1	Control	6			48
20	CA3	Control	6			48
		Forskolin	6			48
	CA1	Control	6			48
21	CA3	Control	6			48
		Forskolin	not imaged	-	bad slice quality	0
	CA1	Control	7	1	pre-bleached area	48

Table 18: Overview of included/ excluded images for the *Ca_v**2.3 dataset.*** *This table includes both staining sets for Ca_v2.3. In grey are the numbers for the "antiserum" staining, which was only used partially for Figures 15, 22 and 26. Note that the number of animals corresponds to the ones from the Ca_v2.2 dataset (Table 17), because I used slices from the same animals for different stainings. In white are the number for the "antibody" staining which was used for the regular analysis.*

Animal	Area	Condition	Nr. of images	Nr. of excluded images	Exclusion reason	Nr. of included measurements	Comment
13	CA3	Control	6	2	stratum oriens	48	used for Figure 26 only
		Forskolin	6			48	used for Figure 15 and Figure 26 only
	CA1	Control	6			48	used for Figure 26 only
14	CA3	Control	6			48	used for Figure 26 only
		Forskolin	6			0	not analyzed
	CA1	Control	6			48	used for Figure 26 only
15	CA3	Control	6			0	not analyzed
		Forskolin	6			0	not analyzed

	CA1	Control	6			0	not analyzed
16	CA3	Control	6			0	not analyzed
		Forskolin	6			0	not analyzed
	CA1	Control	6			0	not analyzed
17	CA3	Control	6			48	used for Figure 26 only
		Forskolin	6			0	not analyzed
	CA1	Control	6			0	not analyzed
18	CA3	Control	6			0	not analyzed
		Forskolin	6			48	used for Figure 26 only
	CA1	Control	6			0	not analyzed
19	CA3	Control	6			48	used for Figure 26 only
		Forskolin	6			48	used for Figure 26 only
	CA1	Control	6			0	not analyzed
20	CA3	Control	6			0	not analyzed
		Forskolin	6			0	not analyzed
	CA1	Control	6			0	not analyzed
21	CA3	Control	6			0	not analyzed
		Forskolin	6			0	not analyzed
	CA1	Control	6			0	not analyzed
22	CA3	Control	6			48	
		Forskolin	6			48	
	CA1	Control	7	1	imaging artefact	48	
23	CA3	Control	6			48	
		Forskolin	6			48	
	CA1	Control	6			48	
24	CA3	Control	6			48	
		Forskolin	6			48	
	CA1	Control	6			48	

25	CA3	Control	6	6	no Homer signal	0	not analyzed
		Forskolin	6	6	no Homer signal	0	not analyzed
	CA1	Control	6	6	no Homer signal	0	not analyzed
26	CA3	Control	6	6	no Homer signal	0	not analyzed
		Forskolin	6	6	no Homer signal	0	not analyzed
	CA1	Control	6	6	no Homer signal	0	not analyzed
27	CA3	Control	6	6	no Homer signal	0	not analyzed
		Forskolin	6	6	no Homer signal	0	not analyzed
	CA1	Control	6	6	no Homer signal	0	not analyzed
28	CA3	Control	6	6	no Homer signal	0	not analyzed
		Forskolin	6	6	no Homer signal	0	not analyzed
	CA1	Control	6	6	no Homer signal	0	not analyzed
29	CA3	Control	6	6	no Homer signal	0	not analyzed
		Forskolin	6	6	no Homer signal	0	not analyzed
	CA1	Control	6	6	no Homer signal	0	not analyzed
30	CA3	Control	6	6	no Homer signal	0	not analyzed
		Forskolin	6	6	no Homer signal	0	not analyzed

	CA1	Control	6	6	no Homer signal	0	not analyzed
31	CA3	Control	7			56	
		Forskolin	6			48	
	CA1	Control	6			48	
32	CA3	Control	6			48	
		Forskolin	6			48	
	CA1	Control	6	6	*stratum oriens*	0	
33	CA3	Control	6			48	
		Forskolin	6			48	
	CA1	Control	6			48	
34	CA3	Control	6			48	
		Forskolin	6			48	
	CA1	Control	6			48	

Table 19

Full Model Synaptic Configuration

Generalized linear mixed model fit by maximum likelihood (Laplace Approximation) ['glmerMod']
Family: Gamma (log)
Formula: Distance ~ Configuration + Condition + (1 | Animal)
Data: config
Control: glmerControl(optimizer = "bobyqa")

AIC	BIC	logLik	deviance	df.resid
11441.7	11466.8	-5715.9	11431.7	1104

Scaled residuals:

Min	1Q	Median	3Q	Max
-1.9353	-0.7135	-0.0907	0.5770	3.7823

Random effects:

Groups	Name	Variance	Std.Dev.
Animal	(Intercept)	0.001686	0.04106
Residual		0.266999	0.51672

Number of obs: 1109, groups: Animal, 11

Fixed effects:

	Estimate	Std. Error	t value	Pr (>|z|)
(Intercept)	4.12415	0.07712	53.480	< 2e-16***
Configurationstrict	0.04535	0.07645	0.593	0.553
ConditionFSK	-0.01266	0.06636	-0.191	0.849

Correlation of Fixed Effects:

	(Intr)	Cnfgrt
Cnfig strict	-0.735	
ConditionFSK	-0.406	-0.007

Table 20

Null Model Configuration

Generalized linear mixed model fit by maximum likelihood (Laplace Approximation) ['glmerMod']
Family: Gamma (log)
Formula: Distance ~ 1 + Condition + (1 | Animal)
Data: config
Control: glmerControl(optimizer = "bobyqa")

AIC	BIC	logLik	deviance	df.resid
11440.1	11460.1	-5716.0	11432.1	1105

Scaled residuals:

Min	1Q	Median	3Q	Max
-1.9321	-0.7027	-0.0812	0.5741	3.7004

Random effects:

Groups	Name	Variance	Std.Dev.
Animal	(Intercept)	0.001766	0.04202
Residual		0.267884	0.51758

Number of obs: 1109, groups: Animal, 11

Fixed effects:

	Estimate	Std. Error	t value	Pr(>|z|)
(Intercept)	4.15799	0.05249	79.215	<2e-16***
ConditionFSK	-0.01240	0.06637	-0.187	0.852

Correlation of Fixed Effects:

	(Intr)
ConditinFSK	-0.603

Table 21

Anova Full and Null Model Synaptic Configuration

Data: config
Models:
NullModel_conf: Distance ~ 1 + Condition + (1 | Animal)
FullModel: Distance ~ Configuration + Condition + (1 | Animal)

	npar	AIC	BIC	logLik	deviance	Chisq	Df	Pr(>Chisq)
NullModel_conf	4	11440	11460	-5716.0	11432			
FullModel	5	11442	11467	-5715.9	11432	0.349	1	0.5547

Table 22

Full Model Cav2.1 Fsk vs control

Generalized linear mixed model fit by maximum likelihood (Laplace Approximation) ['glmerMod']
Family: Gamma (log)
Formula: Distance ~ Condition + (1 | Animal)
Data: Cav2.1_Distance
Control: glmerControl(optimizer = "bobyqa")

AIC	BIC	logLik	deviance	df.resid
11440.1	11460.1	-5716.0	11432.1	1105

Scaled residuals:

Min	1Q	Median	3Q	Max
-1.9321	-0.7027	-0.0812	0.5741	3.7004

Random effects:

Groups	Name	Variance	Std.Dev.
Animal	(Intercept)	0.001766	0.04202
Residual		0.267884	0.51758

Number of obs: 1109, groups: Animal, 11

Fixed effects:

	Estimate	Std. Error	t value	Pr(>|z|)
(Intercept)	4.15799	0.05249	79.215	<2e-16***
ConditionFSK	-0.01240	0.06637	-0.187	0.852

Correlation of Fixed Effects:

	(Intr)
ConditinFSK	-0.603

Table 23

Null Model Cav2.1 Fsk vs control

Generalized linear mixed model fit by maximum likelihood (Laplace Approximation) ['glmerMod']
Family: Gamma (log)
Formula: Distance ~ 1 + (1 | Animal)
Data: Cav2.1_Distance
Control: glmerControl(optimizer = "bobyqa")

AIC	BIC	logLik	deviance	df.resid
11438.1	11453.2	-5716.1	11432.1	1106

Scaled residuals:

Min	1Q	Median	3Q	Max
-1.9316	-0.6952	-0.0770	0.5900	3.6600

Random effects:

Groups	Name	Variance	Std.Dev.
Animal	(Intercept)	0.001794	0.04235
Residual		0.268014	0.51770

Fixed effects:

	Estimate	Std. Error	t value	Pr(>|z|)
(Intercept)	4.15209	0.04195	98.98	<2e-16***

Table 24

Anova Null and Full Model Cav2.1 Fsk vs control

Data: Cav2.1_Distance
Models:
NullModel: Distance ~ 1 + (1 | Animal)
FullModel: Distance ~ Condition + (1 | Animal)

	npar	AIC	BIC	logLik	deviance	Chisq	Df	Pr(>Chisq)
NullModel	3	11438	11453	-5716.1	11432			
FullModel	4	11440	11460	-5716.0	11432	0.0351	1	0.8514

Table 25

Full Model Cav2.1 CA1 vs CA3

Call: glm(formula = Distance ~ 1 + Region, family = Gamma(link = "log"),
data = Cav2.1_CA1_CA3)

Deviance Residuals:

Min	1Q	Median	3Q	Max
-6.2107	-0.4442	-0.0733	0.4024	1.3007

Coefficients:

	Estimate	Std. Error	t value	Pr(>|z|)
(Intercept)	4.00492	0.02538	157.769	<2e-16***
RegionCA3	0.16365	0.03444	4.752	2.29e-06***

(Dispersion parameter for Gamma family taken to be 0.3163911)

Null deviance: 2180.6 on 1074 degrees of freedom
Residual deviance: 2173.5 on 1073 degrees of freedom
AIC: 10775
Number of Fisher Scoring iterations: 7

Table 26

Null Model Cav2.1 CA1 vs CA3

Call:
glm(formula = Distance ~ 1, family = Gamma(link = "log"), data = Cav2.1_CA1_CA3)

Deviance Residuals:

Min	1Q	Median	3Q	Max
-6.1992	-0.3823	-0.0028	0.2991	1.3385

Coefficients:

	Estimate	Std. Error	t value	Pr(>|z|)
(Intercept)	4.09713	0.01724	237.6	<2e-16***

(Dispersion parameter for Gamma family taken to be 0.3196416)

Null deviance: 2180.6 on 1074 degrees of freedom
Residual deviance: 2180.6 on 1074 degrees of freedom
AIC: 10777
Number of Fisher Scoring iterations: 7

Table 27

ANOVA Full and Null Model Cav2.1 CA1 vs CA3

Analysis of Deviance Table

Model 1: Distance ~ 1 + Region
Model 2: Distance ~ 1

	Resid. Df	Resid. Dev	Df	Deviance	Pr(>Chi)
1	1073	2173.5			
2	1074	2180.6	-1	-7.1023	2.159e-06***

Table 28

Marginal Means Cav2.1 CA1 vs CA3

Region	response	SE	df	lower.CL	upper.CL
CA1	54.9	1.39	1073	52.2	57.7
CA3	64.6	1.50	1073	61.7	67.6

Confidence level used: 0.95
Intervals are back-transformed from the log scale

Table 29

Contrast Analysis Cav2.1 CA1 vs CA3

	Contrast ratio	SE	df	null	t.ratio	p.value
CA1 / CA3	0.849	0.0292	1073	1	-4.752	<.0001

Tests are performed on the log scale

Table 30

Full Model Tool Comparison

Call:
glm(formula = Distance ~ 1 + Analysis, family = Gamma(link = "log"),
    data = tools)

Deviance Residuals:

Min	1Q	Median	3Q	Max
-6.1445	-0.5021	-0.0696	0.3544	1.2393

Coefficients:

	Estimate	Std. Error	t value	Pr(>|z|)
(Intercept)	3.74022	0.07690	48.640	<2e-16***
Analysisline	0.01904	0.10875	0.175	0.861

(Dispersion parameter for Gamma family taken to be 0.2838203)

Null deviance: 99.849 on 95 degrees of freedom
Residual deviance: 99.840 on 94 degrees of freedom
AIC: 918.47
Number of Fisher Scoring iterations: 6

Table 31

Null Model Tool Comparison

Call: glm(formula = Distance ~ 1, family = Gamma(link = "log"), data = tools)

Deviance Residuals:

Min	1Q	Median	3Q	Max
-6.1429	-0.5101	-0.0603	0.3490	1.2530

Coefficients:

	Estimate	Std. Error	t value	Pr(>|z|)
(Intercept)	3.74979	0.05417	69.22	<2e-16***

(Dispersion parameter for Gamma family taken to be 0.2816944)

Null deviance: 99.849 on 95 degrees of freedom
Residual deviance: 99.849 on 95 degrees of freedom
AIC: 916.48
Number of Fisher Scoring iterations: 5

Table 32

ANOVA Full and Null Model Tool Comparison

Analysis of Deviance Table

Model 1: Distance ~ 1 + Analysis
Model 2: Distance ~ 1

	Resid. Df	Resid. Dev	Df	Deviance	Pr(>Chi)
1	94	99.840			
2	95	99.849	-1	-0.008697	0.861

Table 33

Full Model Cav 2.2 FSK vs Control

Generalized linear mixed model fit by maximum likelihood (Laplace Approximation) ['glmerMod']
Family: Gamma (log)
Formula: Distance ~ 1 + Condition + (1 | Slice.Number) + (1 | Animal)
Data: Cav2.2_Distance
Control: glmerControl(optimizer = "bobyqa")

AIC	BIC	logLik	deviance	df.resid
7070.6	7093.7	-3530.3	7060.6	734

Scaled residuals:

Min	1Q	Median	3Q	Max
-2.0594	-0.7501	-0.0563	0.6267	4.9250

Random effects:

Groups	Name	Variance	Std.Dev.
Slice.Number	(Intercept)	0.009939	0.09970
Animal	(Intercept)	0.001726	0.04155
Residual		0.223448	0.47270

Number of obs: 739, groups: Slice.Number, 16; Animal, 9

Fixed effects:

	Estimate	Std. Error	t value	Pr(>|z|)
(Intercept)	4.10586	0.06992	58.720	<2e-16***
ConditionForskolin	0.03199	0.09203	0.348	0.728

Correlation of Fixed Effects:

	(Intr)
CndtnFrskln	-0.657

Table 34

Null Model Cav 2.2 FSK vs Control

Generalized linear mixed model fit by maximum likelihood (Laplace Approximation) ['glmerMod']
Family: Gamma (log)
Formula: Distance ~ 1 + (1 | Slice.Number) + (1 | Animal)
Data: Cav2.2_Distance
Control: glmerControl(optimizer = "bobyqa")

AIC	BIC	logLik	deviance	df.resid
7068.8	7087.2	-3530.4	7060.8	735

Scaled residuals:

Min	1Q	Median	3Q	Max
-2.0587	-0.7421	-0.0523	0.6232	4.9582

Random effects:

Groups	Name	Variance	Std.Dev.
Slice.Number	(Intercept)	0.010152	0.10076
Animal	(Intercept)	0.001629	0.04036
Residual		0.223532	0.47279

Number of obs: 739, groups: Slice.Number, 16; Animal, 9

Fixed effects:

	Estimate	Std. Error	t value	Pr(>|z|)
(Intercept)	4.12176	0.05278	78.09	<2e-16***

Table 35

ANOVA Full and Null Model Cav 2.2 FSK vs Control

Data: Cav2.2_Distance
Models:
NullModel: Distance ~ 1 + (1 | Slice.Number) + (1 | Animal)
FullModel: Distance ~ 1 + Condition + (1 | Slice.Number) + (1 | Animal)

	npar	AIC	BIC	logLik	deviance	Chisq	Df	Pr(>Chisq)
NullModel	4	7068.8	7087.2	-3530.4	7060.8			
FullModel	5	7070.6	7093.7	-3530.3	7060.6	0.1198	1	0.7292

Table 36

Full Model Cav 2.2 CA1 vs CA3

Generalized linear mixed model fit by maximum likelihood (Laplace Approximation) ['glmerMod']
Family: Gamma (log)
Formula: Distance ~ 1 + Region + (1 | Image_ID) + (1 | Animal)
Data: Cav2.2_CA1_CA3
Control: glmerControl(optimizer = "bobyqa")

AIC	BIC	logLik	deviance	df.resid
7594.2	7617.6	-3792.1	7584.2	795

Scaled residuals:

Min	1Q	Median	3Q	Max
-1.9253	-0.7127	-0.0533	0.6402	8.2274

Random effects:

Groups	Name	Variance	Std.Dev.
Image_ID	(Intercept)	0.01577	0.12558
Animal	(Intercept)	0.00494	0.07029
Residual		0.24269	0.49263

Number of obs: 800, groups: Image_ID, 100; Animal, 9

Fixed effects:

	Estimate	Std. Error	t value	Pr(>|z|)
(Intercept)	4.01405	0.05286	75.942	<2e-16***
RegionCA3	0.08146	0.05167	1.577	0.115

Correlation of Fixed Effects:

	(Intr)
RegionCA3	-0.442

Table 37

Null Model Cav 2.2 CA1 vs CA3

Generalized linear mixed model fit by maximum likelihood (Laplace Approximation) ['glmerMod']
Family: Gamma (log)
Formula: Distance ~ 1 + (1 | Image_ID) + (1 | Animal)
Data: Cav2.2_CA1_CA3
Control: glmerControl(optimizer = "bobyqa")

AIC	BIC	logLik	deviance	df.resid
7594.6	7613.4	-3793.3	7586.6	796

Scaled residuals:

Min	1Q	Median	3Q	Max
-1.9308	-0.7128	-0.0502	0.6535	7.9831

Random effects:

Groups	Name	Variance	Std.Dev.
Image_ID	(Intercept)	0.016888	0.12995
Animal	(Intercept)	0.004746	0.06889
Residual		0.241998	0.49193

Number of obs: 800, groups: Image_ID, 100; Animal, 9

Fixed effects:

	Estimate	Std. Error	t value	Pr(>|z|)
(Intercept)	4.05045	0.04711	85.98	<2e-16***

Table 38

ANOVA Full and Null Model Cav 2.2 FSK vs Control

Data: Cav2.2_CA1_CA3
Models:
NullModel: Distance ~ 1 + (1 | Image_ID) + (1 | Animal)
FullModel: Distance ~ 1 + Region + (1 | Image_ID) + (1 | Animal)

	npar	AIC	BIC	logLik	deviance	Chisq	Df	Pr(>Chisq)
NullModel	4	7594.6	7613.4	-3793.3	7586.6			
FullModel	5	7594.2	7617.6	-3792.1	7584.2	2.4382	1	0.1184

Table 39

Full Model Cav 2.3 staining comparison

Generalized linear mixed model fit by maximum likelihood (Laplace Approximation) ['glmerMod']
Family: Gamma (log)
Formula: Distance ~ 1 + staining + Condition + Region + (1 | Image_ID) + (1 | Slice.Number) + (1 | Animal)
Data: comparison
Control: glmerControl(optimizer = "bobyqa")

AIC	BIC	logLik	deviance	df.resid
12961.8	13003.7	-6472.9	12945.8	1392

Scaled residuals:

Min	1Q	Median	3Q	Max
-1.9013	-0.7541	-0.1235	0.6255	4.1810

Random effects:

Groups	Name	Variance	Std.Dev.
Image_ID	(Intercept)	0.006001	0.07747
Slice.Number	(Intercept)	0.005602	0.07484
Animal	(Intercept)	0.006236	0.07897
Residual		0.267891	0.51758

Number of obs: 1400, groups: Image_ID, 175; Slice.Number, 21; Animal, 12

Fixed effects:

	Estimate	Std. Error	t value	Pr(>|z|)
(Intercept)	3.90860	0.09389	41.630	<2e-16***
stainingantibody	0.01704	0.10743	0.159	0.874
ConditionForskolin	-0.03098	0.06789	-0.456	0.648
RegionCA3	-0.03095	0.04478	-0.691	0.489

Correlation of Fixed Effects:

	(Intr)	stnngn	CndtnF
stanngntbdy	-0.706		
CndtnFrskln	-0.189	-0.060	
RegionCA3	-0.333	0.042	-0.251

Table 40

Null Model Cav 2.3 staining comparison

Generalized linear mixed model fit by maximum likelihood (Laplace Approximation) ['glmerMod']
Family: Gamma (log)
Formula: Distance ~ 1 + Condition + Region + (1 | Image_ID) + (1 | Slice.Number) + (1 | Animal)
Data: comparison
Control: glmerControl(optimizer = "bobyqa")

AIC	BIC	logLik	deviance	df.resid
12959.8	12996.5	-6472.9	12945.8	1393

Scaled residuals:

Min	1Q	Median	3Q	Max
-1.9007	-0.7535	-0.1232	0.6238	4.1849

Random effects:

Groups	Name	Variance	Std.Dev.
Image_ID	(Intercept)	0.006011	0.07753
Slice.Number	(Intercept)	0.005619	0.07496
Animal	(Intercept)	0.006233	0.07895
Residual		0.268056	0.51774

Number of obs: 1400, groups: Image_ID, 175; Slice.Number, 21; Animal, 12

Fixed effects:

	Estimate	Std. Error	t value	Pr(>|z|)
(Intercept)	3.91912	0.06648	58.953	<2e-16***
ConditionForskolin	-0.03034	0.06784	-0.447	0.655
RegionCA3	-0.03125	0.04474	-0.698	0.485

Correlation of Fixed Effects:

	(Intr)	CndtnF
CndtnFrskln	-0.327	
RegionCA3	-0.429	-0.249

Table 41

ANOVA Full and Null Model Cav 2.3 staining comparison

Data: comparison
Models:
NullModel: Distance ~ 1 + Condition + Region + (1 | Image_ID) + (1 | Slice.Number) + (1 | Animal)
FullModel: Distance ~ 1 + staining + Condition + Region + (1 | Image_ID) + (1 | Slice.Number) + (1 | Animal)

	npar	AIC	BIC	logLik	deviance	Chisq	Df	Pr(>Chisq)
NullModel	7	12960	12996	-6472.9	12946			
FullModel	8	12962	13004	-6472.9	12946	0.025	1	0.8743

Table 42

Full Model Cav2.3 FSK vs control

Generalized linear mixed model fit by maximum likelihood (Laplace Approximation) ['glmerMod']
Family: Gamma (log)
Formula: Distance ~ 1 + Condition + (1 | Image_ID) + (1 | Slice.Number) + (1 | Animal)
Data: Cav2.3_distance_CA3
Control: glmerControl(optimizer = "bobyqa")

AIC	BIC	logLik	deviance	df.resid
6347.1	6374.2	-3167.6	6335.1	674

Scaled residuals:

Min	1Q	Median	3Q	Max
-1.7900	-0.7846	-0.1695	0.6736	3.6952

Random effects:

Groups	Name	Variance	Std.Dev.
Image_ID	(Intercept)	0.002727	0.05222
Slice.Number	(Intercept)	0.005287	0.07271
Animal	(Intercept)	0.009647	0.09822
Residual		0.302138	0.54967

Number of obs: 680, groups: Image_ID, 85; Slice.Number, 14; Animal, 7

Fixed effects:

	Estimate	Std. Error	t value	Pr(>|z|)
(Intercept)	3.89516	0.08240	47.270	<2e-16***
ConditionForskolin	-0.03434	0.07511	-0.457	0.648

Correlation of Fixed Effects:

	(Intr)
CndtnFrskln	-0.457

Table 43

Null Model Cav2.3 FSK vs control

Generalized linear mixed model fit by maximum likelihood (Laplace Approximation) ['glmerMod']
Family: Gamma (log)
Formula: Distance ~ 1 + (1 | Image_ID) + (1 | Slice.Number) + (1 | Animal)
Data: Cav2.3_distance_CA3
Control: glmerControl(optimizer = "bobyqa")

AIC	BIC	logLik	deviance	df.resid
6345.3	6367.9	-3167.7	6335.3	675

Scaled residuals:

Min	1Q	Median	3Q	Max
-1.7904	-0.7812	-0.1724	0.6639	3.7469

Random effects:

Groups	Name	Variance	Std.Dev.
Image_ID	(Intercept)	0.002801	0.05293
Slice.Number	(Intercept)	0.005571	0.07464
Animal	(Intercept)	0.009499	0.09747
Residual		0.302124	0.54966

Fixed effects:

	Estimate	Std. Error	t value	Pr(>|z|)
(Intercept)	3.87792	0.07329	52.91	<2e-16***

Table 44

ANOVA Full and Null Model Cav2.3 FSK vs control

Data: Cav2.3_distance_CA3
Models:
NullModel: Distance ~ 1 + (1 | Image_ID) + (1 | Slice.Number) + (1 | Animal)
FullModel: Distance ~ 1 + Condition + (1 | Image_ID) + (1 | Slice.Number) + (1 | Animal)

	npar	AIC	BIC	logLik	deviance	Chisq	Df	Pr(>Chisq)
NullModel	5	6345.3	6367.9	-3167.7	6335.3			
FullModel	6	6347.1	6374.2	-3167.6	6335.1	0.2055	1	0.6504

Table 45

Full Model Cav2.3 CA1 vs CA3

Generalized linear mixed model fit by maximum likelihood (Laplace Approximation) ['glmerMod']
Family: Gamma (log)
Formula: Distance ~ 1 + Region + (1 | Image_ID) + (1 | Animal)
Data: Cav2.3_CA1_CA3
Control: glmerControl(optimizer = "bobyqa")

AIC	BIC	logLik	deviance	df.resid
5893.4	5915.7	-2941.7	5883.4	627

Scaled residuals:

Min	1Q	Median	3Q	Max
-1.7411	-0.7466	-0.1577	0.5736	3.9793

Random effects:

Groups	Name	Variance	Std.Dev.
Image_ID	(Intercept)	0.008643	0.09297
Animal	(Intercept)	0.016956	0.13021
Residual		0.294959	0.54310

Number of obs: 632, groups: Image_ID, 79; Animal, 7

Fixed effects:

	Estimate	Std. Error	t value	Pr(>|z|)
(Intercept)	3.94079	0.09294	42.400	<2e-16***
RegionCA3	-0.04656	0.05493	-0.848	0.397

Correlation of Fixed Effects:

	(Intr)
RegionCA3	-0.341

Table 46

Null Model Cav2.3 CA1 vs CA3

Generalized linear mixed model fit by maximum likelihood (Laplace Approximation) ['glmerMod']
Family: Gamma (log)
Formula: Distance ~ 1 + (1 | Image_ID) + (1 | Animal)
Data: Cav2.3_CA1_CA3
Control: glmerControl(optimizer = "bobyqa")

AIC	BIC	logLik	deviance	df.resid
5892.1	5909.9	-2942.1	5884.1	628

Scaled residuals:

Min	1Q	Median	3Q	Max
-1.7380	-0.7460	-0.1384	0.5942	4.0852

Random effects:

Groups	Name	Variance	Std.Dev.
Image_ID	(Intercept)	0.009134	0.09557
Animal	(Intercept)	0.016568	0.12872
Residual		0.295263	0.54338

Number of obs: 632, groups: Image_ID, 79; Animal, 7

Fixed effects:

	Estimate	Std. Error	t value	Pr(>|z|)
(Intercept)	3.91360	0.08641	45.29	<2e-16***

Table 47

ANOVA Full and Null Model Cav2.3 CA1 vs CA3

Data: Cav2.3_CA1_CA3
Models:
NullModel: Distance ~ 1 + (1 | Image_ID) + (1 | Animal)
FullModel: Distance ~ 1 + Region + (1 | Image_ID) + (1 | Animal)

	npar	AIC	BIC	logLik	deviance	Chisq	Df	Pr(>Chisq)
NullModel	4	5892.1	5909.9	-2942.1	5884.1			
FullModel	5	5893.4	5915.7	-2941.7	5883.4	0.7153	1	0.3977

Table 48

Full Model Cav comparison CA3

Generalized linear mixed model fit by maximum likelihood (Laplace Approximation) ['glmerMod']
Family: Gamma (log)
Formula: Distance ~ 1 + Condition + Cav + (1 | Slice.Number) + (1 | Animal)
Data: Distances
Control: glmerControl(optimizer = "bobyqa")

AIC	BIC	logLik	deviance	df.resid
25592.4	25633.3	-12789.2	25578.4	2521

Scaled residuals:

Min	1Q	Median	3Q	Max
-1.9324	-0.7359	-0.1016	0.6201	4.6838

Random effects:

Groups	Name	Variance	Std.Dev.
Slice.Number	(Intercept)	0.001520	0.03898
Animal	(Intercept)	0.003984	0.06312
Residual		0.267810	0.51750

Number of obs: 2528, groups: Slice.Number, 52; Animal, 26

Fixed effects:

	Estimate	Std. Error	t value	Pr(>|z|)
(Intercept)	4.147930	0.050994	81.342	<2e-16***
ConditionForskolin	-0.005787	0.039974	-0.145	0.884895
CavCav2.2	0.001228	0.072623	0.017	0.986507
CavCav2.3	-0.271826	0.075447	-3.603	0.000315***

Correlation of Fixed Effects:

	(Intr)	CndtnF	CvC2.2
CndtnFrskln	-0.372		
CavCav2.2	-0.603	-0.009	
CavCav2.3	-0.571	-0.026	0.431

Table 49

Null Model Cav comparison CA3

Generalized linear mixed model fit by maximum likelihood (Laplace Approximation) ['glmerMod']
Family: Gamma (log)
Formula: Distance ~ 1 + Condition + (1 | Slice.Number) + (1 | Animal)
Data: Distances
Control: glmerControl(optimizer = "bobyqa")

AIC	BIC	logLik	deviance	df.resid
25602.7	25631.8	-12796.3	25592.7	2523

Scaled residuals:

Min	1Q	Median	3Q	Max
-1.9370	-0.7217	-0.0930	0.6355	4.7056

Random effects:

Groups	Name	Variance	Std.Dev.
Slice.Number	(Intercept)	0.003143	0.05606
Animal	(Intercept)	0.005841	0.07643
Residual		0.266539	0.51627

Number of obs: 2528, groups: Slice.Number, 52; Animal, 26

Fixed effects:

	Estimate	Std. Error	t value	Pr(>|z|)
(Intercept)	4.07853	0.04303	94.783	<2e-16***
ConditionForskolin	-0.01094	0.04541	-0.241	0.81

Correlation of Fixed Effects:

	(Intr)
CndtnFrskln	-0.523

Table 50

ANOVA Full and Null Model Cav comparison CA3

Data: Distances
Models:
NullModel: Distance ~ 1 + Condition + (1 | Slice.Number) + (1 | Animal)
FullModel: Distance ~ 1 + Condition + Cav + (1 | Slice.Number) + (1 | Animal)

	npar	AIC	BIC	logLik	deviance	Chisq	Df	Pr(>Chisq)
NullModel	5	25603	25632	-12796	25593			
FullModel	7	25592	25633	-12789	25578	14.236	2	0.0008102***

Table 51

Marginal Means Cav comparison CA3

Condition	Cav	response	SE	df	asymp.LCL	asymp.UCL
Control	Cav2.1	63.3	3.23	Inf	57.3	70.0
Forskolin	Cav2.1	62.9	3.26	Inf	56.9	69.7
Control	Cav2.2	63.4	3.70	Inf	56.5	71.1
Forskolin	Cav2.2	63.0	3.69	Inf	56.2	70.7
Control	Cav2.3	48.2	3.01	Inf	42.7	54.5
Forskolin	Cav2.3	48.0	2.97	Inf	42.5	54.1

Confidence level used: 0.95
Intervals are back-transformed from the log scale

Table 52

Marginal Contrast Analysis Cav comparison CA3

contrast	ratio	SE	df	null	z.ratio	p.value
Control Cav2.1 / Forskolin Cav2.1	1.006	0.0402	Inf	1	0.145	1.0000
Control Cav2.1 / Control Cav2.2	0.999	0.0725	Inf	1	-0.017	1.0000
Control Cav2.1 / Forskolin Cav2.2	1.005	0.0829	Inf	1	0.055	1.0000
Control Cav2.1 / Control Cav2.3	1.312	0.0990	Inf	1	3.603	0.0043
Control Cav2.1 / Forskolin Cav2.3	1.320	0.1115	Inf	1	3.287	0.0130
Forskolin Cav2.1 / Control Cav2.2	0.993	0.0826	Inf	1	-0.084	1.0000
Forskolin Cav2.1 / Forskolin Cav2.2	0.999	0.0725	Inf	1	-0.017	1.0000
Forskolin Cav2.1 / Control Cav2.3	1.305	0.1126	Inf	1	3.083	0.0250
Forskolin Cav2.1 / Forskolin Cav2.3	1.312	0.0990	Inf	1	3.603	0.0043
Control Cav2.2 / Forskolin Cav2.2	1.006	0.0402	Inf	1	0.145	1.0000
Control Cav2.2 / Control Cav2.3	1.314	0.1038	Inf	1	3.455	0.0073
Control Cav2.2 / Forskolin Cav2.3	1.322	0.1163	Inf	1	3.169	0.0191
Forskolin Cav2.2 / Control Cav2.3	1.306	0.1164	Inf	1	2.999	0.0324
Forskolin Cav2.2 / Forskolin Cav2.3	1.314	0.1038	Inf	1	3.455	0.0073
Control Cav2.3 / Forskolin Cav2.3	1.006	0.0402	Inf	1	0.145	1.0000

P value adjustment: tukey method for comparing a family of 6 estimates
Tests are performed on the log scale

Table 53

Full Model Cav comparison CA1

Generalized linear mixed model fit by maximum likelihood (Laplace Approximation) ['glmerMod']
Family: Gamma (log)
Formula: Distance ~ 1 + Cav + (1 | Animal)
Data: Distances
Control: glmerControl(optimizer = "bobyqa")

AIC	BIC	logLik	deviance	df.resid
12065.7	12091.1	-6027.8	12055.7	1198

Scaled residuals:

Min	1Q	Median	3Q	Max
-1.7675	-0.6850	-0.1080	0.6564	7.3432

Random effects:

Groups	Name	Variance	Std.Dev.
Animal	(Intercept)	0.003691	0.06076
Residual		0.320114	0.56579

Number of obs: 1203, groups: Animal, 25

Fixed effects:

	Estimate	Std. Error	T value	Pr(>|z|)
(Intercept)	3.99638	0.05588	71.512	<2e-16***
CavCav2.2	0.04890	0.08224	0.595	0.552
CavCav2.3	-0.07867	0.09296	-0.846	0.397

Correlation of Fixed Effects:

	(Intr)	CvC2.2
CavCav2.2	-0.684	
CavCav2.3	-0.588	0.420

Table 54

Null Model Cav comparison CA1

Generalized linear mixed model fit by maximum likelihood (Laplace Approximation) ['glmerMod']
Family: Gamma (log)
Formula: Distance ~ 1 + (1 | Animal)
Data: Distances
Control: glmerControl(optimizer = "bobyqa")

AIC	BIC	logLik	deviance	df.resid
12063.6	12078.8	-6028.8	12057.6	1200

Scaled residuals:

Min	1Q	Median	3Q	Max
-1.7612	-0.6713	-0.0988	0.6658	7.6416

Random effects:

Groups	Name	Variance	Std.Dev.
Animal	(Intercept)	0.003294	0.05739
Residual		0.322376	0.56778

Number of obs: 1203, groups: Animal, 25

Fixed effects:

	Estimate	Std. Error	T value	Pr(>|z|)
(Intercept)	3.99646	0.03568	112	<2e-16***

Table 55

ANOVA Full and Null Model Cav comparison CA1

Data: Distances
Models:
NullModel: Distance ~ 1 + (1 | Animal)
FullModel: Distance ~ 1 + Cav + (1 | Animal)

	npar	AIC	BIC	logLik	deviance	Chisq	Df	Pr(>Chisq)
NullModel	3	12064	12079	-6028.8	12058			
FullModel	5	12066	12091	-6027.8	12056	1.9064	2	0.3855

Part II: Munc Intensity

Table 56

Full Model ZnT-3 area

Call:
glm(formula = Area ~ 1 + Condition + Region + IncTime, family = Gamma(link = "log"),
 data = FilteredData[Staining == "ZnT",])

Deviance Residuals:

Min	1Q	Median	3Q	Max
-2.4961	-1.8576	-1.3529	-0.0383	3.4393

Coefficients:

	Estimate	Std. Error	T value	Pr(>|z|)
(Intercept)	7.6464	0.2761	27.699	<2e-16***
ConditionForskolin	0.3913	0.1989	1.967	0.05005.
RegionCA3b	0.0169	0.2742	0.062	0.95089
RegionCA3c	-0.7740	0.2412	-3.208	0.00148**
IncTime60	-0.3437	0.2259	-1.522	0.12914

(Dispersion parameter for Gamma family taken to be 2.926373)

Null deviance: 889.92 on 308 degrees of freedom
Residual deviance: 824.43 on 304 degrees of freedom
AIC: 4927.2
Number of Fisher Scoring iterations: 10

Table 57

Condition Null Model ZnT-3 area

Call: glm(formula = Area ~ 1 + Region + IncTime, family = Gamma(link = "log"),
data = FilteredData[Staining == "ZnT",])

Deviance Residuals:

Min	1Q	Median	3Q	Max
-2.4276	-1.9041	-1.4216	-0.0043	3.0417

Coefficients:

	Estimate	Std. Error	T value	Pr(>|z|)
(Intercept)	7.847501	0.253618	30.942	<2e-16***
RegionCA3b	-0.006466	0.268865	-0.024	0.980830
RegionCA3c	-0.800342	0.236339	-3.386	0.000801***
IncTime60	-0.341629	0.220247	-1.551	0.121911

(Dispersion parameter for Gamma family taken to be 2.814719)

Null deviance: 889.92 on 308 degrees of freedom
Residual deviance: 836.09 on 305 degrees of freedom
AIC: 4931
Number of Fisher Scoring iterations: 9

Table 58

ANOVA Full and Condition Null Model ZnT-3 area

Analysis of Deviance Table

Model 1: Area ~ 1 + Condition + Region + IncTime
Model 2: Area ~ 1 + Region + IncTime

	Resid. Df	Resid. Dev	Df	Deviance	Pr(>Chi)
1	304	824.43			
2	305	836.09	-1	-11.664	0.04588*

Table 59

Marginal Means Condition ZnT-3 area

Condition	response	SE	df	lower.CL	upper.CL
control	1370	200	304	1027	1827
forskolin	2025	328	304	1473	2785

Results are averaged over the levels of: Region, IncTime
Confidence level used: 0.95
Intervals are back-transformed from the log scale

Table 60

Marginal Contrast Analysis Condition ZnT-3 area

	Contrast ratio	SE	df	null	t.ratio	p.value
Control / forskolin	0.676	0.134	304	1	-1.967	0.0500

Results are averaged over the levels of: Region, IncTime
Tests are performed on the log scale

Table 61

Region Null Model ZnT-3 area

Call: glm(formula = Area ~ 1 + IncTime + Condition, family = Gamma(link = "log"),
data = FilteredData[Staining == "ZnT",])

Deviance Residuals:

Min	1Q	Median	3Q	Max
-2.3659	-1.9208	-1.5053	-0.1997	3.4414

Coefficients:

	Estimate	Std. Error	T value	Pr(>|z|)
(Intercept)	7.3139	0.2237	32.700	<2e-16***
IncTime60	-0.3176	0.2306	-1.378	0.1693
ConditionForskolin	0.4180	0.2054	2.035	0.0427*

(Dispersion parameter for Gamma family taken to be 3.133209)

Null deviance: 889.92 on 308 degrees of freedom
Residual deviance: 870.31 on 306 degrees of freedom
AIC: 4945.5
Number of Fisher Scoring iterations: 9

Table 62

ANOVA Full and Region Null Model ZnT-3 area

Analysis of Deviance Table

Model 1: Area ~ 1 + Condition + Region + IncTime
Model 2: Area ~ 1 + IncTime + Condition

	Resid. Df	Resid. Dev	Df	Deviance	Pr(>Chi)
1	304	824.43			
2	306	870.31	-2	-45.882	0.0003939***

Table 63

Marginal Means Region ZnT-3 area

$emmeans

Region	response	SE	df	lower.CL	upper.CL
CA3a	2144	439	304	1433	3206
CA3b	2180	450	304	1452	3274
CA3c	989	142	304	745	1312

Results are averaged over the levels of: Condition, IncTime
Confidence level used: 0.95
Intervals are back-transformed from the log scale

Table 64

Marginal Contrast Analysis Condition ZnT-3 area

$contrasts

	Contrast ratio	SE	df	null	t.ratio	p.value
CA3a / CA3b	0.983	0.270	304	1	-0.062	0.9979
CA3a / CA3c	2.168	0.523	304	1	3.208	0.0042
CA3b / CA3c	2.205	0.527	304	1	3.306	0.0030

Results are averaged over the levels of: Condition, IncTime
P value adjustment: tukey method for comparing a family of 3 estimates
Tests are performed on the log scale

Table 65

Incubation Time Null Model ZnT-3 area

Call: glm(formula = Area ~ 1 + Region + Condition, family = Gamma(link = "log"), data = FilteredData[Staining == "ZnT",])

Deviance Residuals:

Min	1Q	Median	3Q	Max
-2.3979	-1.8708	-1.3653	0.0161	4.0262

Coefficients:

	Estimate	Std. Error	T value	Pr(>|z|)
(Intercept)	7.39773	0.21176	34.935	<2e-16***
RegionCA3b	0.02226	0.27397	0.081	0.93529
RegionCA3c	-0.76111	0.24133	-3.154	0.00177**
ConditionForskolin	0.38982	0.19832	1.966	0.05025.

(Dispersion parameter for Gamma family taken to be 2.942197)

Null deviance: 889.92 on 308 degrees of freedom
Residual deviance: 831.85 on 305 degrees of freedom
AIC: 4928.9
Number of Fisher Scoring iterations: 9

Table 66

ANOVA Full and Incubation Time Null Model ZnT-3 area

Analysis of Deviance Table

Model 1: Area ~ 1 + Condition + Region + IncTime
Model 2: Area ~ 1 + Region + Condition

	Resid. Df	Resid. Dev	Df	Deviance	Pr(>Chi)
1	304	824.43			
2	305	831.85	-1	-7.4215	0.1113

Table 67

Marginal Means Condition*Region*IncTime ZnT-3 area

Region	Condition	IncTime	response	SE	df	lower.CL	upper.CL
CA3a	control	15	2093	578	304	1216	3603
CA3b	control	15	2129	608	304	1213	3735
CA3c	control	15	965	223	304	612	1522
CA3a	forskolin	15	3096	861	304	1791	5351
CA3b	forskolin	15	3148	911	304	1782	5563
CA3c	forskolin	15	1428	320	304	918	2219
CA3a	control	60	1484	321	304	969	2273
CA3b	control	60	1510	310	304	1008	2261
CA3c	control	60	685	122	304	482	972
CA3a	forskolin	60	2195	527	304	1369	3521
CA3b	forskolin	60	2233	518	304	1414	3525
CA3c	forskolin	60	1012	197	304	690	1486

Confidence level used: 0.95
Intervals are back-transformed from the log scale

Table 68

Marginal Contrast Analysis Condition*Region*IncTime ZnT-3 area

	Contrast ratio	SE	df	null	t.ratio	p.value
CA3a control15 / CA3a fsk15	0.676	0.134	304	1	-1.967	0.0643
CA3b control15 / CA3b fsk15	0.676	0.134	304	1	-1.967	0.0643
CA3c control15 / CA3c fsk15	0.676	0.134	304	1	-1.967	0.0643
CA3a control60 / CA3a fsk60	0.676	0.134	304	1	-1.967	0.0643
CA3b control60 / CA3b fsk60	0.676	0.134	304	1	-1.967	0.0643
CA3c control60 / CA3c fsk60	0.676	0.134	304	1	-1.967	0.0643
CA3a control15 / CA3b control15	0.983	0.270	304	1	-0.062	0.9509
CA3a fsk15 / CA3b fsk15	0.983	0.270	304	1	-0.062	0.9509
CA3a control15 / CA3c control15	2.168	0.523	304	1	3.208	0.0033
CA3a fsk15 / CA3c fsk15	2.168	0.523	304	1	3.208	0.0033
CA3b control15 / CA3c control15	2.205	0.527	304	1	3.306	0.0033
CA3b fsk15 / CA3c fsk15	2.205	0.527	304	1	3.306	0.0033
CA3a control60 / CA3b control60	0.983	0.270	304	1	-0.062	0.9509
CA3a fsk60 / CA3b fsk60	0.983	0.270	304	1	-0.062	0.9509
CA3a control60 / CA3c control60	2.168	0.523	304	1	3.208	0.0033
CA3a fsk60 / CA3c fsk60	2.168	0.523	304	1	3.208	0.0033
CA3b control60 / CA3c control60	2.205	0.527	304	1	3.306	0.0033
CA3b fsk60 / CA3c fsk60	2.205	0.527	304	1	3.306	0.0033

P value adjustment: BH method for 18 tests
Tests are performed on the log scale

Table 69

Full Model ZnT-3 total area

Call: glm(formula = SummedArea ~ 1 + Condition + Region + IncTime,
family = Gamma(link = "log"), data = Area)

Deviance Residuals:

Min	1Q	Median	3Q	Max
-0.32340	-0.11063	-0.00355	0.07906	0.41671

Coefficients:

	Estimate	Std. Error	T value	Pr(>|t|)
(Intercept)	9.03249	0.05032	179.489	<2e-16***
ConditionForskolin	0.05445	0.04089	1.332	0.18920
RegionCA3b	0.01039	0.05032	0.206	0.83729
RegionCA3c	-0.14578	0.05032	-2.897	0.00566**
IncTime60	0.04944	0.04315	1.146	0.25760

(Dispersion parameter for Gamma family taken to be 0.02212157)

Null deviance: 1.3924 on 52 degrees of freedom
Residual deviance: 1.0443 on 48 degrees of freedom
AIC: 912.38
Number of Fisher Scoring iterations: 4

Table 70

Condition Null Model ZnT-3 total area

Call: glm(formula = SummedArea ~ 1 + Region + IncTime, family = Gamma(link = "log"),
data = Area)

Deviance Residuals:

Min	1Q	Median	3Q	Max
-0.35042	-0.09698	-0.00677	0.07780	0.38640

Coefficients:

	Estimate	Std. Error	t value	Pr(>|t|)
(Intercept)	9.062808	0.045776	197.984	<2e-16***
RegionCA3b	0.007262	0.050486	0.144	0.88622
RegionCA3c	-0.149463	0.050486	-2.961	0.00472**
IncTime60	0.049596	0.043299	1.145	0.25760

(Dispersion parameter for Gamma family taken to be 0.02227743)

Null deviance: 1.3924 on 52 degrees of freedom
Residual deviance: 1.0834 on 49 degrees of freedom
AIC: 912.34
Number of Fisher Scoring iterations: 4

Table 71

ANOVA Condition Null and Full model ZnT-3 total area

Analysis of Deviance Table

Model 1: SummedArea ~ 1 + Condition + Region + IncTime
Model 2: SummedArea ~ 1 + Region + IncTime

	Resid. Df	Resid. Dev	Df	Deviance	Pr(>Chi)
1	48	1.0443			
2	49	1.0834	-1	-0.039121	0.1836

Table 72

Region Null Model ZnT-3 total area

Call: glm(formula = SummedArea ~ 1 + Condition + IncTime, family = Gamma(link = "log"), data = Area)

Deviance Residuals:

Min	1Q	Median	3Q	Max
-0.34114	-0.10849	0.01625	0.10882	0.30759

Coefficients:

	Estimate	Std. Error	t value	Pr(>|t|)
(Intercept)	8.98378	0.04364	205.851	<2e-16***
ConditionForskolin	0.05908	0.04396	1.344	0.185
IncTime60	0.05382	0.04640	1.160	0.252

(Dispersion parameter for Gamma family taken to be 0.02558836)

Null deviance: 1.3924 on 52 degrees of freedom
Residual deviance: 1.3117 on 50 degrees of freedom
AIC: 920.51
Number of Fisher Scoring iterations: 4

Table 73

ANOVA Region Null and Full model ZnT-3 total area

Analysis of Deviance Table

Model 1: SummedArea ~ 1 + Condition + Region + IncTime
Model 2: SummedArea ~ 1 + Condition + IncTime

	Resid. Df	Resid. Dev	Df	Deviance	Pr(>Chi)
1	48	1.0443			
2	50	1.3117	-2	-0.26739	0.002373**

Table 74

Marginal Means Region ZnT-3 total area

$emmeans

Region	response	SE	df	lower.CL	upper.CL
CA3a	8817	323	48	8191	9491
CA3b	8909	319	48	8291	9574
CA3c	7621	273	48	7092	8190

Results are averaged over the levels of: Condition, IncTime
Confidence level used: 0.95
Intervals are back-transformed from the log scale

Table 75

Marginal Contrast Analysis Region ZnT-3 total area

$contrasts

	Contrast ratio	SE	df	null	t.ratio	p.value
CA3a / CA3b	0.99	0.0498	48	1	-0.206	0.9768
CA3a / CA3c	1.16	0.0582	48	1	2.897	0.0154
CA3b / CA3c	1.17	0.0580	48	1	3.150	0.0078

Results are averaged over the levels of: Condition, IncTime
P value adjustment: tukey method for comparing a family of 3 estimates
Tests are performed on the log scale

Table 76

Incubation Time Null Model ZnT-3 total area

Call: glm(formula = SummedArea ~ 1 + Condition + Region, family = Gamma(link = "log"), data = Area)

Deviance Residuals:

Min	1Q	Median	3Q	Max
-0.35355	-0.10325	-0.00667	0.08401	0.38049

Coefficients:

	Estimate	Std. Error	t value	Pr(>|t|)
(Intercept)	9.066345	0.041891	216.426	<2e-16***
ConditionForskolin	0.054582	0.040711	1.341	0.18619
RegionCA3b	0.009442	0.050104	0.188	0.85131
RegionCA3c	-0.147776	0.050104	-2.949	0.00487**

(Dispersion parameter for Gamma family taken to be 0.02193598)

Null deviance: 1.3924 on 52 degrees of freedom
Residual deviance: 1.0732 on 49 degrees of freedom
AIC: 911.83
Number of Fisher Scoring iterations: 4

Table 77

ANOVA Incubation Time Null and Full model ZnT-3 total area

Analysis of Deviance Table

Model 1: SummedArea ~ 1 + Condition + Region + IncTime
Model 2: SummedArea ~ 1 + Condition + Region

	Resid. Df	Resid. Dev	Df	Deviance	Pr(>Chi)
1	48	1.0443			
2	49	1.0732	-1	-0.028864	0.2533

Table 78

Full Model Munc13-1 Mean Intensity

Generalized linear mixed model fit by maximum likelihood (Laplace Approximation) ['glmerMod']
Family: Gamma (log)
Formula: Mean ~ 1 + Condition + IncTime + Region + (1 + Region | Animal) + (1 | SampleName)
Data: FilteredData_Munc
Control: glmerControl(optimizer = "bobyqa")

AIC	BIC	logLik	deviance	df.resid
3250.4	3298.9	-1612.2	3224.4	296

Scaled residuals:

Min	1Q	Median	3Q	Max
-3.1647	-0.3823	0.0363	0.6173	2.6283

Random effects:

Groups	Name	Variance	Std.Dev.	Corr
SampleName	(Intercept)	0.019596	0.13998	
Animal	(Intercept)	0.006695	0.08182	
RegionCA3b		0.009439	0.09716	-0.30
RegionCA3c		0.005440	0.07376	-0.27
Residual		0.048632	0.22053	0.22

Number of obs: 309, groups: SampleName, 18; Animal, 7

Fixed effects:

	Estimate	Std. Error	t value	Pr(>|z|)
(Intercept)	5.40168	0.20433	26.436	<2e-16***
ConditionForskolin	-0.33966	0.16121	-2.107	0.0351*
IncTime60	-0.15284	0.20760	-0.736	0.4616
RegionCA3b	0.11775	0.07495	1.571	0.1162
RegionCA3c	0.16350	0.05797	2.820	0.0048

Correlation of Fixed Effects:

	(Intr)	Cndtnf	IncT60	RgnCA3b
Cndtnfrskln	-0.398			
IncTime60	-0.656	-0.048		
RegionCA3b	-0.079	-0.013	0.018	
RegionCA3c	0.012	0.008	-0.042	0.289

Table 79

Condition Null Model Munc13-1 Mean Intensity

Generalized linear mixed model fit by maximum likelihood (Laplace Approximation) ['glmerMod']
Family: Gamma (log)
Formula: Mean ~ 1 + IncTime + Region + (1 + Region | Animal) + (1 | SampleName)
Data: FilteredData_Munc
Control: glmerControl(optimizer = "bobyqa")

AIC	BIC	logLik	deviance	df.resid
3251.7	3296.5	-1613.9	3227.7	297

Scaled residuals:

Min	1Q	Median	3Q	Max
-3.10731	-0.39519	0.07194	0.62351	2.45510

Random effects:

Groups	Name	Variance	Std.Dev.	Corr
SampleName	(Intercept)	0.029312	0.17121	
Animal	(Intercept)	0.002111	0.04595	
RegionCA3b		0.009557	0.09776	-0.55
RegionCA3c		0.005279	0.07266	-0.39
Residual		0.049940	0.22347	0.21

Number of obs: 309, groups: SampleName, 18; Animal, 7

Fixed effects:

	Estimate	Std. Error	t value	Pr(>|z|)
(Intercept)	5.22093	0.20241	25.793	<2e-16***
IncTime60	-0.14380	0.24662	-0.583	0.55984
RegionCA3b	0.11619	0.07448	1.560	0.11876
RegionCA3c	0.16310	0.05720	2.851	0.00435**

Correlation of Fixed Effects:

	(Intr)	IncT60	RgnCA3b
IncTime60	-0.801		
RegionCA3b	-0.108	0.027	
RegionCA3c	0.043	-0.040	0.280

Table 80

ANOVA Condition Null and Full Model Munc13-1 Mean Intensity

Data: FilteredData_Munc
Models:
NullModel_Condition: Mean ~ 1 + IncTime + Region + (1 + Region | Animal) + (1 | SampleName)
FullModel: Mean ~ 1 + Condition + IncTime + Region + (1 + Region | Animal) + (1 | SampleName)

	npar	AIC	BIC	logLik	deviance	Chisq	Df	Pr(>Chisq)
NullModel_Condition	12	3251.7	3296.5	-1613.9	3227.7			
FullModel	13	3250.4	3298.9	-1612.2	3224.4	3.3087	1	0.06891.

Table 81

Region Null Model Munc13-1 Mean Intensity

Generalized linear mixed model fit by maximum likelihood (Laplace Approximation) ['glmerMod']
Family: Gamma (log)
Formula: Mean ~ 1 + Condition + IncTime + (1 | Animal) + (1 | SampleName)
Data: FilteredData_Munc
Control: glmerControl(optimizer = "bobyqa")

AIC	BIC	logLik	deviance	df.resid
3275.6	3298.0	-1631.8	3263.6	303

Scaled residuals:

Min	1Q	Median	3Q	Max
-3.12688	-0.49864	0.05238	0.57402	2.71443

Random effects:

Groups	Name	Variance	Std.Dev.
SampleName	(Intercept)	0.020440	0.14297
Animal	(Intercept)	0.008283	0.09101
Residual	0.054475	0.23340	

Number of obs: 309, groups: SampleName, 18; Animal, 7

Fixed effects:

	Estimate	Std. Error	t value	Pr(>|z|)
(Intercept)	5.5218	0.2147	25.721	<2e-16***
ConditionForskolin	-0.3480	0.1628	-2.137	0.0326*
IncTime60	-0.1275	0.2100	-0.607	0.5436

Correlation of Fixed Effects:

	(Intr)	Cndtnf
Cndtnfrskln	-0.388	
IncTime60	-0.633	-0.043

Table 82

ANOVA Region Null and Full Model Munc13-1 Mean Intensity

Data: FilteredData_Munc
Models:
NullModel_Region: Mean ~ 1 + Condition + IncTime + (1 | Animal) + (1 | SampleName)
FullModel: Mean ~ 1 + Condition + IncTime + Region + (1 + Region | Animal) + (1 | SampleName)

	npar	AIC	BIC	logLik	deviance	Chisq	Df	Pr(>Chisq)
NullModel_Region	6	3275.6	3298.0	-1631.8	3263.6			
FullModel	13	3250.4	3298.9	-1612.2	3224.4	39.161	7	1.821e-06***

Table 83

Marginal Means Region Munc13-1 Mean Intensity

Region	response	SE	df	asymp.LCL	asymp.UCL
CA3a	173	22.8	Inf	134	224
CA3b	195	28.0	Inf	147	258
CA3c	204	29.2	Inf	154	270

Results are averaged over the levels of: Condition, IncTime
Confidence level used: 0.95
Intervals are back-transformed from the log scale

Table 84

Marginal Contrast Analysis Region Munc13-1 Mean Intensity

$contrasts

	Contrast ratio	SE	df	null	z.ratio	p.value
CA3a/CA3b	0.889	0.0666	Inf	1	-1.571	0.2583
CA3a/CA3c	0.849	0.0492	Inf	1	-2.820	0.0133
CA3b/CA3c	0.955	0.0768	Inf	1	-0.569	0.8367

Results are averaged over the levels of: Condition, IncTime
P value adjustment: tukey method for comparing a family of 3 estimates
Tests are performed on the log scale

Table 85

Incubation Time Null Model Munc13-1 Mean Intensity

Generalized linear mixed model fit by maximum likelihood (Laplace Approximation) ['glmerMod']
Family: Gamma (log)
Formula: Mean ~ 1 + Condition + Region + (1 + Region | Animal) + (1 | SampleName)
Data: FilteredData_Munc
Control: glmerControl(optimizer = "bobyqa")

AIC	BIC	logLik	deviance	df.resid
3248.9	3293.7	-1612.5	3224.9	297

Scaled residuals:

Min	1Q	Median	3Q	Max
-3.1636	-0.3892	0.0554	0.6057	2.6058

Random effects:

Groups	Name	Variance	Std.Dev.	Corr
SampleName	(Intercept)	0.021379	0.14621	
Animal	(Intercept)	0.005881	0.07669	
RegionCA3b		0.009673	0.09835	-0.41
RegionCA3c		0.005480	0.07403	-0.36
Residual		0.048870	0.22107	0.24

Number of obs: 309, groups: SampleName, 18; Animal, 7

Fixed effects:

	Estimate	Std. Error	t-value	Pr(>|z|)
(Intercept)	5.30387	0.15511	34.194	<2e-16***
ConditionForskolin	-0.34577	0.17130	-2.018	0.04354*
RegionCA3b	0.11838	0.07531	1.572	0.11597
RegionCA3c	0.16162	0.05749	2.811	0.00494**

Correlation of Fixed Effects:

	(Intr)	Cndtnf	RgnCA3b
Cndtnfrskln	-0.600		
RegionCA3b	-0.153	-0.009	
RegionCA3c	-0.072	0.008	0.295

Table 86

ANOVA Incubation Time Null and Full Model Munc13-1 Mean Intensity

Data: FilteredData_Munc
Models:
NullModel_IncTime: Mean ~ 1 + Condition + Region + (1 + Region | Animal) + (1 | SampleName)
FullModel: Mean ~ 1 + Condition + IncTime + Region + (1 + Region | Animal) + (1 | SampleName)

	npar	AIC	BIC	logLik	deviance	Chisq	Df	Pr(>Chisq)
NullModel_IncTime	12	3248.9	3293.7	-1612.5	3224.9			
FullModel	13	3250.4	3298.9	-1612.2	3224.4	0.5184	1	0.4715

Table 87

Marginal Means Munc13-1 Mean Intensity Condition*Region*IncTime

Region	Condition	IncTime	response	SE	df	asymp.LCL	asymp.UCL
CA3a	control	15	222	45.3	Inf	149	331
CA3b	control	15	249	52.9	Inf	165	378
CA3c	control	15	261	55.6	Inf	172	397
CA3a	forskolin	15	158	32.2	Inf	106	235
CA3b	forskolin	15	178	37.4	Inf	118	268
CA3c	forskolin	15	186	39.6	Inf	123	282
CA3a	control	60	190	32.5	Inf	136	266
CA3b	control	60	214	38.9	Inf	150	306
CA3c	control	60	224	40.0	Inf	158	318
CA3a	forskolin	60	136	21.7	Inf	99	186
CA3b	forskolin	60	152	26.0	Inf	109	213
CA3c	forskolin	60	160	27.0	Inf	115	222

Confidence level used: 0.95
Intervals are back-transformed from the log scale

Table 88

Marginal Contrast Analysis Munc13-1 Mean Intensity Condition*Region*IncTime

	contrast ratio	SE	df	null	z.ratio	p.value
CA3a control 15 / CA3a fsk 15	1.404	0.2264	Inf	1	2.107	0.0632
CA3b control 15 / CA3b fsk 15	1.404	0.2264	Inf	1	2.107	0.0632
CA3c control 15 / CA3c fsk 15	1.404	0.2264	Inf	1	2.107	0.0632
CA3a control 60 / CA3a fsk 60	1.404	0.2264	Inf	1	2.107	0.0632
CA3b control 60 / CA3b fsk 60	1.404	0.2264	Inf	1	2.107	0.0632
CA3c control 60 / CA3c fsk 60	1.404	0.2264	Inf	1	2.107	0.0632
CA3a control 15 / CA3b control 15	0.889	0.0666	Inf	1	-1.571	0.1494
CA3a fsk 15 / CA3b fsk 15	0.889	0.0666	Inf	1	-1.571	0.1494
CA3a control 15 / CA3c control 15	0.849	0.0492	Inf	1	-2.820	0.0216
CA3a fsk 15 / CA3c fsk 15	0.849	0.0492	Inf	1	-2.820	0.0216
CA3b control 15 / CA3c control 15	0.955	0.0768	Inf	1	-0.569	0.5694
CA3b fsk 15 / CA3c fsk 15	0.955	0.0768	Inf	1	-0.569	0.5694
CA3a control 60 / CA3b control 60	0.889	0.0666	Inf	1	-1.571	0.1494
CA3a fsk 60 / CA3b fsk 60	0.889	0.0666	Inf	1	-1.571	0.1494
CA3a control 60 / CA3c control 60	0.849	0.0492	Inf	1	-2.820	0.0216
CA3a fsk 60 / CA3c fsk 60	0.849	0.0492	Inf	1	-2.820	0.0216
CA3b control 60 / CA3c control 60	0.955	0.0768	Inf	1	-0.569	0.5694
CA3b fsk 60 / CA3c fsk 60	0.955	0.0768	Inf	1	-0.569	0.5694

P value adjustment: BH method for 18 tests
Tests are performed on the log scale

Table 89

Full Model ZnT-3 Mean Intensity

Generalized linear mixed model fit by maximum likelihood (Laplace Approximation) ['glmerMod']
Family: Gamma (log)
Formula: Mean ~ 1 + Condition + IncTime + Region + (1 + Region | SampleName)
Data: FilteredData[Staining == "ZnT",]
Control: glmerControl(optimizer = "bobyqa")

AIC	BIC	logLik	deviance	df.resid
2882.1	2926.9	-1429.0	2858.1	297

Scaled residuals:

Min	1Q	Median	3Q	Max
-1.8897	-0.5480	-0.0262	0.4807	5.4782

Random effects:

Groups	Name	Variance	Std.Dev.	Corr
SampleName	(Intercept)	0.02768	0.1664	
	RegionCA3b	0.01050	0.1024	-0.18
	RegionCA3c	0.01698	0.1303	-0.40
Residual		0.02185	0.1478	0.46

Number of obs: 309, groups: SampleName, 18

Fixed effects:

	Estimate	Std.-Error	t-value	Pr(>|z|)
(Intercept)	5.66608	0.21736	26.067	<2e-16***
ConditionForskolin	-0.31087	0.22553	-1.378	0.1681
IncTime60	-0.45984	0.23067	-1.994	0.0462*
RegionCA3b	0.10252	0.04319	2.374	0.0176*
RegionCA3c	0.06935	0.05393	1.286	0.1985

Correlation of Fixed Effects:

	(Intr)	Cndtnf	IncT60	RgnCA3b
Cndtnfrskln	-0.564			
IncTime60	-0.660	0.001		
RegionCA3b	0.027	-0.007	0.015	
RegionCA3c	-0.054	0.017	-0.052	0.486

Table 90

Condition Null Model ZnT-3 Mean Intensity

Generalized linear mixed model fit by maximum likelihood (Laplace Approximation) ['glmerMod']
Family: Gamma (log)
Formula: Mean ~ 1 + IncTime + Region + (1 + Region | SampleName)
Data: FilteredData[Staining == "ZnT",]
Control: glmerControl(optimizer = "bobyqa")

AIC	BIC	logLik	deviance	df.resid
2881.8	2922.9	-1429.9	2859.8	298

Scaled residuals:

Min	1Q	Median	3Q	Max
-1.8984	-0.5314	-0.0148	0.4617	5.5345

Random effects:

Groups	Name	Variance	Std.Dev.	Corr
SampleName	(Intercept)	0.03091	0.1758	
	RegionCA3b	0.01120	0.1058	-0.26
	RegionCA3c	0.01728	0.1314	-0.45
Residual		0.02152	0.1467	0.48

Number of obs: 309, groups: SampleName, 18

Fixed effects:

	Estimate	Std.-Error	t-value	Pr(>|z|)
(Intercept)	5.49613	0.19720	27.871	<2e-16**
IncTime60	-0.45296	0.25547	-1.773	0.0762.
RegionCA3b	0.10216	0.04364	2.341	0.0192*
RegionCA3c	0.06968	0.05451	1.278	0.2011

Correlation of Fixed Effects:

	(Intr)	IncT60	RgnCA3b
IncTime60	-0.802		
RegionCA3b	-0.054	0.009	
RegionCA3c	-0.114	-0.060	0.486

Table 91

ANOVA Condition Null and Full Model ZnT-3 Mean Intensity

Data: FilteredData[Staining == "ZnT",]
Models:
NullModel_Condition: Mean ~ 1 + IncTime + Region + (1 + Region | SampleName)
FullModel: Mean ~ 1 + Condition + IncTime + Region + (1 + Region | SampleName)

	npar	AIC	BIC	logLik	deviance	Chisq	Df	Pr(>Chisq)
NullModel_Condition	11	2881.8	2922.9	-1429.9	2859.8			
FullModel	12	2882.1	2926.9	-1429.0	2858.1	1.7733	1	0.183

Table 92

Region Null Model ZnT-3 Mean Intensity

Generalized linear mixed model fit by maximum likelihood (Laplace Approximation) ['glmerMod']
Family: Gamma (log)
Formula: Mean ~ 1 + Condition + IncTime + (1 + Region | SampleName)
Data: FilteredData[Staining == "ZnT",]
Control: glmerControl(optimizer = "bobyqa")

AIC	BIC	logLik	deviance	df.resid
2882.5	2919.9	-1431.3	2862.5	299

Scaled residuals:

Min	1Q	Median	3Q	Max
-1.8978	-0.5151	-0.0403	0.4973	5.6122

Random effects:

Groups	Name	Variance	Std.Dev.	Corr
SampleName	(Intercept)	0.02974	0.1724	
	RegionCA3b	0.01693	0.1301	-0.27
	RegionCA3c	0.01990	0.1411	-0.45
Residual		0.02202	0.1484	0.59

Number of obs: 309, groups: SampleName, 18

Fixed effects:

	Estimate	Std.-Error	t-value	Pr(>|z|)
(Intercept)	5.6588	0.2118	26.714	<2e-16***
ConditionForskolin	-0.3066	0.2266	-1.353	0.1762
IncTime60	-0.4602	0.2334	-1.972	0.0486*

Correlation of Fixed Effects:

	(Intr)	Cndtnf
Cndtnfrskln	-0.462	
IncTime60	-0.638	0.000

Table 93

ANOVA Region Null and Full Model ZnT-3 Mean Intensity

Data: FilteredData[Staining == "ZnT",]
Models:
NullModel_Region: Mean ~ 1 + Condition + IncTime + (1 + Region | SampleName)
FullModel: Mean ~ 1 + Condition + IncTime + Region + (1 + Region | SampleName)

	npar	AIC	BIC	logLik	deviance	Chisq	Df	Pr(>Chisq)
NullModel_Region	10	2882.5	2919.9	-1431.3	2862.5			
FullModel	12	2882.1	2926.9	-1429.0	2858.1	4.4664	2	0.1072

Table 94

Incubation Time Null Model ZnT-3 Mean Intensity

Generalized linear mixed model fit by maximum likelihood (Laplace Approximation) ['glmerMod']
Family: Gamma (log)
Formula: Mean ~ 1 + Condition + Region + (1 + Region | SampleName)
Data: FilteredData[Staining == "ZnT",]
Control: glmerControl(optimizer = "bobyqa")

AIC	BIC	logLik	deviance	df.resid
2883.4	2924.4	-1430.7	2861.4	298

Scaled residuals:

Min	1Q	Median	3Q	Max
-1.8781	-0.5442	-0.0632	0.4673	5.4319

Random effects:

Groups	Name	Variance	Std.Dev.	Corr
SampleName	(Intercept)	0.03607	0.1899	
	RegionCA3b	0.01136	0.1066	-0.23
	RegionCA3c	0.01752	0.1324	-0.46
Residual		0.02218	0.1489	0.50

Number of obs: 309, groups: SampleName, 18

Fixed effects:

	Estimate	Std.-Error	t-value	Pr(>|z|)
(Intercept)	5.37815	0.19711	27.285	<2e-16***
ConditionForskolin	-0.30086	0.27269	-1.103	0.2699
RegionCA3b	0.10292	0.04374	2.353	0.0186*
RegionCA3c	0.06283	0.05387	1.166	0.2435

Correlation of Fixed Effects:

	(Intr)	Cndtnf	RgnCA3b
Cndtnfrskln	-0.744		
RegionCA3b	-0.007	-0.011	
RegionCA3c	-0.222	0.009	0.495

Table 95

ANOVA Incubation Time Null and Full Model ZnT-3 Mean Intensity

Data: FilteredData[Staining == "ZnT",]
Models:
NullModel_IncTime: Mean ~ 1 + Condition + Region + (1 + Region | SampleName)
FullModel: Mean ~ 1 + Condition + IncTime + Region + (1 + Region | SampleName)

	npar	AIC	BIC	logLik	deviance	Chisq	Df	Pr(>Chisq)
NullModel_IncTime	11	2883.4	2924.4	-1430.7	2861.4			
FullModel	12	2882.1	2926.9	-1429.0	2858.1	3.2905	1	0.06968.

Part III: Synapsin TKO

Table 96: Overview of slice and animal numbers for different experimental groups for field recordings. *Note: all numbers reported for individual experiments are only from the included subset of recordings.*

s = number of slices a = number of animals	**C57BL/6J (4-6 weeks)**	**Synapsin TKO (4-6 weeks)**		**C57BL/6J (17-19 weeks)**	**Synapsin TKO (18 -19 weeks)**
		From Italy (4-5 weeks)	**From Berlin (4-6 weeks)**		
Recorded	s = 67 a = 12	s = 39 a = 9	s = 18 a = 7	s = 29 a = 5	s = 24 a = 5
Included	s = 31 a = 12	s = 24 a = 9	s = 14 a = 4	s = 17 a = 4	s = 19 a = 5
Input-Output Ratio	s = 31 a = 12	s = 23 a = 9	s = 14 a = 4	s = 17 a = 4	s = 18 a = 5
Paired-Pulse Ratio	s = 31 a = 12	s = 20 a = 8	s = 14 a = 4	s = 17 a = 4	s = 19 a = 5
1 Hz Facilitation	s = 31 a = 12	s = 15 a = 5	s = 12 a = 4	s = 17 a = 4	s = 19 a = 5
25 Hz Stimulation	s = 11 a = 5	s = 4 a = 3	s = 8 a = 3	s = 17 a = 4	s = 17 a = 5
PTP + LTP	s = 15 a = 6	s = 13 a = 6	s = 10 a = 3	s = 17 a = 4	s = 19 a = 5

Table 97: Exclusion reasons for field recordings. *Note that several reasons can apply to the same recording.*

Excluded recordings	**C57BL/6J (4-6 weeks)**	**Synapsin TKO (4-6 weeks)**	**C57BL/6J (17-19 weeks)**	**Synapsin TKO (18 -19 weeks)**
Baseline EPSP < 50 µV	4	2	2	2
DCG-IV effect < 75 %	27	14	11	4
Other reasons	6	2	0	1
Total number	36	19	12	5

Table 98: Statistical comparison for experimental values between two cohorts of presymptomatic SynTKO animals.

Experiment	**Measure**	**Presynaptic SynTKO animals from Italy**	**Presynaptic SynTKO animals from Berlin**
Input-Output	Slope of simple linear regression	1.341	0.833
	Ranges of 95 % confidence band	0.5494 to 2.134	0.09287 to 1.573
	p-value slopes (ANCOVA)	0.69	
1 Hz facilitation	Median	4.440	5.955
	Interquartile range	3.760 - 6.260	3.753 - 11.41
	p value (Mann-Whitney *U* test)	0.3473	
Paired-pulse ratio	Median	3.557	4.545
	Interquartile ranges	2.299 - 4.260	2.568 - 6.035
	p-value (Mann-Whitney *U* test)	0.0899	
PTP (norm. fEPSP)	Median	3.469	4.116
	Interquartile ranges	2.118 - 4.589	3.374 - 7.144
	p-value (Mann-Whitney *U* test)	0.1151	
LTP after 30 minutes (norm. fEPSP)	Median	245.2	228.8
	Interquartile ranges	198.3 - 302.9	182.5 - 384.4
	p-value (Mann-Whitney *U* test)	0.8793	

Abbreviations

Table 99: List of abbreviations.

2D	Two-dimensional
3D	Three-dimensional
AC	Adenylyl cyclase
ACSF	Artificial cerebrospinal fluid
AMPA	α-amino-3-hydroxy-5-methyl-4-isoxazolepropionic acid
ANCOVA	Analysis of covariance
ANOVA	Analysis of variance
BAPTA	1,2-bis(o-amino phenoxy)ethane-N,N,N′,N′-tetraacetic acid
BDNF	Brain-derived neurotrophic factor
CA	*Cornu ammonis*
CaMKII	Ca^{2+}/calmodulin-dependent protein kinase II
cAMP	Cyclic adenosine monophosphate
$Ca_v2.1$	α-1A subunit containing voltage-gated calcium channel
$Ca_v2.2$	α-1B subunit containing voltage-gated calcium channel
$Ca_v2.3$	α-1E subunit containing voltage-gated calcium channel
DCG-IV	(2S,1'R,2'R,3'R)-2(2,3-dicarboxycyclopropyl)glycine
DG	Dentate gyrus
DMSO	Dimethyl sulfoxide
EC	Entorhinal cortex
EGTA	ethylene glycol-bis(β-aminoethyl ether)-N,N,N′,N′-tetraacetic acid
Epac2	Exchange protein directly activated by cAMP 2
EphB	Ephrin receptor B
fEPSP	Field excitatory postsynaptic potential
GABA	γ-Aminobutyric acid (*gamma*-aminobutyric acid)
GLM	Generalized linear mixed model
GLMM	Generalized linear mixed model
gSTED	Time-gated stimulated emission depletion
HEPES	(4-(2-hydroxyethyl)-1-piperazineethanesulfonic acid)
hsACSF	High sucrose artificial cerebrospinal fluid

ISI	Inter-stimulus interval
LTP	Long-term potentiation
NA	Numerical aperture
NMDA	*N*-methyl-D-aspartic acid or *N*-methyl-D-aspartate
PB	Phosphate buffer
PBS	Phosphate-buffered saline
PFA	Paraformaldehyde
PFV	Presynaptic fiber volley
PKA	Protein kinase A
PPR	Paired-pulse ratio
PTP	Post-tetanic potentiation
RIM	Rab3-interacting molecule
RIM-BP	RIM-binding protein
ROI	Region of interest
rpm	Rounds per minute
RRID	Research resource identifier
RRP	Readily releasable pool
SEM	Standard error of the mean
SD	Standard deviation
SM	Sec1/Munc18-like
SNAP-25	soluble N-ethylmaleimide-sensitive-factor attachment protein-25
SNARE	soluble N-ethylmaleimide-sensitive-factor attachment receptor
SynDKO	Synapsin double knockout
SynTKO	Synapsin triple knockout
TrkB	Tropomyosin receptor kinase B
VGCC	Voltage-gated calcium channel
WT	Wildtype
ZnT-3	Zinc transporter 3

Statement of Contributions

All experiments in this thesis were conceived and designed by my PhD supervisors Prof. Dr. Dietmar Schmitz, Dr. Jörg Breustedt, Dr. Marta Orlando and myself. All immunohistochemical work, super-resolution and confocal imaging as well as the analysis of imaging data were performed by me. Some of the data presented for the synapsin part were acquired with the help of colleagues. The final analysis was performed by me.

Contributions from my colleagues to the synapsin dataset in this thesis include:

Dr. Laura Moreno-Velasquez (AG Schmitz, Neuroscience Research Centre, Charité Universitätsmedizin Berlin) contributed 62/177 field recordings.

Dr. Alexander Stumpf (AG Schmitz, Neuroscience Research Center, Charité Universitätsmedizin Berlin) contributed 55/177 field recordings.

List of Publications

Related to this Dissertation

Orlando M*, Dvorzhak A*, **Bruentgens F***, Maglione M, Rost BR, Sigrist SJ, et al. (2021) Recruitment of release sites underlies chemical presynaptic potentiation at hippocampal mossy fiber boutons. PLoS Biol 19(6): e3001149. https://doi.org/10.1371/journal.pbio.3001149
(*shared co-first authorship)

Bruentgens F, Moreno Velasquez L, Stumpf A, Parthier D, Breustedt J, Benfenati F, Milovanovic D, Schmitz D, Orlando M (2023) The synapsin-dependent vesicle cluster is crucial for presynaptic plasticity at a glutamatergic synapse in male mice. bioRxiv 2023.08.08.549335; https://doi.org/10.1101/2023.08.08.549335 **(Preprint)**

Non-Related to this Dissertation

Mahn M, Saraf-Sinik I, Patil P, Pulin M, Bitton E, Karalis N, **Bruentgens F**, Palgi S, Gat A, Dine J, Wietek J, Davidi I, Levy R, Litvin A, Zhou F, Sauter K, Soba P, Schmitz D, Lüthi A, Rost BR, Wiegert JS, Yizhar O. Efficient optogenetic silencing of neurotransmitter release with a mosquito rhodopsin. Neuron. 2021 May 19;109(10):1621-1635.e8. doi: 10.1016/j.neuron.2021.03.013. Epub 2021 May 11. PMID: 33979634; PMCID: PMC7611984.

Fleck D, Kenzler L, Mundt N, Strauch M, Uesaka N, Moosmann R, **Bruentgens F**, Missel A, Mayerhofer A, Merhof D, Spehr J, Spehr M. ATP activation of peritubular cells drives testicular sperm transport. Elife. 2021 Jan 27;10:e62885. doi: 10.7554/eLife.62885. PMID: 33502316; PMCID: PMC7840184.

Fleck D, Mundt N, **Bruentgens F**, Geilenkirchen P, Machado PA, Veitinger T, Veitinger S, Lipartowski SM, Engelhardt CH, Oldiges M, Spehr J, Spehr M. Distinct purinergic signaling pathways in prepubescent mouse spermatogonia. J Gen Physiol. 2016 Sep;148(3):253-71. doi: 10.1085/jgp.201611636. PMID: 27574293; PMCID: PMC5004339.